



instituto  
de investigación  
en ingeniería de Aragón



PhD Thesis

---

Theoretical Analysis of  
Autonomic Nervous System  
Effects on Cardiac  
Electrophysiology and its  
Relationship with Arrhythmic  
Risk

---

David Adolfo Sampedro Puente

*Supervisors:*

Pablo Laguna Lasiosa

Esther Pueyo Paules

Jesús Fernández Bes

Zaragoza, February 2020





instituto  
de investigación  
en ingeniería de Aragón



**PhD Thesis**

# Theoretical Analysis of Autonomic Nervous System Effects on Cardiac Electrophysiology and its Relationship with Arrhythmic Risk

**David Adolfo Sampedro Puente**

*Supervisors:*

Pablo Laguna Lasasa

Esther Pueyo Paules

Jesús Fernández Bes

**Zaragoza, February 2020**



*Agus, va por ti*



# Theoretical Analysis of Autonomic Nervous System Effects on Cardiac Electrophysiology and its Relationship with Arrhythmic Risk

David Adolfo Sampedro Puente, 2020

Date of current version: Wednesday 15<sup>th</sup> January, 2020

This thesis was supported by the European Research Council through grant ERC-2014-StG 638284, by MINECO (Spain) through project DPI2016-75458-R, by MULTITOOLS2 HEART-ISCIH, by Gobierno de Aragón (Reference Group BSICoS T39-17R) cofunded by FEDER 2014-2020, by European Social Fund (EU) and Gobierno de Aragón through a personal predoctoral grant, by Campus Iberus and Erasmus+ Program, by Fundación CAI-Ibercaja. Computations simulations were performed by ICTS NANBIOSIS (High Performance Computing Unit of CIBER-BBN at University of Zaragoza).

This thesis was printed thanks to the financial support of BSICoS Group at University of Zaragoza.

The figure displayed in the cover page is extracted and adapted from National Heart Foundation of Australia webpage [www.heartfoundation.org.au](http://www.heartfoundation.org.au).





# Acknowledgements

The path of the doctoral thesis is coming to the end and it is time to thank all the help, support and friendship that I have received during these years.

First of all, I would like to thank my thesis supervisors: Esther, Pablo and Jesús. Thank you very much for trusting in me and giving me this opportunity to grow as a researcher and, more importantly, as a person. And thank you very much for all your support and for the hours you have dedicated to me. You have been the best thesis supervisors that a PhD student could desire.

In addition, I would like to thank all wonderful people who form the BSICoS Group at the University of Zaragoza, thank you very much for making me feel like one more member of the family. Special mention deserve the members of Cursed Lab (Álex, Carlos, Juan and Gonzalo), thank you very much for every tip, every trick and every joke (I hope I was an excellent Padawan).

My research visit at INRIA-Paris has been one of the best moments of my life. I would like to thank Miguel Ángel, Damiano, Fabien, Felipe and all members of INRIA for your friendship, support, help and advice. In addition, I would like to thank *Colegio de España en París* for hosting me, and also, for giving me the opportunity to join the Brunch Team (María and Lucía)

In addition, I would like to thank co-authors of my scientific contributions. Your guidance, help, effort and dedication have significantly improved the quality of all these works.

I would also like to thank all those friends (and their families) who always accompany me on my journey: Manolo, Evaristo, Javi Ruiz, Josh, Taoro, Transi, Rafa, Luis Gan, Juan Omiste, López, Jorge, Javi Lacasta, Ana, Emiliano, Rubén, Mike, Luisca, and many others that I leave unmentioned because of lack of space, but not of affection and gratitude. And of course, thanks to the Unizar Team: Gonzalo, Alberto Hernando and Alberto Badías.

A special mention should be dedicated to Miguel Ángel and all the staff of the Edificio Aida. Thank you very much for welcoming me into your big family and making my life much easier.

I would like to thank the Diputación General de Aragón and the European Social Fund for the predoctoral research contract that I have been awarded over these years. I would also like to thank the CAI-Ibercaja Foundation and the Campus Iberus Erasmus+ for the financial support through which the research visit in research center INRIA Paris was carried out. In addition, I would like to thank the University of Zaragoza, specially to the staff of I3A (*Instituto de Investigación en Ingeniería de Aragón*), for your help and support.

María José, I would like to thank you for showing me what is really important and for bringing a smile to my face everyday. In addition, I would like to thank your family (specially to Valeria, Vega and those who will come), thanks for everything. MJ, always by your side.

Isabel and Jesús, I would like to thank you for giving me life and for all the efforts that you have had to achieve this objective. Without your help, I would not have come this far. All for one, one for all.

A handwritten signature in blue ink, appearing to read 'David', is written over a long, thin horizontal line that extends across the page.

David Adolfo Sampedro Puente

# Agradecimientos

El camino de la tesis doctoral está llegando a su fin y es hora de agradecer toda la ayuda, apoyo y amistad que he ido recibiendo durante estos años.

Primeramente, me gustaría darle las gracias a mis directores de tesis: Esther, Pablo y Jesús. Muchas gracias por confiar en mí y darme esta oportunidad para crecer como investigador, y más importante, para crecer como persona. Muchas gracias por todo vuestro apoyo y por la cantidad de horas que me habéis dedicado. Habéis sido los mejores directores que cualquier estudiante de doctorado puede desear.

Además, me gustaría darle las gracias a toda la gente maravillosa que forma parte del grupo BSICoS de la Universidad de Zaragoza. Muchas gracias por haberme hecho sentir como un miembro más de la familia. Una mención especial se merecen los miembros del Laboratorio Maldito (Álex, Carlos, Juan y Gonzalo), muchas gracias por cada consejo, cada truco y cada chiste (espero haber sido un buen Padawan).

Mi estancia de investigación en INRIA-París ha sido uno de los mejores momentos de mi vida. Me gustaría darle las gracias a Miguel Ángel, Damiano, Fabien, Felipe y al resto de miembros de INRIA por su amistad, apoyo, ayuda y consejo. Además, me gustaría darle las gracias al *Colegio de España en París* por acogerme, y también por darme la oportunidad de unirme al Equipo Brunch (María y Lucía).

Por otro lado, me gustaría darle las gracias a todos los co-autores de mis contribuciones científicas. Vuestra orientación, ayuda, esfuerzo y dedicación han contribuido a mejorar significativamente la calidad de estos trabajos.

También me gustaría darle las gracias a todos esos amigos (y a sus familias) que siempre me acompañan en mi viaje: Manolo, Evaristo, Javi Ruiz, Josh, Taoro, Transi, Rafa, Luis Gan, Juan Omiste, López, Jorge, Javi Lacasta, Ana, Emiliano, Rubén, Mike, Luisca, y otros muchos más que me dejo sin mencionar por falta de espacio, pero no por falta de afecto y gratitud. Y como no, muchas gracias al Equipo Unizar: Gonzalo, Alberto Hernando y Alberto Badías.

Debo dedicar una especial mención a Miguel Ángel y a todo el personal del Edificio Aida. Muchas gracias por dejarme formar parte de vuestra gran familia y por hacerme la vida mucho más fácil.

Quisiera mostrar mi agradecimiento a la Diputación General de Aragón y al Fondo Social Europeo por el contrato de investigador predoctoral que he disfrutado durante estos años. Además, quisiera agradecer a la Fundación CAI-Ibercaja y Campus Iberus Erasmus+ la financiación económica por medio de la cual pudo realizarse la estancia de investigación en el centro de investigación INRIA de París. Además me gustaría darle las gracias a la Universidad de Zaragoza, especialmente a todo el personal del I3A (*Instituto de Investigación en Ingeniería de Aragón*) por vuestra ayuda y apoyo.

María José, muchas gracias por mostrarme qué es realmente importante en la vida y por traerme una sonrisa a la cara todos los días. Además, me gustaría darle las gracias a tu familia por todo lo que hacen por mí (especialmente a Valeria, Vega y a todos los que están por venir). MJ, siempre a tu lado.

Isabel y Jesús, muchas gracias por darme la vida y por todos los esfuerzos que habéis tenido que hacer para conseguir este objetivo. Sin vuestra ayuda, no hubiera llegado hasta aquí. Todos para uno, uno para todos.

A handwritten signature in blue ink, appearing to read 'David', is written over a long, thin horizontal line that extends across the page.

David Adolfo Sampedro Puente

# Abstract

Cardiovascular diseases represent the main cause of mortality and morbidity in industrialized societies. A significant percentage of deaths associated with these diseases is related to the generation of **cardiac arrhythmias**, defined as abnormalities in the electrical functioning of the heart. Three major elements are involved in the development of arrhythmias, which include an arrhythmogenic substrate, a trigger and modulating factors. The **Autonomic Nervous System** (ANS) is the most relevant of these modulators. The ANS is composed of two branches, sympathetic and parasympathetic, which to a certain extent act antagonistically to each other. The possibility of revealing how the sympathetic nervous system modulates the activity of the ventricles (lower heart chambers) and participates in the development of arrhythmias, as reported experimentally, could be crucial to advance in the design of new clinical therapies aimed at preventing or treating these rhythm abnormalities.

This thesis investigates spatio-temporal variability of human ventricular repolarization, its modulation by the sympathetic nervous system, the mechanisms behind highly elevated variability and the relationship to the generation of ventricular arrhythmias. To that end, methodologies combining **signal processing** of ventricular signals and ***in silico* modeling** of human ventricular myocytes are proposed. The developed *in silico* models include coupled theoretical descriptions of electrophysiology, calcium dynamics, mechanical stretch and  $\beta$ -adrenergic signaling. To account for temporal (beat-to-beat) repolarization variability, stochasticity is added into the equations defining the gating of the ion channels of the main currents active during action potential (AP) repolarization, i.e. during the return of the cell to the resting state after an excitation. To account for spatial (cell-to-cell) repolarization variability, a population of models representative of different cellular characteristics are constructed and calibrated based on available experimental data. The theoretical computational research of this study, combined with the processing of clinical and experimental ventricular signals, lays the ground for future studies aiming at improving arrhythmic risk stratification methods and at guiding the search for more efficient anti-arrhythmic therapies.

In **Chapter 2**, a population of experimentally-calibrated stochastic human ventricular computational cell models coupling electrophysiology, mechanics and  $\beta$ -adrenergic signaling are built to investigate spatio-temporal variability. Model calibration is based on experimental ranges of a number of AP-derived markers describing AP duration, amplitude and shape. By using the proposed population of stochastic AP models, the experimentally reported interactions between a particular type of temporal variability associated with low-frequency (LF) oscillations of AP duration (APD) and overall beat-to-beat variability of repolarization (BVR) in response to enhanced sympathetic activity are reproduced. Ionic mechanisms behind correlated increments in both phenomena are investigated and found to be related to downregulation of the

inward and rapid delayed rectifier  $K^+$  currents and the L-type  $Ca^{2+}$  current. Concomitantly elevated levels of LF oscillations of APD and BVR in diseased ventricles are shown to lead to electrical instabilities and arrhythmogenic events.

In **Chapter 3**, the time delay for manifestation of LF oscillations of APD, as a particular form of repolarization variability, is investigated in ventricular myocytes in response to sympathetic provocation. By using an experimentally-calibrated population of human ventricular AP models, as in Chapter 2, this oscillatory latency is demonstrated to be associated with the slow phosphorylation kinetics of the slow delayed rectifier  $K^+$  current  $I_{Ks}$  in response to  $\beta$ -adrenergic stimulation. Prior stimulation of  $\beta$ -adrenoceptors substantially reduces the time required for the development of LF oscillations. In addition, short time lapses are shown to be related to large APD oscillatory magnitudes, as measured in Chapter 2, particularly in cells susceptible to develop arrhythmogenic events in response to sympathetic stimulation.

The experimental calibration of the population of models used in Chapter 2 and Chapter 3, despite ensuring that simulated population measurements lie within experimental limits, does not guarantee that each model in the constructed population represents the experimental measurements of an individual human ventricular cardiomyocyte. It is for that reason that in **Chapter 4** a novel methodology is developed to construct computational populations of human ventricular cell models that more faithfully recapitulate individual available experimental evidences. The proposed methodology is based on the formulation of nonlinear state-space representations and the use of the Unscented Kalman Filter (UKF) to estimate parameters and state variables of an underlying stochastic AP model given any input voltage trace. Tests performed over synthetic and experimental voltage traces demonstrate that this methodology successfully renders a one-to-one match between input AP traces and sets of model parameters (ionic current conductances) and state variables (ionic gating variables and intracellular concentrations). The proposed methodology is shown to be robust for investigation of spatio-temporal variability in human ventricular repolarization.

**Chapter 5** improves the methodology developed in Chapter 4 to more accurately estimate parameters and state variables of stochastic human ventricular cell models from individual input voltage traces and to reduce the converge time so as to provide faster estimation. The improvements are based on the combined use of the UKF method of Chapter 4 together with Double Greedy Dimension Reduction (DGDR) method with automatic generation of biomarkers. Additionally, on top of estimating ionic current conductances at baseline conditions, the approach presented in this chapter also provides a set of  $\beta$ -adrenergic-induced phosphorylation levels, thus contributing to the analysis of spatio-temporal repolarization patterns with and without autonomic modulation.

In **conclusion**, this thesis presents novel methodologies for characterization of spatio-temporal variability of human ventricular repolarization, for dissection of its underlying mechanisms and for ascertainment of the relationship between elevated variability and increased risk for ventricular arrhythmias and sudden cardiac death.

---

Sets of stochastic human computational cell models with representation of ventricular electrophysiology, mechanics and  $\beta$ -adrenergic signaling are developed and used to analyze overall beat-to-beat and cell-to-cell repolarization variability as well as a particular type of variability in the form of LF oscillations. To faithfully reproduce experimentally measured variability patterns in a one-to-one manner, methodologies are proposed to construct populations of human ventricular AP models where the parameters and state variables of a model are estimated from a given input voltage trace. These personalized models open the door to more robust investigation of the causes and consequences of spatio-temporal variability of human ventricular repolarization.





# Resumen y Conclusiones

Las enfermedades cardiovasculares representan la principal causa de mortalidad y morbilidad en las sociedades industrializadas. Un porcentaje significativo de las muertes asociadas a estas enfermedades está relacionado con el desarrollo de **arritmias cardíacas**, siendo éstas definidas como anomalías en el funcionamiento eléctrico del corazón. Tres son los elementos principales que están involucrados en el desarrollo de las arritmias: un sustrato arritmogénico, un desencadenante y factores de modulación. El **Sistema Nervioso Autónomo (SNA)** es el más relevante de estos factores moduladores. El SNA está compuesto por dos ramas, simpática y parasimpática, que en cierta medida actúan de forma antagónica entre sí. La posibilidad de identificar cómo el sistema nervioso simpático modula la actividad ventricular y participa en el desarrollo de arritmias, tal y como se ha observado experimentalmente, podría ser crucial para avanzar en el diseño de nuevas terapias clínicas dirigidas a prevenir o tratar estas anomalías rítmicas.

Esta tesis investiga y analiza la variabilidad espacio-temporal de la repolarización ventricular humana, su modulación por el sistema nervioso simpático, los mecanismos que subyacen a incrementos notables en dicha variabilidad y la relación que existe con la generación de arritmias ventriculares. Para ello, se proponen metodologías que combinan el **procesado de señales** ventriculares y el **modelado *in silico*** de miocitos ventriculares humanos. Los modelos *in silico* desarrollados incluyen descripciones teóricas acopladas de la electrofisiología, la dinámica del calcio, el estiramiento mecánico y la señalización  $\beta$ -adrenérgica. Para tener en cuenta la variabilidad temporal (latido a latido) de la repolarización, se añade estocasticidad en las ecuaciones que definen la apertura y cierre de los canales iónicos de las principales corrientes activas durante la fase de repolarización del potencial de acción (AP), es decir, durante el retorno de la célula al estado de reposo después de una excitación. Por otro lado, para tener en cuenta la variabilidad espacial (célula a célula) de la repolarización, se construye y calibra una población de modelos representativos de diferentes características celulares utilizando para ello datos experimentales disponibles. La investigación teórica y computacional de este estudio, combinada con el procesado de señales ventriculares tanto clínicas como experimentales, sienta las bases para futuros estudios que tengan como objetivo mejorar los métodos de estratificación del riesgo arritmico y guiar la búsqueda de terapias antiarrítmicas más eficaces.

En el **Capítulo 2**, se construye una población de modelos computacionales estocásticos representativos de células ventriculares humanas, los cuales se calibran experimentalmente. Estos modelos combinan la electrofisiología, la mecánica y la señalización  $\beta$ -adrenérgica y se utilizan para caracterizar de modo teórico la variabilidad espacio-temporal. La calibración de los modelos se basa en rangos experimentales de una serie de marcadores derivados del AP que describen su duración, amplitud y morfología. Mediante el uso de esta población de modelos estocásticos de AP se reproducen

las interacciones descritas experimentalmente entre un tipo particular de variabilidad temporal, asociada con las oscilaciones de baja frecuencia (LF) de la duración del AP (APD), y la variabilidad global latido a latido de la repolarización (BVR) en respuesta a un incremento de la actividad simpática. Además, en este capítulo se han estudiado los mecanismos iónicos que están detrás de los incrementos simultáneos de ambos fenómenos y se ha demostrado que dichos mecanismos están asociados con la disminución de las corrientes rectificadora de entrada y rectificadora retardada rápida de  $K^+$  y a su vez de la corriente de  $Ca^{2+}$  tipo L. Finalmente, se ha probado que niveles elevados de oscilaciones de baja frecuencia del APD y de BVR en ventrículos enfermos conducen a inestabilidades eléctricas y al desarrollo de eventos arritmogénicos.

En el **Capítulo 3**, se investiga el retardo necesario para la manifestación de las oscilaciones LF del APD, como una forma particular de variabilidad de la repolarización, en los miocitos ventriculares en respuesta a la provocación simpática. Mediante el uso de una población calibrada experimentalmente de modelos de AP ventriculares humanos, como en el Capítulo 2, se ha demostrado que esta latencia oscilatoria está asociada con la cinética lenta de fosforilación de la corriente rectificadora retardada lenta de  $K^+$  ( $I_{Ks}$ ) en respuesta a la estimulación  $\beta$ -adrenérgica. La estimulación previa de los receptores  $\beta$  reduce sustancialmente el tiempo requerido para el desarrollo de oscilaciones LF. Además, se ha demostrado que lapsos de tiempo cortos están íntimamente relacionados con mayores magnitudes oscilatorias del APD, medidas en el Capítulo 3, particularmente en células susceptibles de desarrollar eventos arritmogénicos en respuesta a la estimulación simpática.

La calibración experimental de la población de modelos utilizados en los Capítulos 2 y 3, pese a asegurar que las medidas simuladas a partir de la población construida se encuentran dentro de límites experimentales descritos en la literatura, no garantiza que cada modelo de la población represente las medidas de un cardiomiocito ventricular humano individual. Es por esta razón que en el **Capítulo 4** se desarrolla una metodología novedosa para construir poblaciones computacionales de modelos celulares ventriculares humanos que recapitulen más fielmente las evidencias experimentales disponibles. La metodología propuesta se basa en la formulación de representaciones estado-espacio no lineales y en el uso del filtro de Kalman unscented (UKF) para la estimación de los parámetros y las variables de estado de un modelo AP estocástico subyacente para cada señal de potencial dada como entrada. Las pruebas realizadas sobre series de potencial sintéticas y experimentales demuestran que esta metodología permite establecer una correspondencia entre las trazas AP de entrada y los conjuntos de parámetros del modelo (conductancias de corriente iónicas) y las variables de estado (variables relacionadas con la apertura/cierre de los canales iónicos y concentraciones iónicas intracelulares). A su vez, se ha demostrado que la metodología propuesta es robusta y adecuada para la investigación de la variabilidad espacio-temporal en la repolarización ventricular humana.

En el **Capítulo 5** se proponen varias mejoras a la metodología desarrollada en el Capítulo 4 para estimar con mayor precisión los parámetros y las variables de estado de los modelos estocásticos de células ventriculares humanas a partir de señales indi-

viduales de AP dadas como entradas y, a su vez, para reducir el tiempo de convergencia a fin de proporcionar una estimación más rápida. Las mejoras se han basado en el uso combinado del método UKF, presentado en el Capítulo 4, junto con el método Double Greedy Dimension Reduction (DGDR) con generación automática de biomarcadores. Además de estimar las conductancias de las corrientes iónicas en condiciones basales, el enfoque presentado en este capítulo también proporciona un conjunto de niveles de fosforilación inducidos por la estimulación  $\beta$ -adrenérgica, contribuyendo así al análisis de patrones de repolarización espacio-temporal con y sin modulación autonómica.

En **conclusión**, esta tesis presenta novedosas metodologías enfocadas hacia la caracterización de la variabilidad espacio-temporal de la repolarización ventricular humana, el análisis de sus mecanismos subyacentes y la determinación de la relación entre aumentos en la variabilidad y el mayor riesgo de sufrir arritmias ventriculares y muerte súbita cardíaca. Se desarrollan conjuntos de modelos computacionales estocásticos celulares humanos con representación de la electrofisiología ventricular, la mecánica y la señalización  $\beta$ -adrenérgica para analizar la variabilidad global de la repolarización, latido a latido y célula a célula, así como de un tipo particular de variabilidad en forma de oscilaciones de baja frecuencia. Para reproducir fielmente los patrones de variabilidad medidos experimentalmente de manera individual, se proponen metodologías para construir poblaciones de modelos AP ventriculares humanos donde los parámetros y las variables de estado de cada modelo se estiman a partir de una serie de potencial de entrada dada. Estos modelos personalizados abren la puerta a una investigación más robusta de las causas y consecuencias de la variabilidad espacio-temporal de la repolarización ventricular humana.



# Contents

<b>Acknowledgements</b>	<b>i</b>
<b>Agradecimientos</b>	<b>iii</b>
<b>Abstract</b>	<b>v</b>
<b>Resumen y Conclusiones</b>	<b>ix</b>
<b>Contents</b>	<b>xii</b>
<b>List of Figures</b>	<b>xix</b>
<b>List of Tables</b>	<b>xxvi</b>
<b>1 Introduction</b>	<b>1</b>
1.1 Cardiac Arrhythmias . . . . .	1
1.2 The Heart . . . . .	3
1.2.1 Anatomy and Function . . . . .	3
1.2.2 Cellular Electrical Activity . . . . .	4
1.2.3 Electromechanical Coupling . . . . .	6
1.2.4 Electrical Propagation in Tissue and throughout the Heart . .	7
1.2.5 Electrograms and Electrocardiograms . . . . .	7
1.3 The Autonomic Nervous System . . . . .	10
1.4 Computational Modeling of Human Ventricular Electrophysiology, Me- chanics and Autonomic Modulation . . . . .	11
1.4.1 <i>In silico</i> Modeling as a Complement to <i>in vitro</i> and <i>in vivo</i> Research	11
1.4.2 Electrophysiological Models of Human Ventricular Cells . . . . .	12
1.4.3 Coupled Models of Electrophysiology and Mechanics in Human Ventricular Cells . . . . .	15
	xiii

1.4.4	Models of $\beta$ -A Modulation of Cellular Ventricular Electro-Mechanical Activity . . . . .	16
1.4.5	The ORd Human Ventricular Cell Model . . . . .	16
1.5	Objectives of the Thesis . . . . .	19
1.6	Outline of the Thesis . . . . .	20
<b>2</b>	<b>Low-Frequency Oscillations and Temporal Variability of Human Ventricular Repolarization: Characterization, Mechanisms and Relation to Arrhythmic Risk</b>	<b>25</b>
2.1	Introduction . . . . .	26
2.2	Materials and Methods . . . . .	27
2.2.1	Human Data . . . . .	27
2.2.2	Stochastic Human Ventricular Models . . . . .	28
2.2.3	Measurements of Repolarization Variability . . . . .	33
2.2.4	Contributors to BVR and LF Oscillations . . . . .	34
2.2.5	Contributors to Arrhythmogenesis . . . . .	36
2.3	Results . . . . .	37
2.3.1	Sympathetic Provocation Increases BVR and LF Oscillations of APD . . . . .	37
2.3.2	Close Interaction between BVR and LF Oscillations of APD, particularly in Response to Sympathetic Provocation . . . . .	38
2.3.3	$K^+$ and $Ca^{2+}$ Current Densities are Common Modulators of BVR and LF Oscillations of APD . . . . .	40
2.3.4	Modulation of BVR and LF Oscillations of APD by $K^+$ and $Ca^{2+}$ Current Densities is Explained by their Effects on Ionic Gating Stochasticity, $\beta$ -AS and Hemodynamic Loading . . . . .	42
2.3.5	Severe Disease Conditions Accentuate both BVR and LF Oscillations of APD, Leading to Electrical Instabilities . . . . .	46
2.4	Discussion . . . . .	47
2.4.1	Relation between Sympathetically Mediated BVR and LF Oscillations of APD in a Human Ventricular Population . . . . .	48

2.4.2	Main Contributors to Increased BVR and LF Oscillations of APD following Enhanced Sympathetic Activity . . . . .	51
2.4.3	Pro-Arrhythmic Events associated with Increased BVR and LF Oscillations of APD under Severe Disease Conditions . . . . .	52
2.4.4	Limitations and Future Work . . . . .	54
2.5	Conclusions . . . . .	55
<b>3</b>	<b>Time Course of Low-Frequency Oscillations of Human Ventricular Repolarization. Relevance for Arrhythmogenesis</b>	<b>57</b>
3.1	Introduction . . . . .	58
3.2	Methods . . . . .	60
3.2.1	Experimental Data . . . . .	60
3.2.2	Electrophysiology Model . . . . .	60
3.2.3	PKA Phosphorylation Model . . . . .	61
3.2.4	Mechanics Model . . . . .	61
3.2.5	Simulation of Enhanced Sympathetic Activity . . . . .	62
3.2.6	Simulation of Disease Conditions . . . . .	62
3.2.7	Quantification of APD Time Lag in Response to Constant $\beta$ -AS and/or Mechanical Stretch . . . . .	62
3.3	Results . . . . .	64
3.3.1	Time Lapse for Development of LF Oscillations in APD . . . . .	64
3.3.2	Contribution of $\beta$ -AS and Mechanical Stretch to Time Lapse of LF Oscillations in APD . . . . .	65
3.3.3	Comparison of APD Time Lapse following $\beta$ -AS in Experiments and Simulations . . . . .	66
3.3.4	Reduction in Time Lapse for LF Oscillations of APD by Prior Low-Level $\beta$ -AS . . . . .	67
3.3.5	Ionic Mechanisms Underlying Time Lapse in LF Oscillations of APD . . . . .	68
3.3.6	Relationship between Time Lapse and Magnitude of LF Oscillations of APD . . . . .	70

3.3.7	Effect of Disease Conditions in Time Lapse of LF Oscillations of APD and Relation to Arrhythmogenesis . . . . .	71
3.4	Discussion . . . . .	72
3.4.1	Inter-Individual Differences in the Time Lapse for Development of LF Oscillations of APD Following Enhanced Sympathetic Activity . . . . .	72
3.4.2	Major Role of $I_{Ks}$ Phosphorylation Kinetics in Determining the Time Lapse for LF Oscillations of APD . . . . .	75
3.4.3	Increased Arrhythmic Risk as a Function of the Time Lapse and Magnitude of LF Oscillations of APD . . . . .	76
3.4.4	Limitations and Future Work . . . . .	77
3.5	Conclusions . . . . .	78
<b>4</b>	<b>Data-Driven Identification of Stochastic AP Models for characterization of Spatio-Temporal Human Ventricular Repolarization Variability</b>	<b>79</b>
4.1	Introduction . . . . .	80
4.2	Materials and Methods . . . . .	82
4.2.1	Human Ventricular Stochastic AP Models . . . . .	82
4.2.2	State-Space Formulation . . . . .	85
4.2.3	Augmented State-Space . . . . .	86
4.2.4	UKF-based Joint State and Parameter Estimation . . . . .	87
4.2.5	Synthetic Data . . . . .	88
4.2.6	Experimental Data . . . . .	90
4.2.7	Methodology Assessment . . . . .	90
4.3	Results . . . . .	92
4.3.1	Noisy AP Filtering . . . . .	92
4.3.2	Sensitivity of the Methodology with respect to its own Parameters	93
4.3.3	Estimation of Model Parameters and Hidden States . . . . .	94
4.3.4	Estimation of AP Markers . . . . .	95
4.3.5	Application onto Experimental Data . . . . .	97



---

4.4	Discussion . . . . .	100
4.4.1	Methodology Calibration . . . . .	100
4.4.2	Filtering Noisy Data . . . . .	100
4.4.3	Identification of Model Parameters and Hidden States . . . . .	101
4.4.4	Application onto Data from Different Origins . . . . .	102
4.4.5	Robustness Analysis . . . . .	103
4.4.6	Limitations and Future Works . . . . .	103
4.5	Conclusions . . . . .	104
<b>5</b>	<b>Fast and Accurate Computational Characterization of Spatio-Temporal Human Ventricular Repolarization Variability</b>	<b>105</b>
5.1	Introduction . . . . .	106
5.2	Methods . . . . .	108
5.2.1	Stochastic AP Models at Baseline and following $\beta$ -AS . . . . .	108
5.2.2	Synthetic Data . . . . .	109
5.2.3	State-Space Formulation and Augmented States . . . . .	111
5.2.4	Individual and Combined DGDR- and UKF-based Methods . . . . .	112
5.2.5	Performance Evaluation . . . . .	115
5.3	Results . . . . .	117
5.3.1	Implementation of DGDR and UKF Methods . . . . .	117
5.3.2	Combined DGDR and UKF Methods: Initialization Effects . . . . .	117
5.3.3	Combined DGDR and UKF Methods: Updating Effects . . . . .	118
5.3.4	Performance Comparison . . . . .	118
5.3.5	Replication of AP Traces and Biomarkers at Baseline . . . . .	120
5.3.6	Estimation of Phosphorylation Factors, AP Traces and Biomarkers under $\beta$ -AS . . . . .	122
5.4	Discussion . . . . .	123
5.4.1	DGDR Method . . . . .	124
5.4.2	UKF Method . . . . .	125

5.4.3	Combined DGDR-UKF Method by Initialization and Updating	125
5.4.4	Estimation of Ionic Current Conductances at Baseline . . . . .	126
5.4.5	Estimation of Phosphorylation Levels of Cellular Substrates under $\beta$ -AS Conditions . . . . .	127
5.4.6	Characterization of Spatio-Temporal AP Variability from Parameter Estimates . . . . .	127
5.4.7	Limitations and Future Works . . . . .	128
5.5	Conclusion . . . . .	129
<b>6</b>	<b>Conclusions and Future Work</b>	<b>131</b>
6.1	Conclusions . . . . .	131
6.1.1	General Conclusions . . . . .	131
6.1.2	Interactions between LF Oscillations and Temporal Variability in Human Ventricular Repolarization following Sympathetic Provocation: Mechanisms and Relation to Risk . . . . .	132
6.1.3	Theoretical Characterization of Spatio-Temporal Variability in Human Ventricular Repolarization at Baseline and following Sympathetic Provocation . . . . .	133
6.2	Future Work . . . . .	134
	<b>Glossary</b>	<b>137</b>
	<b>Publications Derived from the Thesis</b>	<b>141</b>

# List of Figures

1.1	Scheme of the anatomy of the heart and the main vessels. The arrows illustrate blood flow direction. Figure adapted from [7]. . . . .	3
1.2	Illustration of an AP as obtained by the computational ORd human ventricular cell model [5], with an indication of the different AP phases.	5
1.3	Scheme of the patch-clamp technique for cell-attached version. Figure from [12]. . . . .	6
1.4	AP waveforms for cells corresponding to different cardiac regions, with delays between different APs similar to those reported for a healthy human heart. Figure adapted from [18]. . . . .	8
1.5	Unipolar EGM signals ( $ABL_{tip}$ and $ABL_2$ ) recorded at tip and second electrode of an ablation catheter and Bipolar EGM signal ( $ABL_{dist}$ ) from the ablation catheter. Figure extracted from [19]. . . . .	9
1.6	Left: Schematic diagram of some ECG electrode positions. Right: Leads of the standard 12-lead ECG. Figure extracted and adapted from [21]. . . . .	9
1.7	ECG cycle with definition of the main waves, segments and intervals. Figure extracted from [8]. . . . .	10
1.8	Left: Schematic diagram of the Hodgkin-Huxley model showing the cell membrane and the three typologies of ionic channels. Right: Scheme of the equivalent circuit of the Hodgkin-Huxley model with the sodium, potassium and leak currents. Figure extracted and adapted from [24, 25].	13
1.9	Schematic representation of ORd model [5] and ionic currents and fluxes. Figure extracted and adapted from [5]. . . . .	17
2.1	Simulation of 0.1 Hz phasic $\beta$ -AS and stretch effects at baseline and following SP: (a) ISO dose and (b) stretch ratio $\lambda$ . . . . .	31
2.2	Simulated APD series representative of baseline and SP phases (0.1 Hz phasic $\beta$ -AS and stretch effects) for a virtual cell of the population under mild disease conditions. . . . .	32

2.3	Left panel: Experimental zero-mean ARI series ( $\text{ARI} - \overline{\text{ARI}}$ ) and corresponding spectra at rest (left) and following Valsalva maneuver (right). Right panel: Simulated zero-mean APD series ( $\text{APD} - \overline{\text{APD}}$ ) and corresponding spectra at baseline (left) and following SP (right). The LF region of the spectra is shadowed in red and the high frequency region in green. . . . .	37
2.4	Left: Normalized variance $m_{\text{NSD}}$ (top) and Normalized LF power $m_{\text{NPLF}}$ (bottom) at rest and following Valsalva maneuver calculated from experimental ARI series. Right: $m_{\text{NSD}}$ (top) and $m_{\text{NPLF}}$ (bottom) at baseline and following SP calculated from simulated APD series. The cases presented in Fig. 2.3 are highlighted in blue. . . . .	38
2.5	Relationship between $m_{\text{SD}}$ and $m_{\text{PLF}}$ (top) and $m_{\text{NSD}}$ and $m_{\text{NPLF}}$ (bottom) at baseline and following SP for the population of models under simulated mild disease conditions. . . . .	39
2.6	Relevance of ionic current conductances to $m_{\text{PLF}}$ (a), $m_{\text{NPLF}}$ (b), $m_{\text{STV}}$ (c) and $m_{\text{NSTV}}$ (d), calculated from simulated APD series following SP. . . . .	40
2.7	Relevant factors for (a) $m_{\text{STV}}$ and (b) $m_{\text{NSTV}}$ following constant $\beta$ -AS and mechanical stretch. . . . .	41
2.8	Relevant factors for (a) $m_{\text{PLF}}$ , (b) $m_{\text{NPLF}}$ , (c) $m_{\text{STV}}$ , and (d) $m_{\text{NSTV}}$ following SP under physiological conditions. . . . .	42
2.9	Distributions of BVR and LF oscillation measurements for simulated scenarios including individual and combined $\beta$ -AS and mechanical stretch effects, with and without the contribution of SACs. . . . .	43
2.10	(a) Resting membrane potential versus $I_{\text{K1}}$ current conductance in the population of virtual cells; (b) $I_{\text{SAC}}$ current for two examples corresponding to upregulated and downregulated $I_{\text{K1}}$ while keeping all the other currents at their default values in the ORd model; (c) Minimum $I_{\text{SAC}}$ current value versus $I_{\text{K1}}$ current conductance in the population; (d) AP traces and (e) zero-mean APD series ( $\text{APD} - \overline{\text{APD}}$ ) for the examples in (b); (f) $m_{\text{NPLF}}$ values versus $I_{\text{K1}}$ current conductance in the population. . . . .	44
2.11	(a) Minimum APD versus $I_{\text{Kr}}$ current conductance in the population of virtual cells; (b) APD range versus minimum APD; (c) zero-mean APD series ( $\text{APD} - \overline{\text{APD}}$ ) for two examples corresponding to downregulated and upregulated $I_{\text{Kr}}$ while keeping all the other currents at their default values in the ORd model. . . . .	45

2.12	(a) Average triangulation versus $I_{CaL}$ current conductance and (b) $m_{PLF}$ values versus average triangulation for the population of virtual cells; (d) zero-mean APD series ( $APD - \overline{APD}$ ) for two examples corresponding to downregulated and updownregulated $I_{CaL}$ while keeping all the other currents at their default values in the ORd model. . . . .	46
2.13	Pro-arrhythmic events observed following SP in cells under simulated severe disease conditions. . . . .	47
2.14	Violin plots representing the distributions of $\log(m_{PLF})$ , $m_{NPLF}$ , $m_{STV}$ and $m_{NSTV}$ for mild and moderate disease conditions. The whole population of models is divided into two subpopulations: the set of cells presenting (denoted by A) and not presenting (denoted by NA) pro-arrhythmic events following SP under severe disease conditions. . . . .	48
2.15	Relevance of ionic current conductances to pro-arrhythmic events. . . . .	49
2.16	Location of cells presenting (red) and not presenting (gray) pro-arrhythmic events under simulated severe disease conditions as a function of relevant ionic current conductance values. . . . .	50
3.1	Simulation of SP and APD response of two different cells in the population. First row: Phasic ISO application at a frequency of 0.05 Hz. Second row: Phasic stretch ratio variations at the same frequency. Third and fourth rows: APD time series corresponding to two cells (virtual cell 1 and virtual cell 2) presenting LF oscillations in response to SP. . . . .	64
3.2	Histogram of the time lapse (left panel) and LF power (right panel) of APD in response to increased sympathetic activity for all cells in the simulated population. . . . .	65
3.3	Boxplots representing the time lapse (left panel) and the power in the LF band (right panel) for oscillations of APD to develop in response to phasic $\beta$ -AS (ISO 1 $\mu$ M), mechanical stretch (10%) and the combination of both. Statistically significant differences by Wilcoxon signed-rank test (p-value < 0.05) are denoted by *. Since the statistical significance in the comparison of simulated data highly depends on the number of simulated cases, smaller subsets of virtual cells were used to prove that $p = 0.05$ had already been achieved with a much smaller number of virtual cells than those in the whole population. . . . .	66
3.4	Change in APD with respect to baseline following application of a constant 10 nM ISO dose in experiments and simulations on single ventricular myocyte . . . . .	67

- 
- 3.5 Time lapse for LF oscillations of APD to develop in response to phasic  $\beta$ -AS with 1  $\mu$ M ISO dose as a function of prior phasic  $\beta$ -AS with lower ISO doses varying from 0 to 0.07  $\mu$ M. . . . . 68
- 3.6 Left panel: Phosphorylation levels calculated as described in section 3.2.3. Right panel: Time lapse for LF oscillations of APD to develop in response to phasic  $\beta$ -AS when using PKA models with slow (left, [36]) and fast (right, [35])  $I_{K_s}$  phosphorylation and dephosphorylation kinetics. 68
- 3.7  $\tau_{APD}$  (top panels) and  $\log(\text{PLF})$  (bottom panels), presented in terms of median, first quartile (Q1) and third quartile (Q3), for increasingly higher degrees of  $I_{K_s}$  inhibition, both in response to phasic  $\beta$ -AS (ISO 1 $\mu$ M, left panels) and combined with phasic mechanical stretch (10%, right panels) for the population of virtual cells under healthy conditions. 69
- 3.8 Left panel:  $\log(\text{PLF})$  vs.  $\tau_{APD}$  for varying  $I_{K_s}$  phosphorylation and dephosphorylation rate constants ranging from the values in [35] to the values in [36]. Right panel:  $I_{K_s}$  phosphorylation levels for the models with  $I_{K_s}$  phosphorylation and dephosphorylation rate constants as in [35] (gray line) and as in [36] (red line). . . . . 70
- 3.9 Left panel: Zero-mean APD series ( $\text{APD} - \overline{\text{APD}}_{\text{Baseline}}$ ) in response to SP, for healthy (red line) and disease (black line) conditions simulated for a virtual cell of the population. Right panel: Differences in  $\tau_{APD}$  due to  $\text{Ca}^{2+}$  overload and/or RRR with respect to healthy conditions. 71
- 3.10 Pro-arrhythmic events in virtual cells in response to increased sympathetic activity under diseased conditions simulated by  $\text{Ca}^{2+}$  overload, reduced repolarization reserve and increased  $G_{SAC}$ . Phase 2 and phase 3 early afterdepolarizations (EADs) (top panels), EAD bursts (bottom left panel) and spontaneous beats (bottom right panel) could be observed. 72
- 3.11 Left and middle panels: Violin representations of  $\tau_{APD}$  and  $\log(\text{PLF})$ , respectively, calculated under healthy conditions for subpopulations of cells presenting and not presenting pro-arrhythmic events when disease conditions were simulated while pacing at CLs of 1000, 2000 and 2500 ms. Right panel:  $\tau_{APD}$  vs.  $\log(\text{PLF})$  for the same two subpopulations. The slopes of the regression lines for the subpopulations presenting (orange) and not presenting (green) pro-arrhythmic events were statistically significantly different by univariate analysis of variance (p-value < 0.05). . . . . 73

- 3.12 Boxplot of  $\tau_{APD}$  (left panel) and  $\log(\text{PLF})$  (right panel) calculated under healthy conditions for subpopulations of cells presenting and not presenting pro-arrhythmic events when disease conditions were simulated while pacing at CLs of 1000, 2000 and 2500 ms. Statistically significant differences by Wilcoxon rank-sum test (p-value  $< 0.05$ ) are denoted by \*, while non-significant differences are denoted by *n.s.* See comment on statistical comparisons of simulated data in the main manuscript. 74
- 4.1 Scheme of the proposed methodology. A noisy AP trace is the input to a model-based filtering algorithm. This AP may have been synthetically generated using a computational AP model or experimentally recorded. The filtering algorithm outputs a filtered (noiseless) AP and a set of estimated hidden states and model parameters for a computational AP model used as a basis for the work (ORd model in this study). New AP traces can be computed from the estimated model under different simulation conditions. . . . . 88
- 4.2 Last cycle of AP traces: In black, the synthetic noiseless AP trace generated by the original ORd model; in blue line, the noisy version of that AP,  $y(k)$ , which is used as input to the proposed method with two different values for the standard deviation of the measurement noise,  $\sigma_r$ ; in red, the mean estimated voltage at each time instant, denoted by  $\bar{x}$ ; and in grey, the estimated uncertainty bands, i. e.,  $\bar{x} \pm 3\sigma_x$  (with  $\sigma_x$  denoting the estimated standard deviation of voltage). . . . . 92
- 4.3 Root mean square error  $\xi_v$  in AP filtering for different actual ( $\sigma_r$ ) and estimated ( $\hat{\sigma}_r$ ) levels of measurement noise. . . . . 93
- 4.4 Root mean square error  $\xi_v$  in AP filtering (a) and average of mean relative parameter estimation errors  $\bar{\eta}_\theta$  (b) evaluated for different levels of  $\sigma_\theta$ . . . . . 94
- 4.5 Open probability  $X_{Krf}$  of  $I_{Kr}$  (top panel) and open probability  $X_{Ks}$  of  $I_{Ks}$  (bottom panel). The value in the stochastic ORd model is shown in blue, while estimated mean ( $\bar{x}$ ) and uncertainty bands ( $\bar{x} \pm 3\sigma_x$ ) are shown in red and grey, respectively. . . . . 95
- 4.6 Estimation of model parameters. Mean estimates ( $\bar{x}$ ) are shown in red and uncertainty bands ( $\bar{x} \pm 3\sigma_x$ ), in grey. . . . . 96
- 4.7 Mean relative error  $\eta_{\theta'}$  for each of the estimated model parameters over a population of 131 stochastic AP models. . . . . 97
- 4.8 Statistical distributions over a population of 131 AP models of (left)  $m_{\text{APD90}}$  and (right)  $STV$  calculated from actual APs in blue and estimated APs in red. . . . . 97

4.9	AP traces over 2 simulated cycles (top panel) and APD time series over 50 simulated cycles (bottom panel) generated with the stochastic TP06 model (in blue), estimated with the proposed methodology (dashed red) and generated with the stochastic default ORd model (black). . . . .	98
4.10	Experimental AP traces (blue) and estimated AP traces obtained with the proposed methodology based on stochastic versions of epicardial (dotted yellow) and endocardial (dashed red) ORd models. Default stochastic epicardial (solid black) and endocardial (dashed black) ORd models are shown as a reference. Top and bottom panels correspond to two different experimental recordings. . . . .	99
5.1	Left panel: Estimated ( $\hat{\theta}_{NaK}$ ) vs actual ( $\theta_{NaK}$ ) values of the factor multiplying maximal $I_{NaK}$ in the training and validation populations. Right panel: Density of the absolute error in the estimation of $\theta_{NaK}$ for the training and validation sets. . . . .	114
5.2	Average of mean absolute parameter estimation error $E[\bar{\eta}_\theta]$ in the ORd model as a function of the standard deviation of the process noise $\sigma_\theta$ . . . . .	117
5.3	Actual $\theta_{Na}$ value and time course of $\hat{\theta}_{Na}$ as estimated by DGDR, UKF and UKF+INI methods. . . . .	118
5.4	Actual $\theta_{Kr}$ value and time course of $\hat{\theta}_{Kr}$ as estimated by DGDR, UKF and UKF+UP methods. . . . .	119
5.5	Average of mean (left panel) and standard deviation (right panel) of absolute parameter estimation error $\bar{\eta}_\theta$ for the five evaluated methods. . . . .	119
5.6	Boxplots of absolute estimation errors $\eta_\theta$ for the factors multiplying ionic current conductances calculated for the five evaluated methods. . . . .	120
5.7	Left panel: Time course of estimation uncertainty in terms of square root of covariance matrix $\sqrt{P_{NaK}}$ for each of the five evaluated methods. Right panel: Number of beats required by each evaluated method to reach the same level of accuracy as the UKF method, as quantified by the averaged covariance over all estimated model parameters. . . . .	121
5.8	Probability density function of $\Delta$ APD (left panel) and $\Delta$ STV (right panel) for the validation population, with $\Delta$ APD ( $\Delta$ STV, respectively) calculated as the difference between APD (STV, respectively) from the input AP trace and APD (STV, respectively) from the estimated AP trace for each evaluated method under baseline conditions. . . . .	121
5.9	Boxplots of absolute estimation errors $\eta_\theta$ for the factors multiplying ISO-induced phosphorylation levels calculated for three evaluated methods. . . . .	122



---

5.10	Probability density function of $\Delta$ APD (left panel) and $\Delta$ STV (right panel) for the validation population, with $\Delta$ APD ( $\Delta$ STV, respectively) calculated as the difference between APD (STV, respectively) from the input AP trace and APD (STV, respectively) from the estimated AP trace for each evaluated method under $\beta$ -AS conditions. . . . .	123
5.11	Actual and estimated APs (mean over 100 beats) calculated from the set of estimated parameters by each evaluated method at baseline (left panel) and under $\beta$ -AS (right panel) for one of the virtual cells in the validation population. . . . .	124



# List of Tables

2.1	Calibration criteria applied onto human ventricular cell models. . . . .	28
2.2	Number of channels for $I_{Ks}$ , $I_{Kr}$ and $I_{to}$ . . . . .	29
2.3	Simulation protocol of RRR and $Ca^{2+}$ overload and $G_{SAC,ns}$ conductance value for physiological and disease conditions. . . . .	32
2.4	Spearman correlation coefficients between simulated BVR and LF oscillation measures. . . . .	39
3.1	Calibration criteria applied onto human ventricular cell models. . . . .	61
3.2	Factors multiplying ionic conductances of virtual cells 1 and 2 illustrated in Fig. 3.1. . . . .	65
4.1	Number of channels for $I_{Ks}$ , $I_{Kr}$ , $I_{to}$ and $I_{CaL}$ . . . . .	85
4.2	Calibration criteria applied onto human ventricular cell models. . . . .	89
4.3	$\xi_v$ Root Mean Square Error (mV) in AP filtering. . . . .	93
4.4	$\xi_v$ Root Mean Square Error (mV) in fitting experimental AP traces. . . . .	99
4.5	Estimated parameter values for the two experimental AP traces using the human ventricular endocardial ORd model. . . . .	100
5.1	Calibration criteria applied onto ventricular human cell models. . . . .	110



# 1 | Introduction

---

1.1	Cardiac Arrhythmias . . . . .	1
1.2	The Heart . . . . .	3
1.2.1	Anatomy and Function . . . . .	3
1.2.2	Cellular Electrical Activity . . . . .	4
1.2.3	Electromechanical Coupling . . . . .	6
1.2.4	Electrical Propagation in Tissue and throughout the Heart . . . . .	7
1.2.5	Electrograms and Electrocardiograms . . . . .	7
1.3	The Autonomic Nervous System . . . . .	10
1.4	Computational Modeling of Human Ventricular Electrophysiology, Mechanics and Autonomic Modulation . . . . .	11
1.4.1	<i>In silico</i> Modeling as a Complement to <i>in vitro</i> and <i>in vivo</i> Research . . . . .	11
1.4.2	Electrophysiological Models of Human Ventricular Cells . . . . .	12
1.4.3	Coupled Models of Electrophysiology and Mechanics in Human Ventricular Cells . . . . .	15
1.4.4	Models of $\beta$ -A Modulation of Cellular Ventricular Electro-Mechanical Activity . . . . .	16
1.4.5	The ORd Human Ventricular Cell Model . . . . .	16
1.5	Objectives of the Thesis . . . . .	19
1.6	Outline of the Thesis . . . . .	20

---

## 1.1 Cardiac Arrhythmias

Cardiovascular diseases (CVDs) are the first cause of mortality and morbidity in the world, representing over one third of all global deaths [1]. By 2030 the annual number of deaths from CVDs is expected to reach 22 million. In Spain, more than 120,000 people die from CVDs each year, which corresponds to approximately 29% of all deaths [2]. CVDs comprise a group of disorders related to the heart and blood vessels,

including diseases like coronary heart disease, high blood pressure, cerebral heart disease, heart failure and cardiomyopathies, to name a few.

A significant percentage of deaths from CVDs are related to cardiac arrhythmias, defined as abnormalities in the electrical functioning of the heart [3], which may in some cases lead to sudden cardiac death. According to the etymology of the word arrhythmia, this represents a problem in the rhythm of the heartbeat, which may be too fast, too slow or even not present a definite pattern. Of all the different types of cardiac arrhythmias, bradycardias, premature or ectopic beats, atrial fibrillation and ventricular fibrillation are common ones.

Three main elements are involved in the development of arrhythmias, including an arrhythmogenic substrate, a trigger and modulators. The Autonomic Nervous System (ANS) is the most relevant of these modulators. The ANS is composed of two branches, sympathetic and parasympathetic, which to some extent act antagonistically to each other. To date, the action of the ANS on the sino-atrial node, the heart's natural pacemaker, has been exhaustively investigated, mainly by quantifying its effects on the heart rate and its variability. There is, however, much larger uncertainty regarding the effects associated with the autonomic innervation of other regions in the heart, such as the atria and the ventricles, i.e. the upper and lower cavities of the heart, respectively [4].

Considering ventricular arrhythmias that may end up in sudden cardiac death, the possibility of revealing how ANS modulates ventricular activity and participates in the development of arrhythmias could be crucial to advance in the proposal of more robust techniques for arrhythmic risk stratification and in the design of novel clinical strategies aimed at preventing or treating arrhythmias. Based on this, the present thesis investigates spatio-temporal variability in human ventricular electrical activity and its modulation by the ANS, dissects mechanisms underlying autonomically-mediated elevations in repolarization variability and assesses the implications in terms of arrhythmia generation. To conduct these investigations, methodologies are proposed that combine processing of ventricular signals and *in silico* modeling of ventricular electrico-mechanical activity with integrated regulation by the ANS.

In the following sections, a general introduction into the electrical functioning of the heart and the ANS acting as a modulator of such functioning is presented. Subsequently, *in silico* cellular modeling of cardiac electromechanics and  $\beta$ -adrenergic ( $\beta$ -A) signaling is introduced, providing an overview of the main characteristics of computational models so far published in the literature. A more extensive description of the O'Hara-Virág-Varró-Rudy (ORd) human ventricular electrophysiological cell model [5] is presented, as it represents the basis for subsequent computational models developed in this thesis to analyze spatio-temporal variability of human ventricular repolarization.

## 1.2 The Heart

### 1.2.1 Anatomy and Function

The heart is the most important organ of the circulatory system, being responsible for pumping oxygen-rich blood to the rest of the body so that all body parts can function in a correct way [6]. The heart, which is about the size of a fist, is divided into two similar sides, left and right, which beat synchronously, although each side is responsible for a part of the circulatory system. As illustrated in Fig.1.1, the two sides of the heart, each of them comprised by an atrium and a ventricle, are separated by a muscular wall called the septum. Inside the heart, there are four valves that control the blood flow between the atria and the ventricles, so-called atrioventricular (mitral and tricuspid) valves, and between the ventricles and the arteries that deliver blood to the lungs and to the rest of the body, so-called pulmonary and aortic valves.

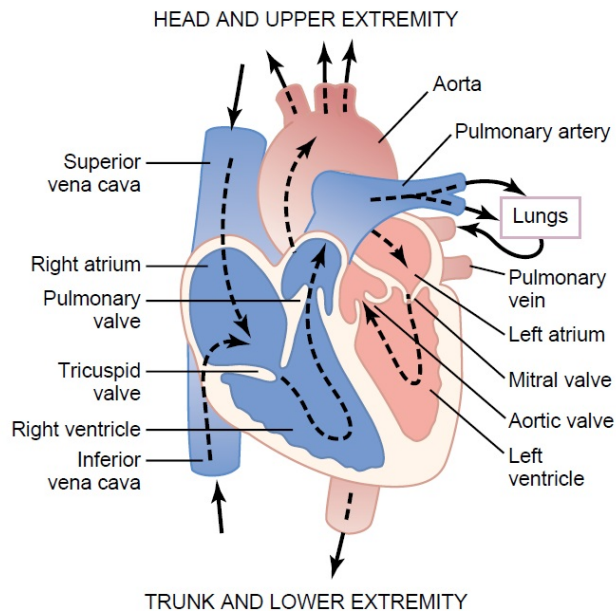


Figure 1.1: Scheme of the anatomy of the heart and the main vessels. The arrows illustrate blood flow direction. Figure adapted from [7].

Under physiological operating conditions, oxygen-poor blood enters the heart through the right atrium and, after atrial contraction, passes into the right ventricle through the tricuspid valve. From there, ventricular contraction pumps the blood to the lungs, through the pulmonary valve, for subsequent blood oxygenation. Mean-

while, on the left side of the heart, oxygen-rich blood enters the atrium from the lungs and, following atrial contraction, passes into the ventricle through the mitral valve. Left ventricular contraction is responsible for pumping this oxygen-rich blood to the rest of the body. On the above basis, it can be understood that proper blood circulation is founded on the perfect mutual interplay of heart's electrical and mechanical functioning, which ensures an appropriate contraction-relaxation cycle following propagation of the electrical impulse throughout the heart. Contraction and relaxation movements are also known as systole and diastole, respectively.

## 1.2.2 Cellular Electrical Activity

Cardiomyocytes are surrounded by a lipid bilayer membrane that restricts the flow of water-soluble substances, such as ions, except for specific ion-permeable pores in the membrane called ion channels. These ion channels are pore-forming proteins embedded in the membrane that selectively allow ions to pass through them. The main ions in the intracellular and extracellular media of cardiomyocytes are potassium ( $K^+$ ), sodium ( $Na^+$ ), calcium ( $Ca^{2+}$ ) and chloride ( $Cl^-$ ), being their movement driven by the electrical gradient force and the chemical gradient force.

This ionic movement across the cell membrane, in relation to the opening and closing of ion channels, generates a transmembrane potential which can be explained by the different ion concentrations between the inside and the outside of the cell and the permeability of each ion. The evolution of this transmembrane potential along a cardiac beat is called action potential (AP). The AP of cardiac myocytes is defined by a fast increase (*depolarization*) followed by a slow decrease (*repolarization*) in transmembrane voltage. This property of excitability, i.e. a brief stimulus produces an electrical response in the form of a change in transmembrane voltage before the eventual return to equilibrium, is one of the main characteristics of atrial and ventricular cardiomyocytes [7].

Fig 1.2 illustrates the AP of a ventricular cell together with an indication of its different phases along a cycle:

- **Phase 0. Rapid Depolarization:** This phase, also known as AP *upstroke*, is caused by a rapid inflow of  $Na^+$  through voltage-gated sodium channels, which generates a sharp increase in transmembrane potential as long as the cell has been excited with an stimulus current of sufficient magnitude to raise voltage over the threshold for sodium channels to open. During this phase, transmembrane potential may change from -85 mV to more than 20 mV in approximately 3-5 ms [8, 9].
- **Phase 1. Early Repolarization:** In this phase, also known as AP *dome*, the sodium channels become inactivated, whereas the outward transient potassium current begins to repolarize the cell, thus transiently reducing the transmembrane potential [8, 9].



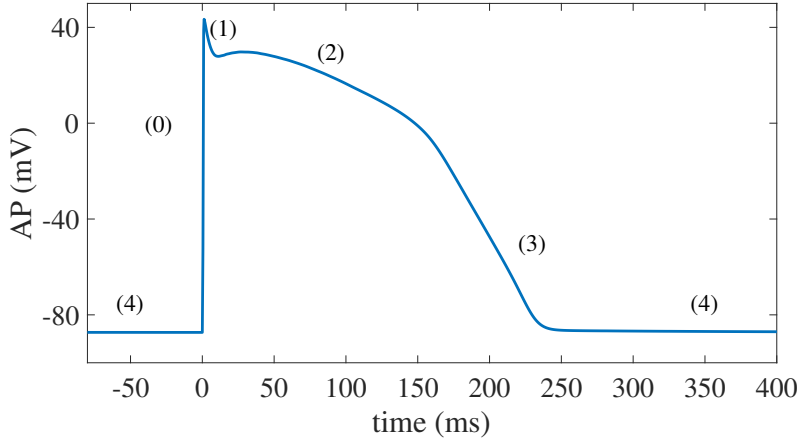


Figure 1.2: Illustration of an AP as obtained by the computational ORd human ventricular cell model [5], with an indication of the different AP phases.

- **Phase 2. Plateau:** This AP *plateau* phase is due to the balance between the influx of  $\text{Ca}^{2+}$  ions through the slow calcium channels and the slow opening of outward  $\text{K}^{+}$  channels [8, 9].
- **Phase 3. Repolarization:** In this phase, the transmembrane potential returns to the resting potential due to inactivation of  $\text{Ca}^{2+}$  channels while  $\text{K}^{+}$  channels are open [8, 9].
- **Phase 4. Resting Potential:** In this final AP phase the transmembrane potential reaches the resting potential value (approximately -85 mV), with a large contribution of outward  $\text{K}^{+}$  currents [8, 9].

The electrical activity of cardiac myocytes can be recorded by several experimental techniques, such as patch-clamp and optical mapping. Patch-clamp allows studying the electrophysiological properties from the whole-cell to single ion channels. Erwin Neher and Bert Sakmann earned the Nobel Prize for developing this technique [10]. By measuring the ionic current that passes through a patch formed by the tip of a glass pipette and the cell membrane, the system injects the opposite amount of current to clamp the membrane potential to a specific voltage. The two main configurations of the patch-clamp technique are the whole-cell, where the electrical activity of the entire cell is recorded, and the cell-attached, where the electrical activity of a specific area or a single channel is recorded (Fig. 1.3)[10, 11]. One limitation of the patch-clamp technique is that the system can not clamp voltage for multiple cells connected to each other, as when they are forming the so-called myocardial syncytium.

On the other hand, the optical mapping technique allows obtaining an estimation of the evolution of voltage along time for cardiac cells and tissues. This technique exploits the fluorescent properties of voltage-dependent dyes that are used to load

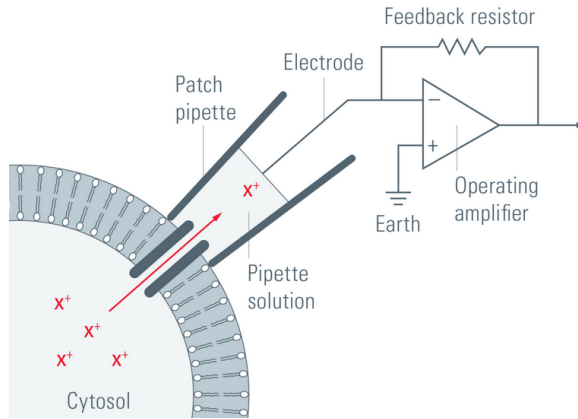


Figure 1.3: Scheme of the patch-clamp technique for cell-attached version. Figure from [12].

the cells or tissues with. An optical mapping equipment, with specific filters and fast recording cameras, measures changes in fluorescence along time as an indirect measurement of transmembrane voltage. One important advantage of this approach is that it can be used to simultaneously record the transmembrane potential and the intracellular calcium transient of a cardiac cell, tissue or even the whole heart with high spatio-temporal resolution [13].

### 1.2.3 Electromechanical Coupling

Cardiac electromechanical coupling is responsible for an appropriate contraction - relaxation cycle of the heart, with electrical depolarization triggering contraction of cardiac cells. The opening of calcium channels, caused by depolarization of the cell membrane, generates an inward calcium current into the cell that results in the AP plateau phase. This entry of calcium ions through the L-type calcium channels leads to an increase in the calcium concentration of the dyadic space (an internal subspace composed by T-tubules), which triggers the opening of the calcium-sensitive ryanodine receptors (RyR) in the adjacent sarcoplasmic reticulum (SR). This, in turn, leads to a calcium release from the SR, so-called *calcium-induced calcium release*, which increases calcium availability in the cytosol. Part of the calcium in the cytosol binds to troponin and calmodulin. Binding of calcium to troponin promotes myofilament contraction, as the binding produces a conformational change that allows myosin heads to interact with actin filaments in the so-called *crossbridge cycling*, which generates tension. When contraction ends, the SR Ca-ATPase (SERCA) pump returns the intracellular calcium ions to the SR. The joint ordered contraction of cardiac cells in a small period of time allows blood to be pumped by the heart.

So far, excitation-contraction coupling has been described. However, not only does

electrical excitation influence mechanical contraction, but also the deformation of the heart alters cellular excitation as a result of the so-called mechano-electrical feedback (MEF). MEF has been shown to play an important role in cardiac arrhythmias. One of the MEF mechanisms has to do with the effect of myofilament length on calcium dynamics, as the buffer ability of troponin increases when myofilaments are stretched [14], which has an impact on the AP [15]. Another relevant MEF mechanism is through mechano-sensitive ion channels, like the stretch-activated channels (SAC) in the cell membrane, whose current is closely controlled by the contraction of the medium. Upon stretch of cardiac cells or tissues, SACs alter AP properties, including duration, resting membrane potential, refractory period or rate dependence [16, 17].

### 1.2.4 Electrical Propagation in Tissue and throughout the Heart

Properly synchronized electrical activation of different regions in the heart is key for correct heart functioning. Each cardiac cycle commonly starts when an AP is fired by the natural pacemaker of the heart, the sinoatrial (SA) node, which is a group of cells located in the upper part of the right atrium, specifically at the junction of the right atrium and the superior vena cava. SA node cells are self-activated at a rate of about 70-80 beats per minute. From the SA node, the electrical impulse propagates throughout the atria, first activating the right atria and subsequently the left atria. Before reaching the ventricles, the electrical impulse propagates through the atrioventricular (AV) node, where it is delayed to allow blood to pass from the atria to the ventricles before the valves separating them become closed. Once the impulse traverses the AV node, it goes through the bundle of His, which is subsequently divided into the right and left bundle branches. These branches get ramified into the Purkinje fibers, which are connected to the ventricles and allow the impulse to quickly spread throughout the ventricles. Upon electrical depolarization, the ventricles contract and pump out blood to the lungs and to the rest of the body.

Fig. 1.4 shows APs corresponding to different cardiac regions, with delays between different APs similar to those reported for a healthy human heart. Not only do APs from different regions present varied AP durations, but also varied AP shapes.

### 1.2.5 Electrograms and Electrocardiograms

An intracardiac electrogram (EGM) is a signal obtained by placing directly, and thus invasively, electrodes on the heart surface to measure localized electrical activity in the region of the heart where the recording electrodes are positioned. The EGM represents the instantaneous difference between signals recorded from two electrodes. If the two are intracardiac, a bipolar EGM is obtained, whereas if one is intracardiac and the other one is positioned remotely, a unipolar EGM is obtained. If the two electrodes are nearly located, the EGM signal is more insensitive to far-field components and more closely reflects the near-field component, even if this is at the cost of a lower amplitude

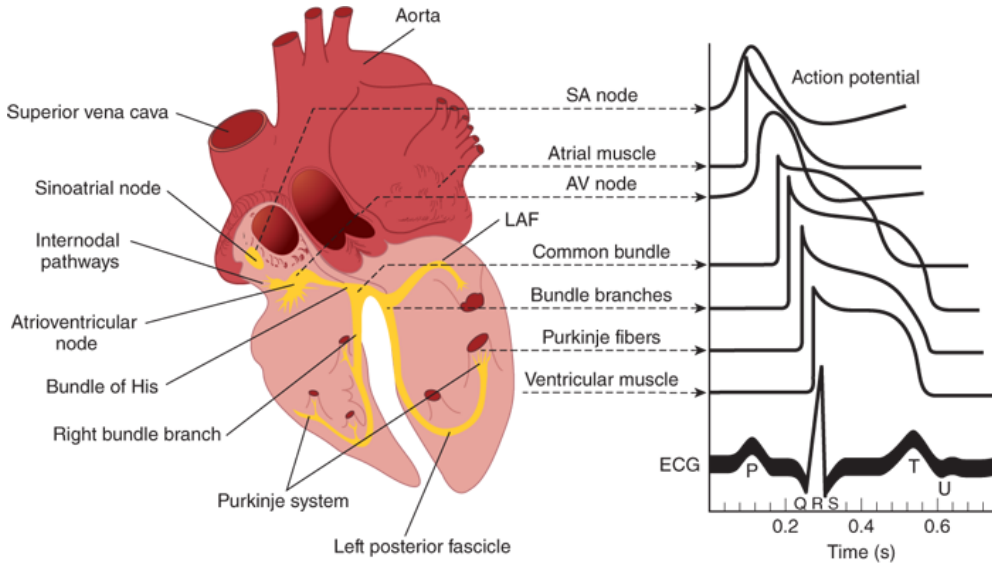


Figure 1.4: AP waveforms for cells corresponding to different cardiac regions, with delays between different APs similar to those reported for a healthy human heart. Figure adapted from [18].

signal. On the other hand, if the two electrodes are far apart, the EGM signal will collect information from a larger cardiac region and will show larger amplitude, but the local potential will be more contaminated from far-field components. An example of an EGM signal is presented in Fig.1.5.

In this thesis, measurements from unipolar EGM signals sampled at 512 Hz from patients with an implanted biventricular pacing resynchronization device are used. EGMs are recorded from an epicardial electrode of the device, which allows ambulatory recording of electrophysiological signals. Activation-recovery intervals (ARIs) are obtained from EGMs as surrogate measures of AP duration (APD). ARIs are measured from the time of the minimum derivative of the QRS complex in the EGM, representing local activation time, to the time of the maximum derivative of the subsequent T-wave, representing local repolarization time [20].

An electrocardiogram (ECG) is a signal obtained by placing electrodes at specific locations on the body surface to measure the electrical activity of the heart. As depolarization and repolarization occur throughout the heart, electrical currents spread in the body, since this acts as a volume conductor. In a standard 12-lead ECG, electrodes are placed on the arms and legs, which serve to record standard (I, II, III) and augmented (aVR, aVL, aVF) limb leads, and six electrodes are placed at specific locations on the chest, which serve to measure precordial leads (V1, V2, V3, V4, V5, V6). These leads measure voltage differences between electrodes. In the case of standard limb leads, these are bipolar and measure the voltage difference between a positive

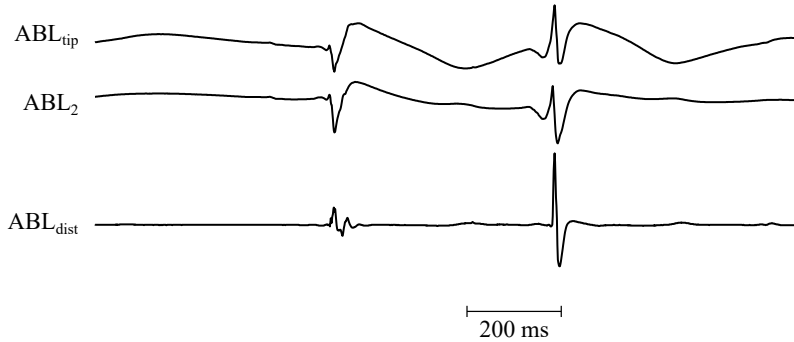


Figure 1.5: Unipolar EGM signals ( $ABL_{tip}$  and  $ABL_2$ ) recorded at tip and second electrode of an ablation catheter and Bipolar EGM signal ( $ABL_{dist}$ ) from the ablation catheter. Figure extracted from [19].

and a negative electrode in the limbs. In the case of the augmented leads and precordial leads, these are unipolar and measure the voltage difference between a positive electrode and a combination of other electrodes to serve as a negative electrode. Fig. 1.6 shows the electrode positions and the leads of a standard 12-lead ECG.

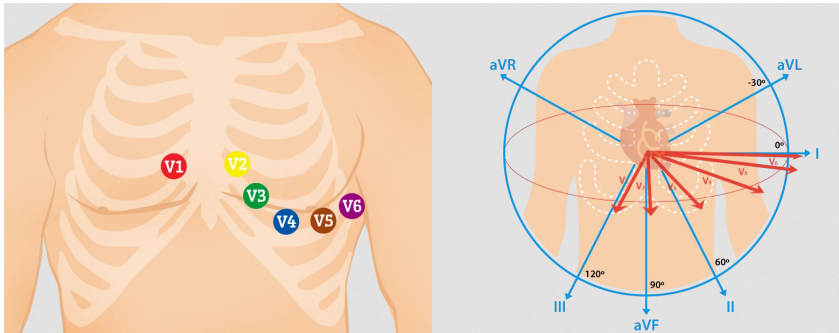


Figure 1.6: Left: Schematic diagram of some ECG electrode positions. Right: Leads of the standard 12-lead ECG. Figure extracted and adapted from [21].

Each cardiac cycle in the ECG is represented by characteristic waveforms, segments and intervals, as illustrated in Fig. 1.7:

- The P-wave represents the sequential activation of the right and left atria.
- The QRS complex represents the activation of the right and left ventricles, with a greater contribution from the left ventricle due to its larger mass. Atrial repolarization is masked within the QRS complex.
- The T-wave represents the repolarization of the ventricles.

- The QT interval represents the time for ventricular depolarization and repolarization.
- The ST segment, between ventricular depolarization and repolarization, represents an isoelectric segment under physiological conditions.

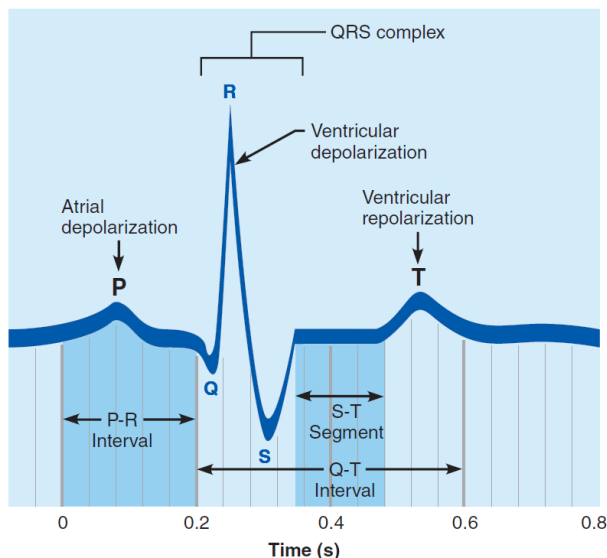


Figure 1.7: ECG cycle with definition of the main waves, segments and intervals. Figure extracted from [8].

### 1.3 The Autonomic Nervous System

As mentioned above, the ANS is a very relevant modulator of cardiac electrical activity and plays a major role in the generation of arrhythmias. Activation of the sympathetic branch of the ANS leads to increases in heart rate (HR), conduction velocity, contractility and rate of myocyte relaxation, while activation of the parasympathetic branch produces just the opposite effects. Autonomic effects on cardiac function are mediated by the release of neurotransmitters. Sympathetic nerves release norepinephrine, which binds to  $\alpha$ - and  $\beta$ -A receptors (adrenoceptors) of cardiac cells to activate signaling pathways. On the other hand, parasympathetic nerves release acetylcholine that binds to muscarinic receptors to regulate cardiac performance.

Of all adrenoceptors,  $\beta$ -adrenoceptors, and in particular  $\beta_1$ -adrenoceptors, are the main mediators of sympathetic stimulation in ventricular myocytes. When catecholamines, including norepinephrine, are released from the sympathetic nerves, they

bind to  $\beta$ 1-adrenoceptors and this activates a receptor-bound stimulatory G-protein (Gs) pathway that stimulates adenylyl cyclases to produce the ubiquitous second messenger 3'-5'-cyclic adenosine monophosphate (cAMP) and activate protein kinase A (PKA). PKA activation leads to phosphorylation of cellular substrates involved in excitation-contraction coupling. Some of these substrates include the L-type calcium current ( $I_{CaL}$ ), slow delayed rectifier potassium current ( $I_{Ks}$ ), fast sodium current ( $I_{Na}$ ), sodium-potassium pump current ( $I_{NaK}$ ), RyR, phospholamban (PLB) and Troponin I (TnI). PKA activation increases intracellular calcium transient amplitude and rate of decay.

At the level of the cellular ventricular AP,  $\beta$ -A stimulation ( $\beta$ -AS) shortens the APD and increases the slope of the APD restitution curve, among other effects. At the whole-ventricular level,  $\beta$ -AS increases spatial repolarization gradients, both transmural and apico-basal gradients, as the degree of  $\beta$ -AS-induced APD shortening is heterogeneous along the ventricles.

## 1.4 Computational Modeling of Human Ventricular Electrophysiology, Mechanics and Autonomic Modulation

### 1.4.1 *In silico* Modeling as a Complement to *in vitro* and *in vivo* Research

As in many fields of science, *in silico* modeling of cardiac electrophysiology has become a powerful tool to complement experimental and clinical research. As a result of advances in mathematical methods and computer processing performance, realistic computational simulations that were unaffordable a few years ago due to their high computational cost can now be carried out. In the field of cardiac electrophysiology, detailed computational models covering spatial scales ranging from sub-cellular, cellular, tissue and up to whole organ have been published that enable a large number of simulation possibilities to deepen our understanding of cardiac electrophysiology in health and disease. Models for most cardiac regions and species are now available based on extensive experimental data used for model development, calibration and validation.

The intrinsic characteristics of cardiac electrophysiology, where changes at the subcellular scale influence all the other spatial scales, from cell to whole organ and even to torso, encourage the use of computational models where different underlying ionic mechanisms and their macroscopic effects can be analyzed systematically. Furthermore, cardiac models can offer the possibility to integrate in a single model the descriptions of the electrical function of a cell or tissue together with the descriptions of the mechanical function and the modulation by other systems like the ANS, as

described above.

The applications of computational modeling are extensive. It has been shown that *in silico* modeling and simulation can guide the design and testing of new drug compounds, as well as of other therapeutic interventions, and to contribute to monitoring processes. This *in silico* evaluation complements *in vitro* and *in vivo* experimentation, helping to avoid, at least partially, unnecessary testing on animals before going into human trials. In addition, *in silico* modeling can be of great help in simulating scenarios that are not feasible to perform through *in vivo* experimentation due to ethical considerations or high implementation costs. Furthermore, another important benefit of cardiac modeling is in improving currently used systems for medical decision making and personalized therapy by the development of personalized computational models that reproduce as faithfully as possible the individual behavior e.g. in response to ANS maneuvers, the effects of treatment and/or of diseased conditions.

## 1.4.2 Electrophysiological Models of Human Ventricular Cells

### 1.4.2.1 Hodgkin & Huxley Model

In 1952, Alan Lloyd Hodgkin & Andrew Fielding Huxley proposed the first action-reaction electrophysiological model (called HH) [22], based on precise measurements of sodium and potassium ion channel kinetics and electrical activity of the squid giant axon by the voltage-clamp technique [23]. Hodgkin & Huxley were the first to describe the electrical activity of an excitable cell in terms of a simple electrical circuit containing resistors (ion channels), capacitors (cell membrane) and voltage sources. The HH model described the electrical activity of the squid giant axon with only four different ionic currents, displayed in parallel as shown in Fig. 1.8: sodium current ( $I_{Na}$ ), potassium current ( $I_K$ ), leak current ( $I_L$ ) and capacitive current ( $I_C$ ). It is interesting to highlight that the leak current comprises the current generated by the rest of ions. In the next paragraphs, the mathematical formulations used by Hodgkin & Huxley to describe this electrical circuit are presented.

Ionic movement across the cell membrane is mediated by electrostatic attraction/repulsion forces and diffusion forces. The equilibrium between these two forces is calculated by the *Nernst Equation* as follows:

$$V_x = -\frac{RT}{z_x F} \log\left(\frac{[x]_i}{[x]_o}\right), \quad (1.1)$$

where  $V_x$  is the Nernst Potential for a specific ion  $x$ ,  $R$  is the ideal gas constant,  $T$  is the absolute temperature,  $z_x$  is the ion valence,  $F$  is Faraday's constant,  $[x]_o$  is the ionic concentration in the extracellular media and  $[x]_i$  is the ionic concentration in the intracellular media.

As can be observed from the right panel of Fig. 1.8, the diffusion force can be modeled by a voltage source (a battery) following the Nernst equation. On the other



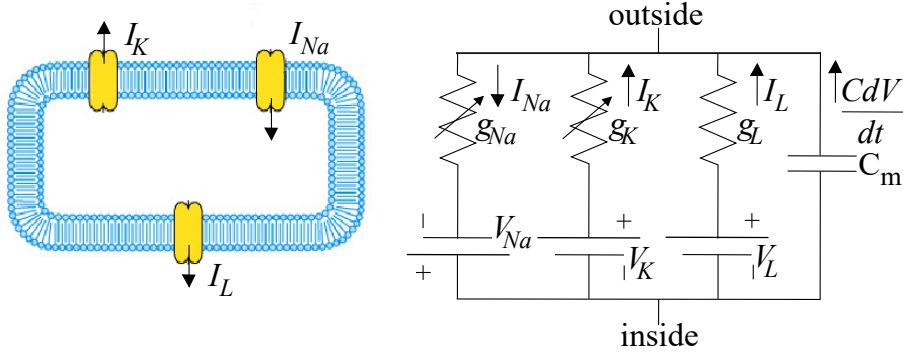


Figure 1.8: Left: Schematic diagram of the Hodgkin-Huxley model showing the cell membrane and the three typologies of ionic channels. Right: Scheme of the equivalent circuit of the Hodgkin-Huxley model with the sodium, potassium and leak currents. Figure extracted and adapted from [24, 25].

hand, by the use of Ohm's law, it is straightforward to obtain the conductance per unit area,  $g_x$ , for a specific ion  $x$  as in Eq. 1.2, where  $I_x$  is the current through the ion channels of type  $x$ ,  $V_m$  is the transmembrane voltage and  $V_x$  is the Nernst potential.

$$g_x = \frac{I_x}{V_m - V_x}. \quad (1.2)$$

Following the HH formulation, each type of ion is only able to pass across channels that are specifically selective for that ion type, being the opening and closing of the channels regulated by the transmembrane voltage  $V_m$ . In the HH model for a squid giant axon, potassium channels are composed by four equal  $n$  type (activation) gates, whereas sodium channels are composed by three  $m$  type (activation) gates and one  $h$  type (inactivation) gate. The activation gates have the ability to open when voltage increases while they remain closed during the resting AP phase. On the other hand, inactivation gates are open during the resting AP phase and have the capability to close when transmembrane potential increases. In this way, the potassium and sodium ionic currents can be calculated by the following equations:

$$I_K = g_K(V_m - V_K) = g_{K_{max}} n^4 (V_m - V_K) \quad (1.3)$$

$$I_{Na} = g_{Na}(V_m - V_{Na}) = g_{Na_{max}} m^3 h (V_m - V_K), \quad (1.4)$$

where  $g_{K_{max}}$  and  $g_{Na_{max}}$  represent the maximal conductances of potassium and sodium channels, respectively. Following the HH formulation, the  $n$ ,  $m$  and  $h$  variables represent the gates used to define the open probability of each typology of ionic channel. It is interesting to highlight that, for a specific ion channel, if all the gates are in the open state, the ionic conductance is equal to the maximal ionic conductance.

The intrinsic opening/closing behavior of a specific ionic gate  $y$  is modeled by the following ODE:

$$\frac{dy}{dt} = \alpha_y(1 - y) - \beta_y y, \quad (1.5)$$

where  $\alpha_y$  is the transfer rate coefficient for particles from closed to open state,  $\beta$  is the transfer rate coefficient from open to closed state and  $y$  is the proportion of channels in the open state.

Based on the descriptions above, the total current through the cell membrane can be obtained in the HH model as the sum of each ionic current (potassium, sodium and leak) and the capacitive current as is indicated in Eq. 1.6:

$$I_{tot} = C_m \frac{dV_m}{dt} + I_K + I_{Na} + I_{leak}. \quad (1.6)$$

The HH-based mathematical definition of channel opening probability is formulated using the subunit-based approach, where the open probability of a certain channel is the probability that every gate is in the open state. However, the channel-based approach described by [26] defines this opening probability as the proportion of channels in the open state with respect to the total number of channels of the analyzed typology. Using as an example a channel composed by two different ionic gates  $r$  and  $s$ , the four possible channel states are  $r_{open-s_{open}}$ ,  $r_{open-s_{close}}$ ,  $r_{close-s_{open}}$  and  $r_{close-s_{close}}$ . The opening probability is defined as the proportion of channels in the  $r_{open-s_{open}}$  state with respect the total number of channels. This methodology is fully detailed in Chapter 4.

### 1.4.2.2 Human Ventricular Cell Models

Ten years after the HH model was presented, Denis Noble proposed the first mathematical mammalian model for cardiac cells based on the HH model. Specifically, this first cardiac model was developed to reproduce the electrical activity of Purkinje cells, whose behavior is far away from the neuron activity modeled by HH. The Noble model, with only four ODEs, has been the foundation for the development of the presently available set of cardiac computational models, both for humans and animals, for different types of cardiomyocytes.

The Noble model was developed when calcium ion channels had not yet been discovered. As experimentation in ionic channels has progressed, the computational models have become more complex, with more number of variables and ODEs, to reproduce the available experimental evidences. Four years after the Noble model was published, Krause *et al.* [27] formulated the first mammalian ventricular model and thirty two years later, Priebe & Beuckelmann [28] proposed the first human ventricular cell model with a total of 22 ODEs.

At present, tens of computational models have been proposed in the literature to reproduce the electrical activity of human ventricular cells, tissue and whole heart.

Some cellular models have been developed from scratch, such as [28, 29], whereas other models represent extensions of previous models aimed at improving their performances [30, 31]. In this thesis, populations of cellular AP models with representations of spatio-temporal variability,  $\beta$ -AS and mechanical stretch are built taking the ORd model [5] as a basis.

### 1.4.3 Coupled Models of Electrophysiology and Mechanics in Human Ventricular Cells

To investigate how electrical and mechanical activities of human ventricular myocytes influence each other, models coupling electrophysiology, calcium dynamics and mechanical stretch are used. In the literature, both strongly coupled and weakly coupled models are used [32]. Under the assumption that the mechano-electrical feedback can be neglected, weakly coupled models calculate electrical activation independently from the mechanical description and use such electrical activation as an input to solve the mechanical model. On the other hand, if for the problem at hand the mechano-electrical feedback wants to be accounted for, electrical activation should be solved while taking into consideration the mechanical description, as done in strongly coupled models [16, 33].

In this thesis strongly coupled electro-mechanical models are used. The free cytoplasmic  $\text{Ca}^{2+}$  concentration computed according to the electrophysiological model is used as an input to the mechanical model. The mechanical model feeds back the amount of  $\text{Ca}^{2+}$  buffered to troponin, computed as a function of sarcomere length (SL), into the electrophysiological model.

For the mechanical model, a version of the Niederer-Hunter-Smith model [14] adjusted to human cell characteristics is used following an approach as that described in [16] and [33], which involves modifications in the relaxation rates  $\alpha_{r1}$  and  $\alpha_{r2}$  to account for increases in these rates under higher body temperatures as well as modifications in the parameters  $T_{\text{ref}}$  and  $\text{Ca}_{50\text{ref}}$  determining contractile tension.

Models for SACs can be introduced in the electromechanical cell models by defining the total current through SACs as the sum of the current through  $\text{K}^+$ -selective SACs and the current through non-specific cationic SACs. For the current through non-selective cationic SACs, a linear time-independent formulation is commonly used, while the current through  $\text{K}^+$ -selective SACs is usually modeled as an outwardly-rectifying current [16, 33].

## 1.4.4 Models of $\beta$ -A Modulation of Cellular Ventricular Electro-Mechanical Activity

Due to the high complexity of  $\beta$ -AS effects on ventricular electrophysiology, *in silico* modeling and simulation can be of major benefit to shed light into the involved mechanisms, both in health and in disease. A number of models have been proposed in the literature to describe  $\beta$ -AS in ventricular myocytes with varied levels of detail. Saucerman and McCulloch first integrated the cAMP/PKA signaling pathway in a ventricular myocyte model [34]. Soltis and Saucerman later published a computational model that includes PKA as well as calmodulin kinase II (CaMKII) pathways [35]. Xie and coworkers updated the model by Soltis and Saucermann to slow down the  $I_{Ks}$  phosphorylation and dephosphorylation rate constants to fit experimental observations [36]. Also, PKA-mediated phosphorylation of phospholemman (PLM) was accounted for by increasing the  $\text{Na}^+$ - $\text{K}^+$ -ATPase (NKA) affinity for the intracellular  $\text{Na}^+$  concentration [36]. Negroni *et al.* later proposed a model that incorporates  $\beta$ -AS effects on properties like myofilament  $\text{Ca}^{2+}$  sensitivity and titin stiffness as well as cross-bridge cycling rate [37]. The use of this model allows dissecting the contribution of  $\beta$ -AS-induced effects on myofilament properties to the ventricular AP separately from the contribution of  $\beta$ -AS-induced effects on ionic currents and fluxes. Heijman *et al.* proposed a model that is novel in that it includes localized signaling domains, it incorporates  $\beta 1$  and  $\beta 2$  receptor isoforms and it uses a detailed population-based approach to integrate the  $\beta$ -adrenoceptors and  $\text{Ca}^{2+}$ /CaMKII signaling pathways while considering a wide range of cellular substrates.

For the purposes of this thesis, the Xie-Grandi-Puglisi-Sato-Bers model [36] is used that includes definition of graded and dynamic phosphorylation levels of cellular PKA substrates. Main PKA cellular substrates include  $I_{CaL}$ , RyR gating, PLB-dependent SERCA, PLM-dependent NKA,  $I_{Ks}$ , cystic fibrosis transmembrane regulator current (ICFTR) and myofilament sensitivity.

## 1.4.5 The ORd Human Ventricular Cell Model

### 1.4.5.1 Overall Description

The ORd model [5], developed from extensive undiseased human ventricular data, is the most detailed human ventricular computational AP model to date and presents thoroughly validated descriptions of cardiac electrophysiology. This model has the ability to reproduce the electrical activity of epicardial, endocardial and midmyocardial cells. It contains a total of 41 state variables (41 ODEs) and reproduces the activity of 16 different ionic currents (12 myoplasmic currents and 4 subspace currents), as shown in Fig. 1.9. The main novelties of the ORd model with respect to previous human ventricular models published in the literature are the formulations of major ionic currents like the transient outward potassium current ( $I_{to}$ ), the inward rectifier

potassium current ( $I_{K1}$ ), the sodium-calcium exchanger current ( $I_{NaCa}$ ),  $I_{Ks}$ ,  $I_{Kr}$ ,  $I_{Na}$  and the late sodium current ( $I_{NaL}$ ). An additional interesting feature of the ORd model is that it presents formulations to reproduce the effects of phosphorylation by CaMKII in the ionic gates of  $I_{to}$ ,  $I_{Na}$  and  $I_{CaL}$  currents.

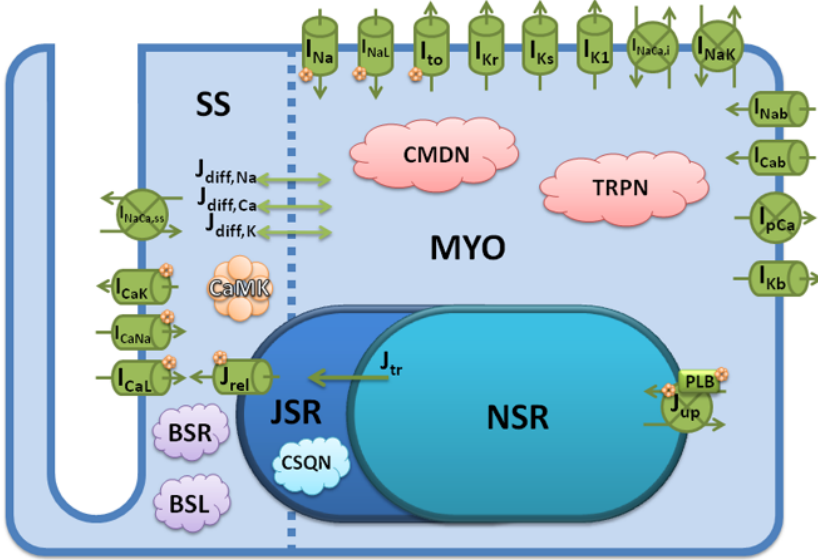


Figure 1.9: Schematic representation of ORd model [5] and ionic currents and fluxes. Figure extracted and adapted from [5].

This model is used in this thesis as a basis to construct the populations of deterministic and stochastic human ventricular cell models with representation of spatio-temporal variability of repolarization. Each of the models of the constructed population is coupled to mechanical and  $\beta$ -A signaling models.

### 1.4.5.2 Main Ionic Currents

#### Potassium currents

- *Transient outward potassium current* ( $I_{to}$ ): it has large influence in phase 1 of the AP. Their ion channels are modeled by an activation gate  $a$  and an inactivation part composed by two gates,  $i_{fast}$  and  $i_{slow}$ .
- *Slow delayed rectified potassium current* ( $I_{Ks}$ ): it has influence in the AP repolarization phase. In the ORd model, this current has less influence on the AP than in previously published human ventricular computational models in the absence of  $\beta$ -AS. Their channels are modeled by one activation gate  $x_{s1}$  and one deactivation gate  $x_{s2}$ .

- *Rapid delayed rectified potassium current* ( $I_{Kr}$ ): it is the principal current responsible for AP repolarization. Their channels are modeled by one activation/deactivation fast gate  $x_{r,fast}$  and one activation/deactivation slow gate  $x_{r,slow}$ .
- *Inward rectifier potassium current* ( $I_{K1}$ ): it is closely related with the resting membrane potential and it is modeled by an instantaneous rectification gate and a time-dependent inactivation gate  $x_{k1}$ .

### Sodium currents

- *Fast sodium inward current* ( $I_{Na}$ ): it is a very relevant component of the sodium current in human ventricular cells and it is responsible for AP depolarization. Their ion channels are modeled by three activation gates  $m$  and two inactivation gates  $h$  and  $j$ .
- *Late sodium inward current* ( $I_{NaL}$ ): it remains activated during the AP plateau and repolarization. It is considered to be another mode of the global sodium current together with the fast sodium current. Under diseased conditions, it has large impact in the development of early and delayed afterdepolarizations. Their ion channels are modeled by one activation gate  $m_L$  and one inactivation gate  $h_L$ .

### Calcium current

- *L-type calcium inward current* ( $I_{CaL}$ ): it has large influence in the AP *plateau* phase and it is integrated by one activation gate  $d$  and a combination of voltage-dependent and  $\text{Ca}^{2+}$ -dependent inactivation gates  $f$  and  $f_{Ca}$ , respectively.
- The ORd model presents two other related currents defined as  $I_{CaNa}$ , i.e. *sodium current through L-type channels*, and  $I_{CaK}$ , i.e. *potassium current through L-type channels*.

### Pump, Exchanger and Background currents

- Other important ionic currents in the ORd model include the *sodium-potassium ATPase pump current* ( $I_{NaK}$ ), the *sodium-calcium exchanger current* ( $I_{NaCa}$ ), the *sarcolemmal calcium pump current* ( $I_{pCa}$ ) and the *sodium, potassium and calcium background currents*, i.e  $I_{Nab}$ ,  $I_{Kb}$ ,  $I_{Cab}$ , respectively.

## 1.5 Objectives of the Thesis

This thesis **aims** at providing a comprehensive theoretical characterization of temporal and spatial variability in human ventricular function, both under basal conditions and in response to enhanced sympathetic activity. On the basis of such characterization, a more profound knowledge on the mechanisms underlying sympathetically-mediated increments in temporal and spatial dispersion of repolarization is aimed at being achieved. The dissected mechanisms are expected to allow discovering new strategies for arrhythmic risk stratification and for the design of more efficient therapies to prevent or treat ventricular arrhythmias.

The **specific objectives** of this thesis are:

*1. Theoretical characterization of repolarization in human ventricular cells, with representation of spatial and temporal heterogeneities*

Clinical, experimental and computational studies have provided evidence on the key role of spatio-temporal variability in human ventricular repolarization at a range of scales covering from the cellular AP to the body surface ECG. Although different methodologies have been proposed in the literature for theoretical characterization of spatio-temporal heterogeneities in human ventricular repolarization, there is still a long way to go for such characterization to realistically represent available experimental data. In this thesis novel methodologies for identification of the parameters and state variables of an underlying computational AP model given any experimental voltage trace are proposed. Those methodologies combine fast estimation techniques based on biomarkers' information with other more complex methodologies based on full voltage traces' information. The ability of the proposed methodologies to characterize spatio-temporal variability of human ventricular repolarization is assessed.

*2. Evaluation of the modulation of spatio-temporal variability of ventricular repolarization by the sympathetic nervous system*

At the level of the heart, the sympathetic nerves innervate the ventricular myocardium and elicit changes in a number of ion channels, pumps and transporters that regulate the ventricular AP and contractile function. Sympathetically-induced changes in human ventricular AP repolarization are a critical component of ventricular arrhythmias and, thus, it is of major interest to fully understand how the sympathetic nervous system modulates temporal and spatial heterogeneities in human ventricular repolarization. In this thesis, stochastic computational models with coupled descriptions of electrophysiology, calcium dynamics, mechanics and  $\beta$ -AS of human ventricular myocytes are developed to assess AP response to sympathetic provocation (SP) in a population of cells with distinct ionic characteristics while additionally evaluating beat-to-beat AP repolarization changes.

*3. Unraveling of the mechanisms underlying changes in spatio-temporal variability of human ventricular repolarization mediated by the sympathetic nervous system*

Different studies in the literature have investigated the mechanisms underlying changes in temporal and spatial variability of ventricular repolarization mediated by the action of the sympathetic nervous system. Although evidence has been provided on the role of  $\beta$ -AS as a contributor to enhanced spatial repolarization dispersion and to increased beat-to-beat variability, particularly under conditions of reduced repolarization reserve, it is still unclear how particular forms of arrhythmogenic variability, such as low-frequency (LF) oscillations of APD, are modulated by the sympathetic action. In this thesis, stochastic electrophysiology-mechanics-adrenergic signaling models together with statistical methods based on Automatic Relevance Determination are used to unravel the major ionic contributors to augmented overall beat-to-beat variability as well as LF oscillations of APD in response to SP.

*4. Determination of the relationship between elevated spatio-temporal variability in human ventricular repolarization and increased risk for ventricular arrhythmias in response to sympathetic provocation*

Instabilities in the repolarization phase of the ventricular AP are relevant to arrhythmogenesis. There is substantial evidence that elevated variability of ventricular repolarization is associated with ventricular arrhythmias and sudden cardiac death. However, a full explanation of how the sympathetic nervous system contributes to such elevated variability, particularly in the form of LF oscillations, and of its role in arrhythmogenesis is still lacking. In this thesis, a computational approach is used to establish a relationship between the mechanisms dissected as underlying sympathetically-mediated elevation of spatio-temporal repolarization variability and arrhythmogenesis. Statistical methods grounded on Canonical Correlation Analysis are employed.

## 1.6 Outline of the Thesis

The thesis is organized as follows:

- **Chapter 2: Low Frequency Oscillations and Temporal Variability of Human Ventricular Repolarization.** This chapter theoretically characterizes the experimentally reported interactions between overall beat-to-beat repolarization variability (BVR) and a particular type of variability in the form of LF oscillations of APD in response to SP. An experimentally-calibrated population of computational stochastic human ventricular cell models are generated to reproduce such interactions, to analyze their underlying ionic mechanisms and to link elevated BVR and LF oscillations of APD with increased risk for ventricular arrhythmias. The results of this chapter have been published in two scientific



papers and have been presented in two international conferences:

- **D. A. Sampedro-Puente**, J. Fernandez-Bes, B. Porter, S. Duijvenboden, P. Taggart E. Pueyo. “Mechanisms Underlying Interactions between Low-Frequency Oscillations and Beat-to-Beat Variability of Cellular Ventricular Repolarization in Response to Sympathetic Stimulation: Implications for arrhythmogenesis.” *Frontiers in Physiology*, 2019. DOI: 10.3389/fphys.2019.00916.
  - S. van Duijvenboden, B. Porter, E. Pueyo, **D. A. Sampedro Puente**, J. Fernandez-Bes, B. Sidhu, J. Gould, M. Orini, Martin Bishop, B. Hanson, P. Lambiase, R. Razavi, C. A. Rinaldi, J. S. Gill and P. Taggart. “Complex Interaction between Low-Frequency APD Oscillations and Beat-to-Beat APD Variability in Humans is Governed by the Sympathetic Nervous System.” *Frontiers in Physiology*, 2019. DOI: 10.3389/fphys.2019.01582 .
  - **D. A. Sampedro-Puente**, J. Fernandez-Bes, B. Porter, S. Duijvenboden, P. Taggart, E. Pueyo. “Mechanisms underlying interactions between low-frequency oscillations and beat-to-beat repolarization variability in human ventricles under sympathetic provocation.” *European Working Group on Cardiac Cellular Electrophysiology EWGCCE*. Essen (Germany). June 2018.
  - **D. A. Sampedro-Puente**, J. Fernandez-Bes, B. Porter, S. Duijvenboden, P. Taggart, E. Pueyo. “Mechanisms underlying interactions between low-frequency oscillations and beat-to-beat repolarization variability under sympathetic provocation.” *V Virtual Physiological Human Conference VPH 2018*. Zaragoza (Spain). September 2018, p.33.
- **Chapter 3: Time Course of Low-Frequency Oscillations of Human Ventricular Repolarization.** This chapter analyzes the time course for the development of the LF oscillatory behavior investigated in Chapter 2. The ionic mechanisms underlying the time lag for the manifestation of LF oscillations of APD in response to enhanced sympathetic activity are dissected, which serves to establish a relationship between concomitant short time lags/large magnitudes of APD oscillations and arrhythmic risk under simulated disease conditions. The results of this chapter have been published in a scientific journal paper and have also been presented in two international conferences:
    - **D. A. Sampedro-Puente** , J. Fernandez-Bes, N. Szentandrassy, P. P. Nánasi, P. Taggart and E. Pueyo. “Time Course of Low-Frequency Oscillatory Behavior in Human Ventricular Repolarization Following Enhanced Sympathetic Activity and Relation to Arrhythmogenesis.” *Frontiers in Physiology*, 2019. DOI: 10.3389/fphys.2019.01547.
    - J. Fernandez Bes, **D. A. Sampedro-Puente**, P. Taggart, E. Pueyo. “Time Course of Cardiac Electrical Oscillatory Behavior in Response to Enhanced

- Sympathetic Activity and Relation to Arrhythmogenesis.” *10th European Study Group on Cardiovascular Oscillations ESGCO*. Viena (Austria). September 2018.
- **D. A. Sampedro Puente**, J. Fernandez-Bes, A. Olivan-Viguera, M. Perez-Zabalza, S. Orós, S. van Duijvenboden, B. Porter, P. Taggart, E. Pueyo. “The interplay of autonomic and mechanical modulation of ventricular repolarization in Human.” *8th International Workshop Cardiac Mechano-Electric Coupling and Arrhythmias*. Freiburg (Germany). September 2019.
- **Chapter 4: Data-Driven Identification of Stochastic AP Models for the Study of Spatio-Temporal Human Ventricular Repolarization Variability.** This chapter introduces a novel methodology for the construction of populations of computational AP models more faithfully representing available experimental data. The proposed methodology jointly estimates the parameters and state variables of stochastic human ventricular AP models given an input voltage trace, as could be measured experimentally. This methodology, based on formulation of nonlinear state-space representations and Unscented Kalman Filter (UKF) contributes to improve the characterization of spatio-temporal repolarization variability. The results of this chapter have been published in a scientific journal paper and have been presented in four scientific conferences:
    - **D. A. Sampedro-Puente**, J. Fernandez Bes, L. Virág, A. Varró, E. Pueyo. “Data-driven Identification of Stochastic Model Parameters and State Variables: Application to the Study of Cardiac Beat-to-beat Variability.” *IEEE Journal of Biomedical and Health Informatics*, 2019. DOI: 10.1109 / JBHI.2019.2921881.
    - **D. A. Sampedro-Puente**, J. Fernandez Bes, E. Pueyo Paules. “Unscented Kalman Filter for Unobservable Parameter Estimation in Heart Cell Signals.” *V Jornada de Jóvenes Investigadores del I3A*. Zaragoza (Spain). May 2016, pp. 27-28.
    - J. Fernandez-Bes, **D. A. Sampedro-Puente**, E. Pueyo. “Identification of Parameters describing Phenomenological Cardiac Action Potential Models using Sigma-Point Methods.” *XLIV International Conference on Computing in Cardiology CINC*. Rennes (France). September 2017, pp. 1-4. DOI: 10.22489/CinC.2017. 060-109.
    - J. Fernandez-Bes, **D. A. Sampedro-Puente**, E. Pueyo. “Unscented Kalman Filter para el ajuste de parámetros de modelos fenomeno-lógicos de potencial de acción.” *XXXV Congreso de la Sociedad Española de Ingeniería Biomédica CASEIB*. Bilbao (Spain). November 2017, pp. 499-502.
    - J. Fernandez-Bes, **D. A. Sampedro-Puente**, E. Pueyo Paules. “A Bayesian Filtering methodology to identify key drivers of ventricular repolarization variability.” *V Virtual Physiological Human Conference VPH2018*. Zaragoza, (Spain). September 2018, p.19.

- **Chapter 5: Fast and Accurate Computational Characterization of Spatio-Temporal Human Ventricular Repolarization Variability.** This chapter presents several improvements to the methodology presented in Chapter 4. The UKF method for model and state variable estimation is combined with the Double Greedy Dimension Reduction method with automatic biomarker generation, leading to more accurate results in reproducing input AP traces and statistical distributions of AP-derived biomarkers. Also, the convergence of the new method is made significantly faster. Importantly, the proposed methodology is tested not only over AP signals measured under baseline conditions but also in response to  $\beta$ -AS. This chapter contains the work developed during a research visit to the REO Group (Mathematical Modelling and Numerical Simulation of Biological Flows) from *Institut National de Recherche en Informatique et en Automatique INRIA* (Paris, France) under the supervision of Dr. Damiano Lombardi. The results of this chapter have led to a scientific journal paper that has been submitted to IEEE Journal of Biomedical and Health Informatics:
  - **D. A. Sampedro-Puente**, F. Raphael, J. Fernandez-Bes, P. Laguna, D. Lombardi, E. Pueyo. “Characterization of Spatio-Temporal Cardiac Variability at Baseline and under  $\beta$ -Adrenergic Stimulation by Combined Unscented Kalman Filter and Double Greedy Dimension Reduction.” IEEE Journal of Biomedical and Health Informatics, 2019. Submitted, under review process.
- Chapter 6 presents the most relevant conclusions of the thesis and indicates research lines for future investigations.



# 2 | Low-Frequency Oscillations and Temporal Variability of Human Ventricular Repolarization: Characterization, Mechanisms and Relation to Arrhythmic Risk

---

2.1	Introduction . . . . .	26
2.2	Materials and Methods . . . . .	27
2.2.1	Human Data . . . . .	27
2.2.2	Stochastic Human Ventricular Models . . . . .	28
2.2.3	Measurements of Repolarization Variability . . . . .	33
2.2.4	Contributors to BVR and LF Oscillations . . . . .	34
2.2.5	Contributors to Arrhythmogenesis . . . . .	36
2.3	Results . . . . .	37
2.3.1	Sympathetic Provocation Increases BVR and LF Oscillations of APD . . . . .	37
2.3.2	Close Interaction between BVR and LF Oscillations of APD, particularly in Response to Sympathetic Provocation . . . . .	38
2.3.3	$K^+$ and $Ca^{2+}$ Current Densities are Common Modulators of BVR and LF Oscillations of APD . . . . .	40
2.3.4	Modulation of BVR and LF Oscillations of APD by $K^+$ and $Ca^{2+}$ Current Densities is Explained by their Effects on Ionic Gating Stochasticity, $\beta$ -AS and Hemodynamic Loading . . . . .	42

2.3.5	Severe Disease Conditions Accentuate both BVR and LF Oscillations of APD, Leading to Electrical Instabilities . . . . .	46
2.4	Discussion . . . . .	47
2.4.1	Relation between Sympathetically Mediated BVR and LF Oscillations of APD in a Human Ventricular Population . . . . .	48
2.4.2	Main Contributors to Increased BVR and LF Oscillations of APD following Enhanced Sympathetic Activity . . . . .	51
2.4.3	Pro-Arrhythmic Events associated with Increased BVR and LF Oscillations of APD under Severe Disease Conditions . . . . .	52
2.4.4	Limitations and Future Work . . . . .	54
2.5	Conclusions . . . . .	55

---

## 2.1 Introduction

BVR is an inherent property of ventricular electrical function [38, 39]. When enhanced, this temporal variability has been associated with arrhythmia vulnerability in patients with structural heart disease [40], drug-induced long QT syndrome [41], heart failure [42], and catecholaminergic polymorphic ventricular tachycardia [43]. A link between increased BVR and arrhythmogenesis has been established in a range of animal models as well [39, 44, 45]. Various approaches have been proposed in the literature to quantify BVR at the level of the body surface ECG, including measurements of QT interval variability [38], T-wave alternans, [46] or T-wave morphology variations [47].

Recent studies have shown that BVR presents a clear LF oscillatory pattern that can be quantified from the ECG by measuring LF oscillations of the T-wave vector, so-called Periodic Repolarization Dynamics (PRD) [48, 49]. PRD has been shown to be unrelated to heart rate variability or respiratory activity and has been postulated to most likely reflect the effect of phasic sympathetic activity on the ventricular myocardium. Increases in PRD have been associated with destabilization of repolarization leading to ventricular arrhythmias and sudden cardiac death [48, 50]. The described T-wave oscillations have been suggested to reflect oscillations of the ventricular APD [20, 49, 51]. In *in vivo* studies on heart failure patients, APD has been shown to indeed oscillate at the same LF range [20]. Additional studies have demonstrated that both LF oscillations of APD and BVR are significantly augmented in response to physiologically-induced increased sympathetic activity, with a close interaction between both observed increments [51, 52].

The mechanisms underlying the interactions between BVR and LF patterning of APD in response to SP and its potential link to arrhythmogenesis remain to be

investigated. Regarding BVR, a growing number of studies, both experimental and computational, have provided evidence on the role of ion channel stochasticity and  $\text{Ca}^{2+}$  cycling variations as underlying mechanisms of temporal variability at different scales, covering from isolated cells [53–58] to coupled cells / tissue [55, 56, 58–60] to whole heart [38, 61]. Furthermore, the action of adrenergic stimulation in modulating those BVR mechanisms and facilitating arrhythmia initiation by the formation of afterdepolarizations and triggered activity has been reported in single cells [62–66] and in the whole heart [45]. In respect of LF oscillations of APD, computational investigations in single cells have suggested that sympathetic nerve activity promotes their generation by both a direct  $\beta$ -A action and through the intermediary of mechano-electric feedback [33]. In the presence of disease-related conditions, like  $\text{Ca}^{2+}$  overload and reduced repolarization reserve (RRR), these oscillations have been shown to contribute to pro-arrhythmia [33].

In the work presented in this chapter, which builds on the work published in [33], a set of stochastic human ventricular AP models are developed to reproduce the sympathetically-mediated interactions between BVR and LF patterning of APD observed experimentally, to investigate their underlying mechanisms and to establish a link to arrhythmic risk. The developed models are representative of a whole range of AP characteristics and include biophysically detailed descriptions of the electrophysiology,  $\text{Ca}^{2+}$  dynamics,  $\beta$ -A signaling and mechanics of human ventricular cells in health and disease. Stochastic gating of ion channels are incorporated into major currents active during AP repolarization. An approach based on the Automatic Relevance Determination (ARD) technique [67] is adopted to unravel the major ionic contributors to augmented BVR and LF oscillations of APD in response to SP, with subsequent analysis of the involved mechanisms. The relationship between the unraveled mechanisms and arrhythmogenesis is established by a methodology grounded on Canonical Correlation Analysis (CCA) [68].

## 2.2 Materials and Methods

### 2.2.1 Human Data

Previously acquired human data has been described in detail elsewhere [51]. Briefly, eleven heart failure patients with cardiac resynchronization therapy defibrillator devices had ARIs recorded from left ventricular epicardial electrodes alongside simultaneous non-invasive blood pressure and respiratory recordings. Heart rate was clamped by right ventricular pacing. Recordings took place during resting conditions and following an autonomic stimulus (Valsalva maneuver). The study was approved by the West London Ethics Committee and conformed to the standards set by the Declaration of Helsinki (latest revision: 64th WMA General Assembly). Informed consent was obtained in writing from all subject.

## 2.2.2 Stochastic Human Ventricular Models

### 2.2.2.1 Models of Electrophysiology

The ORd human ventricular epicardial cell model [5] served as a basis to construct a set of AP models covering a range of experimentally observed electrophysiological characteristics. Each AP model in the dataset, which represents a different virtual cell, was obtained by varying the ionic conductances of the following currents: slow delayed rectifier  $K^+$  current,  $I_{Ks}$ ; rapid delayed rectifier  $K^+$  current,  $I_{Kr}$ ; transient outward  $K^+$  current,  $I_{to}$ ; L-type  $Ca^{2+}$  current,  $I_{CaL}$ ; inward rectifier  $K^+$  current,  $I_{K1}$ ; sodium current,  $I_{Na}$ ;  $Na^+$ - $K^+$  pump current,  $I_{NaK}$ ; and  $Na^+$ - $Ca^{2+}$  exchanger current,  $I_{NaCa}$ . A total of 500 models were initially generated by sampling the nominal conductance values of the ORd model in the range  $\pm 100\%$  using the Latin Hypercube Sampling method, [33, 69].

Out of all the generated models, only those satisfying the calibration criteria shown in Table 2.1 were retained. Such criteria were based on experimentally available human ventricular measures of steady-state AP characteristics taken from [5, 70–73]. These characteristics included:  $APD_{90|50}$ , denoting 1 Hz steady-state APD at 90%|50% repolarization (expressed in ms); RMP, standing for resting membrane potential (in mV);  $V_{peak}$ , measuring peak membrane potential following stimulation (in mV); and  $\Delta APD_{90}$ , calculated as the percentage of change in  $APD_{90}$  with respect to baseline when selectively blocking  $I_{Ks}$ ,  $I_{Kr}$  or  $I_{K1}$  currents (measured in ms). After applying the described calibration criteria, the initial set of 500 models was reduced to a set of 161 selected models. In addition, models leading to pro-arrhythmic events at baseline conditions were excluded because they did not allow quantification of BVR or LF oscillations of APD, thus resulting in a final population of 123 models. For each of those models, the parameters  $\theta_{Ks}$ ,  $\theta_{Kr}$ ,  $\theta_{to}$ ,  $\theta_{CaL}$ ,  $\theta_{K1}$ ,  $\theta_{Na}$ ,  $\theta_{NaCa}$  and  $\theta_{NaK}$  were defined to take the values of the factors multiplying the nominal conductances of  $I_{Ks}$ ,  $I_{Kr}$ ,  $I_{to}$ ,  $I_{CaL}$ ,  $I_{K1}$ ,  $I_{Na}$ ,  $I_{NaK}$  and  $I_{NaCa}$ , respectively, with respect to the original ORd model, i.e.  $I_j = \theta_j I_{j,ORd}$ , where  $I_{j,ORd}$  represents current  $j$  in the ORd model, with  $j$  being one of the elements in the set  $\{Ks, Kr, to, CaL, K1, Na, NaCa, NaK\}$ .

Table 2.1: Calibration criteria applied onto human ventricular cell models.

AP characteristic	Min. acceptable value	Max. acceptable value
Under baseline conditions [5, 70, 71]		
$APD_{90}$ (ms)	178.1	442.7
$APD_{50}$ (ms)	106.6	349.4
RMP (mV)	-94.4	-78.5
$V_{peak}$ (mV)	7.3	-
Under 90% $I_{Ks}$ block [5]		
$\Delta APD_{90}$ (%)	-54.4	62
Under 70% $I_{Kr}$ block [73]		
$\Delta APD_{90}$ (%)	34.25	91.94
Under 50% $I_{K1}$ block [72]		
$\Delta APD_{90}$ (%)	-5.26	14.86



Stochasticity was incorporated into the equations describing the ionic gating of four major currents active during AP repolarization, namely  $I_{Ks}$ ,  $I_{Kr}$ ,  $I_{to}$  and  $I_{CaL}$ , following the approach described in [56]. For a gating variable  $x$ , the temporal evolution of the probability of this gate being open was calculated as in Eq. 2.1, where the variance of the stochastic term introduced to formulate the Stochastic Differential Equation (SDE) describing ionic fluctuations was inversely proportional to the number of channels of each species. In equation 2.1,  $x_\infty$  and  $\tau_x$  represent the steady-state value of  $x$  and the time constant to reach that steady-state value, with  $x$ ,  $x_\infty$  and  $\tau_x$  being functions of voltage, while  $w$  is a Wiener process. The number of channels  $N$  associated with each species  $j$  were obtained for each virtual cell by multiplying the ionic factor  $\theta_j$  of that cell by the corresponding number of channels in the ORd model, i.e.  $N_j = \theta_j N_{j,ORd}$ .

$$dx = \frac{x_\infty - x}{\tau_x} dt + \frac{\sqrt{x_\infty + (1 - 2x_\infty)x}}{\sqrt{\tau_x N}} dw. \quad (2.1)$$

The number of channels  $N_{ORd}$  of each ionic species “x” was computed as follows. For  $I_{Ks}$ ,  $I_{Kr}$  and  $I_{to}$ , experimentally measured unitary conductance values were available and were used to calculate  $N_{x,ORd}$  as the maximum conductance of ion channel “x” in the ORd model, denoted by  $G_{x,ORd}$ , divided by the unitary conductance of ion channel “x”, denoted by  $g_x$ . Table 2.2 presents the values used in the computations, where values for  $G_{x,ORd}$  correspond to the epicardial version of the ORd model and a capacitance value of  $C_m = 153.4$  pF, and values for  $g_x$  are taken from [56, 74, 75] and adjusted to temperature and/or extracellular  $K^+$  concentration following [76, 77].

Table 2.2: Number of channels for  $I_{Ks}$ ,  $I_{Kr}$  and  $I_{to}$ .

	$G_s$ (pS)	$g_s$ (pS)	$N_s$
$I_{Ks}$	1140	6.74	<b>169</b>
$I_{Kr}$	9174	2.53	<b>3621</b>
$I_{to}$	12272	20.2644	<b>606</b>

For  $I_{CaL}$  the number of channels was computed by dividing the maximum  $I_{CaL}$  current by the single-channel current  $i_{CaL}$  times the channel opening probability. Considering the value of  $i_{CaL} = -0.12$  pA for  $V = 0$  mV and  $[Ca^{2+}] = 2$  mM reported in [78], the calculated number of  $I_{CaL}$  channels was  $N_{CaL} = 20121 \simeq \mathbf{20000}$ .

### 2.2.2.2 Models of PKA Phosphorylation

$\beta$ -AS effects were modeled as in [33] by using a modified version of the Xie model [36], with definition of graded and dynamic phosphorylation levels of cellular PKA substrates. This model was updated from the original  $\beta$ -A signaling formulation proposed

in [35] to slow down the  $I_{Ks}$  phosphorylation and dephosphorylation rate constants to fit experimental observations. PKA-mediated phosphorylation of PLM was accounted for by increasing the NKA affinity for the intracellular  $\text{Na}^+$  concentration, as in [36]. RyR phosphorylation was described in this work following the formulation proposed in [79].

### 2.2.2.3 Models of Electromechanical Coupling

An extended version of the Niederer model [14], adjusted to human cell characteristics, as in [16] and [33], was used for the electromechanical coupling model. The current through SACs,  $I_{\text{SAC}}$ , was introduced as in [33], with the total current obtained as the sum of the current through  $\text{K}^+$ -selective and non-specific cationic SACs.

The current through SACs was defined as the current through  $\text{K}^+$ -selective and non-specific cationic SACs. A linear time-independent formulation was used for the current through non-selective cationic SACs [80, 81]:

$$I_{\text{SAC,ns}} = G_{\text{SAC}}((\lambda - 1)/(\lambda_{\text{max}} - 1))(V - E_{\text{SAC,ns}}), \quad \text{if } \lambda > 1 \quad (2.2)$$

$$I_{\text{SAC,ns}} = 0, \quad \text{if } \lambda < 1 \quad (2.3)$$

where  $\lambda$  is the ratio between SL and the resting SL defined in the model and  $\lambda_{\text{max}}$  is set to 1.1 [16, 80]. The reversal potential  $E_{\text{SAC,ns}}$  was set to -10 mV [82, 83] and the conductance  $G_{\text{SAC,ns}}$  to 0.006 nS/pF for physiological as well as mild and moderate disease conditions [84, 85]. When simulating severe disease conditions,  $G_{\text{SAC,ns}}$  was set to 0.01 nS/pF following studies showing higher stretch sensitivity of these channels in disease [82]. The current through  $\text{K}^+$ -selective SACs was modeled as an outwardly-rectifying current [80, 81]:

$$I_{\text{SAC,K}} = G_{\text{SAC}}((\lambda - 1)/(\lambda_{\text{max}} - 1))(1/(1 + \exp((V - 19.05)/29.98))), \quad \text{if } \lambda > 1 \quad (2.4)$$

$$I_{\text{SAC,K}} = 0, \quad \text{if } \lambda < 1 \quad (2.5)$$

The conductance  $G_{\text{SAC,K}}$  was set to match experimental current values measured in epicardium [86].

### 2.2.2.4 Simulation of Baseline and Sympathetic Provocation

A 0.1 Hz periodic stepwise dose of the  $\beta$ -A agonist Isoproterenol (ISO) was simulated, in accordance with the pattern of muscle sympathetic nerve activity in humans [87]. For the first half of the simulated ISO period, the ISO dose was set to either  $0.01 \mu\text{M}$ , for simulated baseline conditions, or  $1 \mu\text{M}$ , for simulated SP, while it was  $0 \mu\text{M}$  for the second half in both cases. Additionally, phasic changes in hemodynamic loading accompanying enhanced sympathetic activity were simulated at the same 0.1 Hz frequency by varying the stretch ratio following a sinusoidal waveform with a maximum change of 1% for baseline conditions and 10% for SP. Sympathetically induced changes in  $\beta$ -AS and hemodynamic loading were considered to be in-phase with each other. A total of 640 beats (320 for baseline and 320 for SP) were simulated while pacing the cells at 1 Hz frequency. Fig. 2.1 illustrates simulation of  $\beta$ -AS and stretch effects at baseline and in response to SP, while Fig. 2.2 illustrates the APD time series of a cell in the generated population in response to the simulated protocol. For comparison purposes, additional simulations were run under constant  $\beta$ -AS and/or hemodynamic loading.

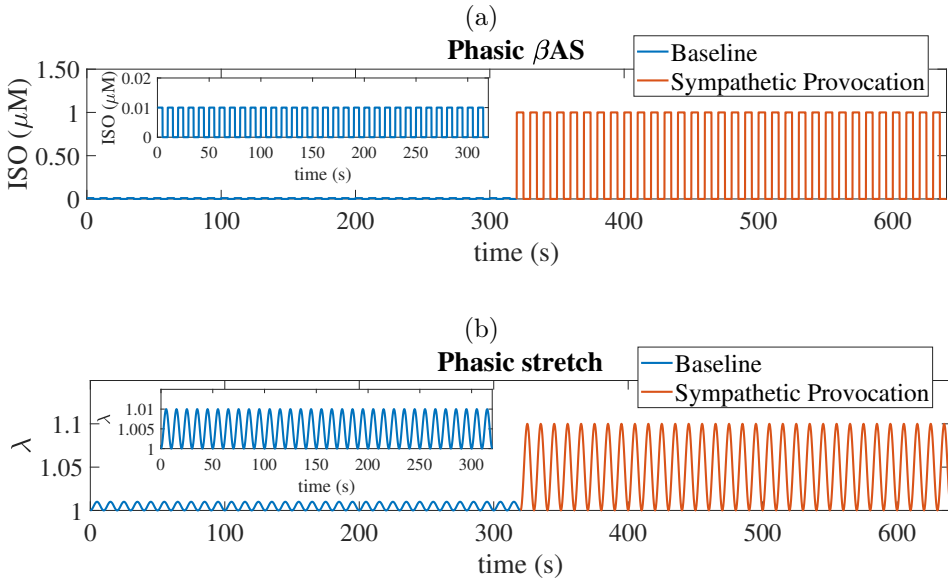


Figure 2.1: Simulation of 0.1 Hz phasic  $\beta$ -AS and stretch effects at baseline and following SP: (a) ISO dose and (b) stretch ratio  $\lambda$ .

### 2.2.2.5 Simulation of Disease-Related Conditions

On top of simulating physiological conditions, models describing disease conditions were built by including representations of: RRR, defined by simultaneous blockades

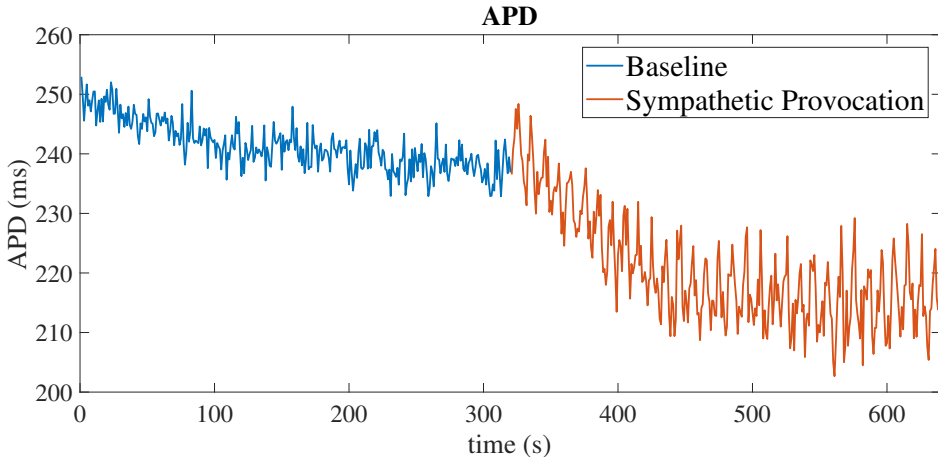


Figure 2.2: Simulated APD series representative of baseline and SP phases (0.1 Hz phasic  $\beta$ -AS and stretch effects) for a virtual cell of the population under mild disease conditions.

of  $I_{Ks}$  and  $I_{Kr}$  currents; and  $Ca^{2+}$  overload, defined by increases in the extracellular  $Ca^{2+}$  levels. In both cases, an approach like the one described in [33] was used. Mild disease conditions were simulated by a 1.5-fold increment in the extracellular  $Ca^{2+}$  concentration and 7.5% and 20% inhibitions of  $I_{Kr}$  and  $I_{Ks}$  currents, respectively. Moderate disease conditions were simulated by a 2.5-fold increment in the extracellular  $Ca^{2+}$  concentration and 22.5% and 60% inhibitions of  $I_{Kr}$  and  $I_{Ks}$  currents, respectively. Severe disease conditions were simulated by a 4-fold increment in the extracellular  $Ca^{2+}$  concentration, 30% and 80% inhibitions of  $I_{Kr}$  and  $I_{Ks}$  currents, respectively, and by additionally increasing the conductance of non-specific cationic SACs as described in [83] ( $G_{SAC,ns}$  changed from 0.006 nS/pF for physiological, mild and moderate disease conditions to 0.01 nS/pF for severe disease conditions). Table 2.3 summarizes how physiological as well as mild, moderate and severe disease conditions were simulated in this study.

Table 2.3: Simulation of RRR and  $Ca^{2+}$  overload and  $G_{SAC,ns}$  conductance value for physiological as well as mild, moderate and severe disease conditions.

	RRR		$Ca^{2+}$ overload (factor on $Ca_o^{2+}$ )	$G_{SAC,ns}$ (nS/pF)
	$I_{Ks}$ (% Block)	$I_{Kr}$ (% Block)		
Physiological	0	0	1	0.006
Mild	20	7.5	1.5	0.006
Moderate	60	22.5	2.5	0.006
Severe	80	30	4	0.01

### 2.2.3 Measurements of Repolarization Variability

For each of the developed AP models, APD at 90% repolarization, denoted as APD in the following, was calculated for every beat of the stochastic realizations. A triangulation measure (T1) was calculated as the difference between APD at 90% and 50% repolarization. The last  $L = 120$  beats of each condition (baseline and SP) were used for evaluation of measures describing BVR and LF oscillatory behavior. Averages of those measures over stochastic realizations were computed.

#### 2.2.3.1 Beat-to-beat Variability of Repolarization

The following BVR measures were evaluated:

- Standard deviation of APD over the last  $L$  beats:

$$m_{\text{SD}} = \sqrt{\frac{1}{L-1} \sum_{l=1}^L (\text{APD}(l) - \overline{\text{APD}})^2} \quad (2.6)$$

where  $\overline{\text{APD}}$  is the average APD over those  $L$  beats.

- Normalized variance of APD over the last  $L$  beats:

$$m_{\text{NSD}} = \frac{m_{\text{SD}}^2}{\overline{\text{APD}}^2}. \quad (2.7)$$

- Short-Term Variability (STV) of APD, defined as the average distance perpendicular to the identity line in the Poincaré plot, computed as the average over windows of  $L_{\text{win}} = 30$  beats sliding every one beat along the last  $L = 120$  simulated beats:

$$m_{\text{STV}} = \frac{1}{L - L_{\text{win}} + 1} \left( \sum_{l=1}^{L-L_{\text{win}}+1} \sum_{i=l}^{l+L_{\text{win}}-1} \frac{|\text{APD}(i+1) - \text{APD}(i)|}{(L_{\text{win}} - 1)\sqrt{2}} \right). \quad (2.8)$$

- Normalized STV:

$$m_{\text{NSTV}} = \frac{m_{\text{STV}}^2}{\overline{\text{APD}}^2}. \quad (2.9)$$

#### 2.2.3.2 Low-frequency Repolarization Variability

Spectral analysis was performed to compute LF variability measures following the methodology described in [51]. The APD time series of the last  $L = 120$  beats,

for either baseline or SP, was linearly detrended. Power Spectral Density (PSD) was estimated after fitting an autoregressive model to the detrended APD time series using the Yule-Walker method. The optimal order of the autoregressive model was chosen in the range between  $L/3$  and  $L/2$  to minimize Akaike's Information Criterion, with a requisite on the residuals to pass a whiteness test. Two measures were extracted from the estimated PSD:

- LF power ( $m_{\text{PLF}}$ ), calculated as the integral of the PSD over the  $[0.04, 0.15]$  Hz band.
- Normalized LF power ( $m_{\text{NPLF}}$ ): LF power normalized by the total power in the  $[0.04, 0.5]$  Hz frequency band.

## 2.2.4 Contributors to BVR and LF Oscillations

ARD was used to unravel individual and common factors, in the form of ionic conductance levels, contributing to BVR and LF oscillations of APD in response to SP. ARD is a Bayesian sparsity method, first proposed in the context of neural network models [67], which has been successfully used to determine the relevance of various input features to given measures, see e.g. [88].

In a regression problem where an output variable (in this case, a BVR or LF oscillatory measure) is aimed to be predicted by several input variables (in this case, the conductances of ionic currents), it commonly happens that some of the variables are irrelevant to the prediction. However, when a finite dataset is analyzed, random correlations between the irrelevant inputs and the output are always obtained, diminishing the capability of the techniques employed for the prediction. A method like ARD, able to infer which input variables are relevant and prune all the irrelevant ones, is advantageous. ARD works by adjusting multiple weight constants, one associated with each input, which are inferred from the data and automatically set to be large for the relevant features and small for the irrelevant ones. The fact that ARD renders a sparse set of explanatory variables makes its results more interpretable than for other correlation-based methods (see e.g. [89] for the relation between sparsity and interpretability).

Each virtual cell  $n$  out of the  $N$  simulated models was considered as a data point determined by its  $D = 8$  parameters (factors multiplying ionic conductances). Those factors were stacked in a row vector  $\mathbf{x}^{(n)} = [\theta_{\text{Ks}}^{(n)}, \theta_{\text{Kr}}^{(n)}, \theta_{\text{to}}^{(n)}, \theta_{\text{CaL}}^{(n)}, \theta_{\text{K1}}^{(n)}, \theta_{\text{Na}}^{(n)}, \theta_{\text{NaCa}}^{(n)}, \theta_{\text{NaK}}^{(n)}]$ , representing the feature vector of each data point. All data were stacked in the feature matrix  $\mathbf{X}$ , i.e.,  $\mathbf{X} = [\mathbf{x}^{(1)}; \dots; \mathbf{x}^{(N)}]$ . Hence an element of  $\mathbf{X}$ , denoted as  $x_{n,i}$ , was the value of the  $i$ -th conductance parameter of virtual cell  $n$ . In addition,  $\mathbf{y}$  is used as a wildcard to denote the column vector with the values of the analyzed variability measure for the data points. Hence, the values in  $\mathbf{y}$  can either correspond to a temporal BVR measure or a measure of the magnitude of APD LF oscillations:  $m_{\text{SD}}$ ,  $m_{\text{NSD}}$ ,

$m_{\text{STV}}$ ,  $m_{\text{NSTV}}$ ,  $m_{\text{PLF}}$  and  $m_{\text{NPLF}}$ . To simplify the training process of the algorithm, the values of  $\mathbf{y}$  were standardized to zero mean and unit variance. Using this input-output definition the following regression model is posed

$$\mathbf{y}^{(n)} = f(\mathbf{x}^{(n)}) + r^{(n)} \quad (2.10)$$

where  $r^{(n)}$  is additive random Gaussian noise with variance  $\sigma_r^2$  and  $f$  is a function linking the inputs and the outputs. Typical choices for  $f$  include linear, polynomial or neural network functions, with the ones most extensively used by the Bayesian learning community being Gaussian Processes [88], which represent a powerful and flexible non-parametric option:

$$f(\mathbf{x}^{(n)}) \sim \mathcal{GP} \left( m(\mathbf{x}^{(n)}), c(\mathbf{x}^{(n)}, \mathbf{x}^{(n')}) \right) \quad (2.11)$$

where  $m(\mathbf{x}^{(n)})$  is the mean function and  $c(\mathbf{x}^{(n)}, \mathbf{x}^{(n')})$  is the covariance function between data points  $n$  and  $n'$ . In its simplest form,  $m(\mathbf{x}^{(n)}) = 0$  and all the complexity of the model is captured by the covariance function. The covariance is commonly described by linear, polynomial or radial basis functions, or other more complicated functions, see e. g. [88]. In this work, a linear function was used for the covariance:

$$c(\mathbf{x}^{(n)}, \mathbf{x}^{(n')}) = \sum_{i=1}^D \sigma_{d,i}^2 x_{n,i} x_{n',i}. \quad (2.12)$$

Considering this choice,  $f(\mathbf{x}^{(n)})$  can be shown to define a set of linear functions with respect to  $\mathbf{x}^{(n)}$ , where directions (i.e. the different factors contained in each  $\mathbf{x}^{(n)}$ ) are weighted according to  $\sigma_{d,i}^2$ .

ARD was applied to optimize type II Maximum Likelihood (ML-II) with respect to  $\sigma_{d,i}^2$  and  $\sigma_r^2$ . Specifically, a quasi-Newton method (in the case of this implementation, L-BFGS, see e.g. [90]) was used to find the values of the hyperparameters leading to maximization of the following function:

$$\begin{aligned} \mathcal{L}(\sigma_{d,1}^2, \dots, \sigma_{d,8}^2, \sigma_r^2) &= \frac{1}{2} \log \det \mathbf{C}_{\text{ext}}(\sigma_{d,1}^2, \dots, \sigma_{d,8}^2, \sigma_r^2) \\ &+ \frac{1}{2} \mathbf{y}^T \mathbf{C}_{\text{ext}}(\sigma_{d,1}^2, \dots, \sigma_{d,8}^2, \sigma_r^2)^{-1} \mathbf{y} + \frac{N}{2} \log(2\pi) \end{aligned} \quad (2.13)$$

where  $\mathbf{C}_{\text{ext}}(\sigma_{d,1}^2, \dots, \sigma_{d,8}^2, \sigma_r^2) = \mathbf{C}(\sigma_{d,1}^2, \dots, \sigma_{d,8}^2) + \sigma_r^2 \mathbf{I}$ , with  $\mathbf{I}$  being the identity matrix and  $\mathbf{C}(\sigma_{d,1}^2, \dots, \sigma_{d,8}^2)$  being the matrix obtained by evaluating the covariance function  $c(\mathbf{x}^{(n)}, \mathbf{x}^{(n')})$  for every pair of data points in  $\mathbf{X}$ . To avoid overfitting, ten-fold cross validation was applied. Results are presented after averaging the ten corresponding values for each  $\sigma_{d,i}^2$ . The higher the value of  $\sigma_{d,i}^2$ , the more relevant the  $i$ -th factor (input parameter) is for the prediction.

This methodology allows establishing which factors are more relevant to predict a given output measure (i.e. a BVR or LF oscillatory measure). In the following, these relevance values are presented as normalized values so that they add up to one to facilitate assessment of the relative relevance of each factor. Since relevance factors do not account for the sign of the contribution, that is, whether an increase in the BVR or LF oscillation measure corresponds to upregulation or downregulation of an ionic current, the Gaussian Process regression was interpreted as a linear regression where the covariance matrix is  $\mathbf{C}_{\text{ext}}$  and the sign of each contribution was calculated as

$$\mathbf{s}_{\theta_i} = \text{sign}((\mathbf{C}_{\text{ext}}^{-1}\mathbf{X})^T \mathbf{y}) \quad (2.14)$$

where  $\theta_i$  is each of the conductance parameters and  $T$  denotes matrix transposition.

Finally, to address the fact that a factor may only be relevant in association with another one, the same methodology was applied after removing one factor (ionic conductance) at a time. If after removing a specific factor, the relevance associated with another factor was found to be significantly changed, a tight relationship between the effects of the two factors was postulated and common mechanisms underlying such a relationship were explored.

## 2.2.5 Contributors to Arrhythmogenesis

CCA [68, 91] was used to identify the ionic conductances with the largest contribution to the occurrence of arrhythmogenic events under simulated diseased conditions. This method has been widely used in several different applications (see e.g. [92–94] for some representative examples).

Similarly to the description of ARD above, the data were stacked in the feature matrix  $\mathbf{X}$ , with  $x_{n,i}$ , being the value of the  $i$ -th factor for virtual cell  $n$ . A binary vector  $\mathbf{z}$  of length  $N$  was generated, which contained a value of 1 in the positions corresponding to virtual cells for which pro-arrhythmic events were observed following SP and 0 otherwise.

Given  $\mathbf{X}$  and  $\mathbf{z}$ , CCA was applied to compute the values of the *canonical variables*  $\mathbf{w}_x$  and  $w_z$  such that:

$$(\mathbf{w}_x^*, w_z^*) = \arg \max_{\mathbf{w}_x, w_z} \text{corr}(\mathbf{X}\mathbf{w}_x, \mathbf{z}w_z) \quad (2.15)$$

with  $\text{corr}$  being the linear correlation between the projected versions of  $\mathbf{X}$  and  $\mathbf{z}$ , i.e.,  $\mathbf{X}\mathbf{w}_x$ ,  $\mathbf{z}w_z$ . The elements of vector  $\mathbf{w}_x^*$  represent the projection of ionic factors into a subspace common with  $\mathbf{z}w_z^*$  and can be interpreted as the correlations of each of these factors with the presence of pro-arrhythmic events. Hence, the higher the value of an element in  $\mathbf{w}_x^*$ , the higher the relevance of such factor to the events in  $\mathbf{z}$ .



## 2.3 Results

### 2.3.1 Sympathetic Provocation Increases BVR and LF Oscillations of APD

Fig. 2.3 shows representative examples of zero-mean time series of experimental ARI ( $\text{ARI} - \overline{\text{ARI}}$ , with  $\overline{\text{ARI}}$  denoting temporal mean of ARI, left panel) and simulated APD ( $\text{APD} - \overline{\text{APD}}$ , with  $\overline{\text{APD}}$  denoting temporal mean of APD, right panel) and corresponding PSDs at baseline and following SP. In both experiments and simulations, a remarkable increase in BVR in response to SP can be clearly appreciated from the APD series. Also, the experimental and simulated spectra corresponding to SP show notably more marked peaks in the LF band as compared to baseline.

Of note, the peaks in the high frequency band present in the experimentally recorded data were not analyzed in this study, as vagal or respiratory effects were not included in these simulations for being out of the scope of the present study. The simulated results presented in this and the next sections correspond to simulation of mild disease conditions, since these are compared with experimental results obtained from heart failure patients (see section 2.2.1). Results for physiological conditions remained qualitatively unchanged with respect to those shown for mild disease conditions.

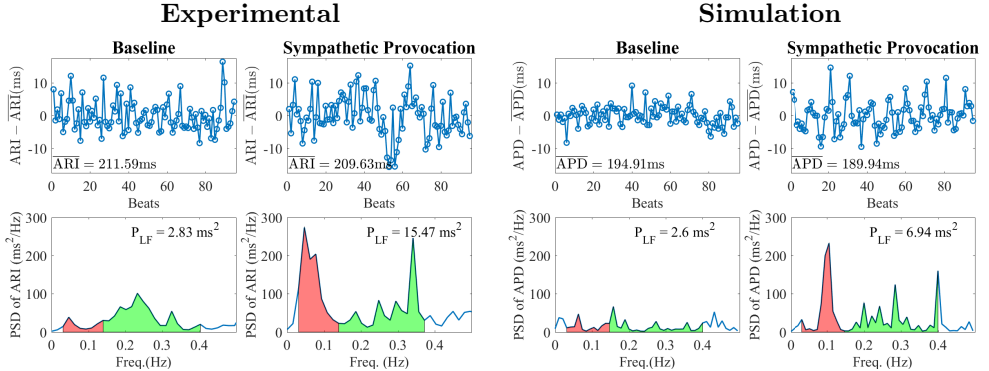


Figure 2.3: Left panel: Experimental zero-mean ARI series ( $\text{ARI} - \overline{\text{ARI}}$ ) and corresponding spectra at rest (left) and following Valsalva maneuver (right). Right panel: Simulated zero-mean APD series ( $\text{APD} - \overline{\text{APD}}$ ) and corresponding spectra at baseline (left) and following SP (right). The LF region of the spectra is shadowed in red and the high frequency region in green.

Fig. 2.4 shows relative measures of BVR and LF oscillations at baseline and following SP for each individual of the experimental and simulated datasets (the cases shown in Fig. 2.3 are highlighted in blue). For the vast majority of individuals,  $m_{\text{NSD}}$  and  $m_{\text{NPLF}}$  increased in response to augmented sympathetic activity. Importantly, both the level of BVR and LF oscillations as well as the magnitude of change in response to SP presented a high degree of variation between individuals, as shown in

Fig. 2.4. As expected, the  $m_{\text{NSD}}$  values in the simulations were higher than in the experiments, as simulations correspond to single epicardial cells while experimental data is from left ventricular epicardial EGMs and, thus, includes the effects of intercellular coupling acting to mitigate cell-to-cell variability.

In both experiments and simulations, the sympathetically-mediated increases in BVR and LF oscillations were confirmed either when quantified in absolute terms by  $m_{\text{SD}}$ ,  $m_{\text{STV}}$  and  $m_{\text{PLF}}$  or in relative terms by  $m_{\text{NSD}}$ ,  $m_{\text{NSTV}}$  and  $m_{\text{NPLF}}$ .

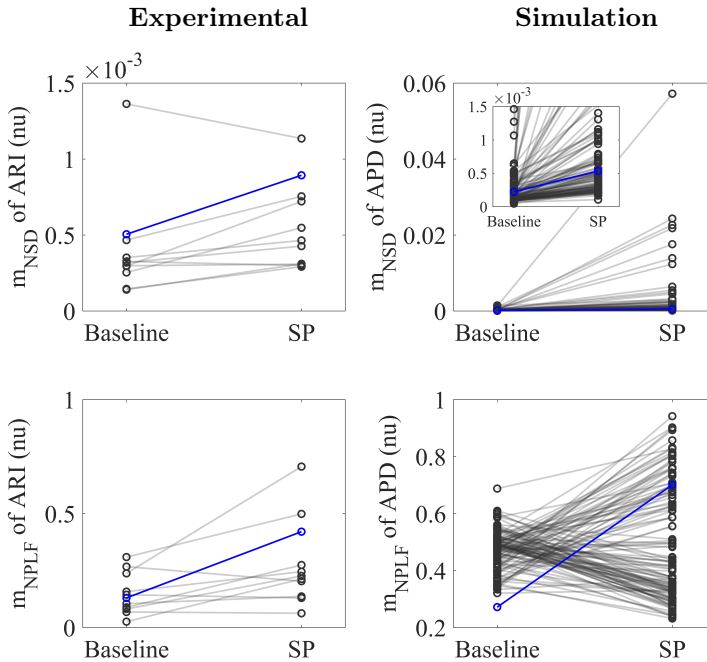


Figure 2.4: Left: Normalized variance  $m_{\text{NSD}}$  (top) and Normalized LF power  $m_{\text{NPLF}}$  (bottom) at rest and following Valsalva maneuver calculated from experimental ARI series. Right:  $m_{\text{NSD}}$  (top) and  $m_{\text{NPLF}}$  (bottom) at baseline and following SP calculated from simulated APD series. The cases presented in Fig. 2.3 are highlighted in blue.

### 2.3.2 Close Interaction between BVR and LF Oscillations of APD, particularly in Response to Sympathetic Provocation

Table 2.4 shows correlation values between measures of BVR and LF oscillations of APD, both calculated using absolute and normalized indices. As can be seen in Table 2.4, the LF power of APD,  $m_{\text{PLF}}$ , was highly correlated with BVR measured by the short-term variability of APD,  $m_{\text{STV}}$ , and, even to a larger extent, by the standard deviation of APD,  $m_{\text{SD}}$ . This observation held true when the correlation was evaluated

both at baseline and in response to SP. The strong association found between BVR and LF oscillations of APD in these SP simulations was in line with the one measured experimentally, where the Spearman correlation coefficient between  $m_{\text{PLF}}$  and  $m_{\text{SD}}$  was 0.679.

Table 2.4: Spearman correlation coefficients between simulated BVR and LF oscillation measures.

	Baseline		Sympathetic Provocation	
	$m_{\text{PLF}}$ ( $\text{ms}^2$ )	$m_{\text{NPLF}}$ (nu)	$m_{\text{PLF}}$ ( $\text{ms}^2$ )	$m_{\text{NPLF}}$ (nu)
$m_{\text{SD}}$ (ms)	0.9744	-0.1606	0.9439	0.5969
$m_{\text{NSD}}$ (nu)	0.8528	-0.1602	0.8784	0.5721
$m_{\text{STV}}$ (ms)	0.9096	-0.3381	0.8341	0.4054
$m_{\text{NSTV}}$ (nu)	0.7646	-0.3530	0.7638	0.3868

When normalized measures were considered, Table 2 shows that the correlation between the normalized LF power of APD,  $m_{\text{NPLF}}$ , and the normalized BVR measures,  $m_{\text{NSTV}}$  and  $m_{\text{NSD}}$ , was notably reduced. This highlights the relevance of absolute APD values in modulating the interactions between BVR and LF oscillations of APD. The reduction in correlation after considering normalized measures was particularly so for baseline conditions, while following SP there was still a high interaction between normalized BVR and LF oscillations of APD.

Fig. 2.5 illustrates the simulated relationships between the absolute measures  $m_{\text{PLF}}$  and  $m_{\text{SD}}$  and between the relative measures  $m_{\text{NPLF}}$  and  $m_{\text{NSD}}$  at baseline and in response to SP.

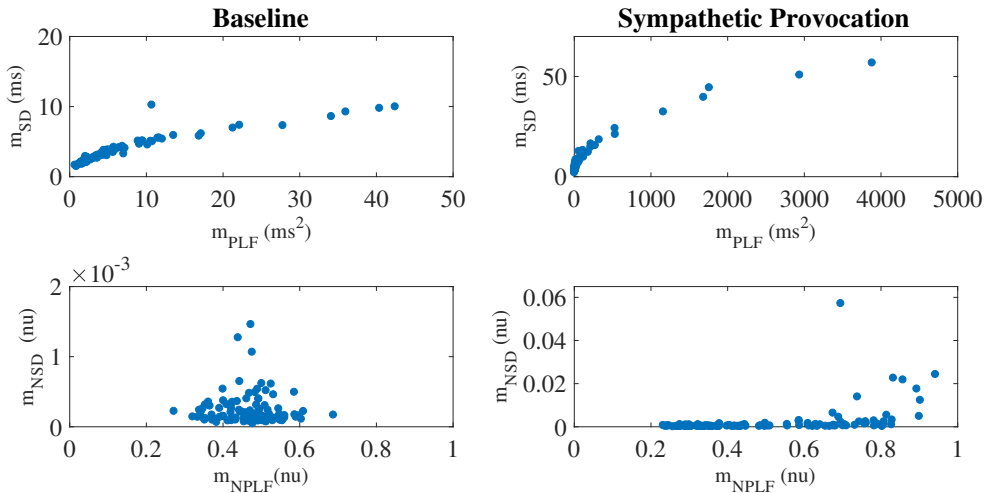


Figure 2.5: Relationship between  $m_{\text{SD}}$  and  $m_{\text{PLF}}$  (top) and  $m_{\text{NSD}}$  and  $m_{\text{NPLF}}$  (bottom) at baseline and following SP for the population of models under simulated mild disease conditions.

Based on the fact that the two ways of evaluating BVR, i.e. by standard deviation and by short-term variability of APD, led to very similar outcomes in terms of the relationship with LF oscillations of APD, the results in the next sections will be shown for  $m_{STV}$  and its normalized counterpart  $m_{NSTV}$ . For APD oscillatory behavior,  $m_{PLF}$  and  $m_{NPLF}$  will be used.

### 2.3.3 $K^+$ and $Ca^{2+}$ Current Densities are Common Modulators of BVR and LF Oscillations of APD

Fig. 2.6 illustrates the major contributors to the values of  $m_{STV}$ ,  $m_{NSTV}$ ,  $m_{PLF}$  and  $m_{NPLF}$  found in the simulated population in response to SP. The sign of the relationship between the contributing ionic current conductances and the evaluated BVR or LF oscillation measurements was negative in all relevant cases, meaning that downregulation of the ionic current density led to an increment in the analyzed measurement. Note that each bar in the graphs of Fig. 2.6 represents relative relevance with respect to the other evaluated factors, all adding up to one.

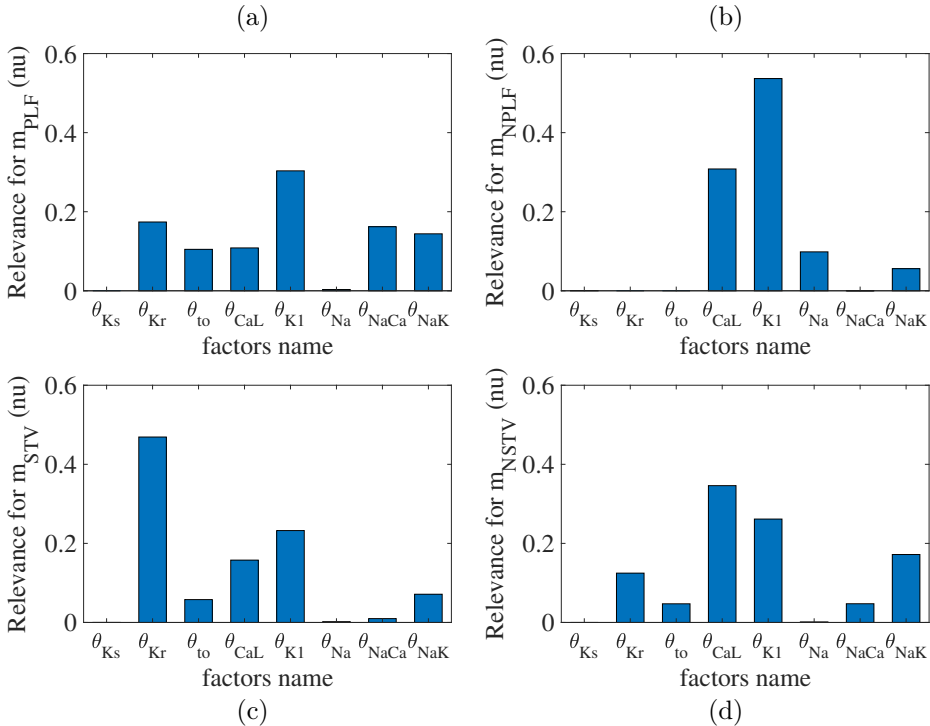


Figure 2.6: Relevance of ionic current conductances to  $m_{PLF}$  (a),  $m_{NPLF}$  (b),  $m_{STV}$  (c) and  $m_{NSTV}$  (d), calculated from simulated APD series following SP.

According to the results in Fig. 2.6,  $m_{STV}$  and  $m_{PLF}$  shared the same major contributors to their observed values following SP. Specifically, the three ionic conductances with the most relevant role in determining the values of  $m_{STV}$  and  $m_{PLF}$

were those of  $I_{K_r}$ ,  $I_{K1}$  and  $I_{CaL}$  currents. For the normalized measurements  $m_{NSTV}$  and  $m_{NPLF}$ , a substantial reduction in the relevance of  $I_{K_r}$  conductance was observed with respect to that quantified for the non-normalized measurements.  $I_{K1}$  and  $I_{CaL}$  current conductances remained as the two most relevant contributors to the values of  $m_{NSTV}$  and  $m_{NPLF}$  following SP.

To assess potential associations between ionic conductances in their contributions to the evaluated BVR and LF oscillations measures, the same ARD technique was applied after removing one ionic conductance at a time. For the majority of cases, the computed relevance levels were highly similar after such removals, meaning that there is no co-dependency in the contribution of the different ionic conductances. However, when  $I_{K1}$  conductance was removed from the analysis, the relevance of other repolarization currents, like  $I_{K_r}$  and  $I_{K_s}$ , in their contribution to  $m_{NSTV}$  was notably increased. This increment reveals common mechanisms in the contributions of all these repolarization currents to the  $m_{NSTV}$  values following SP.

Since the same ionic conductances were found to modulate BVR and LF oscillations of APD following SP, simulations were ran in which  $\beta$ -AS and stretch were modeled as constant, with assigned values corresponding to the maximal effects in the above simulations. As can be seen in Fig. 2.7, in those cases  $I_{K_r}$  and  $I_{K1}$  were still the major modulators of BVR whereas the contribution of  $I_{CaL}$  was drastically decreased. Thus,  $I_{CaL}$  modulation of BVR was mediated by the increment in the LF oscillations of APD, while the role of  $I_{K_r}$  and  $I_{K1}$  as modulators of BVR did not present such a strong dependence.

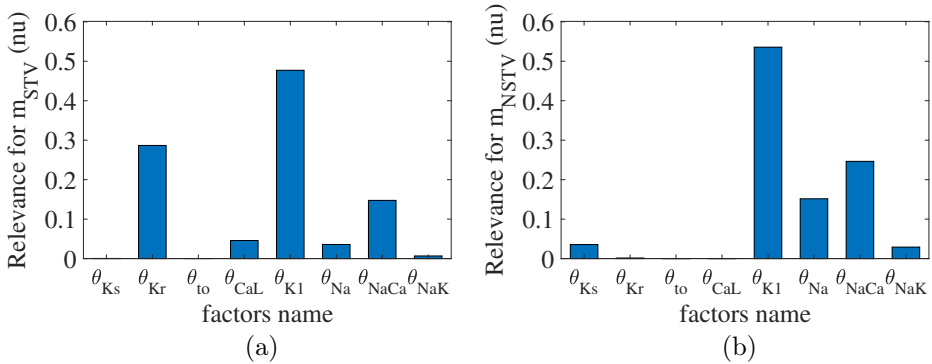


Figure 2.7: Relevant factors for (a)  $m_{STV}$  and (b)  $m_{NSTV}$  following constant  $\beta$ -AS and mechanical stretch.

For healthy conditions, results were essentially the same as those shown in Fig. 2.6 for mild disease conditions, with only a slight decrease in the relevance of  $I_{NaCa}$  contribution to  $m_{P_{LF}}$ . This is illustrated in Fig. 2.8.

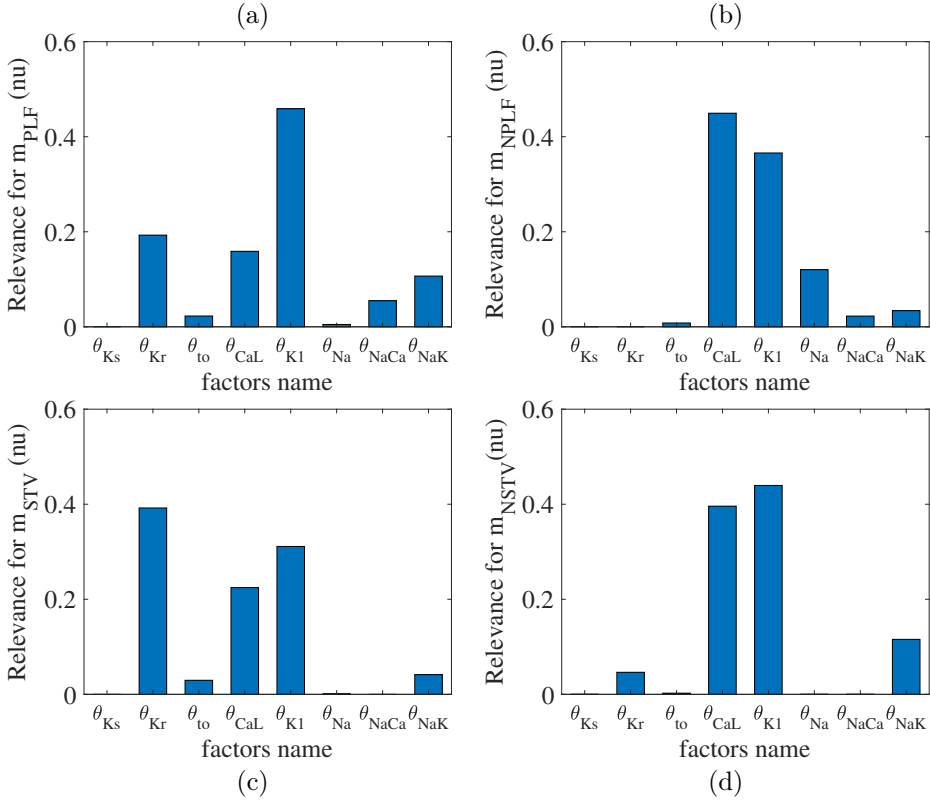


Figure 2.8: Relevant factors for (a)  $m_{\text{PLF}}$ , (b)  $m_{\text{NPLF}}$ , (c)  $m_{\text{STV}}$ , and (d)  $m_{\text{NSTV}}$  following SP under physiological conditions.

### 2.3.4 Modulation of BVR and LF Oscillations of APD by $\text{K}^+$ and $\text{Ca}^{2+}$ Current Densities is Explained by their Effects on Ionic Gating Stochasticity, $\beta$ -AS and Hemodynamic Loading

Before describing the mechanisms by which  $I_{\text{Kr}}$ ,  $I_{\text{K1}}$  and  $I_{\text{CaL}}$  current densities modulate BVR and LF oscillatory measures following SP, the differential effects of the two components associated with enhanced sympathetic activity, namely  $\beta$ -AS and mechanical stretch, to such measures were analyzed. Fig. 2.9 illustrates the variations in BVR and LF oscillation measurements in the simulated population for different scenarios, including combined phasic  $\beta$ -AS and mechanical stretch, only phasic  $\beta$ -AS, only phasic mechanical stretch and only phasic mechanical stretch without SACs. Results showed that the largest contribution to LF oscillations, measured either by  $m_{\text{PLF}}$  or  $m_{\text{NPLF}}$ , was caused by phasic mechanical stretch, particularly when SACs were included in the models. Regarding BVR, both effects contributed to  $m_{\text{STV}}$  and  $m_{\text{NSTV}}$ , even if

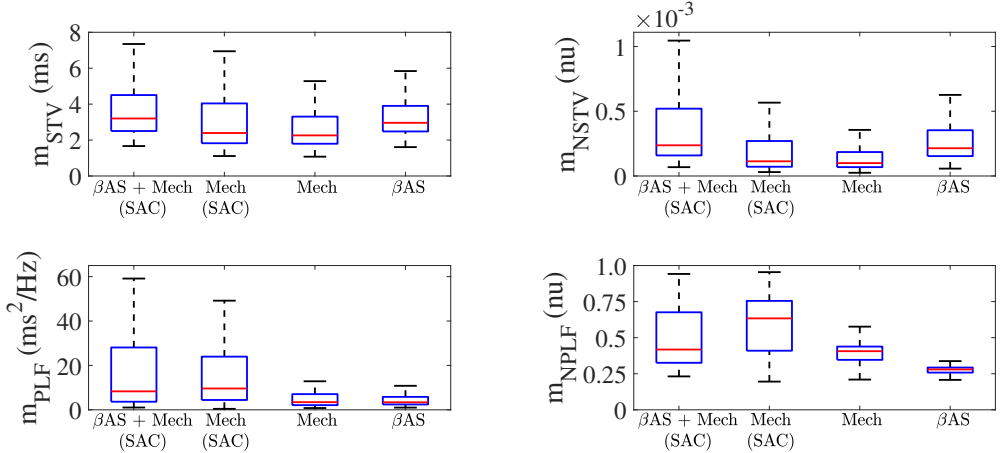


Figure 2.9: Distributions of BVR and LF oscillation measurements for simulated scenarios including individual and combined  $\beta$ -AS and mechanical stretch effects, with and without the contribution of SACs.

not in an additive manner and with the contribution of  $\beta$ -AS being larger than that of mechanical stretch. Additional effects associated with stochastic ionic gating of currents active during AP repolarization added to the BVR values presented in Fig. 2.9.

#### 2.3.4.1 Mechanisms Underlying the Role of $I_{K1}$ as a Modulator of BVR and LF Oscillations of APD

The role of  $I_{K1}$  current density as a modulator of APD oscillatory behavior following SP was only relevant when phasic mechanical stretch was simulated and particularly so when SACs were included in the models. The mechanism of action was as follows. Downregulation of  $I_{K1}$  increased resting membrane potential (Fig. 2.10 a) and this increment was associated with an enhancement of the total  $I_{SAC}$  current in the zenith of the oscillation, where phasic stretch reached maximal values (Fig. 2.10 b and c). These effects altered the AP shape at the end of the repolarization phase (Fig. 2.10 d) and this, in turn, had an impact on the calculated APD. In particular, the magnitude of the APD oscillations was amplified (Fig. 2.10 e), which led to increases in both  $m_{PLF}$  and  $m_{NPLF}$  (Fig. 2.10 f).

Furthermore,  $I_{K1}$  current density had an impact on modulating BVR following SP, especially when including the effects of SACs. Specifically, the above described alterations in AP morphology induced by  $I_{K1}$  downregulation, manifested as a slowing down of the final part of AP repolarization, rendered the AP more sensitive to the effects of stochastic ionic gating. This led to increased variability in APD values of consecutive beats, thus enlarging  $m_{STV}$  and  $m_{NSTV}$ .

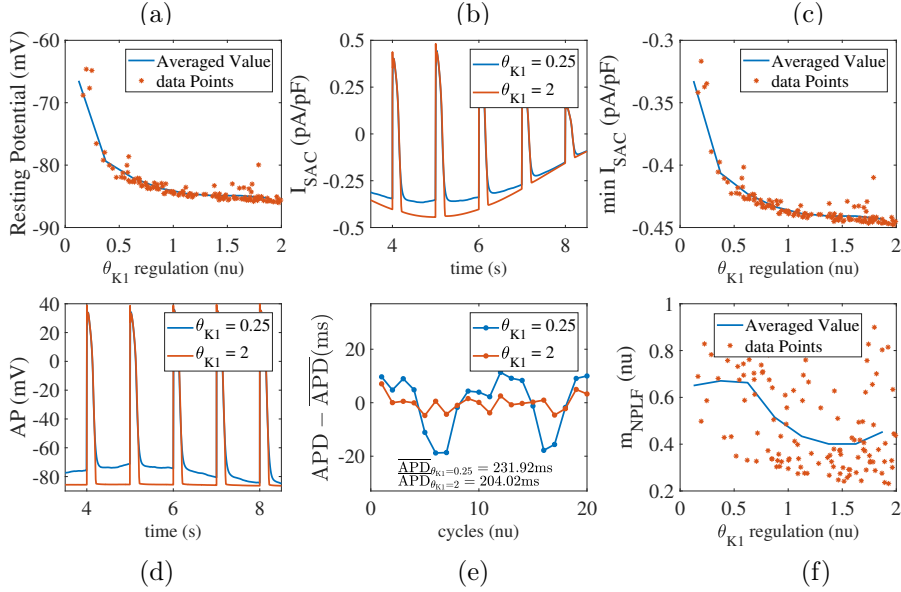


Figure 2.10: (a) Resting membrane potential versus  $I_{K1}$  current conductance in the population of virtual cells; (b)  $I_{SAC}$  current for two examples corresponding to upregulated and downregulated  $I_{K1}$  while keeping all the other currents at their default values in the ORd model; (c) Minimum  $I_{SAC}$  current value versus  $I_{K1}$  current conductance in the population; (d) AP traces and (e) zero-mean APD series ( $APD - \overline{APD}$ ) for the examples in (b); (f)  $m_{NPLF}$  values versus  $I_{K1}$  current conductance in the population.

### 2.3.4.2 Mechanisms Underlying the Role of $I_{Kr}$ as a Modulator of BVR and LF Oscillations of APD

The impact of  $I_{Kr}$  current density on the magnitude of BVR and LF oscillations of APD was related to modulation of AP repolarization duration. This is evidenced by the fact that the contribution of  $I_{Kr}$  conductance was very relevant in the modulation of  $m_{PLF}$  and  $m_{STV}$  but was notably reduced for their normalized counterparts  $m_{NPLF}$  and  $m_{NSTV}$ .

In the case of  $m_{PLF}$ , the mechanism of action was as follows.  $I_{Kr}$  downregulation led to AP prolongation, which in these simulations including phasic  $\beta$ -AS and stretch could be seen as an increase in both the minimum and the average APD within each oscillation period (Fig. 2.11 a). The observed AP lengthening correlated with an increment in the magnitude of the APD oscillations, quantified by the APD range (Fig. 2.11 b). This was the result of amplified effects of  $\beta$ -AS and stretch on the prolonged AP. In relation to the amplified oscillation amplitude,  $m_{PLF}$  was increased. Representative examples are shown in Fig. 2.11 c, where the case with longer APD induced by downregulated  $I_{Kr}$  was associated with larger LF oscillations.



In the case of  $m_{STV}$ , the lengthening of AP repolarization induced by  $I_{Kr}$  down-regulation led to more accentuated temporal voltage variations. This occurred under phasic  $\beta$ -AS, stretch and the combination of both effects associated with enhanced sympathetic activity.

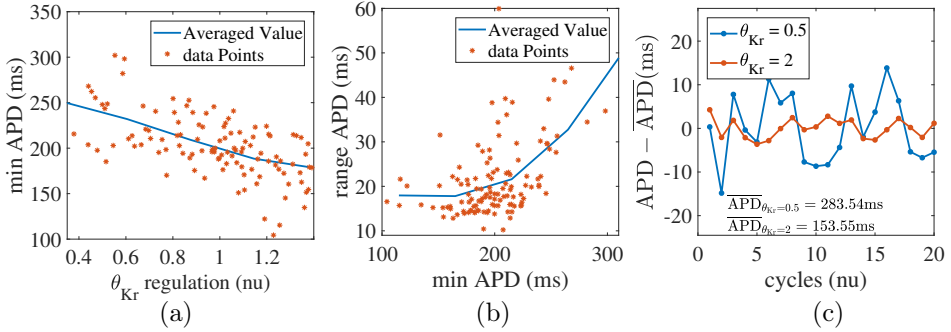


Figure 2.11: (a) Minimum APD versus  $I_{Kr}$  current conductance in the population of virtual cells; (b) APD range versus minimum APD; (c) zero-mean APD series ( $APD - \overline{APD}$ ) for two examples corresponding to downregulated and upregulated  $I_{Kr}$  while keeping all the other currents at their default values in the ORD model.

### 2.3.4.3 Mechanisms Underlying the Role of $I_{CaL}$ as a Modulator of BVR and LF Oscillations of APD

The contribution of  $I_{CaL}$  to BVR and LF oscillations was relevant under both simulated  $\beta$ -AS and mechanical stretch, with an important role of SACs in explaining  $I_{CaL}$  modulation of APD oscillations.

$I_{CaL}$  downregulation shortened the AP plateau, leading to more triangular APs (Fig. 2.12 a). This, in turn, magnified the effects of phasic  $\beta$ -AS and accentuated the APD differences within each simulated oscillation period. This change produced an increase in the magnitude of LF oscillations of APD, associated with increments in both  $m_{PLF}$  and  $m_{NPLF}$  (Fig. 2.12 b). Representative examples of low and high BVR and LF oscillations of APD related to up- and downregulation of  $I_{CaL}$  current are presented in Fig. 2.12 c. In close correspondence with the above described mechanisms, the more triangular AP induced by  $I_{CaL}$  downregulation facilitated larger voltage fluctuations. This was seen as increased  $m_{STV}$  and  $m_{NSTV}$ .

Under simulated mechanical stretch on top of  $\beta$ -AS, there was an additional change in the amplitude and duration of intracellular and subspace  $Ca^{2+}$  concentrations as well as in the  $I_{SAC}$  current. All these effects modified the AP repolarization morphology, enhancing the differences within each simulated oscillation period. As a consequence,  $m_{PLF}$  and  $m_{NPLF}$  were further increased and, correspondingly,  $m_{STV}$  and  $m_{NSTV}$  too.

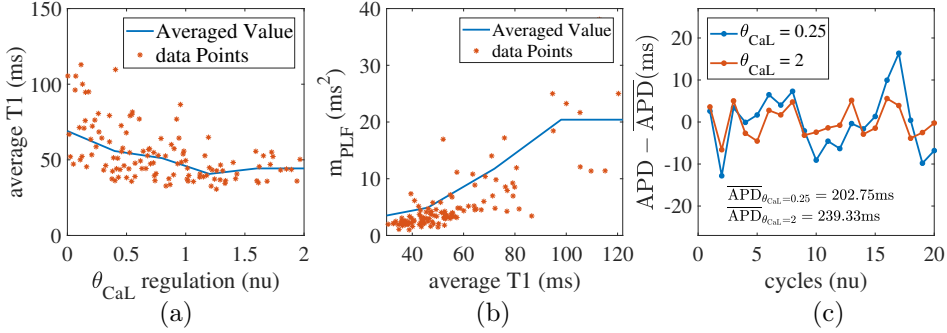


Figure 2.12: (a) Average triangulation versus  $I_{CaL}$  current conductance and (b)  $m_{PLF}$  values versus average triangulation for the population of virtual cells; (d) zero-mean APD series ( $APD - \overline{APD}$ ) for two examples corresponding to downregulated and updownregulated  $I_{CaL}$  while keeping all the other currents at their default values in the ORd model.

### 2.3.5 Severe Disease Conditions Accentuate both BVR and LF Oscillations of APD, Leading to Electrical Instabilities

Disease conditions simulated by  $Ca^{2+}$  overload and RRR had an impact on sympathetically mediated BVR and LF oscillations of APD. Specifically, when severe disease conditions were simulated, including also an associated increase in the conductance of non-specific cationic SACs, pro-arrhythmic events could be observed. These occurred in 35% of the cases in the population and took the form of early afterdepolarizations (EADs), EAD bursts and spontaneous beats. Examples are presented in Fig. 2.13.

For those cases where arrhythmogenic events were observed under severe disease conditions (denoted as subpopulation A), BVR and LF oscillations of APD were increasingly accentuated for higher levels of disease conditions, as illustrated in Fig. 2.14. As can be noted from the figure,  $m_{NSTV}$  and  $m_{NPLF}$  took larger values for progressively higher levels of  $Ca^{2+}$  overload and RRR. Similarly occurred for the non-normalized indices  $m_{STV}$  and  $m_{PLF}$ . Those cases not presenting arrhythmogenic events under severe disease conditions (denoted as subpopulation NA) showed lower values of BVR and LF oscillation measures for both mild and moderated disease conditions. This can be appreciated in Fig. 2.14 as well.

The results of CCA performed to assess major contributors to pro-arrhythmic events under severe disease conditions are presented in Fig. 2.15. According to these results, the ionic currents with a major involvement in pro-arrhythmicity were  $I_{Kr}$ ,  $I_{CaL}$ ,  $I_{K1}$  and  $I_{NaK}$ , the first three being major modulators of BVR and LF oscillations of APD. The sign of the relationship between ionic conductances and pro-arrhythmicity was negative (i.e. current downregulation facilitating pro-arrhythmic events) in all cases except for  $I_{CaL}$ .

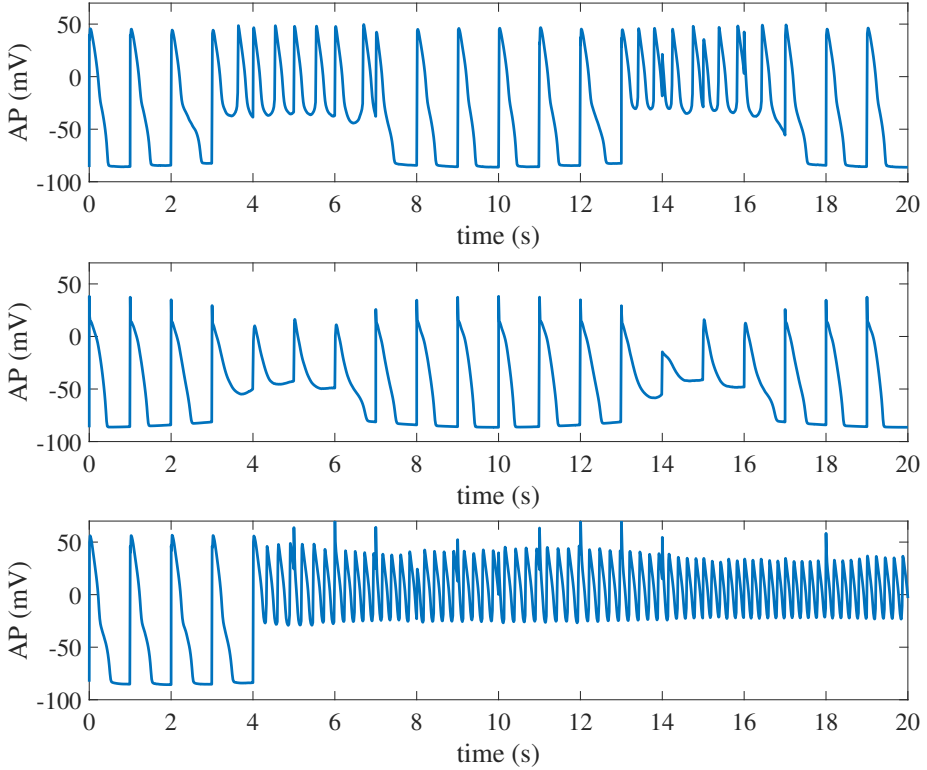


Figure 2.13: Pro-arrhythmic events observed following SP in cells under simulated severe disease conditions.

The role of  $I_{K_r}$ ,  $I_{CaL}$  and  $I_{K1}$  in contributing to pro-arrhythmicity is further illustrated in Fig. 2.16, which shows the distribution of virtual cells as a function of their  $I_{K_r}$ ,  $I_{CaL}$  and  $I_{K1}$  conductances ( $\theta_{K_r}$ ,  $\theta_{CaL}$  and  $\theta_{K1}$ , respectively). As can be appreciated, pro-arrhythmic cells were most commonly located in regions with low  $\theta_{K_r}$  and  $\theta_{K1}$ , thereby exemplifying how  $I_{K_r}$  and  $I_{K1}$  downregulation contribute to pro-arrhythmicity. The effect of  $I_{CaL}$  was only significant in the region where  $\theta_{K_r} < 1$ , implying that the role of  $I_{CaL}$  was dependent on  $I_{K_r}$  expression.

## 2.4 Discussion

A population of human ventricular stochastic AP models was built and shown to reproduce a range of responses in terms of BVR and LF oscillations of APD following enhanced sympathetic activity, as reported experimentally [51]. The models included descriptions of electrophysiology,  $\beta$ -A signaling, mechanics and ionic gating stochasticity and served to investigate the interactions between the two investigated phenomena,

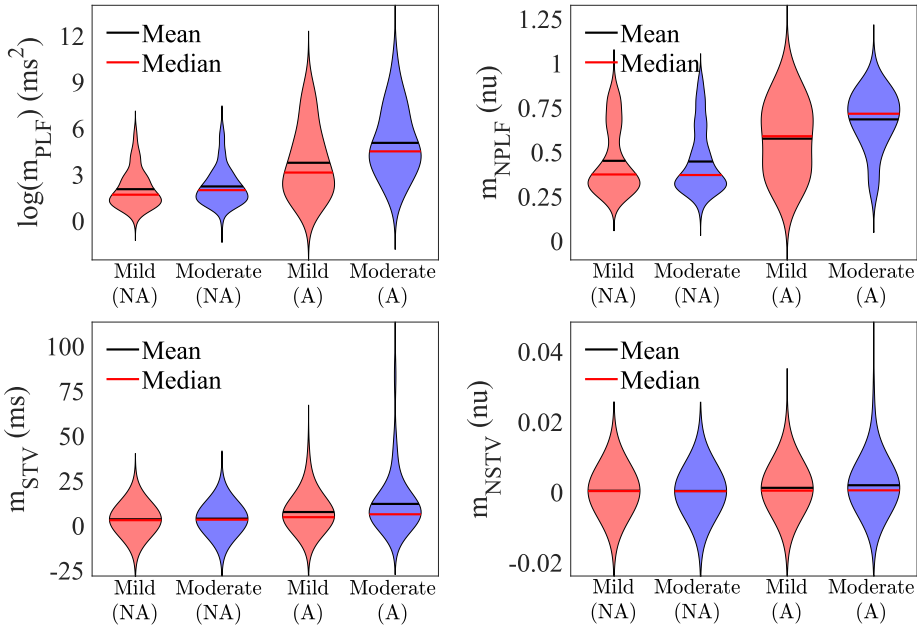


Figure 2.14: Violin plots representing the distributions of  $\log(m_{\text{PLF}})$ ,  $m_{\text{NPLF}}$ ,  $m_{\text{STV}}$  and  $m_{\text{NSTV}}$  for mild and moderate disease conditions. The whole population of models is divided into two subpopulations: the set of cells presenting (denoted by A) and not presenting (denoted by NA) pro-arrhythmic events following SP under severe disease conditions.

namely temporal variability and LF oscillatory behavior of APD, following SP. Ionic mechanisms underlying inter-individual differences in those phenomena were ascertained and individual characteristics associated with concomitantly large beat-to-beat variability and LF oscillations of repolarization were established. These were linked to higher susceptibility to electrical instabilities in the presence of disease conditions like  $\text{Ca}^{2+}$  overload and RRR.

### 2.4.1 Relation between Sympathetically Mediated BVR and LF Oscillations of APD in a Human Ventricular Population

Increases in LF oscillations of repolarization in response to enhanced sympathetic activity have been described at the level of the electrocardiographic T-wave and QT interval in humans and animals [48, 49, 95] and at the level of the ventricular APD in ambulatory patients [20, 51]. A direct effect related to enhanced activity of the sympathetic nerves innervating ventricular myocardium, rather than just an effect attributable to heart rate variability, has been proved [48, 51, 95]. In this study, phasic  $\beta$ -AS and mechanical stretch were simulated in association with muscle sympathetic

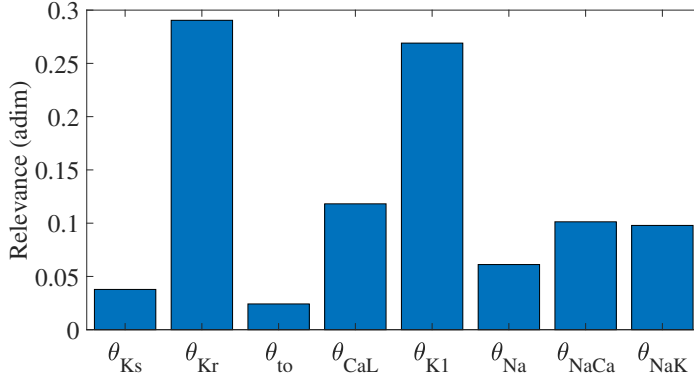


Figure 2.15: Relevance of ionic current conductances to pro-arrhythmic events.

nerve activity patterns during enhanced sympathetic activity [87]. Pacing at a constant rate was applied to the models. In accordance with experimental observations, increments in absolute and normalized LF power of APD have been overall measured in this population. Nevertheless, there is a high degree of inter-individual variability, with some individual cases showing no change or even a decrease in LF oscillations of APD in response to SP, which is in line with experimental reports as well.

Additionally, clinical and experimental studies have reported that enhanced sympathetic activity leads to increased BVR in patients with the long QT syndrome type 1 [96] and animal models of this disease [45] as well as in heart failure patients [52]. Human ventricular AP models, by including stochastic expressions of ionic current gating, allowed investigation of BVR at baseline and in response to SP. In agreement with experimental evidences, most of the models in the diseased population have shown sympathetically-mediated increments in BVR. The increase in BVR in the referred experimental/clinical studies as well as in the simulations of disease could be explained by  $\beta$ -AS effects under conditions of reduced  $I_{Ks}$ , which is indeed the case in the simulations and in long QT syndrome type 1 investigations and could also be the case in heart failure following previous reports suggesting downregulation of this current in failing hearts [97]. Also, mechanical effects associated with increased sympathetic activity could synergistically enhance BVR. Furthermore, in these simulations, a wide range of individual behaviors in terms of BVR patterns could be characterized following SP, in line with experimental data.

The interactions between BVR and LF oscillations of APD have been recently investigated in ambulatory patients with heart failure following a standard SP maneuver [51]. In the present study, a strong correlation between BVR and LF oscillation measures has been measured as well by simulation of SP through phasic  $\beta$ -AS and mechanical stretch in human ventricular myocytes. This holds true for physiological conditions and for disease conditions, simulated by  $Ca^{2+}$  overload and RRR, which are characteristic of diseased hearts like those of heart failure patients. In both simulations and experiments the variability measurements  $m_{SD}$ ,  $m_{NSD}$ ,  $m_{PLF}$  and  $m_{PLF}$

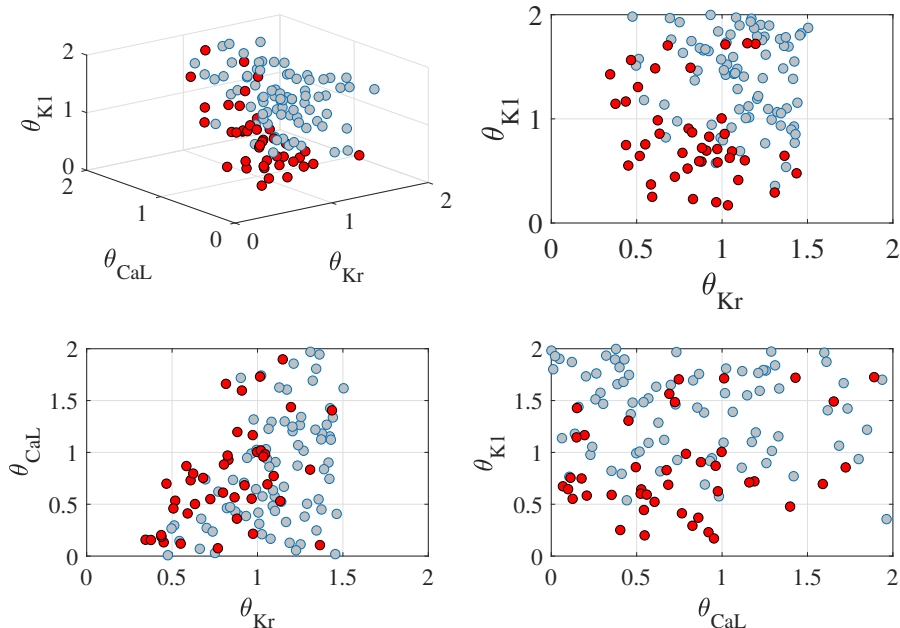


Figure 2.16: Location of cells presenting (red) and not presenting (gray) pro-arrhythmic events under simulated severe disease conditions as a function of relevant ionic current conductance values.

were quantified. In addition, the BVR measurement  $m_{STV}$ , which accounts for information on the APD variation between consecutive beats and has been extensively used for arrhythmic risk prediction [42, 98], was included in this work together with its APD-normalized version  $m_{NSTV}$ .

The strong correlation between  $m_{STV}$  and  $m_{PLF}$  found in simulations and experiments can be explained in light of the simulation outcomes. On the one hand, an increment in temporal APD variability associated with random ionic gating directly augments the LF power of APD, as it induces a rise in the power of APD at all frequencies. Although the measurement  $m_{NPLF}$  normalizes  $m_{PLF}$  by the total power, this marker turns out to be more insensitive to the amplitude of the LF oscillations of APD than  $m_{PLF}$ , while still indicative of the presence or absence of such oscillatory behavior. In the case of BVR, the normalized measurement  $m_{NSTV}$  has been quantified on top of  $m_{STV}$  to correct for the dependence on the APD. Even if the applied APD correction is able to reduce the correlation between APD and  $m_{NSTV}$  to a good extent, it does not abolish it completely. The very strong correlation between  $m_{PLF}$  and  $m_{STV}$ , both at baseline and following SP, dropped to very low correlation when  $m_{NPLF}$  and  $m_{NSTV}$  were evaluated at baseline. Following SP, the correlation between  $m_{NPLF}$  and  $m_{NSTV}$  was still remarkable, which can be explained by the fact that the presence of a marked LF oscillatory pattern directly impacts the temporal APD variability by increasing beat-to-beat APD differences.

### 2.4.2 Main Contributors to Increased BVR and LF Oscillations of APD following Enhanced Sympathetic Activity

The tight relationship between BVR and LF oscillations of APD following enhanced sympathetic activity suggests there could be common modulators of both phenomena. By building a population of virtual cells representing a range of experimentally reported characteristics, in this work it was possible to elucidate the ionic current conductances with a major contribution to inter-individual differences in absolute ( $m_{\text{STV}}$  and  $m_{\text{PLF}}$ ) and normalized ( $m_{\text{NSTV}}$  and  $m_{\text{NPLF}}$ ) BVR and LF oscillation markers. For such elucidation, an approach based on the ARD technique was developed. Similar approaches have been proposed in the context of magnetoencephalography [99] and wireless communications [100], among others, but to the best of our knowledge this is the first time an ARD-based technique is used to identify ionic modulators of cardiac electrophysiological phenomena.

In [33] the mechanisms underlying LF oscillations of ventricular APD were investigated by simulating phasic  $\beta$ -AS and mechanical stretch in association with enhanced sympathetic activity. Differential  $I_{\text{Ks}}$  and  $I_{\text{CaL}}$  phosphorylation and dephosphorylation kinetics in response to  $\beta$ -AS together with variations in  $\text{Ca}^{2+}$  cycling and SACs in response to stretch were found to synergistically underlie LF oscillatory behavior under SP. While that study provided meaningful insights into the bases for LF oscillations of ventricular repolarization, only an average cell was modeled, which did not allow investigation of inter-individual differences in LF oscillations of APD as in the present study. Also, the models of the population built here are stochastic, as opposed to the deterministic models employed in [33], thus allowing to quantify BVR at baseline and its change in response to SP. This is of major relevance for investigation of the interactions between BVR and LF oscillations of APD and of their modulators in a whole population.

Our results highlighted the relevance of  $I_{\text{Kr}}$ ,  $I_{\text{CaL}}$  and  $I_{\text{K1}}$  conductances in modulating inter-individual differences in both BVR and LF oscillatory pattern of APD under SP. Regarding  $I_{\text{Kr}}$ , its downregulation was shown to be a key factor for augmentation of  $m_{\text{STV}}$  and  $m_{\text{PLF}}$  but less important when considering their normalized counterparts  $m_{\text{NSTV}}$  and  $m_{\text{NPLF}}$ . Concerning LF oscillations of APD, there is little investigation in the literature into factors acting to modulate their magnitude. In [33], a reduction in the repolarization current was shown to amplify APD oscillatory behavior. Results are in line with such observations. Considering the fact that  $m_{\text{NPLF}}$  does not reflect the magnitude of the oscillations but mostly its presence or absence, this normalized marker was found not to be modulated by  $I_{\text{Kr}}$ . Regarding BVR, a variety of experimental, clinical and computational studies have addressed the role of ionic current conductances in modulating beat-to-beat temporal variability quantified by markers such as  $m_{\text{STV}}$  or  $m_{\text{SD}}$ . In accordance with the results presented in [56] for baseline conditions and [65] for  $\beta$ -AS, this work has shown  $I_{\text{Kr}}$  downregulation to act as a contributor of BVR magnification. Since such a contribution is to a large extent mediated by APD lengthening, it becomes importantly reduced when measured by

markers that include APD normalization, such as  $m_{\text{NSTV}}$  or  $m_{\text{NSD}}$ .

Another very relevant current in the modulation of BVR and LF oscillatory behavior of APD was  $I_{\text{CaL}}$ . Although no previous studies in the literature have investigated the role of  $I_{\text{CaL}}$  as a modulator of LF oscillation amplitude, there have been a number of studies addressing its role as a modulator of BVR. In [55],  $I_{\text{CaL}}$  downregulation was shown to increase the random channel fluctuation effects in guinea pig models, which is in good agreement with the presented results. On top of the contribution of  $I_{\text{CaL}}$ , a role for  $I_{\text{Ks}}$  and persistent  $I_{\text{Na}}$  currents in enhancing BVR was also demonstrated in [55]. It could not have been found such a role for those two currents, which could be due to differences between species (guinea pig in [55] and human in this study) and to the fact that this study investigated conditions of enhanced sympathetic activity rather than baseline conditions.

Regarding  $I_{\text{K1}}$  regulation, this is, to the best of our knowledge, the first work identifying its relevance to BVR and LF oscillations of APD. In these results,  $I_{\text{K1}}$  downregulation appears as a relevant contributor when SACs are incorporated into the models to simulate mechanical stretch changes associated with SP. Under downregulated  $I_{\text{K1}}$ , SACs contribute to alter the AP shape during the last part of repolarization in a phasic manner, leading to increments in both BVR and LF oscillations.

As chronotropic effects of SP have been well documented in *in vivo* studies, computational simulations were additionally carried out while pacing the virtual cells at higher frequencies. The main ionic contributors  $I_{\text{Kr}}$ ,  $I_{\text{K1}}$  and  $I_{\text{CaL}}$  are confirmed to remain very relevant to explain inter-individual differences in BVR and LF oscillatory behavior in response to SP. Of note, the relevance of  $I_{\text{NaK}}$  in determining LF oscillations of APD increases when the analysis is performed for pacing frequencies above 1 Hz.

### 2.4.3 Pro-Arrhythmic Events associated with Increased BVR and LF Oscillations of APD under Severe Disease Conditions

$\text{Ca}^{2+}$  overload and RRR are properties commonly present in diseased hearts, like those of patients with heart failure, ischemic heart disease or post-myocardial infarction, [101–106]. In this study, BVR and LF oscillations of APD have been found to become increasingly accentuated in response to disease progression. These results are in line with those reported in previous clinical, experimental and theoretical studies of the literature. In isolated myocytes and animal models of diseases like diabetes, heart failure or post-myocardial infarction, exaggerated temporal APD variability has been observed in association with  $\text{Ca}^{2+}$  overload and RRR, [106–109]. In the long QT syndrome type 1, involving loss of  $I_{\text{Ks}}$  function, elevated ventricular repolarization variability in response to  $\beta$ -AS has been documented and mechanisms have been proposed based on animal models, isolated myocytes and computer simulation research,



[45, 63, 65, 66]. In chronic atrioventricular block dogs, where ventricular remodeling importantly compromises repolarization reserve, beat-to-beat APD variability has been found to be augmented with respect to healthy dogs, [110]; an observation also confirmed at the level of ventricular myocytes, [53]. A mechanical challenge in the form of preload variability has been reported to be essential in that augmentation, with mechano-electrical feedback through SACs postulated as a major mechanism, [110]. In [33], the presence of disease conditions has been reported to lead to notably augmented LF oscillations of APD.

Under severe disease conditions, arrhythmogenic manifestations have been found to arise in individual cases of the population presenting large temporal repolarization variability, either quantified at the LF band (LF oscillations) or at all frequencies (BVR). These observations are in agreement with studies relating disproportionate APD fluctuations, particularly in response to enhanced sympathetic activity, and the generation of afterdepolarizations and arrhythmias. In [45] the authors used an *in vivo* canine model of the long QT syndrome type 1 to demonstrate that  $\beta$ -AS enhanced temporal and spatial variability of ventricular repolarization, which precipitated Torsades de Pointes (TdP) arrhythmias. The association between increased BVR and the onset of TdP arrhythmias has also been demonstrated in dogs with chronic atrioventricular block [39, 44]. In ventricular myocytes and wedge preparations from human end-stage failing hearts,  $\beta$ -AS has been shown to generate electrical abnormalities that result in EADs and delayed afterdepolarizations (DADs), [111, 112]. Using a rabbit model mimicking electrophysiological and contractile alterations in human HF,  $\beta$ -AS has been reported to be a key factor in inducing DADs and increasing the propensity for triggered arrhythmias, [113]. At the level of the surface ECG, increased BVR and LF oscillations of repolarization have been shown to be risk predictors of ventricular arrhythmias and sudden cardiac death [38, 48, 50, 109].

Provided the tight relationship between magnification of BVR and LF oscillations of APD and pro-arrhythmic risk, the existence of common modulators has been explored in the present study. Canonical Correlation Analysis has been proposed to identify ionic factors contributing to pro-arrhythmic risk following enhanced sympathetic activity. CCA revealed the important role of  $I_{K1}$ ,  $I_{Kr}$  and  $I_{CaL}$  in the development of pro-arrhythmic events. These same factors are those primarily involved in modulation of sympathetically-mediated BVR and LF oscillations of APD. The role of  $I_{K1}$  in contributing to arrhythmogenesis has been reported in a rabbit model of heart failure, where the combination of upregulated  $I_{NaCa}$ , downregulated  $I_{K1}$  and residual  $\beta$ A responsiveness has been shown to increase the propensity for triggered arrhythmias [113]. In this work, the contribution of  $I_{K1}$  downregulation to pro-arrhythmicity in association with elevated temporal variability might have been more prominent if the population of stochastic AP models had been built based on an electrophysiological model more likely producing delayed afterdepolarizations under downregulated  $I_{K1}$ , and possibly upregulated  $I_{NaCa}$ , as compared to the ORd model. The role of  $I_{Kr}$  in arrhythmogenesis has been well established in a variety of previously published investigations. In [106], the loss of repolarizing currents, including  $I_{Kr}$ , has been described to

lead to increased BVR, repolarization instability and afterdepolarizations in myocytes from dogs susceptible to sudden cardiac death. In [33] reduced  $I_{Kr}$  and  $I_{Ks}$  have been reported to cause AP irregularities associated with enhanced LF oscillations of APD induced by SP. The implications of  $I_{Kr}$  inhibition in promoting ventricular arrhythmias associated with increased temporal APD dispersion has been further demonstrated in animal models of disease [110]. On top of  $K^+$  currents, the present work has identified  $I_{CaL}$  current as another relevant contributor to pro-arrhythmia associated with elevated BVR and LF oscillations of APD, even if conditioned to the presence of reduced  $I_{Kr}$ . In line with these results, increased  $I_{CaL}$  has been demonstrated to facilitate electrical abnormalities in the form of EADs in ventricular myocytes from human failing hearts [111]. The contribution of increased  $I_{CaL}$  to arrhythmogenesis during  $\beta$ -AS has been also shown in [66] under reduced  $I_{Ks}$ .

In this study, other currents, like  $I_{Ks}$  and  $I_{NaL}$ , were found to have minor relevance as contributors to arrhythmogenesis in association with temporal dispersion of repolarization. This is contrast to previous studies showing major roles of  $I_{Ks}$  down-regulation and  $I_{NaL}$  upregulation [45, 63, 65, 66, 108, 109, 114]. This discrepancy may be explained by differences between species, modeling characteristics and, importantly, investigated conditions, since this work has focused on the investigation of arrhythmic events occurring following enhanced sympathetic activity.

#### 2.4.4 Limitations and Future Work

The stochastic models built in this work included random gating descriptions for major ionic currents active during AP repolarization like  $I_{Ks}$ ,  $I_{Kr}$ ,  $I_{to}$  and  $I_{CaL}$ , as in previous studies of the literature [57, 115]. Future studies could include stochasticity in other currents like  $I_{NaL}$ , whose contribution to BVR has been reported in canine ventricular models [65].

In the present work the ORd ventricular AP model has been used, which was developed based on extensive undiseased human data. In this model the effect of varying the  $I_{Ks}$  current on AP is significantly smaller than in other human ventricular cell models, like the ten Tusscher-Panfilov model [31]. The low relevance of  $I_{Ks}$  as an ionic modulator of BVR and LF oscillations of APD found in this work may have to do with it. In [33], which served as a starting point for the present work, several electrophysiological, mechanical and  $\beta$ -A signaling models were tested and only some quantitative differences could be found, while the conclusions remained qualitatively the same for all models. Nevertheless, the role of certain ionic currents in modulating inter-individual differences in BVR and LF oscillatory behavior, as investigated in this study, might still be different if another AP model were used as a basis. This should be addressed in future works.

Also in relation to the use of the ORd model as a basis for the development of the population of models in this work, it should be noted that other ventricular AP models with updated mechanisms of  $Ca^{2+}$  induced  $Ca^{2+}$  release could provide additional

insight into the occurrence of spontaneous  $\text{Ca}^{2+}$  release and delayed afterdepolarizations in association with elevated BVR and LF oscillations of APD. Indeed, previous studies have been shown that  $\text{Ca}^{2+}$  handling abnormalities are a major driver of BVR during  $\beta$ -AS [66] and a link between  $\text{Ca}^{2+}$  handling and arrhythmia liability during increased sympathetic activity has been demonstrated, particularly in the setting of heart failure [116].

The population of human ventricular cells used in this work was generated by varying the conductances of eight ionic currents. Ionic parameters other than maximal current conductances might also represent relevant mechanisms underlying the interactions between BVR and LF oscillations of APD. In particular for the  $I_{\text{CaL}}$  current, previous studies have proved that modulation of other biophysical properties, like a reduction in the amplitude of the non-inactivating pedestal component of  $I_{\text{CaL}}$ , allows to effectively suppress EADs without blocking peak  $I_{\text{CaL}}$ , thus preserving excitation-contraction coupling [117]. Future work could address the investigations of the present work by generating a population of virtual cells where biophysical ionic parameters other than maximal conductances were varied, which could eventually lead to findings that developed into more clinically useful therapeutic approaches.

The present chapter has focused on single cells, while the available experimental data on the interactions between BVR and LF oscillations of human APD are from *in vivo* measurements in ambulatory heart failure patients. Simulated results qualitatively reproduced the behavior observed in the experiments. Future work could include assessment of those interactions in tissue and whole-heart models. Nonetheless, cell-to-cell coupling has been shown to be remarkably reduced in heart failure and other disease conditions, which would render cell and tissue results close to each other.

Statistical approaches based on ARD and CCA have been used in this study. Future works could investigate generalization of these techniques to consider nonlinear relationships by using kernel functions, even if a larger number of simulations would be required to avoid overfitting.

## 2.5 Conclusions

Human ventricular models including descriptions of cell electrophysiology, ion channel stochasticity,  $\beta$ -A signaling and mechanical stretch were developed. These models reproduced experimentally reported interactions between beat-to-beat variability and low-frequency oscillations of repolarization in response to enhanced sympathetic activity. Ionic factors underlying correlated increments in both phenomena were investigated, which included downregulation of the inward and rapidly activating delayed rectifier  $\text{K}^+$  currents and the L-type  $\text{Ca}^{2+}$  current. Concomitantly elevated levels of beat-to-beat repolarization variability and its low-frequency oscillations in diseased ventricles led to electrical instabilities and arrhythmogenic events. This investigation

serves as a basis for future studies aiming at improving arrhythmic risk stratification and guiding the search for more efficient anti-arrhythmic therapies.

# 3 | Time Course of Low-Frequency Oscillations of Human Ventricular Repolarization. Relevance for Arrhythmogenesis

---

3.1	Introduction . . . . .	58
3.2	Methods . . . . .	60
3.2.1	Experimental Data . . . . .	60
3.2.2	Electrophysiology Model . . . . .	60
3.2.3	PKA Phosphorylation Model . . . . .	61
3.2.4	Mechanics Model . . . . .	61
3.2.5	Simulation of Enhanced Sympathetic Activity . . . . .	62
3.2.6	Simulation of Disease Conditions . . . . .	62
3.2.7	Quantification of APD Time Lag in Response to Constant $\beta$ -AS and/or Mechanical Stretch . . . . .	62
3.3	Results . . . . .	64
3.3.1	Time Lapse for Development of LF Oscillations in APD . . . . .	64
3.3.2	Contribution of $\beta$ -AS and Mechanical Stretch to Time Lapse of LF Oscillations in APD . . . . .	65
3.3.3	Comparison of APD Time Lapse following $\beta$ -AS in Experiments and Simulations . . . . .	66
3.3.4	Reduction in Time Lapse for LF Oscillations of APD by Prior Low-Level $\beta$ -AS . . . . .	67
3.3.5	Ionic Mechanisms Underlying Time Lapse in LF Oscillations of APD . . . . .	68

---

3.3.6	Relationship between Time Lapse and Magnitude of LF Oscillations of APD . . . . .	70
3.3.7	Effect of Disease Conditions in Time Lapse of LF Oscillations of APD and Relation to Arrhythmogenesis . . . . .	71
3.4	Discussion . . . . .	72
3.4.1	Inter-Individual Differences in the Time Lapse for Development of LF Oscillations of APD Following Enhanced Sympathetic Activity . . . . .	72
3.4.2	Major Role of $I_{Ks}$ Phosphorylation Kinetics in Determining the Time Lapse for LF Oscillations of APD . . . . .	75
3.4.3	Increased Arrhythmic Risk as a Function of the Time Lapse and Magnitude of LF Oscillations of APD . . . . .	76
3.4.4	Limitations and Future Work . . . . .	77
3.5	Conclusions . . . . .	78

---

### 3.1 Introduction

As described in Chapter 2, ventricular repolarization exhibits an LF oscillatory pattern following enhanced sympathetic activity. In humans, this has been demonstrated by quantification of PRD in the T-wave vector of the ECG [48, 49] as well as by *in vivo* evaluation of LF components in ARIs of ventricular EGMs [20, 51]. In post-infarction patients, an increased magnitude of LF oscillations in ECG repolarization has been proved to be a significant predictor of total mortality and sudden cardiac death [50]. Most notably, a very recent study has shown that those periodic repolarization dynamics are able to predict the efficacy of implanting a cardioverter defibrillator in patients undergoing primary prophylactic treatment [118]. *In silico* studies have provided insight into the cellular mechanisms underlying this oscillatory pattern of ventricular repolarization, which have been explained by the synergistic effect of phasic  $\beta$ -AS and mechanical stretch, both accompanying enhanced sympathetic nerve activity. In brief, differential phosphorylation kinetics of calcium ( $I_{Ca}$ ) and potassium ( $I_K$ ) currents upon phasic  $\beta$ -AS as well as changes in calcium cycling and the action of SACs in response to phasic mechanical stretch have been shown to generate LF oscillations in cellular APD [33]. Chapter 2 investigated inter-individual differences in LF oscillations of ventricular APD, concluding that calcium and potassium currents,  $I_{Ca}$  and  $I_K$  (specifically, the rapid delayed rectifier  $I_{Kr}$  and inward rectifier  $I_{K1}$ ), are major ionic modulators of such inter-individual differences. Importantly, these identified ionic factors are key for the development of arrhythmic events following enhancement of APD oscillations' magnitude. A very recent investigation has experimentally con-

firmed in an arrhythmogenic *in vivo* dog model that ventricular remodeling associated with chronic atrioventricular block (CAVB) augments LF oscillations of APD [119]. Most importantly, the oscillation magnitude has been reported to be larger in dogs susceptible to dofetilide-induced TdP arrhythmias as compared to non-inducible dogs [119].

For LF oscillations in the ventricular APD to become clearly manifested following increased sympathetic activity, computational research has shown that some tens of seconds or even a few minutes are required [33]. This requisite on a relatively long exposure to enhanced sympathetic activity for repolarization oscillations to develop may explain why experimentally measured APD oscillations appear to come and go and do not remain as sustained oscillations for long recording periods [20]. Chapter 2 and [33] have shown that, upon a sympathetic rise, the cellular ventricular APD shows a global trend of shortening, or brief prolongation followed by more prominent shortening, which masks concurrent LF oscillations overlapping with the global APD trend. The individual and combined roles of  $\beta$ -AS and mechanical stretch in determining the time lapse for LF oscillations to become visibly manifested are yet to be explored. Experimental investigations in canine ventricular myocytes have shown that APD presents slow time-dependent changes following application of a constant dose of the  $\beta$ -A agonist ISO [120]. The slow activation of  $I_K$  currents (in particular, slow  $I_{Ks}$  and rapid  $I_{Kr}$  delayed rectifier currents), as compared to the very fast activation of the  $I_{Ca}$  current, has been demonstrated to be behind such APD lag following sudden ISO exposure. The distinctively slow response of  $I_{Ks}$  to  $\beta$ -AS and its implications in terms of APD adaptation time have been also described in other species, like the rabbit [121]. On the other hand, APD dynamicity in response to constant mechanical stretch or to the combination of constant  $\beta$ -AS and mechanical stretch has been less studied experimentally.

The work presented in this chapter investigates the cellular ventricular APD response to phasic, rather than constant,  $\beta$ -AS and mechanical stretch, in closer correspondence with the experimentally reported LF patterns of efferent sympathetic nerve activity [87, 122]. The global trend of APD response is in this case expected to be concurrent with periodic changes in APD occurring at the frequency of sympathetic activity. For this investigation, a population of computational cellular AP models representative of experimentally reported human ventricular electrophysiological characteristics is developed and coupled to models of  $\beta$ -AS and mechanics. By using the developed models, the amount of time required for LF fluctuations of APD to arise in response to phasic sympathetic activation is characterized and the ionic mechanisms underlying cell-to-cell differences in APD time lag are dissected. Experimental confirmation of the obtained results is obtained. A relationship between the quantified time lapse and the magnitude of APD oscillations is established, which serves to set links to pro-arrhythmic risk under disease conditions associated with  $\text{Ca}^{2+}$  overload and reduced RRR, both being commonly present in failing hearts.

## 3.2 Methods

### 3.2.1 Experimental Data

Ventricular myocytes were isolated from the left ventricular wall of adult beagle dogs as described in [120]. The isolation procedure followed a protocol approved by the local ethical committee according to the principles outlined in the 1964 Declaration of Helsinki and its later amendments. The cells used for the work described in this chapter were obtained from the subepicardial layer.

Transmembrane potentials were measured at 37 °C by using 3 M KCl-filled sharp glass microelectrodes with tip resistance 20-40 M $\Omega$  [120]. The electrodes were connected to the input of an Axoclamp-2B amplifier (Molecular Devices, Sunnyvale, CA, USA). Cardiomyocytes were paced at 1 s using 1-ms wide rectangular current pulses with 120% threshold amplitude until steady-state. ISO was applied at a concentration of 10 nM for 5 minutes. APs were sampled by periods of 30 s following ISO application, with a sampling frequency of 200 kHz using Digidata 1200 A/D card (Axon Instruments Inc., Foster City, CA, USA).

### 3.2.2 Electrophysiology Model

Similar to the description in Chapter 2, a population of human ventricular AP models representative of a wide range of experimentally observed electrophysiological characteristics was built based on the ORd epicardial model [5]. The population was obtained by varying the ionic conductances of eight ionic currents in the ORd model, namely:  $I_{Ks}$ , slow delayed rectifier potassium current;  $I_{Kr}$ , rapid delayed rectifier potassium current;  $I_{to}$ , transient outward potassium current;  $I_{CaL}$ , L-type calcium current;  $I_{K1}$ , inward rectifier potassium current;  $I_{Na}$ , sodium current;  $I_{NaK}$ , sodium-potassium pump current; and  $I_{NaCa}$ , sodium-calcium exchanger current.

Initially, 500 models were generated by using the Latin Hypercube Sampling method to sample the conductances of the above described currents in the range  $\pm 100\%$ , [33, 69]. A set of calibration criteria based on experimentally available human ventricular measures of steady-state AP characteristics [5, 70–73] were imposed, as described in Table 3.1. AP characteristics used for model calibration included:  $APD_{90|50}$ , which represents steady-state APD at 90%|50% repolarization corresponding to 1 Hz pacing (expressed in ms); RMP, representing resting membrane potential (in mV);  $V_{peak}$ , representing peak membrane potential measured in the AP upstroke (in mV); and  $\Delta APD_{90}$ , representing the percentage of change in  $APD_{90}$  with respect to baseline following individual inhibitions of  $I_{Ks}$ ,  $I_{Kr}$  or  $I_{K1}$  currents (measured in ms). Of the initial 500 models, only 218 meeting all the calibration criteria were selected. Additionally, models showing pro-arrhythmic behavior at baseline and/or under SP were discarded, which led to a population of 188 models for the analysis of this work.



Table 3.1: Calibration criteria applied onto human ventricular cell models.

AP characteristic	Min. acceptable value	Max. acceptable value
Under baseline conditions [5, 70, 71]		
APD <sub>90</sub> (ms)	178.1	442.7
APD <sub>50</sub> (ms)	106.6	349.4
RMP (mV)	-94.4	-78.5
V <sub>peak</sub> (mV)	7.3	-
Under 90% $I_{Ks}$ block [5]		
$\Delta$ APD <sub>90</sub> (%)	-54.4	62
Under 70% $I_{Kr}$ block [73]		
$\Delta$ APD <sub>90</sub> (%)	34.25	91.94
Under 50% $I_{K1}$ block [72]		
$\Delta$ APD <sub>90</sub> (%)	-5.26	14.86

### 3.2.3 PKA Phosphorylation Model

A modified version of the  $\beta$ -A signaling model proposed Xie *et al.* in [36] was used as a basis to describe phosphorylation levels of cellular PKA substrates, as reported in [33] and Chapter 2. The Xie model [36] represents an evolution from the Soltis *et al.* signaling model [35] in which  $I_{Ks}$  phosphorylation and dephosphorylation rate constants were updated to better match experimental observations reported in [121]. Also, as described in [36], PKA-mediated phosphorylation of PLM involved an increase in the NKA affinity for the intracellular  $\text{Na}^+$  concentration. In the modified model of this work, RyR phosphorylation was defined by using the formulation described in [79].

For a specific set of simulations,  $I_{Ks}$  phosphorylation and dephosphorylation kinetics were defined as reported in [35] to assess the effects of faster phosphorylation kinetics on the time lapse for APD oscillations development.

### 3.2.4 Mechanics Model

An updated version of the Niederer model was employed to describe cell mechanics [14], with the values of some constants being adjusted to represent human cell characteristics as in [16] and [33].  $I_{SAC}$ , denoting the current through SACs, was accounted for as in [33] and Chapter 2. Specifically,  $I_{SAC}$  was defined as the current through non-specific cationic SACs plus the current through  $\text{K}^+$ -selective SACs.

### 3.2.5 Simulation of Enhanced Sympathetic Activity

Enhanced sympathetic activity was simulated by the combination of phasic  $\beta$ -AS and mechanical stretch effects. Similarly to Chapter 2, phasic  $\beta$ -AS was simulated by a periodic stepwise profile of the  $\beta$ -A agonist ISO according to muscle sympathetic nerve activity patterns in humans [87]. The periodicity of the ISO profile corresponded to a frequency of 0.05 Hz, this being within the reported Mayer wave frequency range (0.03-0.15 Hz). The 20-second ISO period was composed of a 10-second time interval where the ISO concentration was set to 1  $\mu$ M and a subsequent 10-second time interval where the ISO concentration was 0. Phasic changes in hemodynamic loading, a known accompaniment of enhanced sympathetic activity, were simulated by phasic mechanical stretch changes at the same 0.05 Hz frequency. Specifically, the stretch ratio was varied during the 20-second period following a sinusoidal waveform with maximal change being 10%, being such level of change in line with those of previous experimental and computational studies [123, 124]. Phasic  $\beta$ -AS and mechanical stretch effects were defined to be in-phase. A total of 500 beats at baseline and 500 beats following enhanced sympathetic activity were simulated while pacing at 1 Hz frequency.

### 3.2.6 Simulation of Disease Conditions

For specific simulations, disease conditions were simulated by RRR and  $\text{Ca}^{2+}$  overload. RRR was defined by concomitant inhibition of  $I_{K_T}$  and  $I_{K_S}$  currents by 30% and 80%, respectively.  $\text{Ca}^{2+}$  overload was defined by a 4-fold increment in the extracellular  $\text{Ca}^{2+}$  level.

### 3.2.7 Quantification of APD Time Lag in Response to Constant $\beta$ -AS and/or Mechanical Stretch

APD was evaluated at 90% repolarization in both simulations and experiments. The simulated or experimentally measured APD time series following  $\beta$ -AS and/or mechanical stretch is denoted by  $a[k]$ , where the discrete index  $k$  represents cycle number. Thus,  $k$  varies from 0 to  $K$ , with  $K$  being the number of cycles following  $\beta$ -AS and/or mechanical stretch.

The time lapse,  $\tau_{\text{APD}}$ , for APD to reach a new steady-state following application of  $\beta$ -AS and/or stretch was defined as the time taken by the APD time series to attain convergence, with convergence characterized by the derivative of the APD time series being below a predefined threshold. Specifically, the following steps were used to compute the APD time lapse:

#### 1. Smoothing

To remove short-term variability and make the estimation of the convergence

time more robust, moving average smoothing was applied onto the APD time series  $a[k]$  to obtain a smooth version of it,  $\hat{a}[k]$ :

$$\hat{a}[k] = \frac{1}{T} \sum_{k'=k}^{k+T} a[k'] \quad (3.1)$$

where  $T$  was set to the period in cycles of the sympathetic activity,  $T = 20$  cycles.

## 2. Numerical Derivative

From  $\hat{a}[k]$ , the derivative  $d[k]$  was numerically estimated by computing the central difference for the interior data points of  $\hat{a}[k]$  and single-side difference for the edges of  $\hat{a}[k]$ :

$$d[k] = \frac{\hat{a}[k+1] - \hat{a}[k-1]}{2}, \quad 0 < k < K \quad (3.2)$$

$$d[0] = \hat{a}[1] - \hat{a}[0] \quad (3.3)$$

$$d[K] = \hat{a}[K] - \hat{a}[K-1] \quad (3.4)$$

## 3. Time Lapse Calculation

A threshold on the maximum allowed variation in the derivative of the APD time series for convergence to be attained was defined in this work by setting  $\theta = 0.5$  ms. The number of cycles,  $k_{\text{APD}}$ , for APD convergence following  $\beta$ -AS and/or stretch was defined as:

$$k_{\text{APD}} = \min_{0 \leq k \leq K} \left\{ \left| \sum_{k'=k}^K d[k'] \right| < \theta \right\} \quad (3.5)$$

The time lapse  $\tau_{\text{APD}}$  was obtained by converting  $k_{\text{APD}}$  into minutes:

$$\tau_{\text{APD}} = k_{\text{APD}} \frac{CL}{60} \quad (3.6)$$

where  $CL$  is the cycle length in seconds (constant period between stimuli applied to the cells to elicit APs).

Values of  $\tau_{\text{APD}}$  equal to 0 represent cases where convergence of the APD time series was immediate.

### 3.3 Results

#### 3.3.1 Time Lapse for Development of LF Oscillations in APD

Fig. 3.1 shows examples of APD time series for two different human ventricular cells of the simulated population presenting LF oscillations following SP. From this figure, it is clear that not only the magnitude of the oscillations is different for the two cells but also the time lapse required for LF oscillations of APD to become evident is remarkably distinct. For the first virtual cell illustrated in Fig. 3.1, the time lapse was  $\tau_{\text{APD}} = 139$  s, whereas for the second virtual cell,  $\tau_{\text{APD}} = 0$  s. The characteristics of these two cells in terms of ionic current conductances are presented in Table 3.2.

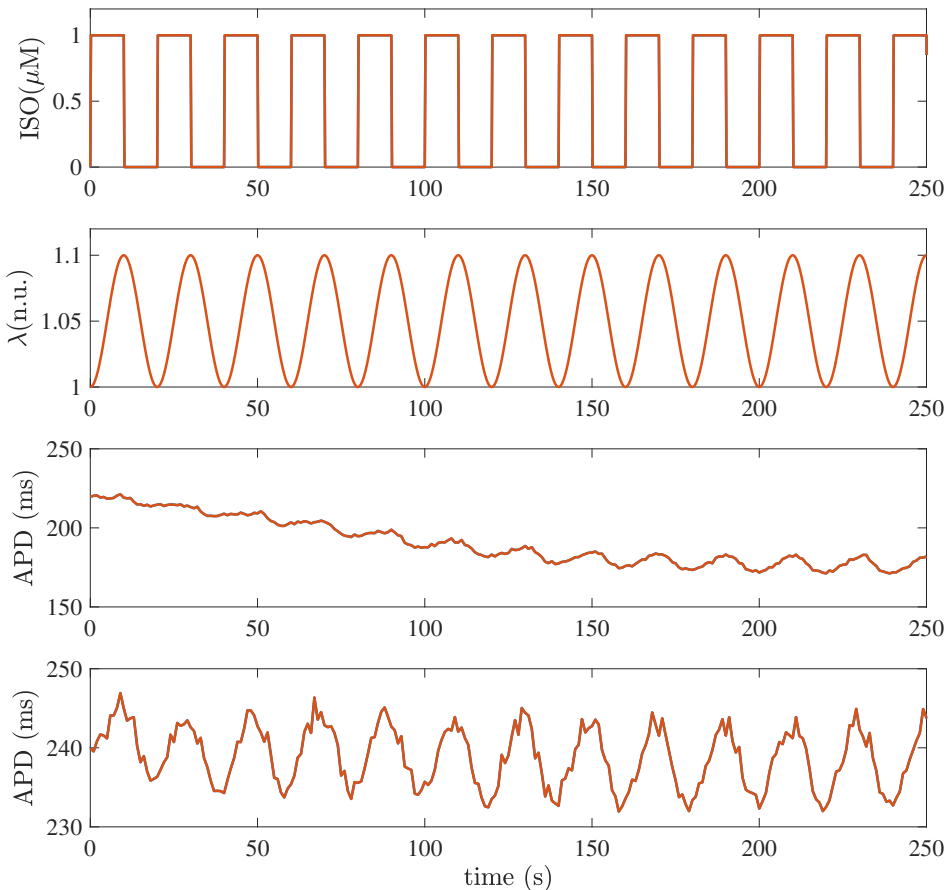


Figure 3.1: Simulation of SP and APD response of two different cells in the population. First row: Phasic ISO application at a frequency of 0.05 Hz. Second row: Phasic stretch ratio variations at the same frequency. Third and fourth rows: APD time series corresponding to two cells (virtual cell 1 and virtual cell 2) presenting LF oscillations in response to SP.

Table 3.2: Factors multiplying ionic conductances of virtual cells 1 and 2 illustrated in Fig. 3.1.

Ionic factors	$\theta_{Ks}$	$\theta_{Kr}$	$\theta_{to}$	$\theta_{CaL}$	$\theta_{K1}$	$\theta_{Na}$	$\theta_{NaCa}$	$\theta_{NaK}$
Virtual cell 1	1.83	0.88	0.78	0.46	1.16	1.70	0.40	1.37
Virtual cell 2	0.49	1.11	1.98	1.37	1.34	0.42	1.82	1.97

Fig. 3.2, left panel, presents a histogram of the time lapse for APD oscillations developed in response to a rise in sympathetic activity for all the cells in our virtual population. Inter-individual differences in the ionic characteristics of the virtual cells had an impact on  $\tau_{APD}$ , which ranged from just a few seconds for some virtual cells to more than three minutes for other cells. Similarly, Fig. 3.2, right panel, shows a histogram of the power in the LF band (PLF) for APD oscillations under SP, represented in terms of  $\log(PLF)$ . Large inter-individual variability also exists in  $\log(PLF)$ , with values covering from 0 to 10  $\text{ms}^2$ , although most cells present PLF values below 5  $\text{ms}^2$ .

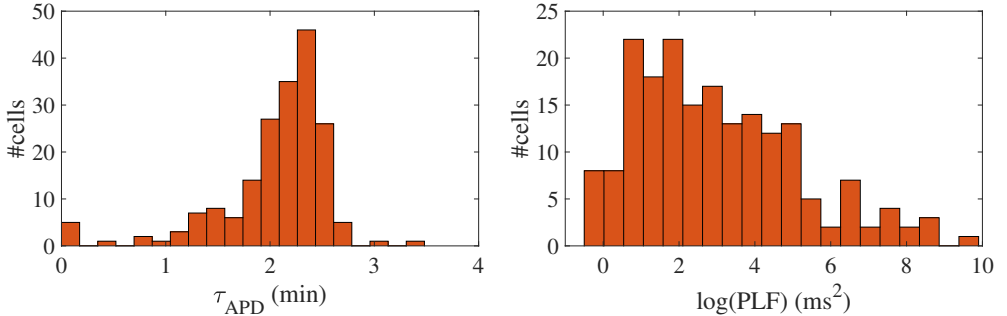


Figure 3.2: Histogram of the time lapse (left panel) and LF power (right panel) of APD in response to increased sympathetic activity for all cells in the simulated population.

### 3.3.2 Contribution of $\beta$ -AS and Mechanical Stretch to Time Lapse of LF Oscillations in APD

The individual and combined contributions of phasic  $\beta$ -AS and mechanical stretch to the time lapse in the occurrence of LF oscillations of APD is presented in Fig. 3.3, left panel. As can be observed from the figure, individual application of phasic  $\beta$ -AS had a major role in the time required for APD oscillations to develop, whereas individual mechanical stretch had a more marginal influence, with the vast majority of simulated cells developing LF oscillations in response to phasic stretch in less than one minute. When the effects of  $\beta$ -AS and stretch were combined, the APD convergence time was reduced with respect to that corresponding to only  $\beta$ -AS for practically all cells.

Additionally, Fig. 3.3, right panel, illustrates the oscillation magnitudes in terms

of  $\log(\text{PLF})$  for individual and combined  $\beta$ -AS and mechanical stretch. Individual mechanical stretch led to the largest oscillations magnitudes, in association with the shortest time delays, whereas individual  $\beta$ -AS led to the smallest magnitudes, in association with the largest time lapses. Nevertheless, high inter-individual variability could be observed in all cases.

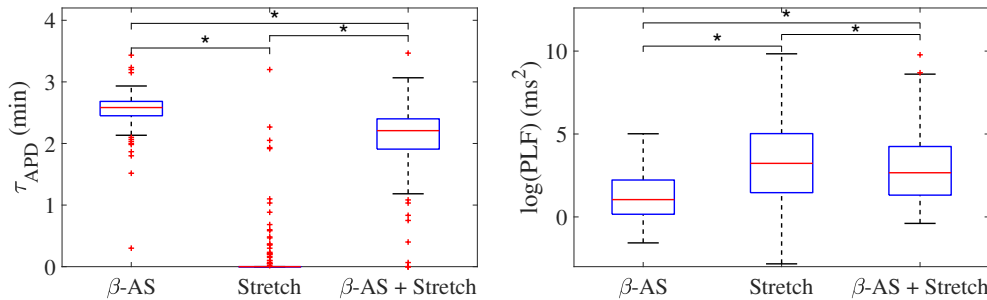


Figure 3.3: Boxplots representing the time lapse (left panel) and the power in the LF band (right panel) for oscillations of APD to develop in response to phasic  $\beta$ -AS (ISO  $1\mu\text{M}$ ), mechanical stretch (10%) and the combination of both. Statistically significant differences by Wilcoxon signed-rank test (p-value  $< 0.05$ ) are denoted by \*. Since the statistical significance in the comparison of simulated data highly depends on the number of simulated cases, smaller subsets of virtual cells were used to prove that  $p = 0.05$  had already been achieved with a much smaller number of virtual cells than those in the whole population.

### 3.3.3 Comparison of APD Time Lapse following $\beta$ -AS in Experiments and Simulations

Based on the results presented in sections 3.3.1 and 3.3.2 and the fact that LF oscillations of APD are superimposed to the general trend of APD decrease following enhanced sympathetic activity, the time lapse for the development of APD oscillations can equivalently be determined by the time required for APD to converge to steady-state following constant  $\beta$ -AS.

The temporal evolution of APD following constant application of an ISO dose of 10 nM was investigated in simulations based on the generated population of cells and compared with the experimental data recorded by using the same  $\beta$ -AS protocol with the same ISO dose. Fig. 3.4 presents  $\Delta\text{APD}$ , calculated by subtracting the mean APD value at baseline (prior to ISO application) to the APD time series measured following  $\beta$ -AS, for both simulated and experimental data from single ventricular myocytes. It can be noted from the figure that large cell-to-cell variability exists in the time lag of measured APD responses, with the transition times required to reach steady-state following ISO application varying by several minutes. This cell-to-cell heterogeneity in the APD response to constant  $\beta$ -AS serves as a basis to explain the cell-to-cell differences in the data presented in Fig. 3.3 (left column), corresponding to phasic

$\beta$ -AS at a  $1 \mu\text{M}$  ISO dose, which includes APD oscillations overlapped with the decrease in APD. Of note, the simulated time lags in the virtual population of cells are representative of the values measured experimentally in ventricular cardiomyocytes.

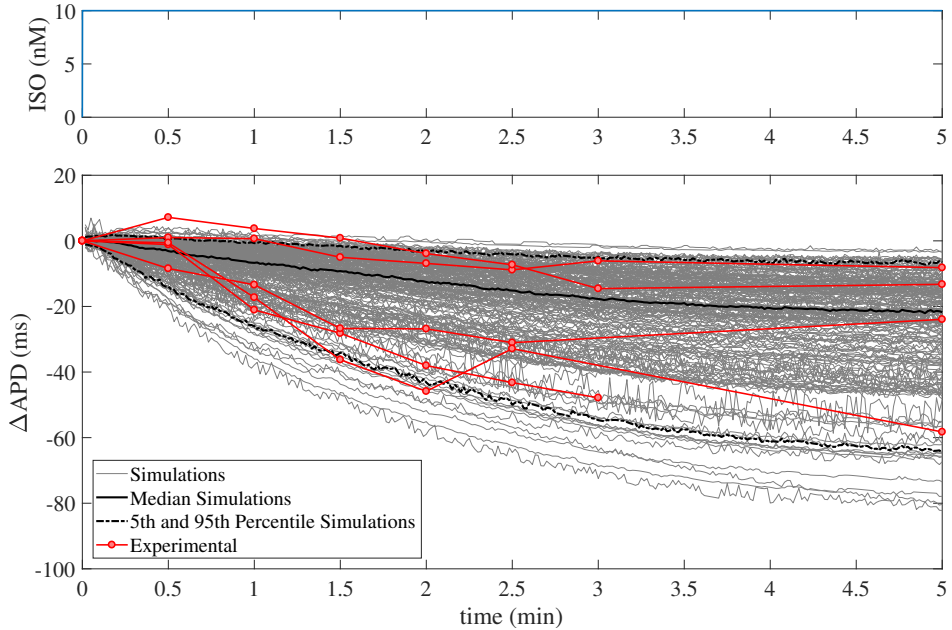


Figure 3.4: Top panel: ISO dose in nM, where time zero indicates the time when the solution containing ISO arrived to the cells and analogously for simulations. Bottom panel: Change in APD with respect to baseline following application of a constant 10 nM ISO dose in experiments ( $n=5$ , red) and simulations (grey) on single ventricular myocytes.

### 3.3.4 Reduction in Time Lapse for LF Oscillations of APD by Prior Low-Level $\beta$ -AS

The possibility that prior stimulation of  $\beta$ -adrenoceptors could reduce the time required for APD to develop LF oscillations in response to enhanced sympathetic activity was next explored. Fig. 3.5 presents results of the time lapse for oscillations development in response to phasic  $1 \mu\text{M}$  ISO application for eight different cases with prior  $\beta$ -AS corresponding to ISO levels varying from 0 to  $0.07 \mu\text{M}$  in  $0.01 \mu\text{M}$ -steps, with each of these pre-stimulation periods applied for 500 beats at 1 Hz pacing frequency. From this figure, it is clear that the time lapse was remarkably reduced as a function of the pre-stimulation level. For a prior stimulation with an ISO dose of  $0.05 \mu\text{M}$ , ie. 50 nM, most virtual cells developed LF oscillations in APD practically in an instantaneous way after applying the maximal ISO dose of  $1 \mu\text{M}$ . There are still some cells for which the time lapse is above three minutes even if  $\beta$ -adrenoceptors were previously stimulated.

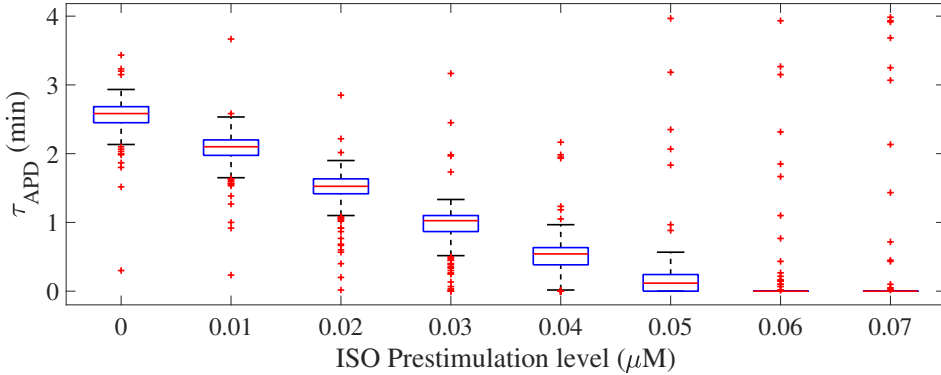


Figure 3.5: Time lapse for LF oscillations of APD to develop in response to phasic  $\beta$ -AS with  $1 \mu\text{M}$  ISO dose as a function of prior phasic  $\beta$ -AS with lower ISO doses varying from 0 to  $0.07 \mu\text{M}$ .

### 3.3.5 Ionic Mechanisms Underlying Time Lapse in LF Oscillations of APD

To ascertain the ionic mechanisms underlying the time required for APD to develop LF oscillations following phasic  $\beta$ -AS, the effect of phosphorylation and dephosphorylation kinetics of all cellular PKA substrates was investigated. Fig. 3.6, left panel, presents the phosphorylation levels of all these substrates in response to 5-minute  $\beta$ -AS. As can be observed from the figure, the substrates presenting slower phosphorylation responses are the slow delayed rectifier channels, associated with the  $I_{K_s}$  current, and ryanodine receptors, RyR.

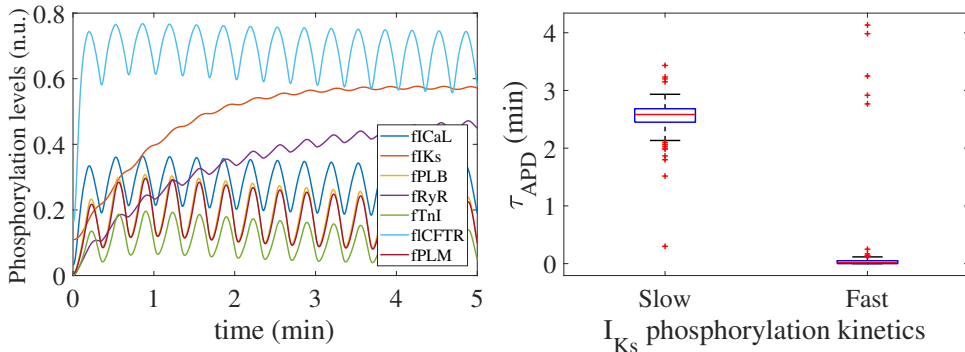


Figure 3.6: Left panel: Phosphorylation levels calculated as described in section 3.2.3. Right panel: Time lapse for LF oscillations of APD to develop in response to phasic  $\beta$ -AS when using PKA models with slow (left, [36]) and fast (right, [35])  $I_{K_s}$  phosphorylation and dephosphorylation kinetics.



To assess the extent to which variations in the phosphorylation and dephosphorylation kinetics of  $I_{K_s}$  influenced the time for development of APD oscillations, simulations were run where the  $I_{K_s}$  phosphorylation and dephosphorylation rate constants were increased to the values described in [35] from which an update was presented in a subsequent study by [36] to more reliably recapitulate PKA-dependent regulation of  $I_{K_s}$ . Specifically, the  $I_{K_s}$  phosphorylation rate constant was changed from 8.52 to 84  $\text{s}^{-1}$  and the  $I_{K_s}$  dephosphorylation rate constant was changed from 0.19 to 1.87  $\text{s}^{-1}$ . According to the results presented in Fig. 3.6, right panel, it is clear that the time lapse for APD oscillations was very notably reduced after increasing those rate constants, thus indicating the dependence of the APD oscillatory time lapse on  $I_{K_s}$  phosphorylation kinetics. On the other hand, variations in the phosphorylation kinetics of RyR had no impact on the time lapse for APD oscillations to develop, even if these were varied by a factor of up to ten times their nominal values.

Based on the above results, and considering that cell-to-cell differences in the population of models correspond to different ionic current conductance contributions, it was hypothesized that inter-individual differences in the time lapse for APD oscillation development was based on their differential  $I_{K_s}$  contributions. Simulations were run where  $I_{K_s}$  was inhibited at different levels and a monotonic decrease in oscillation time lapse could be quantified for increasingly larger inhibitions, as illustrated in Fig. 3.7. For full  $I_{K_s}$  blockade, APD oscillations became apparent almost immediately.

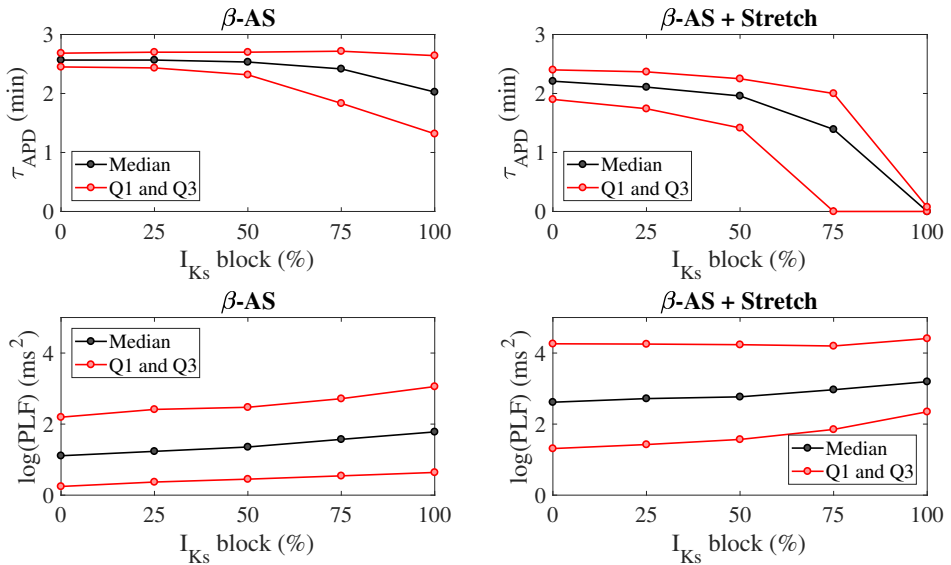


Figure 3.7:  $\tau_{APD}$  (top panels) and  $\log(\text{PLF})$  (bottom panels), presented in terms of median, first quartile (Q1) and third quartile (Q3), for increasingly higher degrees of  $I_{K_s}$  inhibition, both in response to phasic  $\beta$ -AS (ISO 1  $\mu\text{M}$ , left panels) and combined with phasic mechanical stretch (10%, right panels) for the population of virtual cells under healthy conditions.

### 3.3.6 Relationship between Time Lapse and Magnitude of LF Oscillations of APD

To assess the relationship between the time lapse for development of LF oscillations in APD and the magnitude of such oscillations, a set of models was built in such a way that they all share the same characteristics of the ORd-Xie coupled electrophysiology- $\beta$ -A signaling model, except for  $I_{Ks}$  phosphorylation and dephosphorylation rate constants, which were varied from model to model so that they covered from the slowest dynamics reported in [36] to the fastest dynamics reported in [35]. Fig 3.8, left panel, shows the relation between the magnitude of LF oscillations in APD, quantified by the LF power in the 0.04-0.15 Hz band denoted by PLF, and the time lapse for oscillation development, quantified by  $\tau_{APD}$ . It can be observed from the figure that the models with the fastest  $I_{Ks}$  phosphorylation dynamics are those presenting the shortest time lapse and the highest APD oscillatory magnitude.

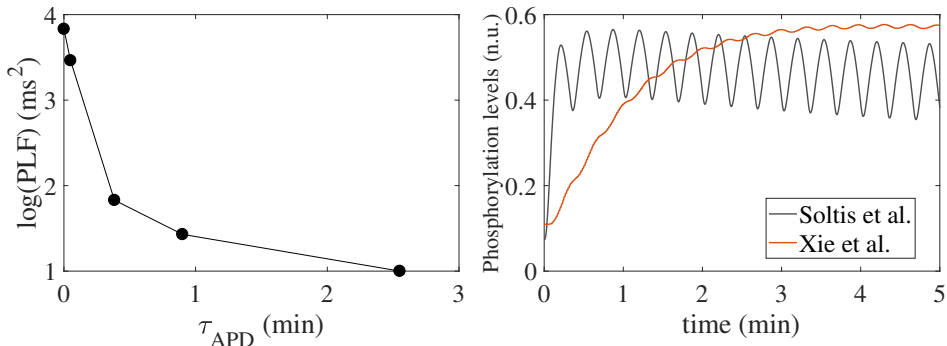


Figure 3.8: Left panel:  $\log(\text{PLF})$  vs.  $\tau_{APD}$  for varying  $I_{Ks}$  phosphorylation and dephosphorylation rate constants ranging from the values in [35] to the values in [36]. Right panel:  $I_{Ks}$  phosphorylation levels for the models with  $I_{Ks}$  phosphorylation and dephosphorylation rate constants as in [35] (gray line) and as in [36] (red line).

To substantiate this result, Fig. 3.8, right panel, shows  $I_{Ks}$  phosphorylation levels calculated according to the signaling models in [36] and [35], corresponding to the two most extreme points shown in Fig. 3.8, left panel. It can be observed from the graphic that, for the model in [35], not only are the  $I_{Ks}$  phosphorylation dynamics faster but also the associated oscillations are of larger magnitude. These enhanced oscillations in  $I_{Ks}$  phosphorylation have an impact on the AP, which is manifested by a larger oscillatory magnitude of APD.

In the whole population of virtual cells, where all cells present the same phosphorylation kinetics but the conductance of  $I_{Ks}$  varies from one cell to another, consequently modulating the influence of  $I_{Ks}$  phosphorylation fluctuations on APD oscillatory behavior, the inverse relationship between PLF and  $\tau_{APD}$  can still be appreciated. This is shown in Fig. 3.11, which presents PLF vs  $\tau_{APD}$  for cells under healthy conditions divided into two groups depending on the presence/absence of pro-arrhythmic

effects when disease conditions were simulated, as described in the next section.

### 3.3.7 Effect of Disease Conditions in Time Lapse of LF Oscillations of APD and Relation to Arrhythmogenesis

Simulation of disease conditions by  $\text{Ca}^{2+}$  overload and RRR in the population of models led to a sharp decrease in the APD oscillatory time lapse following increased sympathetic activity. This is illustrated in Fig. 3.9, left panel, which shows zero-mean APD time series (after subtraction of the corresponding baseline value to facilitate comparison) for one of the cells in the virtual population under healthy and pathological conditions. The value of  $\tau_{\text{APD}}$  decreased from 130 ms to 0 ms due to the effects of disease. Fig. 3.9, right panel, summarizes the observed changes in  $\tau_{\text{APD}}$  when simulating disease conditions in the subpopulation of cells that did not present pro-arrhythmic events. Whereas  $\text{Ca}^{2+}$  overload had mild effects on  $\tau_{\text{APD}}$ , the effects of RRR, individually or in the presence of  $\text{Ca}^{2+}$  overload, contributed to a very remarkable reduction in the oscillatory time lapse.

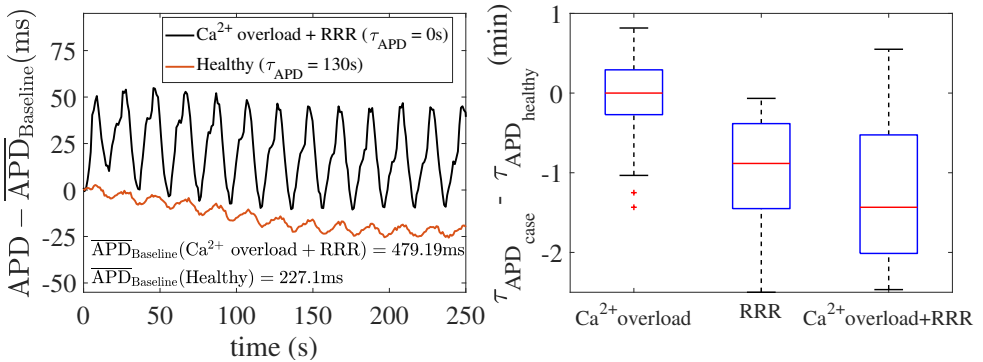


Figure 3.9: Left panel: Zero-mean APD series ( $\text{APD} - \overline{\text{APD}}_{\text{Baseline}}$ ) in response to SP, for healthy (red line) and disease (black line) conditions simulated for a virtual cell of the population. Right panel: Differences in  $\tau_{\text{APD}}$  due to  $\text{Ca}^{2+}$  overload and/or RRR with respect to healthy conditions.

When disease conditions were simulated as accompanied by an increase in the conductance of non-specific cationic SACs in accordance with experimental evidences [82, 125], arrhythmogenic events were generated in some of the virtual cells of the population following SP. These were in the form of afterdepolarizations and spontaneous beats and occurred in 46.34% of the virtual cells that did not show any pro-arrhythmic manifestation at baseline. Examples are illustrated in Fig. 3.10. To assess whether individual cell oscillatory characteristics evaluated under healthy conditions were related to pro-arrhythmicity, the time lapse, quantified by  $\tau_{\text{APD}}$ , and the magnitude of APD oscillations, quantified by PLF, were compared between the groups of cells presenting and not presenting arrhythmogenic events. Results are presented in Fig. 3.11, left and

middle panels. As can be observed from the figure, little differences in the mean or median  $\tau_{APD}$  were found between the two groups. On the other hand, larger differences in PLF were seen between the groups, with the one presenting arrhythmogenic events in response to increased sympathetic activity being associated with remarkably larger mean and median PLF (note that the logarithm of PLF is represented in Fig. 3.11). Boxplots of  $\tau_{APD}$  and  $\log(\text{PLF})$  for the groups of cells presenting and not presenting arrhythmogenic events are shown in Fig. 3.12.

The relationship between PLF and  $\tau_{APD}$  in the population of cells prior to introducing disease conditions is presented in Fig. 3.11, right panel, for the pro-arrhythmic and non-pro-arrhythmic groups. In both groups, larger values of PLF were associated with shorter values of  $\tau_{APD}$ , although high inter-individual variability could be noticed. The Spearman correlation coefficient was  $\rho = -0.82$  in the pro-arrhythmic group and  $\rho = -0.57$  in the non-pro-arrhythmic group.

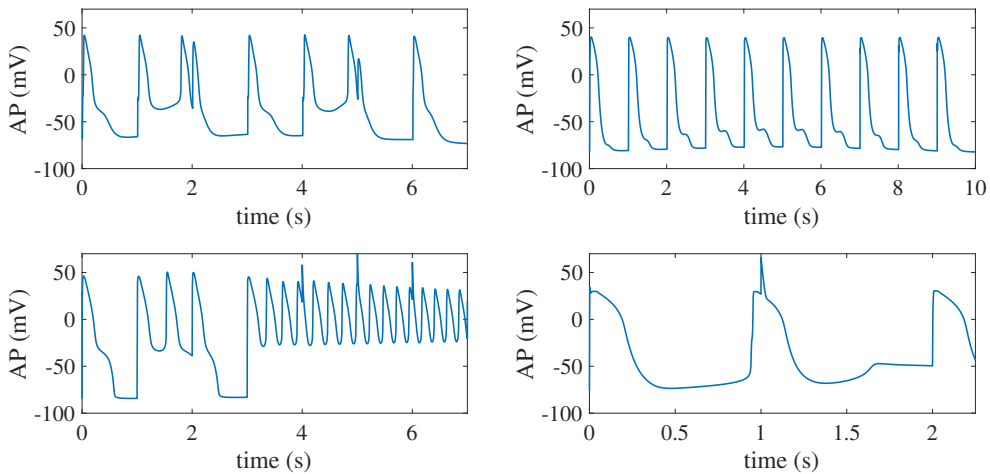


Figure 3.10: Pro-arrhythmic events in virtual cells in response to increased sympathetic activity under diseased conditions simulated by  $\text{Ca}^{2+}$  overload, reduced repolarization reserve and increased  $G_{SAC}$ . Phase 2 and phase 3 early afterdepolarizations (EADs) (top panels), EAD bursts (bottom left panel) and spontaneous beats (bottom right panel) could be observed.

## 3.4 Discussion

### 3.4.1 Inter-Individual Differences in the Time Lapse for Development of LF Oscillations of APD Following Enhanced Sympathetic Activity

The research presented in this chapter has shown that LF oscillations of human ventricular repolarization, reported in the T-wave of the ECG and locally in ARIs of

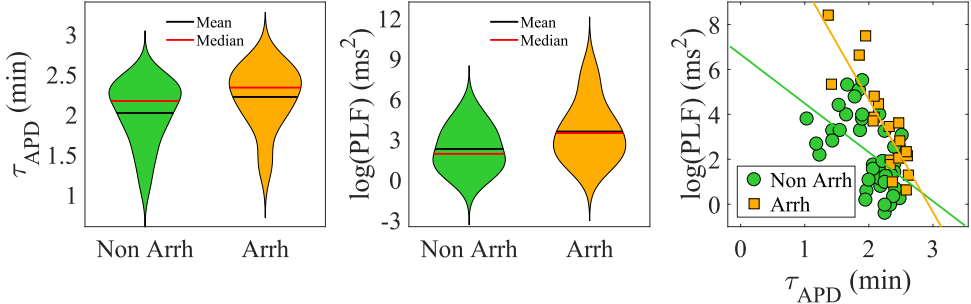


Figure 3.11: Left and middle panels: Violin representations of  $\tau_{APD}$  and  $\log(PLF)$ , respectively, calculated under healthy conditions for subpopulations of cells presenting and not presenting pro-arrhythmic events when disease conditions were simulated while pacing at CLs of 1000, 2000 and 2500 ms. Right panel:  $\tau_{APD}$  vs.  $\log(PLF)$  for the same two subpopulations. The slopes of the regression lines for the subpopulations presenting (orange) and not presenting (green) pro-arrhythmic events were statistically significantly different by univariate analysis of variance (p-value < 0.05).

unipolar epicardial EGMs, do not develop immediately upon a sympathetic rise but take some time to become apparent. An algorithm has been proposed to robustly quantify the time lapse required for APD to develop sympathetically-mediated LF oscillations. This time lapse has been shown to be highly variable from one cell to another, ranging from just a few seconds to more than three minutes depending on the ionic characteristics of each individual cell. Following enhanced sympathetic activity, the APD shows a trend of shortening, or brief prolongation followed by more sustained shortening, which masks overlapping oscillations. Only when such APD shortening has been completed, APD oscillations become manifest.

The range of time lags for APD oscillatory behavior following SP is of the order of adaptation lags reported for the QT interval of the ECG in response to increases in sympathetic activity leading to abrupt heart rate increases, either measured from ambulatory Holter recordings [126] or following tilt test [127, 128]. Those repolarization dynamics have also been recently investigated in experimental studies using fully innervated Langendorff-perfused mouse and rabbit hearts, where the APD response to bilateral sympathetic nerve stimulation has been described [129]. In those studies ventricular repolarization was modulated both by direct sympathetic action on the ventricular myocardium as well as indirectly by heart rate-related effects. In the present study, CL was kept constant and the ventricular response was thus only assessed as due to sympathetic effects on the ventricle, as in *in vivo* EGM recordings from patients where LF oscillations of ARI have been characterized while controlling CL with right ventricular pacing [20, 51].

The prolonged time lags for LF oscillatory behavior of APD following enhanced sympathetic activity quantified in this work can help to explain why oscillations seem to appear and disappear, as observed in *in vivo* studies [20], where APD oscillatory

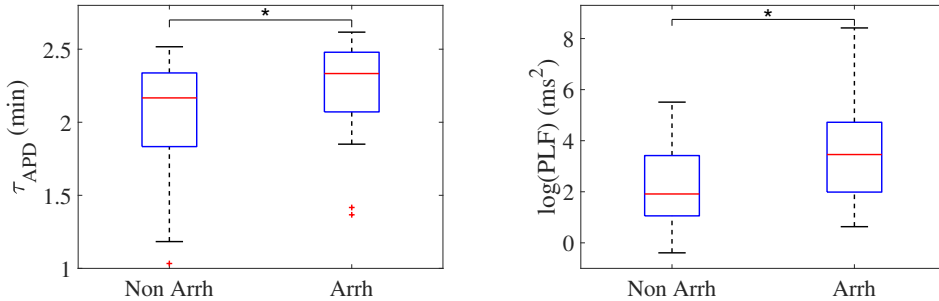


Figure 3.12: Boxplot of  $\tau_{APD}$  (left panel) and  $\log(\text{PLF})$  (right panel) calculated under healthy conditions for subpopulations of cells presenting and not presenting pro-arrhythmic events when disease conditions were simulated while pacing at CLs of 1000, 2000 and 2500 ms. Statistically significant differences by Wilcoxon rank-sum test (p-value < 0.05) are denoted by \*, while non-significant differences are denoted by *n.s.* See comment on statistical comparisons of simulated data in the main manuscript.

behavior could only be measured at certain time intervals of the analyzed recordings. Those time intervals could be speculated to be associated with sustained sympathetic activation so that enough time was allowed for LF oscillations in APD to develop.

In this work SP was simulated by concomitant phasic changes in  $\beta$ -AS and mechanical stretch. The involvement of each of these two components in the protracted LF oscillatory response to a sympathetic rise has been assessed. Results have determined that mechanical stretch induces LF oscillations of APD in an almost instantaneous manner, whereas  $\beta$ -AS entails much longer APD time courses until LF oscillations can be clearly appreciated. Based on the fact that the time lapse is mainly due to the slow response to  $\beta$ -AS, this work has next validated the calculated time lapses against *in vitro* data from ventricular myocytes following sudden exposure to ISO. Both in the experiments and the simulations of this work, the time required for APD to reach steady-state following sudden  $\beta$ -AS was found to highly vary from cell to cell. Simulated time lapses were comprised within the experimental limits quantified for the ventricular myocytes of this and other studies [120, 121], thus confirming validation of the population of models to reproduce available evidences on the APD time course in response to  $\beta$ -AS.

To further support the conclusions on the key role of  $\beta$ -AS in determining the time lapse for LF oscillations of APD to develop, the effects of pre-stimulating ventricular cells with a lower dose of the  $\beta$ -A agonist ISO have been tested. Results have confirmed that the oscillatory time lapse is highly dependent on  $\beta$ -adrenoceptors' state. The higher the prior stimulation level of  $\beta$ -adrenoceptors, the shorter the time for development of LF oscillations. This reduction in the oscillatory time lapse by prior ISO exposure agrees with common knowledge on pre-stimulation of  $\beta$ -adrenoceptors altering the impact of  $\beta$ -AS. Under conditions associated with high sympathetic tone, as in failing or aged ventricles, sympathetic surge would thus be expected to induce LF oscillations of repolarization with shorter latency. Consequently, due to the less

stringent requirements on the time period of sustained sympathetic activation for LF oscillatory behavior to ensue in failing or aged ventricles, this is anticipated to facilitate the occurrence of such oscillations, with the corresponding potentially adverse consequences, as described in Chapter 2 and [33, 48, 50].

### 3.4.2 Major Role of $I_{K_s}$ Phosphorylation Kinetics in Determining the Time Lapse for LF Oscillations of APD

The mechanisms underlying the slow appearance of APD oscillations following SP, particularly related to the protracted response to  $\beta$ -AS, have been ascertained in this work by comparing the phosphorylated levels of all cellular substrates accounted for in the modified  $\beta$ -A signaling model by [36] used as a basis for this study. Two cellular substrates, namely  $I_{K_s}$  and RyR, have been shown to present responses to  $\beta$ -AS being remarkably slower than those of all other substrates. The time required for  $I_{K_s}$  and RyR phosphorylation levels to reach steady-state upon  $\beta$ -AS is around three minutes, this being close to the maximum time lapse for APD oscillations to appear in simulated population of models, while the phosphorylation levels of the remaining cellular substrates reach steady-state in no more than 20-30 seconds. In other  $\beta$ -A signaling models, as in the model by [79],  $I_{K_s}$  and RyR present slow kinetics too, although there are other substrates, like the  $\text{Na}^+$ - $\text{K}^+$ -ATPase current, with even slower kinetics.

The impact of the slow  $I_{K_s}$  and RyR phosphorylation kinetics on the APD time course following sympathetic stimulation has been assessed by varying their phosphorylation and dephosphorylation rate constants. Whereas variations in the kinetics of  $I_{K_s}$  are proved to have relevant effects on the time lapse for APD oscillations, the influence of variations in the RyR kinetics is negligible. The irrelevant role of RyR phosphorylation on  $\tau_{\text{APD}}$  as compared to that of  $I_{K_s}$  phosphorylation can be explained on the basis of their very distinct impact on APD. RyR phosphorylation has been described in this work according to the formulation proposed in [79], where it has been shown that disabling RyR phosphorylation leads to little variations in APD with respect to measurements when all substrates are phosphorylated. On the other hand,  $I_{K_s}$  phosphorylation has much more prominent effects on APD [36]. To further support the role of  $I_{K_s}$  in determining the APD oscillatory latency, this current has been inhibited to various extents and it has been confirmed that the larger the  $I_{K_s}$  current amplitude, the longer the latency. These results lead us to conclude that the high inter-individual variability in the time lapse for APD oscillations characterized in the population of models can be explained by differential  $I_{K_s}$  contributions from one cell to another.

The important role of  $I_{K_s}$  during  $\beta$ -AS has been pointed out in numerous studies [62, 63, 66, 130, 131]. Reduced  $I_{K_s}$  responsiveness to  $\beta$ -AS has been suggested to increase arrhythmia susceptibility in a heart failure animal model [62]. In ventricular myocytes, loss of  $I_{K_s}$  current has been experimentally shown to exaggerate beat-to-

beat APD variability in response to  $\beta$ -AS [63, 66] and computationally proved to facilitate the generation of pro-arrhythmic early afterdepolarizations [131]. Results provide additional support to the role of  $I_{K_s}$  during  $\beta$ -AS, as reduced  $I_{K_s}$  shortens the oscillatory latency and thus facilitates the occurrence of LF oscillations of APD. This oscillatory behavior of ventricular repolarization can be seen as a particular form of beat-to-beat variability restricted to frequencies in the Mayer wave frequency range (0.03-15 Hz).

### 3.4.3 Increased Arrhythmic Risk as a Function of the Time Lapse and Magnitude of LF Oscillations of APD

RRR, individually or combined with  $\text{Ca}^{2+}$  overload, has been found to dramatically reduce the time lapse for sympathetically-induced oscillatory behavior. This can be understood on the basis that under RRR the amount of  $I_{K_s}$  current is reduced and, provided phosphorylation kinetics are not varied, this leads to a reduction in the oscillation time lag of the APD. Since the above holds for each of the virtual cells in the population built in this work, the time lapse values measured under pathological conditions are lower than the ones corresponding to non-pathological conditions.

A comparison for time lapses calculated for cells under healthy conditions has been established while considering two groups of interest, one composed of cells presenting and the other one not presenting arrhythmogenic events after simulation of disease conditions. Results have been shown to be comparable. However, in both the pro-arrhythmic and non-pro-arrhythmic groups, there is an inverse relationship between the magnitude of LF oscillations of APD, measured by PLF, and the time required for such oscillations to develop. These findings indicate that cells in which APD oscillations appear rapidly in response to enhanced sympathetic activity are associated with larger oscillatory magnitudes. Although the inverse relationship between PLF and the oscillatory time lapse holds true for both groups, such a relationship is steeper in the pro-arrhythmic group, with given low time lapse values associated with larger oscillatory magnitudes. Those enhanced magnitudes may facilitate the occurrence of arrhythmic events that can act as triggers for arrhythmias and at the same time they may contribute to a more vulnerable substrate by increasing spatial repolarization inhomogeneities between regions being at different oscillating phases. This increased arrhythmia susceptibility associated with elevated LF oscillations of repolarization has been postulated by *in silico* studies, such as [33] and Chapter 2, and confirmed by *in vivo* research on a CAVB dog model [119] as well as clinical studies in post-infarction patients [50]. These results are in line with studies associating higher levels of temporal repolarization variability, in the form of alternans or in other forms, with increased arrhythmic risk [132, 133].

The role of  $I_{K_s}$  expression and phosphorylation dynamics in pro-arrhythmia that has been uncovered in the present work is in line with previous studies investigating ventricular repolarization response to  $\beta$ -AS. The slow  $I_{K_s}$  phosphorylation kinetics as



compared to the fast  $I_{Ca}$  kinetics have been reported to be behind the generation of transient arrhythmogenic early afterdepolarizations [36, 121] and APD alternans [134] upon sudden ISO application. In this work, the fact of simulating a whole population of cells allows to additionally reveal the importance of  $I_{Ks}$  conductance in determining  $\tau_{APD}$ , as  $I_{Ks}$  conductance modulates the relevance of  $I_{Ks}$  dynamics on APD time course during  $\beta$ -AS. Additionally, differential  $I_{Ks}$  and  $I_{Ca}$  activation kinetics in response to sudden  $\beta$ -AS have been shown to promote the transition from ventricular tachycardia to ventricular fibrillation by transiently steepening APD restitution in simulated ventricular tissues [135]. This same ionic mismatch has been suggested as a plausible mechanism underlying a transitory increase in the risk for arrhythmias by application of sudden adrenergic stress in isolated innervated rabbit hearts treated with a potassium channel blocker and subjected to sustained parasympathetic stimulation [136].

### 3.4.4 Limitations and Future Work

In the work presented in this chapter, simulations have been run to quantify the time lapse for development of sympathetically-mediated LF oscillations of APD in a large population of human ventricular AP models developed based on available experimental data. After confirming the role of  $\beta$ -AS, over the role of mechanical stretch, in determining such oscillatory time lapse, these simulated results were compared with available *in vitro* data from isolated canine ventricular myocytes in response to sudden administration of a  $\beta$ -A agonist. Despite differences between species, experimental studies have shown that ventricular repolarization characteristics of canine cardiomyocytes closely resemble those of human cardiomyocytes [137, 138]. If additional *in vitro* and/or *in vivo* data became available to analyze the time required for ARI or APD oscillations to become manifest following SP, further validation of the results obtained in the present work could be performed.

The simulated results presented in this chapter correspond to single cells. As a continuation of this investigation, tissue models built on the basis of the present population of AP models could be used to assess whether other tissue-specific factors could play a relevant role in the time required for APD oscillations to develop, in the magnitude of such oscillations as well as in the associated consequences in terms of pro-arrhythmic risk.

The population of human ventricular computational models built in this work used the [5] model as a basis to describe human ventricular electrophysiology and calcium dynamics, whereas mechanics were described by a modified version of the [14] model. For  $\beta$ -A signaling, the [36] model was used as a basis and the [35] model was used for additional comparisons. These selections might have an impact on the conclusions reached in this study, particularly regarding quantitative values for the time required for LF oscillations of APD to develop. Nevertheless, in [33], different human and animal cell models were tested for APD oscillatory behavior, confirming model-

independence in qualitative terms with only some quantitative differences between different electrophysiological models, particularly for different species. Future studies could address the investigations conducted in this work while using other cellular models as a basis for construction of a population of models representative of human or animal ventricular electrophysiological characteristics reported experimentally and compare with the results of this study.

The developed population of human ventricular AP models was deterministic. Future work could include incorporation of stochasticity into the main ionic currents active during AP repolarization. This would allow accounting for beat-to-beat repolarization variability, which might have an effect in the time course for development of LF oscillations of APD.

An ISO dose of  $0 \mu\text{M}$  was used to represent  $\beta$ -AS under baseline conditions. Although results are anticipated to be very similar to those obtained for a low ISO dose slightly above 0, somewhat different time lapse values for APD oscillations might be quantified.

### 3.5 Conclusions

Human ventricular repolarization presents low-frequency oscillations that develop following enhanced sympathetic activity at time lapses varying from a few seconds to more than three minutes depending on individual cells characteristics. The latency in the oscillatory development is due to the slow ventricular response to  $\beta$ -AS and, specifically, it is associated with the slow phosphorylation kinetics of the  $I_{K_s}$  current. Prior stimulation of  $\beta$ -adrenoceptors reduces the time required for the development of repolarization oscillations. Short time lapses are associated with large APD oscillatory magnitudes, particularly in cells susceptible to develop arrhythmogenic events in response to sympathetic stimulation.

# 4 | Data-Driven Identification of Stochastic AP Models for characterization of Spatio-Temporal Human Ventricular Repolarization Variability

---

4.1	Introduction . . . . .	80
4.2	Materials and Methods . . . . .	82
4.2.1	Human Ventricular Stochastic AP Models . . . . .	82
4.2.2	State-Space Formulation . . . . .	85
4.2.3	Augmented State-Space . . . . .	86
4.2.4	UKF-based Joint State and Parameter Estimation . . . . .	87
4.2.5	Synthetic Data . . . . .	88
4.2.6	Experimental Data . . . . .	90
4.2.7	Methodology Assessment . . . . .	90
4.3	Results . . . . .	92
4.3.1	Noisy AP Filtering . . . . .	92
4.3.2	Sensitivity of the Methodology with respect to its own Parameters	93
4.3.3	Estimation of Model Parameters and Hidden States . . . . .	94
4.3.4	Estimation of AP Markers . . . . .	95
4.3.5	Application onto Experimental Data . . . . .	97
4.4	Discussion . . . . .	100

---

4.4.1	Methodology Calibration . . . . .	100
4.4.2	Filtering Noisy Data . . . . .	100
4.4.3	Identification of Model Parameters and Hidden States . . . . .	101
4.4.4	Application onto Data from Different Origins . . . . .	102
4.4.5	Robustness Analysis . . . . .	103
4.4.6	Limitations and Future Works . . . . .	103
4.5	Conclusions . . . . .	104

---

## 4.1 Introduction

As mentioned in Chapter 2 and Chapter 3, beat-to-beat and cell-to-cell variability in ventricular electrophysiology has been well documented, this being an important contributor to cardiac electrical function [57, 66, 139–141]. Enhanced levels of spatio-temporal variability in ventricular repolarization have shown value to assess cardiotoxic drug effects and to identify individuals at high arrhythmic risk [42, 142–144], among others.

Temporal (beat-to-beat) variability in cellular ventricular electrophysiology has been associated with randomness in ion channel gating and variations in intracellular calcium handling [53–56, 65, 145, 146]. On the other hand, spatial (cell-to-cell) variability has been suggested to be at least partly mediated by differential ionic contributions to the electrophysiology of individual cells [56, 64, 145, 147]. In this regard, the effect of variations in ion channel numbers to differences across cells has been well established, while that of variations in other characteristics related to ionic activation or inactivation is less clear [148, 149]. Computational modeling and simulation has greatly helped to shed light on the mechanisms underlying cardiac electrophysiological variability and its ability to predict arrhythmic risk in different settings [56, 145, 148]. Specifically, computational approaches have been developed to investigate experimentally observed cell-to-cell electrophysiological differences [56, 150–153] and/or beat-to-beat AP variations, the latter after including stochasticity in modeled ionic currents [55–57, 65, 153]. Despite these advances, there is still limited understanding of the causes and consequences of ventricular repolarization variability, particularly in humans, where the less availability of data has hampered its research.

The most commonly available experimental measurement in ventricular cells is transmembrane potential. Identification of individual characteristics of underlying AP models, including estimation of model parameters and state variables, from available voltage measurements would allow characterization of temporal and spatial variability without the need of performing additional unaffordable experiments, which would at

most provide partial descriptions of some model parameters/variables. In the present chapter, similarly to other modeling works [115, 154], the estimated model parameters are maximal ionic current conductances, whose variations have been established to have a major impact on both temporal and spatial variability. This estimation problem has been addressed in the literature by using a variety of methods, even if typically considering deterministic rather than stochastic cell models, thus only aiming at tackling cell-to-cell variability while not targeting representation of beat-to-beat variability, which is an important focus of the present work. As an example, approaches based on the construction of populations of models calibrated according to experimentally measured ranges [57, 152] or distributions [115, 149] of AP-derived markers or based on emulation [155] have been proposed. These approaches, among which the ones used in Chapter 2 and Chapter 3 are included, provide a set of model parameter estimates for a whole population of cells, but do not provide robust identification of model parameters for each cell individually. The method proposed in this chapter works on an individual cell basis and uses the whole transmembrane voltage recording, comprising several APs rather than a single AP from a unique beat, as an input for the estimation, which is expected to provide more accurate representations of experimental measurement distributions even if at higher computational cost. In ventricular electrophysiology research, and yet more notably in humans, available experimental data is scarce, thus making this individual cell-based identification a feasible approach. In [154, 156], a Markov Chain Monte Carlo (MCMC) method was proposed to estimate the ionic conductances of AP models directly from voltage traces as well. The methodology presented in this chapter, which departs from the hypothesis that model parameter and variable estimation can benefit from taking into account beat-to-beat variations in voltage signals, involves lower computational complexity than the one in [154, 156] and additionally provides an estimation of hidden states together with model parameters. Other approaches using optimization methods like Genetic Algorithms [157] or Moment Matching [115] have also been considered for estimation of model parameters, but not state variables, from transmembrane voltage measurements. Importantly, none of the above cited schemes deals with stochastic models to account for beat-to-beat AP variability, as does the methodology proposed in this chapter. In the case of the optimization-based methods, the sequential nature of the AP data is sometimes not even considered but all samples are pooled together when solving the optimization problem [157]. Furthermore, these optimization-based methods do not always offer uncertainty measurements for the estimations, as can be obtained with the proposed methodology or with the method proposed in [154, 156]. As a conclusion, this work is, to the best of our knowledge, the first one providing individual cell-based identification of cardiac model parameters and variables while accounting for temporal AP variability.

The methodology here proposed is based on formulating the identification problem by means of a nonlinear state-space representation [158] and using the Unscented Kalman Filter (UKF) [159] to infer the parameters and non-measured dynamic state variables of an underlying human ventricular AP model. In this work a stochastic version of the ORd AP model [5] was developed and used as a basis for the state-space

representations. The employed UKF filter, framed within the family of Sigma-Point filters [160], offers a probabilistic inference method to estimate the hidden variables of a non-linear system in a consistent and online manner. This constitutes a very powerful tool to reproduce both steady-state and dynamic characteristics of individual cells. Performance evaluation of the proposed methodology is carried out using sets of synthetic data generated from human ventricular AP models contaminated with different levels of noise. The methodology is subsequently tested on experimentally measured voltage traces. Preliminary results of a more simple methodology developed based on a human ventricular phenomenological AP model were presented as a conference contribution [161].

## 4.2 Materials and Methods

In this chapter, lowercase normal letters were used to denote scalar quantities, lowercase boldface letters to denote column vectors and uppercase boldface letters to denote matrices. Those quantities that are time-varying are written as  $x(t)$  for continuous time and  $x(k)$  for discrete time. The notation  $T$  denotes matrix and vector transpose.

### 4.2.1 Human Ventricular Stochastic AP Models

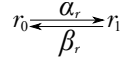
Stochastic AP models were built based on the ORd human ventricular epicardial model [5]. The ordinary differential equations representing ion channel gating were converted into reflected stochastic differential equations, following the approach presented in [26, 57]. This allowed physiologically realistic representation of stochastic ionic gating fluctuations contributing to beat-to-beat AP variability. Let vector  $\mathbf{s}(t)$  denote the proportion of ion channels of species “s” in each state of the corresponding Markov formulation for time  $t$ . The temporal evolution of  $\mathbf{s}(t)$  was simulated according to:

$$d\mathbf{s}(t) = \mathbf{A} \mathbf{s}(t) dt + \frac{1}{\sqrt{N_s}} \mathbf{E} \mathbf{D}(\mathbf{s}(t)) d\mathbf{w} + \mathbf{k}(t). \quad (4.1)$$

In the above equation, the first term represents the standard deterministic model of ion channel dynamics, where matrix  $\mathbf{A}$  contains the transition rates. The second term accounts for the stochastic fluctuations due to intrinsic noise, which was formulated using Wiener increments [57, 162]. The magnitude of this second term is inversely proportional to the square root of the number of ion channels of species “s” in the cell denoted by  $N_s$ , following the derivation of [57, 162]. The third term,  $\mathbf{k}(t)$ , represents the projection that serves to ensure that  $\mathbf{s}(t)$  remains in the probability simplex [163], as described in [26].

Stochasticity was included in the ionic gating of four different currents, namely  $I_{Ks}$ ,  $I_{Kr}$ ,  $I_{to}$  and  $I_{CaL}$ , which are major currents active during AP repolarization

[57, 154, 164]. Following the derivations of [26, 57], matrices  $\mathbf{A}$ ,  $\mathbf{E}$  (stoichiometry) and  $\mathbf{D}$  (containing the rate of each transition as a function of  $\mathbf{s}$ ) in Eq. 4.1 for the stochastic ORd model were calculated as described in the following. For ionic currents defined by one ionic gate  $r$  in the ORd model, the possible channel states are open and closed. The vector  $\mathbf{s}$  of the proportions of channels in each state is  $\mathbf{s} = [r_1, r_0]^T$ :



where the transition rates  $\alpha_r$  and  $\beta_r$  are defined by:

$$\alpha_r = \frac{r_\infty}{\tau_r} \quad (4.2)$$

$$\beta_r = \frac{1}{\tau_r} - \alpha_r \quad (4.3)$$

with  $r_\infty$  and  $\tau_r$  defined as in the ORd model. Letting the proportion of channels in the open and closed states be denoted by  $r_1$  and  $r_0$ , respectively, the matrices  $\mathbf{D}$ ,  $\mathbf{E}$  and  $\mathbf{A}$  in the Markov formulation are as follows:

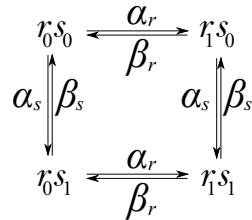
$$\mathbf{D} = \begin{bmatrix} \sqrt[2]{r_0} & \alpha_r + r_1 & \beta_r \end{bmatrix}$$

$$\mathbf{E} = \begin{bmatrix} 1 \\ -1 \end{bmatrix}$$

$$\mathbf{A} = \begin{bmatrix} -\beta_r & \alpha_r \\ \beta_r & -\alpha_r \end{bmatrix}$$

This scheme with only one ionic gate, and thus two different channel states, was used for each of the fast and slow  $I_{Kr}$  currents that are weighted averaged to obtain the  $I_{Kr}$  current.

For ionic currents defined by the product of two ionic gates  $r$  and  $s$  in the ORd model, there are four possible channel states. The vector of proportions of channels in those states is  $\mathbf{s} = [r_1 s_1, r_0 s_1, r_1 s_0, r_0 s_0]^T$ , with transition rates  $\alpha_r$ ,  $\beta_r$ ,  $\alpha_s$  and  $\beta_s$  defined analogously to those reported in the above paragraph:



Letting the proportion of channels in each of the four states be denoted by:

- $r_0s_0$ : proportion of channels in the state with the two gates  $r$  and  $s$  closed.
- $r_1s_0$ : proportion of channels in the state with the  $r$  gate open and the  $s$  gate closed.
- $r_0s_1$ : proportion of channels in the state with the  $r$  gate closed and the  $s$  gate open.
- $r_1s_1$ : proportion of channels in the state with the two gates  $r$  and  $s$  open.

the matrices  $\mathbf{D}$ ,  $\mathbf{E}$  and  $\mathbf{A}$  in the Markov formulation are as follows:

$$\mathbf{D} = \text{diag} \left( \begin{array}{c} \frac{\sqrt[2]{r_0s_1} \alpha_r + r_1s_1 \beta_r}{\sqrt[2]{r_0s_0} \alpha_r + r_1s_0 \beta_r} \\ \frac{\sqrt[2]{r_1s_0} \alpha_s + r_1s_1 \beta_s}{\sqrt[2]{r_0s_0} \alpha_s + r_0s_1 \beta_s} \end{array} \right)$$

$$\mathbf{E} = \begin{bmatrix} 1 & 0 & 1 & 0 \\ -1 & 0 & 0 & 1 \\ 0 & 1 & -1 & 0 \\ 0 & -1 & 0 & -1 \end{bmatrix}$$

$$\mathbf{A} = \begin{bmatrix} -(\beta_r + \beta_s) & \alpha_r & \alpha_s & 0 \\ \beta_r & -(\alpha_r + \beta_s) & 0 & \alpha_s \\ \beta_s & 0 & -(\alpha_s + \beta_r) & \alpha_r \\ 0 & \beta_s & \beta_r & -(\alpha_r + \alpha_s) \end{bmatrix}$$

This scheme with two ionic gates, and four channel states, was used for  $I_{Ks}$  and  $I_{to}$  currents. In particular, in the case of  $I_{to}$ , the total current was decomposed as a weighted average of four individual currents, each of which represented by the product of two ionic gates:  $a i_{\text{fast}}$ ,  $a i_{\text{slow}}$ ,  $a_{\text{CaMK}} i_{\text{CaMK,fast}}$  and  $a_{\text{CaMK}} i_{\text{CaMK,slow}}$ .

For  $I_{CaL}$ , ordinary differential equations representing gating variables were converted into stochastic differential equations following the subunit-based approach used in [56]. For a gating variable  $x_s$ , the evolution of the probability of this gate being open was calculated as:

$$dx_s(t) = \frac{x_{s\infty} - x_s}{\tau_s} dt + \frac{\sqrt{x_{s\infty} + (1 - 2x_{s\infty})x_s}}{\sqrt{\tau_s} N_s} dw. \quad (4.4)$$

The number of channels  $N_s$  of each ionic species “s” was computed as follows. For  $I_{Ks}$ ,  $I_{Kr}$  and  $I_{to}$ , experimentally measured unitary current values were available and were used to calculate  $N_s$  as the maximum conductance of ion channel “s” in the ORd model, denoted by  $G_s$ , divided by the unitary conductance of ion channel “s”, denoted by  $g_s$ . Values for  $g_s$  were taken from [56, 74, 75] and adjusted for temperature and/or extracellular potassium concentration following [76, 77]. For  $I_{CaL}$ , the number of channels was computed by dividing the maximum  $I_{CaL}$  current by the single-channel current  $i_{CaL}$  times the channel opening probability. Table 4.1 shows the values used in the computations for the default ORd model.



Table 4.1: Number of channels for  $I_{Ks}$ ,  $I_{Kr}$ ,  $I_{to}$  and  $I_{CaL}$ .

	$I_{Ks}$	$I_{Kr}$	$I_{to}$	$I_{CaL}$
$N_s$	169	3621	606	20121

## 4.2.2 State-Space Formulation

State-space representations were formulated to describe non-stationary stochastic processes with measured and hidden variables [158]. Specifically, the stochastic ORd model, described in section 4.2.1, but with unknown ionic current conductances, was casted into a non-linear discrete-time state-space model, following numerical integration with the Euler-Maruyama method. As an example, Eq. 4.1 for vector  $\mathbf{s}(t)$  was written in the form:

$$\begin{aligned} \mathbf{s}(k) &= \mathbf{s}(k-1) + \mathbf{A} \mathbf{s}(k-1) \Delta_t \\ &+ \frac{1}{\sqrt{N_s}} \mathbf{E} \mathbf{D}(\mathbf{s}(k-1)) d\mathbf{w} + \mathbf{k}(k-1) \end{aligned} \quad (4.5)$$

where  $k$  is a discrete index ( $k \in \mathbb{N}$ ),  $\Delta_t$  is the integration time step (constant in this work) and  $d\mathbf{w}$  is a vector of independent Wiener increments sampled from a Gaussian distribution with zero mean and variance equal to  $\Delta_t$ . The overall state-space representation was described by the following two equations:

$$\mathbf{x}(k) = f(\mathbf{x}(k-1), \mathbf{q}(k-1), \boldsymbol{\theta}) \quad (4.6)$$

$$y(k) = h(\mathbf{x}(k)) + r(k). \quad (4.7)$$

Equation 4.6, called the process or transition equation, collects the discretized set of differential equations that define the state variables of the stochastic ORd model, stacked in vector  $\mathbf{x}(k)$ , thus including the equations that model the temporal evolution of transmembrane voltage, intracellular ion concentrations and proportion of channels in each state for each ionic species. The non-linear function  $f(\cdot)$  in Eq. 4.6 has three input vectors, namely the vector  $\mathbf{x}(k)$  of model state variables, the vector  $\mathbf{q}(k)$  of non-additive process noises (related to the Wiener increments) described in 4.2.1 and the vector  $\boldsymbol{\theta}$  of model parameters. The components of vector  $\mathbf{q}(k)$  take values sampled from independent Gaussian distributions with zero mean and variance equal to  $\Delta_t$  for such components corresponding to the stochastic gating variables and zero for all other components.

The ORd model was parametrized with factors multiplying the conductances of the following ionic currents [115]: slow delayed rectifier potassium current,  $I_{Ks}$ ; rapid delayed rectifier potassium current,  $I_{Kr}$ ; transient outward potassium current,  $I_{to}$ ; L-type calcium current,  $I_{CaL}$ ; inward rectifier potassium current,  $I_{K1}$ ; and sodium current,  $I_{Na}$ . Hence, the vector  $\boldsymbol{\theta} = \{\theta_{Ks}, \theta_{Kr}, \theta_{to}, \theta_{CaL}, \theta_{K1}, \theta_{Na}\}$  of static model parameters, represents variations in the ionic conductances of  $I_{Ks}$ ,  $I_{Kr}$ ,  $I_{to}$ ,  $I_{CaL}$ ,  $I_{K1}$

and  $I_{Na}$  relative to the default values in the ORd model,  $I_j = I_{j,ORd} \theta_j$ . Note that the same factor  $\theta_j$  applies to the number of ion channels of each species (Table 4.1):  $N_j = N_{j,ORd} \theta_j$ , as the unitary conductance of each ionic species was assumed to be constant based on previously reported experimental findings [165]. The values of the parameters in  $\boldsymbol{\theta}$  were inferred for each input AP trace.

In Eq. 4.7, called the measurement equation,  $y(k)$  is the measured variable (transmembrane voltage), which is defined as  $y(k) = v(k) + r(k)$ , where  $v(k)$  represents the noiseless transmembrane potential and  $r(k)$  is additive white Gaussian noise. Hence, the function  $h(\cdot)$  in Eq. 4.7 is linear, as it takes only the component of  $\mathbf{x}(k)$  corresponding to the transmembrane voltage,  $v(k)$ .

### 4.2.3 Augmented State-Space

A *state augmentation* approach [158] was used to jointly estimate the parameters and state variables of the stochastic ORd model for a given input (synthetic or experimental) AP trace. Following the notation introduced in 4.2.2, the static parameters in vector  $\boldsymbol{\theta}$  were replaced with a new vector of time-varying variables  $\tilde{\boldsymbol{\theta}}(k)$  using a random walk model with drift:

$$\tilde{\boldsymbol{\theta}}(k) = \tilde{\boldsymbol{\theta}}(k-1) + \boldsymbol{\delta}(k) \quad (4.8)$$

where the components of the artificial noise  $\boldsymbol{\delta}(k)$  introduced in the definition of  $\tilde{\boldsymbol{\theta}}(k)$  dynamics are i.i.d. zero-mean Gaussian processes with very small variance. This artificial noise allows adapting the parameter values in an online manner while the input AP trace is being filtered and can be given an interpretation similar to the small constant step size in adaptive filtering theory [166]. In this work, this artificial noise had the same variance,  $\sigma_{\delta}^2$ , for all six individual parameters.

In addition to the augmentation due to the inclusion of the parameters as additional state variables, the noise process  $\mathbf{q}(k)$  was also incorporated as part of the augmented state space. This is a standard approach for estimation when dealing with non-additive noise processes (see e.g. [158, Chap. 5]). By stacking the vector  $\mathbf{x}(k)$  of model state variables, the new vector  $\tilde{\boldsymbol{\theta}}(k)$  of model parameters and the vector  $\mathbf{q}(k)$  of process noises, a new ‘‘augmented’’ state vector  $\mathbf{z}(k)$  was defined as:

$$\mathbf{z}(k) = [\mathbf{x}(k), \mathbf{q}(k), \tilde{\boldsymbol{\theta}}(k)]^T. \quad (4.9)$$

The resulting state-space model has the following formulation:

$$\mathbf{z}(k) = f_a(\mathbf{z}(k-1)) + \boldsymbol{\epsilon}(k) \quad (4.10)$$

$$y(k) = h_a(\mathbf{z}(k)) + r(k) \quad (4.11)$$

where  $f_a$  and  $h_a$  are the augmented versions of  $f$  and  $h$  from Eq. 4.6 and 4.7. The vector  $\boldsymbol{\epsilon}(k)$  contains two types of noises, those associated with the Wiener increments

of the stochastic model (accounted for by  $\mathbf{q}(k)$ ) and those associated with the new parameter vector  $\tilde{\boldsymbol{\theta}}(k)$  (accounted for by  $\boldsymbol{\delta}(k)$ ). The components in vector  $\boldsymbol{\epsilon}(k)$  corresponding to the original state variables  $\mathbf{x}(k)$  take a value of zero, while the rest of components are zero-mean Gaussian noises with variance equal to the integration time step,  $\Delta_t$ , for the components corresponding to  $\mathbf{q}(k)$  and variance equal to  $\sigma_\theta^2$  for the components corresponding to  $\tilde{\boldsymbol{\theta}}(k)$ .

#### 4.2.4 UKF-based Joint State and Parameter Estimation

As the state-space representation defined in Eq. 4.10 and 4.11 is nonlinear, the UKF [159] was used for state and parameter inference. UKF is based on approximating the posterior distribution  $p(\mathbf{z}(k)|y_{1:k})$ , with  $y_{1:k}$  denoting all the samples up to time  $k$  of the measured variable  $y$ , by using a deterministic set of suitably chosen points called *Sigma Points*. UKF has shown better performance than the Extended Kalman Filter (EKF) at a comparable computational cost [167]. Also, UKF involves much lower computational cost than Monte Carlo-based methods, like *Particle Filters* [158].

A scheme of the proposed methodology is shown in Fig. 4.1. A noisy (synthetic or experimental) AP trace is provided as an input for UKF to infer the evolution of a set of state variables (transmembrane voltage, ionic concentrations and ion channel states) and model parameters (ionic current conductance factors) based on the state-space representation described in Eq. 4.10 and 4.11.

Being  $L_s$  the dimension of this state-space representation,  $2L_s + 1$  *Sigma Points* were deterministically generated for each time step. These *Sigma Points* were propagated through the model transition function  $f_a(\cdot)$  and used to approximate the posterior mean and covariance according to the so called Unscented Transform [159]. Since the dimension of  $\mathbf{z}(k)$  was 95 (56 state variables, 33 process noises and 6 model parameters), 191 *Sigma Points* were computed.

For the estimation process, two free *hyper-parameters* required prior definition: the process noise variance  $\sigma_\theta^2$  related to model parameter estimation and the measurement noise variance  $\sigma_r^2$ . The practical selection of these parameters is not trivial and its effects are explored for different scenarios in Section 4.3. In addition, the UKF algorithm has three parameters, namely  $\alpha$ ,  $\beta$  and  $\kappa$ , which in this work were assigned the following values:  $\alpha = 1$ ,  $\beta = 0$ ,  $\kappa = 3 - L_s$ , as in [161].

In the following the notation  $\hat{a}$  was used to denote the estimate of a generic variable  $a$ . Analogously,  $\hat{a}(k)$  was used for a time-varying estimate. When in the following a unique estimated value, e.g. for the parameter vector  $\boldsymbol{\theta}$ , is provided, the average of the estimated values over the last  $N = 5$  cycles was considered, as using a larger number of cycles did not render improved estimation performance.

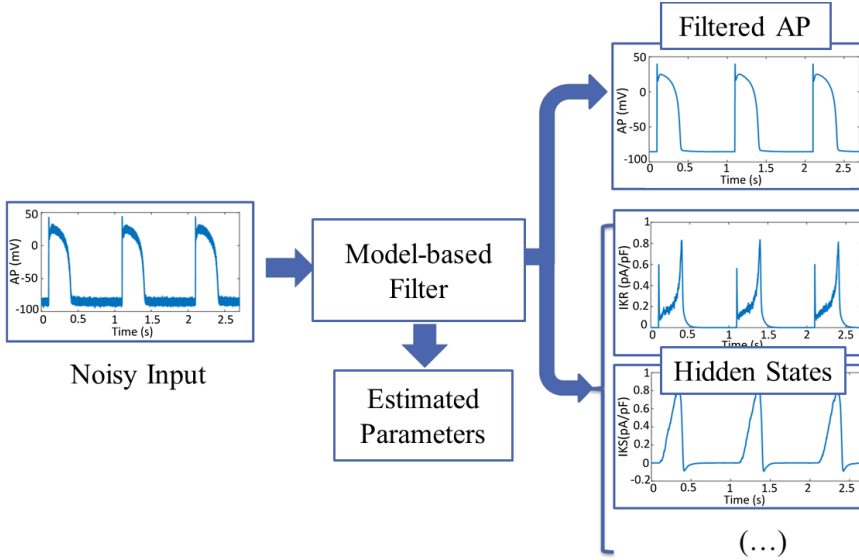


Figure 4.1: Scheme of the proposed methodology. A noisy AP trace is the input to a model-based filtering algorithm. This AP may have been synthetically generated using a computational AP model or experimentally recorded. The filtering algorithm outputs a filtered (noiseless) AP and a set of estimated hidden states and model parameters for a computational AP model used as a basis for the work (ORd model in this study). New AP traces can be computed from the estimated model under different simulation conditions.

### 4.2.5 Synthetic Data

A set of AP models was built based on the ORd human ventricular epicardial model [5]. Each AP model in the dataset was obtained by varying the conductances defined as parameters of the model:  $I_{Ks}$ ,  $I_{Kr}$ ,  $I_{to}$ ,  $I_{CaL}$ ,  $I_{K1}$ , and  $I_{Na}$ . These models aimed to represent inter-cellular variability and were used to validate the presented methodology.

Similarly to previous chapters, a total of 500 models were initially generated by sampling the nominal conductance values of the ORd model in the range  $\pm 100\%$  using the Latin Hypercube Sampling method [57, 69, 152]. Out of all generated models, only those satisfying the calibration criteria shown in Table 4.2 were retained. Such criteria were based on experimentally available human ventricular measures of steady-state AP characteristics [5, 70–73]. These characteristics included:  $APD_{90|50}$ , denoting 1 Hz steady-state APD at 90%|50% repolarization (expressed in ms); RMP, standing for resting membrane potential (in mV);  $V_{peak}$ , measuring peak membrane potential following stimulation (in mV); and  $\Delta APD_{90}$ , which was calculated as the percentage of change in  $APD_{90}$  with respect to baseline when selectively blocking  $I_{Ks}$ ,  $I_{Kr}$  or  $I_{K1}$  currents (measured in ms). For some of the above characteristics, only experimental values of the mean and standard error of the mean, rather than minimum and

maximum limits, were available. In those cases, limits were defined by mean  $\pm$  three calculated standard deviations, as this would cover 99% of the measurements if the data followed a normal distribution. After applying the described calibration criteria, the initial set of 500 models was reduced to a set of 131 selected models.

Table 4.2: Calibration criteria applied onto human ventricular cell models.

AP characteristic	Min. acceptable value	Max. acceptable value
Under baseline conditions [5, 70, 71]		
APD <sub>90</sub> (ms)	178.1	442.7
APD <sub>50</sub> (ms)	106.6	349.4
RMP (mV)	-94.4	-78.5
V <sub>peak</sub> (mV)	7.3	-
Under 90% $I_{Ks}$ block [5]		
$\Delta$ APD <sub>90</sub> (%)	-54.4	62
Under 70% $I_{Kr}$ block [73]		
$\Delta$ APD <sub>90</sub> (%)	34.25	91.94
Under 50% $I_{K1}$ block [72]		
$\Delta$ APD <sub>90</sub> (%)	-5.26	14.86

In each model of this synthetic dataset, the variation in the conductances of the four stochastic ionic currents with respect to the default ORd model was correspondent with a proportional variation in the number of ion channels (used in the stochastic term of the differential equations).

In addition to this synthetic dataset generated with the ORd model, additional AP traces were generated with a stochastic version of the ten Tusscher-Panfilov (TP06) epicardial AP model [31]. Those additional AP traces were used to test the performance of the proposed methodology over data obtained from a different human ventricular cell model.

Trains of 550 beats paced at a frequency of 1 Hz were simulated by using the Euler-Maruyama scheme with an integration time step of  $dt = 0.02$  ms. The stimulus current was a 1-ms duration rectangular pulse of 52-pA/pF amplitude. Only the last 50 simulated beats were used as input signals to the estimation methodology to guarantee that steady-state had been reached. Gaussian noise, denoted by  $r(t)$ , with zero mean and noise variance  $\sigma_r^2$  was added to the simulated membrane potential to account for noise present in experimental recordings. The effect on the estimation results of varying the values of  $\sigma_r$  to represent different signal-to-noise ratios (SNRs) was analyzed.

## 4.2.6 Experimental Data

Two ten-second AP recordings acquired using conventional microelectrode techniques in trabecular preparations from right ventricles of undiseased human donor hearts, as described in [5], were available for this work. The recordings were obtained from previous studies, with tissue preparations having been donated for research in compliance with the Declaration of Helsinki and approved by the Scientific and Research Ethical Committee of the Medical Scientific Board of the Hungarian Ministry of Health (ETT-TUKEB), under ethical approval No 4991-0/2010-1018EKU (339/PI/010). Pacing frequency was 1 Hz. Each AP trace was linearly interpolated to a sampling interval of 0.02 ms and was replicated five times. The resulting 50-cycle trace was fed as an input to the estimation algorithm to ensure convergence to stable values for the last analyzed replication.

## 4.2.7 Methodology Assessment

The proposed methodology was assessed as follows:

### Noisy AP Filtering Capability

For synthetic data, the root mean square error  $\xi_v$  between the original noiseless AP trace,  $v(k)$ , and the estimated AP trace,  $\hat{v}(k)$ , was calculated over the last  $N = 5$  simulated cycles:

$$\xi_v = \sqrt{\frac{1}{K_N} \sum_{k=0}^{K_N-1} |v(k) - \hat{v}(k)|^2}, \quad (4.12)$$

where  $K_N$  is the number of samples contained within the last  $N = 5$  cycles.

### State and Parameter Estimation

For the synthetic dataset generated with the ORd model, estimates of model parameters (i.e. factors multiplying maximal ionic conductances) and hidden states (i.e. model state variables) computed using the proposed methodology were compared with the original values used to generate the synthetic input AP traces. The mean relative error ( $\eta_{z_j}$ ) between the actual and estimated values of each state variable was calculated over the last  $N = 5$  simulated cycles:

$$\eta_{z_j} = \frac{1}{K_N} \sum_{k=0}^{K_N-1} \left\{ \frac{|z_j(k) - \hat{z}_j(k)|}{|z_j(k)|} \right\}, \quad (4.13)$$

where  $z_j$  is the actual value of the state variable  $j$  and  $\hat{z}_j$  is the estimated value, with  $j = 1, \dots, L_s$ , being  $L_s$  the length of the augmented state vector  $\mathbf{z}(k)$ . The

mean relative error  $\eta_{z_j}$  in the estimation of each model parameter  $z_j$  was analogously calculated.

A global accuracy measurement of model parameter estimation was defined as the average of the mean relative errors (adimensional by definition) for all estimated parameters:

$$\bar{\eta}_{\boldsymbol{\theta}} = \frac{1}{M} \sum_{\theta' \in \boldsymbol{\theta}} \eta_{\theta'}, \quad (4.14)$$

where  $\eta_{\theta'}$  is the mean relative error for model parameter  $\theta' \in \boldsymbol{\theta}$  and  $M = 6$  (the number of estimated model parameters).

### Reproducibility of AP Markers

For both synthetic and experimental data, the performance of the proposed methodology was additionally assessed by comparing AP-derived markers from input and estimated AP traces. Specifically, given an input AP trace, estimates of the stochastic ORd model parameters were computed using the proposed methodology and that estimated model was then simulated to generate new AP traces from which AP-derived markers were computed.

The following steady-state and temporal variability measurements of repolarization were calculated over those input and simulated AP traces:

- Average of APD at 90% repolarization ( $\text{APD}_{90}$ ) over the last  $N = 30$  cycles:

$$m_{\text{APD}_{90}} = \frac{1}{N} \sum_{n=1}^N \text{APD}_{90}(n), \quad (4.15)$$

and standard deviation of  $\text{APD}_{90}$  over the last  $N = 30$  cycles:

$$s_{\text{APD}_{90}} = \sqrt{\frac{1}{N-1} \sum_{n=1}^N (\text{APD}_{90}(n) - m_{\text{APD}_{90}})^2}. \quad (4.16)$$

- *STV* of  $\text{APD}_{90}$ , defined as the average distance perpendicular to the identity line in the Poincaré plot, computed for the last  $N = 30$  cycles as:

$$\text{STV} = \sum_{n=1}^{N-1} \frac{|\text{APD}_{90}(n+1) - \text{APD}_{90}(n)|}{(N-1)\sqrt{2}}. \quad (4.17)$$

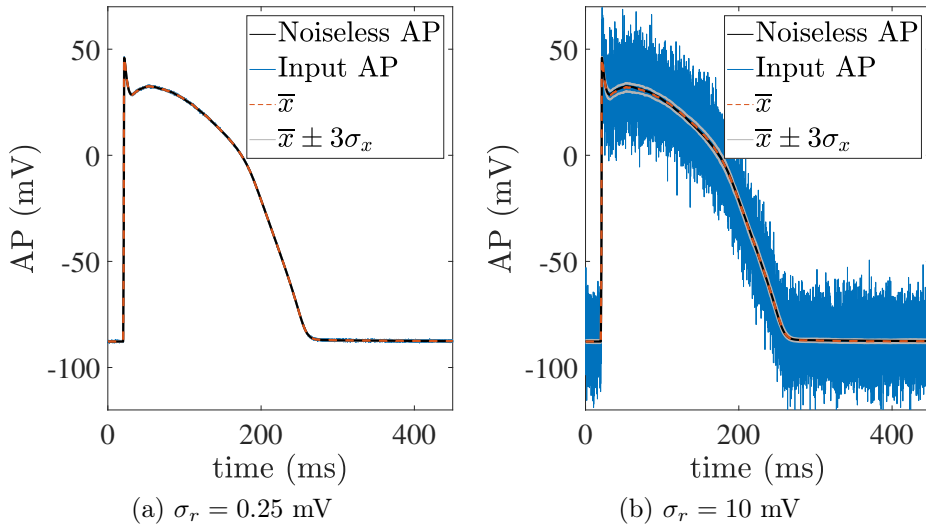


Figure 4.2: Last cycle of AP traces: In black, the synthetic noiseless AP trace generated by the original ORd model; in blue line, the noisy version of that AP,  $y(k)$ , which is used as input to the proposed method with two different values for the standard deviation of the measurement noise,  $\sigma_r$ ; in red, the mean estimated voltage at each time instant, denoted by  $\bar{x}$ ; and in grey, the estimated uncertainty bands, i. e.,  $\bar{x} \pm 3\sigma_x$  (with  $\sigma_x$  denoting the estimated standard deviation of voltage).

## 4.3 Results

### 4.3.1 Noisy AP Filtering

The proposed methodology was able to filter out the measurement noise in input AP signals even in cases of low SNR. Fig. 4.2 presents the last cycle of a synthetic noiseless AP trace generated with the stochastic ORd model on top of two noisy APs obtained by adding Gaussian noises with zero mean and standard deviation values of  $\sigma_r = 0.25$  mV and  $\sigma_r = 10$  mV, respectively, and the filtered APs output by the proposed methodology assuming the level of measurement noise was known. In this figure, as well as in all subsequent figures,  $\bar{x}$  denotes the mean estimated value of the represented variable and  $\sigma_x$ , the estimated standard deviation. For both levels of noise, the methodology (with  $\sigma_\theta = 10^{-12}$ ) was able to accurately estimate the synthetic noiseless AP, thus rendering it useful to evaluate AP markers from noisy AP traces as those obtained from experimental recordings.

In Table 4.3, root mean square error values  $\xi_v$  calculated according to Eq. 4.12 for the two different SNR levels are presented. As can be observed, the proposed method was able to almost entirely reduce the noise in the input AP traces even for a high level of measurement noise.



Table 4.3:  $\xi_v$  Root Mean Square Error (mV) in AP filtering.

$\sigma_r$ (mV)	0.25	10
$\xi_v$ (mV)	0.0160	0.1429

### 4.3.2 Sensitivity of the Methodology with respect to its own Parameters

When the level of measurement noise is unknown, the value of  $\sigma_r$  needs to be set according to some criteria. While under homoscedastic conditions  $\sigma_r$  could be readily estimated during the resting phase of the AP, such an estimation might be poor under other conditions. In Fig. 4.3 assessment of the sensitivity of the proposed methodology with respect to the estimated value of  $\sigma_r$  is presented. Specifically, the effect of varying the estimated measurement noise,  $\hat{\sigma}_r$ , on the error  $\xi_v$  is presented for two different levels of noise added to input AP traces generated with the stochastic ORd model, being these two levels correspondent with  $\sigma_r = 0.25$  mV and  $\sigma_r = 10$  mV. As can be observed from the figure, in both cases there was a broad range of  $\hat{\sigma}_r$  values with similarly good performance in terms of AP filtering (note the log-scale for the x-axis).

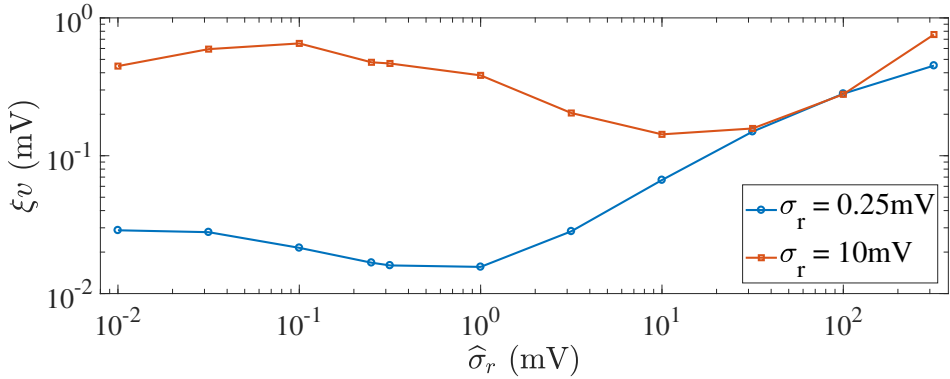


Figure 4.3: Root mean square error  $\xi_v$  in AP filtering for different actual ( $\sigma_r$ ) and estimated ( $\hat{\sigma}_r$ ) levels of measurement noise.

An apparently counter-intuitive result is that the optimal value of  $\hat{\sigma}_r$  did not exactly match the value of  $\sigma_r$ , but it was slightly higher. This may be explained because  $\hat{\sigma}_r$  accounts not only for measurement noise but also for model misspecification. Under high SNR (low  $\sigma_r$ ), this misspecification, which could be due to small errors in model parameter estimation, can be comparable to the input noise.

Regarding the sensitivity of the methodology with respect to  $\sigma_\theta$ , Fig. 4.4(a) shows that varying  $\sigma_\theta$  did not significantly affect the error in AP filtering. However, it more notably affected the error in parameter estimation, particularly when very small or very large  $\sigma_\theta$  values were used, as shown in Fig 4.4(b).

In particular, the estimation error  $\eta_\theta$  was increased for very small values of  $\sigma_\theta$  due to lack of convergence in the estimation for 50 simulated APs. For very large  $\sigma_\theta$  values ( $\geq 10^{-6}$ ),  $\eta_\theta$  was increased due to the algorithm being stuck in local minima where its performance was not satisfactory and could not be improved in any direction or due to notable oscillations around the mean estimated value. Consequently, the selection of the value for  $\sigma_\theta$  was deemed to be important to obtain an accurate model parameter estimation.

According to the results shown in Fig. 4.3 and Fig. 4.4,  $\sigma_\theta = 10^{-12}$  was selected and all results presented in the following Sections 4.3.3 and 4.3.4 correspond to that value, while the measurement noise variance was taken as  $\hat{\sigma}_r = \sigma_r$ .

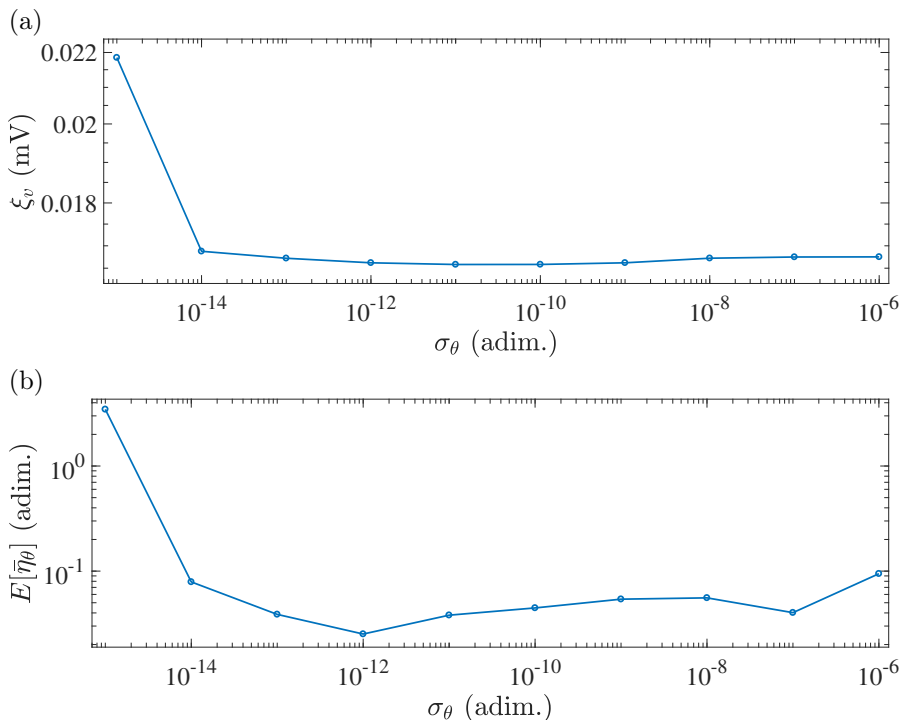


Figure 4.4: Root mean square error  $\xi_v$  in AP filtering (a) and average of mean relative parameter estimation errors  $\bar{\eta}_\theta$  (b) evaluated for different levels of  $\sigma_\theta$ .

### 4.3.3 Estimation of Model Parameters and Hidden States

The proposed methodology was able to additionally estimate hidden states from a given input AP trace according to the stochastic model described by  $f_a(\cdot)$  in Eq. 4.10. In particular, for the case of input AP traces being synthetically generated using the stochastic ORd model, a comparison could be established between actual and estimated values of model parameters and hidden states.

Fig. 4.5 illustrates the input and estimated (mean  $\pm$  three standard deviations) proportions of open channels for  $I_{K_r}$  and  $I_{K_s}$  in the last two simulated cycles. The proposed methodology was not only able to track the mean value of the state variables describing the proportions of open channels at each time instant but also provided uncertainty ranges, which were larger for  $I_{K_s}$  than for  $I_{K_r}$ .

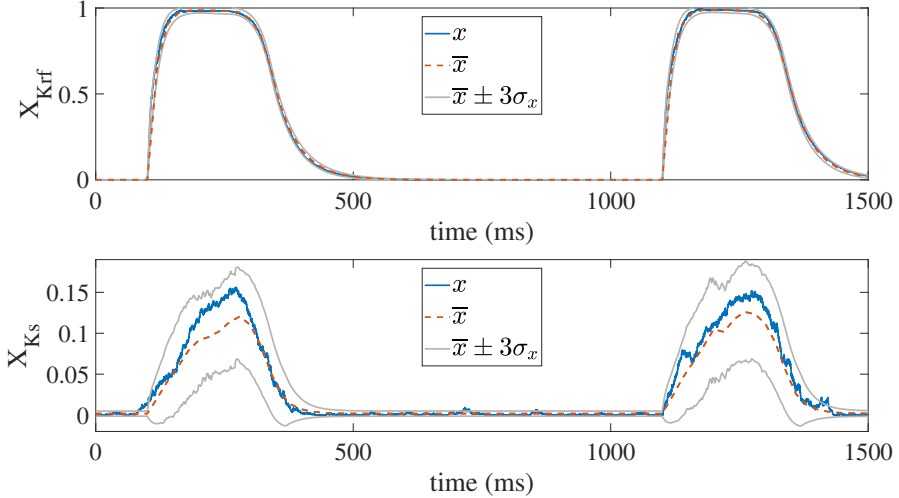


Figure 4.5: Open probability  $X_{K_{rf}}$  of  $I_{K_r}$  (top panel) and open probability  $X_{K_s}$  of  $I_{K_s}$  (bottom panel). The value in the stochastic ORD model is shown in blue, while estimated mean ( $\bar{x}$ ) and uncertainty bands ( $\bar{x} \pm 3\sigma_x$ ) are shown in red and grey, respectively.

Fig. 4.6 illustrates the estimated (mean  $\pm$  three standard deviations) model parameters along 50 simulated cycles. The mean estimated values converged to the input value in less than 40 cycles. Uncertainty ranges in the estimation were provided as well.

Results of model parameter estimation for the population of 131 stochastic AP models described in Section 4.2.5 are presented in Fig. 4.7. As can be observed, the estimation accuracy was very high for most parameters in the majority of tested models. The maximum relative error  $\eta_{\theta'}$  was obtained for  $\theta_{K_s}$  due to the almost negligible effect of its variations on the baseline AP.

#### 4.3.4 Estimation of AP Markers

In this section the performance of the proposed methodology is evaluated in terms of its ability to replicate input AP traces and AP-derived markers. Fig. 4.8 shows the statistical distributions of  $m_{APD90}$  and  $STV$  over the population of stochastic cell models described in Section 4.2.5, calculated from both actual and estimated APs. A very good match was observed between both distributions for each of the two AP markers.

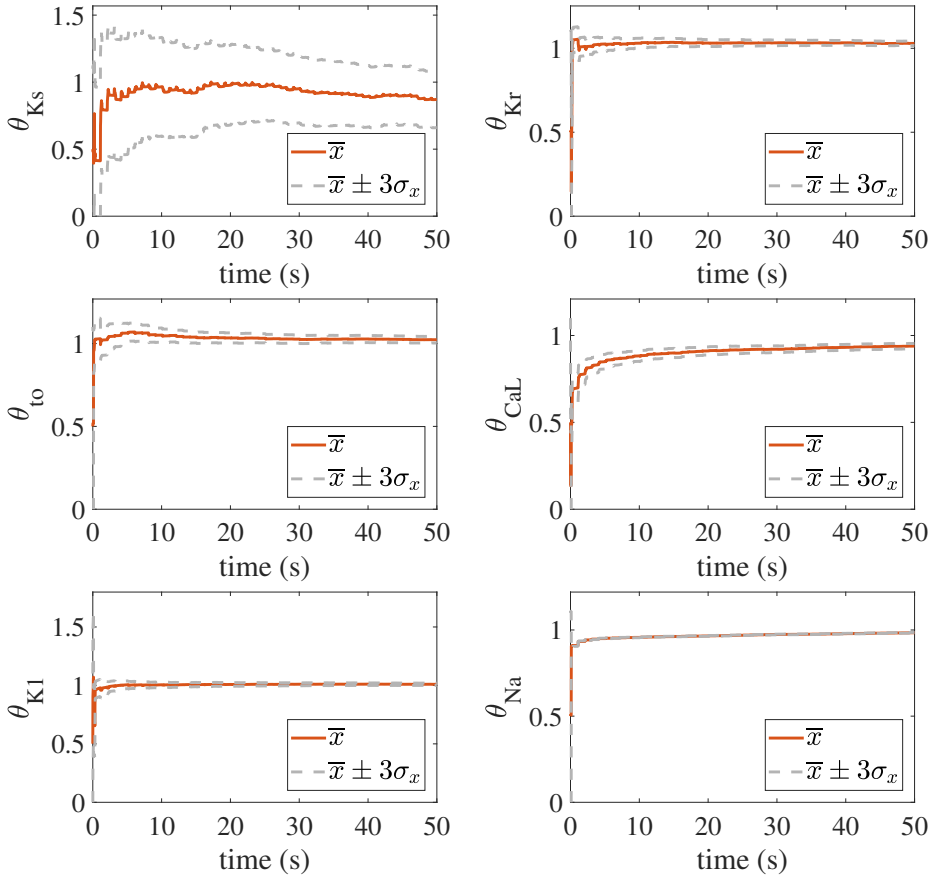


Figure 4.6: Estimation of model parameters. Mean estimates ( $\bar{x}$ ) are shown in red and uncertainty bands ( $\bar{x} \pm 3\sigma_x$ ), in grey.

Additionally, the accuracy of the proposed methodology to reproduce AP markers measured from synthetic data was tested over APs generated with a different human ventricular cell model, namely a stochastic version of the TP06 model [31]. Fig. 4.9 (top panel) shows input APs generated with the stochastic TP06 model, APs estimated with the proposed methodology as well as APs generated with the default ORd model (used as a basis for the proposed methodology) for comparison. Intrinsic differences between the ORd and TP06 models (e.g. the TP06 model produces a much more square AP) may explain the lack of complete match between input and estimated APs. In terms of the root mean square error  $\xi_v$ , this took a value of 6.96 mV for the proposed methodology versus 22.89 mV for the reference ORd model.

In addition, Fig. 4.9 (bottom panel) presents corresponding APD time series over 50 simulated cycles calculated for APs computed from the stochastic TP06 model, the proposed methodology and the default stochastic ORd model. The match between

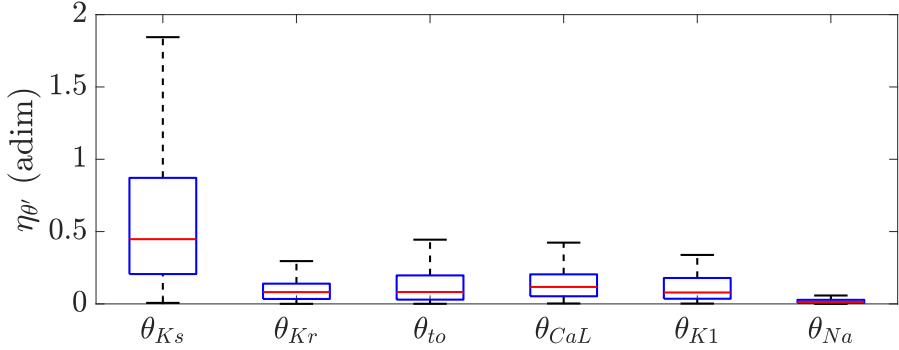


Figure 4.7: Mean relative error  $\eta_{\theta'}$  for each of the estimated model parameters over a population of 131 stochastic AP models.

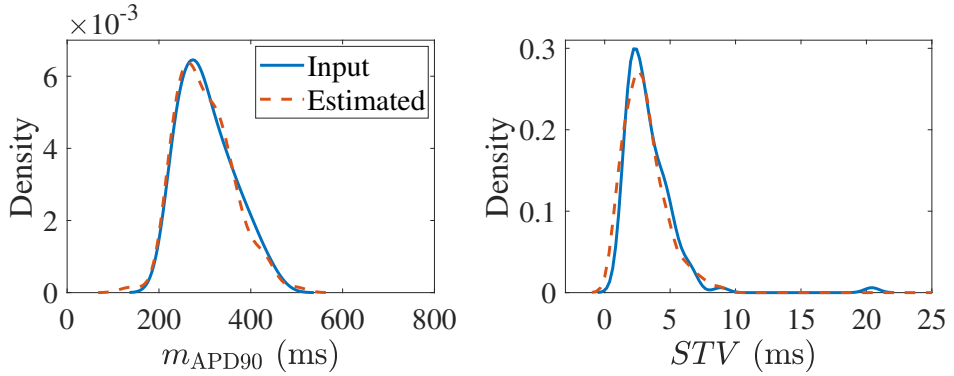


Figure 4.8: Statistical distributions over a population of 131 AP models of (left)  $m_{APD90}$  and (right)  $STV$  calculated from actual APs in blue and estimated APs in red.

input and estimated APDs was very good, with a mean absolute error of 0.16 ms between average APDs, while such an error was of 71.68 ms for the default ORd model. Beat-to-beat variability was, however, larger for the input data generated with the TP06 model than for the estimated data or the data generated with the default ORd model ( $STV$  being 3.42 ms, 1.69 ms and 1.89 ms, respectively).

### 4.3.5 Application onto Experimental Data

Application of the proposed methodology onto experimentally recorded input AP signals is illustrated in Fig.4.10. The value for the algorithmic parameter  $\sigma_{\theta}$  was selected by searching for in the range between  $10^{-15}$  to  $10^{-6}$ . The best results were obtained for  $10^{-7}$ , which is the value used for the results presented in the following. Also, the value  $\sigma_r = 1$  mV was set. Of note, when applying the proposed methodology onto experimental data, which presents AP shapes different from the one of the default

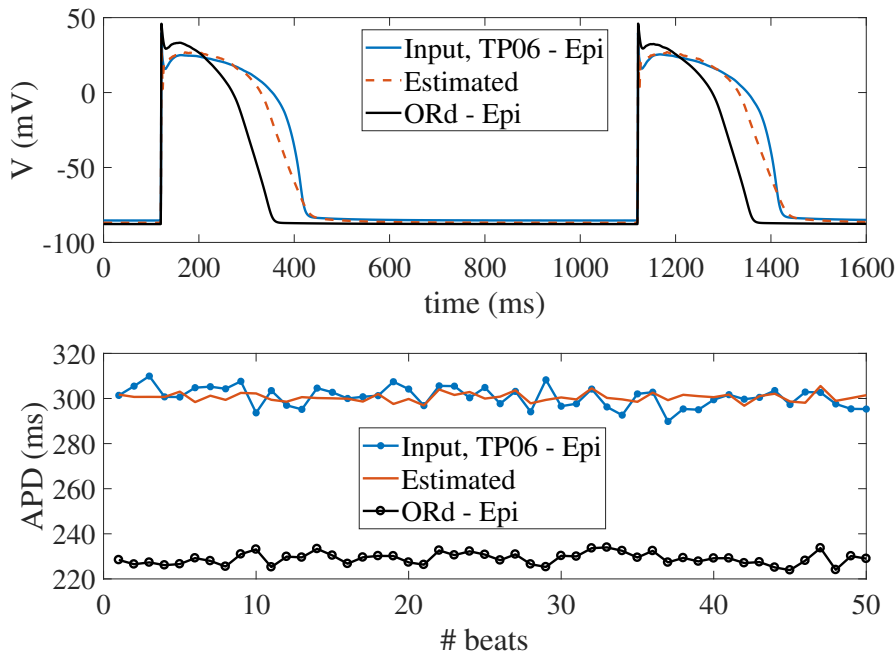


Figure 4.9: AP traces over 2 simulated cycles (top panel) and APD time series over 50 simulated cycles (bottom panel) generated with the stochastic TP06 model (in blue), estimated with the proposed methodology (dashed red) and generated with the stochastic default ORd model (black).

ORd model, issues regarding the estimation algorithm being stuck in local minima are more common. For that reason, the choice of the value for  $\sigma_\theta$  is especially important, as too large or too small values might lead to estimated models not generating valid AP traces.

In this section, methodological performance is evaluated by comparing experimental AP traces and AP traces built from the parameterized ORd model with the parameter values estimated by the proposed approach. This methodology departed from the default ORd model (for both epicardial and endocardial cells) and refined it to best fit the input AP trace. A satisfactory match was found between input and estimated APs, with some differences in the plateau and resting phases, but with good overall agreement and very close AP durations. APs generated with the default epicardial and endocardial ORd models are shown for comparison.

Table 4.4 shows the root mean square errors  $\xi_v$  obtained in the estimation from experimental human AP traces, while Table 4.5 shows the estimated parameter values. As can be noted, the estimation errors obtained by the proposed methodology for the two human AP traces were clearly lower than those obtained with epicardial and endocardial ORd models.

The performance of the proposed methodology was in this case not evaluated in terms of variability measurements, as simulated APs corresponded to single cells whereas experimental AP traces were recorded in tissue, where electrotonic coupling notably mitigates the effects of ionic current fluctuations contributing to beat-to-beat variability.

Table 4.4:  $\xi_v$  Root Mean Square Error (mV) in fitting experimental AP traces.

	(mV) AP trace 1	(mV) AP trace 2
$\xi_v$ (This Method - Endo)	8.2432	6.3393
$\xi_v$ (ORd - Endo)	11.5096	10.1043
$\xi_v$ (This Method - Epi)	5.0071	10.3788
$\xi_v$ (ORd - Epi)	9.0270	14.8517

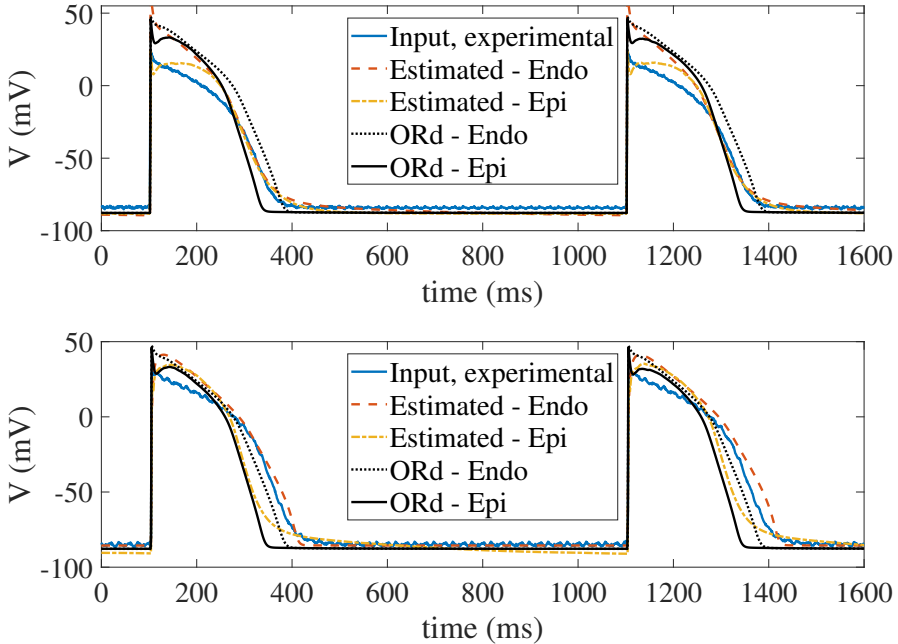


Figure 4.10: Experimental AP traces (blue) and estimated AP traces obtained with the proposed methodology based on stochastic versions of epicardial (dotted yellow) and endocardial (dashed red) ORd models. Default stochastic epicardial (solid black) and endocardial (dashed black) ORd models are shown as a reference. Top and bottom panels correspond to two different experimental recordings.

Table 4.5: Estimated parameter values for the two experimental AP traces using the human ventricular endocardial ORd model.

	$\theta_{K_s}$	$\theta_{K_r}$	$\theta_{t_o}$	$\theta_{C_{aL}}$	$\theta_{K_1}$	$\theta_{N_a}$
Exp.1	1.9997	1.9996	1.9996	1.8027	0.0538	1.4840
Exp.2	0.5481	1.4217	0.7214	1.5032	1.2950	0.1368

## 4.4 Discussion

In this work, a novel approach based on formulation of state-space representations and the use of UKF has been proposed as a method to estimate the non-measured state variables and parameters of ventricular nonlinear stochastic computational models. The proposed methodology was able to reproduce individual input AP traces and replicate statistical distributions of AP-derived markers like APD or STV. As such, the methodology can be a powerful tool to investigate the ionic mechanisms underlying human ventricular AP traces and their associated beat-to-beat variability, particularly when experimental measurements are scarce, as is usually the case with human data, and previously proposed methodologies are either not applicable or present considerable limitations.

In the following subsections, relevant characteristics of the proposed methodology as well as major benefits and shortcomings associated with its use are discussed.

### 4.4.1 Methodology Calibration

According to the presented results, calibration of two parameters of the proposed methodology,  $\sigma_r$  and  $\sigma_\theta$ , turns out to be important to obtain an accurate estimation. The first one,  $\sigma_r$ , accounts for both measurement noise and model-to-data mismatch, hence its calibration is relatively easy in most cases. Although, in principle, the definition of  $\sigma_\theta$  should not be so straightforward, results show that a wide range of values for  $\sigma_\theta$  provide similarly good estimation performance. Specifically, the analysis on the synthetic data described in Section 4.2.5 has demonstrated that this feasible range spans several orders of magnitude. In other cases where the model adjusts poorly to the input AP trace, the optimal value for  $\sigma_\theta$  can be found by sweeping over a large range of values and selecting the one leading to the best match to the input data.

### 4.4.2 Filtering Noisy Data

The proposed methodology is able to filter out the measurement noise even for AP recordings with very low SNR levels. This can be very useful to improve the accuracy in the evaluation of AP markers from experimental noisy AP traces like, for instance, those measured using optical mapping techniques.



### 4.4.3 Identification of Model Parameters and Hidden States

In this work a state-augmentation approach was used for joint state and parameter estimation, considering the compromise between performance and computational cost. Other joint estimation techniques like Expectation Maximization or Rao-Blackwellization [158] introduce a large penalty in the computational cost, associated with the need to perform several passes over the hundreds of thousands of samples of AP traces, and were thus discarded for this problem. Importantly, the probabilistic methodology presented in this chapter provides estimation errors for each variable along time, thus offering uncertainty measures associated with the estimation process, which could be used as a basis for further Uncertainty Quantification studies (see e.g. [168]).

Results prove to be accurate for all estimated ionic factors except for the factor related to the  $I_{K_s}$  conductance (Fig. 4.7). This lack of accuracy in the estimation of one of the model parameters is related to the issues of identifiability and observability, the latter possibly being in practice more difficult to satisfy [169]. Previous studies targeting estimation of neuron model parameters from voltage time series have dealt with this [170]. For the augmented state-space considered in this study, a formal identifiability / observability analysis would be of high interest.

In this case, and in line with reported experimental and simulated evidences on the lack of effects of  $I_{K_s}$  variations on baseline AP [73, 171, 172], the cellular ORd model used as a basis for this work led to similar AP traces for a relatively large range of  $I_{K_s}$  conductance values and, in such scenario, the estimation algorithm may fail to identify the corresponding conductance value. Nevertheless, the intrinsic characteristics of the proposed approach provide some advantages with respect other works. This methodology, by using stochastic models, leads to a significant reduction in parameter uncertainty as compared to other studies where a cell model is fit to only one (averaged or not) AP [173] rather than to a whole AP trace comprising several consecutive beats. The fact of including data across several beats allows integrating temporal variability information into the estimation process, thus making it more robust, as different parameter combinations might lead to comparable APs but dissimilar beat-to-beat AP variability measurements. In addition, the proposed methodology is also able to estimate model hidden states, including ionic gating characteristics and intracellular concentrations, thus facilitating assessment of whether the model renders physiologically plausible outcomes. Furthermore, Bayesian methodology explicitly delivers precision measurements for each estimated variable. When a parameter value is difficult to identify, the proposed approach provides an associated high estimation variance, as was for instance the case for  $\theta_{K_s}$  (Fig. 4.6).

The above described uncertainty in the estimation of one of the model parameters could be classified as ‘practical unidentifiability’ according to the classification provided in [174], meaning that, by using input data obtained with a different protocol, it could be possible to increase the amount of available information for the estimation. In this case, one option would be to consider data measured at different pacing frequencies as in [115, 154, 157] or to consider combined data measured under control

and following ionic inhibitions as in [115]. Future studies should address the application of the methodology proposed in this work onto AP data measured at different stimulation frequencies or under ionic inhibitions.

#### 4.4.4 Application onto Data from Different Origins

The presented methodology is able to adjust a developed stochastic version of the ORd model to fit a population of input AP data in such a way that a one-to-one correspondence is established between each individual AP and a set of model parameters underlying it. This ability has been successfully tested over a synthetic population of cellular AP data generated with the ORd model, where the proposed methodology has additionally shown to provide a robust way to approximate distributions of AP markers of interest.

For data presenting AP shapes markedly different from that of the ORd model used as a basis for the estimation, either being recorded experimentally or generated by other human ventricular computational models, the proposed methodology is still able to reproduce the corresponding AP traces. Nevertheless, in those cases, some differences exist between input and estimated APs due to the fact that some specific characteristics of the ORd model cannot be modified by just varying maximal ionic conductances. In particular, APs generated with the TP06 model show higher beat-to-beat variability, for a comparable mean APD, than those generated with the ORd model, as shown in the results. Remarkable differences in several ionic currents between the two models, including  $I_{Ks}$  characteristics, may explain such a divergence in terms of beat-to-beat variability. In the case of the analyzed experimental AP traces, beat-to-beat variability measurements could not be compared between input and estimated APs, as variability observed in tissue is considerably lower than in isolated cells due to electrotonic coupling effects. Unfortunately, only human ventricular data recorded in tissue, not in isolated cells, was available for this study. Nevertheless, the proposed methodology was able to estimate the experimental AP traces, rendering similar average APDs.

To the best of our knowledge this is the first work where stochastic cell models are used as a basis for model parameter and state variable estimation from ventricular AP data, thus aiming at providing a method to reproduce variability measurements and investigate the mechanisms behind it. In [154] a method is presented to fit different types of AP data but not to reproduce beat-to-beat variability. In [57], stochastic cell models are used but model parameters representing ionic current conductances are identified to replicate ranges of beat-to-beat variability measures only, while not necessarily the actual statistical distribution of such measures or the corresponding AP shapes. In other works based on the population-of-models approach, such as [115, 149], methods are developed to reproduce distributions of AP markers, but in this case without targeting beat-to-beat variability. The proposed approach can approximate statistical distributions of AP markers and has the additional advantage of producing

a one-to-one correspondence between individual AP traces (and corresponding AP-based markers) and a set of parameter values for an underlying cell model. This can be of significant help to unravel ionic mechanisms involved in different investigated electrophysiological behaviors, including temporal variability.

#### 4.4.5 Robustness Analysis

The proposed methodology is evaluated in a range of scenarios using both synthetically generated and experimentally measured AP data. In the case of synthetic input data, the ability of the presented approach for model parameter and state variable estimation is assessed by considering different SNR and a wide range of possible parameter values. The robustness of the method is verified, with similar performance of the method achieved in all tested cases. In the case of experimental input data, with available AP signals contaminated by non-Gaussian noise and artifacts, the method still provides reliable voltage estimation. Importantly, this methodology provides uncertainty estimation measures for all parameter and state variables, which is a useful tool for performance evaluation.

#### 4.4.6 Limitations and Future Works

The proposed methodology renders very good estimation performance even in very noisy scenarios. Since only additive Gaussian noise was considered in this work for synthetic AP data generation, future works could include other types of noise, like impulsive noise, and assess the filtering ability of the methodology. Also, the variance of this noise could be estimated jointly with other model parameters.

Further studies could also expand the investigation performed in this work on the sensitivity of the proposed methodology to algorithmic parameters. Efficient automatic approaches to select optimal values for algorithmic parameters could be explored to help detecting and avoiding local minima in the estimation process.

Stochasticity was included in four ionic currents being active during ventricular repolarization, namely  $I_{Ks}$ ,  $I_{Kr}$ ,  $I_{to}$  and  $I_{CaL}$ . Future studies could address incorporation of stochasticity in other ionic currents, like  $I_{NaL}$ , which may have a relevant contribution to beat-to-beat AP variability. In addition, other investigations could assess whether estimating the maximal value of the sodium-potassium pump ( $I_{NaK}$ ) and the sodium-calcium exchanger ( $I_{NaCa}$ ) currents could add to the estimation performance. This would increase the computational complexity of the proposed methodology, particularly if longer AP recordings were considered for that purpose, but could in turn render more accurate results. Also, estimation accuracy could be improved by including more diverse input AP data, as those obtained after pacing at different stimulation frequencies or following specific ionic current inhibitions.

In this work limited experimental tissue data was used to provide a proof-of-concept on the ability of the proposed methodology to reproduce individual experimentally measured AP characteristics. Provided human ventricular AP traces recorded in isolated cells were available for future studies, the performance of the proposed methodology to replicate beat-to-beat variability and refine the match to cellular AP shapes could be additionally tested. Also, other lines of research could build tissue models based on the single cell models developed in the present chapter to compare experimental and simulated tissue data.

## 4.5 Conclusions

A novel methodology based on state-space representations and UKF has been proposed and tested over synthetic data and experimental human ventricular data. The methodology has proven to successfully reproduce given input AP traces and identify hidden states and parameters of underlying computational models. Based on the provided one-to-one match between AP traces and sets of model variables, the proposed methodology is able to replicate statistical distributions of AP-based markers and is suitable for investigation of spatio-temporal variability in human ventricular repolarization.

# 5 | Fast and Accurate Computational Characterization of Spatio-Temporal Human Ventricular Repolarization Variability

---

5.1	Introduction . . . . .	106
5.2	Methods . . . . .	108
5.2.1	Stochastic AP Models at Baseline and following $\beta$ -AS . . . . .	108
5.2.2	Synthetic Data . . . . .	109
5.2.3	State-Space Formulation and Augmented States . . . . .	111
5.2.4	Individual and Combined DGDR- and UKF-based Methods . . . . .	112
5.2.5	Performance Evaluation . . . . .	115
5.3	Results . . . . .	117
5.3.1	Implementation of DGDR and UKF Methods . . . . .	117
5.3.2	Combined DGDR and UKF Methods: Initialization Effects . . . . .	117
5.3.3	Combined DGDR and UKF Methods: Updating Effects . . . . .	118
5.3.4	Performance Comparison . . . . .	118
5.3.5	Replication of AP Traces and Biomarkers at Baseline . . . . .	120
5.3.6	Estimation of Phosphorylation Factors, AP Traces and Biomarkers under $\beta$ -AS . . . . .	122
5.4	Discussion . . . . .	123
5.4.1	DGDR Method . . . . .	124

5.4.2	UKF Method . . . . .	125
5.4.3	Combined DGDR-UKF Method by Initialization and Updating	125
5.4.4	Estimation of Ionic Current Conductances at Baseline . . . . .	126
5.4.5	Estimation of Phosphorylation Levels of Cellular Substrates under $\beta$ -AS Conditions . . . . .	127
5.4.6	Characterization of Spatio-Temporal AP Variability from Parameter Estimates . . . . .	127
5.4.7	Limitations and Future Works . . . . .	128
5.5	Conclusion . . . . .	129

---

## 5.1 Introduction

Chapter 2, Chapter 3 and Chapter 4 have presented clinical, experimental and computational evidences on the important role of cardiac spatio-temporal variability in electrical function at a whole-range of scales from the cellular AP to the body surface ECG [38, 46, 57, 66, 139–141, 175]. Specifically regarding variability in ventricular repolarization, numerous investigations have associated elevated temporal and/or spatial variability with pro-arrhythmicity and sudden cardiac death [42, 142–144].

$\beta$ -AS has been shown to produce exaggerated increases in BVR, particularly under conditions of reduced repolarization reserve [45, 63, 66]. *In vitro* experiments in isolated cardiomyocytes have suggested that this elevation in BVR by  $\beta$ -AS is a relevant contributor to arrhythmogenesis by the development of afterdepolarizations and triggered activity [62–66]. In an *in vivo* animal model of long-QT1 syndrome,  $\beta$ -AS has been shown to induce increments in both temporal and spatial dispersion of repolarization and to facilitate the development of EADs and left ventricular aftercontractions, altogether providing the substrate and triggers for the ignition of TdP [45]. Computational investigations, including those presented in Chapter 2 and Chapter 3, have further contributed to shed light into the mechanisms underlying the relationship between  $\beta$ -AS-induced elevation in BVR and pro-arrhythmic risk [33, 55, 65, 145]. Nevertheless, most of the computational approaches employed so far in the literature do not account for realistic modeling of cell-to-cell or beat-to-beat AP differences, which should be fundamental to better understand the relationship between BVR and arrhythmogenesis and its modulation by  $\beta$ -AS.

For the above reasons, the development of stochastic cardiac computational AP models fed with information acquired from human cells or tissues becomes of major interest. In recent years, different methodologies have been proposed to integrate information from cardiac AP signals, or from a set of markers derived from them, by

identifying the values of parameters and/or state variables of an underlying electrophysiological model. This allows obtaining a population of virtual AP models representative of a set of experimental data of interest, with the advantage of facilitating assessment of the causes and consequences of BVR by simultaneous assessment of voltage and ionic currents and concentrations. In [115, 149, 155], methodologies based on Genetic Algorithms, Moment-Matching and Gaussian Process Emulators were designed for parameter identification at a population level, thus allowing to reproduce the overall AP characteristics in the investigated cell population but hampering individual identification of the parameters associated with each cellular AP trace. In [154, 156] ionic parameters were estimated from voltage signals by using MCMC-based methods, which enable parameter estimation for each individual cell. However, on top of the high computational load associated with these methods, they do not account for beat-to-beat variability and do not provide an estimation for other non-measurable state variables of the model, such as ionic concentrations or channel open probabilities, as neither do the methods proposed in [115, 149, 155]. In Chapter 4, a methodology based on nonlinear state-space representations [158] and the UKF [167] was proposed to identify the parameters and state variables of stochastic human ventricular AP models. This methodology provided robust one-to-one model parameter and state estimation for each AP trace individually, but the computational load was high and it required a long AP signal for accurate estimation.

On the basis of the above described limitations, a methodology for AP model parameter and state estimation that combines fast methodologies based on biomarkers' information with other more complex methodologies based on AP traces' information could be most useful. When condensing AP data into a set of biomarkers, it is important to keep a sufficient amount of information to avoid any risk of degradation in the estimation. To ensure this, the number of biomarkers, also called dictionary entries, can be potentially substantial (hundreds, thousands, ...) and even higher than the sample size. In this regime, various phenomena can appear, referred as curse of dimensionality [176], which require data processing to improve classification or regression. Recent studies have addressed this by using Double Greedy Dimension Reduction (DGDR) [177]. In DGDR, the parameter estimations from AP signals are obtained by building a low-dimensional classifier input, which is generated by projecting the dictionary entries into a low-dimensional linear subspace to improve the success rate of a given classification problem. This linear subspace is automatically built by a sparse linear combination of the dictionary entries to prevent any over-fitting risk [178].

The present study proposes the combined use of DGDR- and UKF-based methodologies to extract information from AP signals at baseline and under  $\beta$ -AS. Initial DGDR parameter estimates are used to initialize and/or update subsequent UKF estimates so as to facilitate that these remain close to their actual values. To assess the performance of our proposed methodology, a population of stochastic human ventricular cell models is constructed and used to run simulations at baseline conditions and following  $\beta$ -AS. Methodological performance is first tested over the synthetic AP signals generated for baseline conditions, from which a set of ionic current conductances

are inferred for each virtual cell. In a second step, the methodology is tested over synthetic AP signals of the same population following  $\beta$ -AS, from which the phosphorylation levels of a set of cellular substrates are inferred, considering the previously identified ionic conductances. The ability of our methodology to characterize spatial and temporal variability in human ventricular repolarization is demonstrated, showing remarkable improvement with respect to the individual use of DGDR- or UKF-based methods while keeping the computational load at affordable levels.

To the best of our knowledge, this is the first work where a biomarker-based estimation method, like DGDR, and an AP-driven method, like the one grounded on state-space representations and UKF (developed in Chapter 4), are combined to obtain a more robust and faster parameter and state variable identification for cardiac AP models. Another major novelty of the present study lies on the fact that parameters and state variables of an underlying cardiac AP model are not only identified for baseline conditions, but, importantly, for  $\beta$ -AS conditions. This is particularly relevant provided the role of  $\beta$ -AS in modulating spatio-temporal ventricular repolarization variability and facilitating the development of arrhythmias at tissue and whole-heart levels.

## 5.2 Methods

In this Chapter, scalar quantities are denoted by lowercase letters, vectors are denoted by lowercase boldface letters and matrices are denoted by uppercase boldface letters. Time-varying quantities are written as  $x(t)$  for continuous time and  $x(k)$  for discrete time. Superscript  $T$  is used for matrix and vector transposition.

### 5.2.1 Stochastic AP Models at Baseline and following $\beta$ -AS

#### Stochastic Human Ventricular ORd Model

A stochastic version of the ORd human ventricular epicardial AP model [5] was developed to reproduce experimentally observed BVR. Following the subunit-based approach described in [56], the set of ODEs describing ion channel gating for the four principal currents active during AP repolarization, namely  $I_{Ks}$  (slow delayed rectifier potassium current),  $I_{Kr}$  (rapid delayed rectifier potassium current),  $I_{to}$  (transient outward potassium current) and  $I_{CaL}$  (L-type calcium current), were transformed into SDEs by adding a stochastic term of the form shown in Eq. 5.1 for a generic ionic gate  $x_g$ :

$$dx_g = \frac{x_{g\infty} - x_g}{\tau_{x_g}} dt + \frac{\sqrt{x_{g\infty} + (1 - 2x_{g\infty})x_g}}{\sqrt{\tau_{x_g} N_g}} dw. \quad (5.1)$$



The added stochastic term containing the increments of a Wiener process multiplied by a factor inversely proportional to the number of ion channels of the corresponding type was added to the deterministic term defining  $x_g$  gating. By including this stochastic term with an accurately estimated number of channels, realistic fluctuations in the ionic gates and the whole-cell ionic currents are reproduced, which are the source for BVR in cellular AP. The number of channels associated with  $I_{Ks}$ ,  $I_{Kr}$ ,  $I_{to}$  and  $I_{CaL}$  were calculated by dividing the default ionic conductance values in the ORd model by the corresponding single channel conductances reported in literature, as described in Chapter 4.

### $\beta$ -A Signaling Model

$\beta$ -AS effects were modeled following the approach described in previous chapters and [33], where a modified version of the Xie model [36], with definition of graded and dynamic phosphorylation levels of cellular PKA substrates, was used. The Xie model was updated from the original  $\beta$ -A signaling formulation proposed in [35] to slow down the  $I_{Ks}$  phosphorylation and dephosphorylation rate constants to fit experimental observations. PKA-mediated phosphorylation of PLM was accounted for in [36] by increasing the NaK pump affinity for intracellular  $\text{Na}^+$  concentration.

#### 5.2.2 Synthetic Data

A population of stochastic AP models was constructed to reproduce the experimentally reported inter-individual variability in human ventricular electrophysiological properties. An initial population of virtual cells was generated by using a Monte-Carlo method in which the conductances of eight main ionic currents were varied in the range  $\pm 100\%$  of their nominal values in the ORd model, with those currents being:  $I_{Ks}$ ,  $I_{Kr}$ ,  $I_{to}$ ,  $I_{CaL}$ ,  $I_{K1}$ ,  $I_{Na}$ ,  $I_{NaCa}$  and  $I_{NaK}$ . This corresponded to definition of eight multiplying conductance factors, namely  $\theta_{Ks}$ ,  $\theta_{Kr}$ ,  $\theta_{to}$ ,  $\theta_{CaL}$ ,  $\theta_{K1}$ ,  $\theta_{Na}$ ,  $\theta_{NaCa}$ ,  $\theta_{NaK}$ , varying between 0 and 2. From the 8000 initially generated models, only 2373 models presenting electrophysiological properties within physiologically plausible limits, were retained, with those limits shown in Table 5.1 as determined based on [5, 70–73, 179, 180]. The quantified properties included APD at 90% ( $\text{APD}_{90}$ ) and 50% repolarization ( $\text{APD}_{50}$ ), RMP, peak membrane potential ( $V_{\text{peak}}$ ), percentage of change in  $\text{APD}_{90}$  after blocking individual ionic currents ( $\Delta\text{APD}_{90}$ ) as well as maximal concentrations of intracellular sodium ( $\text{Na}_i^+$ ) and calcium ( $\text{Ca}_i^{2+}$ ). The retained models represent virtual cells with distinct ionic properties.

To simulate a range of potentially different  $\beta$ -AS effects in the constructed population of stochastic AP models, multiplying factors  $\theta_{fCaL}$ ,  $\theta_{fKs}$  and  $\theta_{fNaK}$  for the PKA phosphorylation levels  $f_{CaL}$ ,  $f_{Ks}$  and  $f_{NaK}$  were varied so that these phosphorylation levels ranged between the values at baseline (i.e. without ISO) and the values after

application of an ISO dose of  $1\mu\text{M}$  associated with maximal effects. This population of phosphorylation levels, generated by using a Monte-Carlo method, was combined with the above described population of stochastic AP models to obtain a global population of 2373 models with 11 simultaneously varying parameters. This population was divided into training and validation subpopulations with 2000 and 373 models, respectively.

Table 5.1: Calibration criteria applied onto ventricular human cell models.

AP characteristic	Min. acceptable value	Max. acceptable value
Under baseline conditions [5, 70, 71]		
APD <sub>90</sub> (ms)	178.1	442.7
APD <sub>50</sub> (ms)	106.6	349.4
RMP (mV)	-94.4	-78.5
V <sub>peak</sub> (mV)	7.3	-
Under 90% $I_{Ks}$ block [5]		
$\Delta\text{APD}_{90}$ (%)	-54.4	62
Under 70% $I_{Kr}$ block [73]		
$\Delta\text{APD}_{90}$ (%)	34.25	91.94
Under 50% $I_{K1}$ block [72]		
$\Delta\text{APD}_{90}$ (%)	-5.26	14.86
$Na_i^+$ Concentration in baseline conditions [179]		
Max. Conc. ( $\mu\text{M}$ )	-	39.27
$Ca_i^{2+}$ Concentration in baseline conditions [180]		
Max. Systolic ( $\mu\text{M}$ )	-	2.23
Max. Diastolic ( $\mu\text{M}$ )	-	0.40

AP traces of 1100 beats were simulated at baseline and following  $\beta$ -AS, respectively, by applying 1-ms rectangular stimulus pulses of 52 pA/pF amplitude delivered at 1 Hz pacing frequency. The Euler-Maruyama scheme was used to solve the SDEs with an integration time step of  $dt = 0.02$  ms. The last 100 beats of each condition (baseline,  $\beta$ -AS) were used for further analysis to ensure convergence had been reached.

Independent standard Gaussian noise was added to the synthetically generated AP data, as described in Chapter 4, to simulate recording noise as in experimentally acquired data. These noisy APs were input to the estimation methodologies tested in this study.

### 5.2.3 State-Space Formulation and Augmented States

#### State-Space Formulation

The stochastic version of the ORd model with unknown ionic conductance factors (for baseline conditions) or phosphorylation levels (for  $\beta$ -AS conditions) was formulated as a non-linear discrete-time state-space model [158] following the approach described in Chapter 4. In these state-space models the only measured variable was considered to be transmembrane voltage, while there were a number of hidden variables, including ionic concentrations and opening probabilities of ionic gates.

For baseline conditions, model parameters to be estimated were the factors multiplying the nominal conductances of  $I_{Ks}$ ,  $I_{Kr}$ ,  $I_{to}$ ,  $I_{CaL}$ ,  $I_{K1}$ ,  $I_{Na}$ ,  $I_{NaCa}$  and  $I_{NaK}$ . Hence, the vector of static model parameters was  $\boldsymbol{\theta} = \{\theta_{Ks}, \theta_{Kr}, \theta_{to}, \theta_{CaL}, \theta_{K1}, \theta_{Na}, \theta_{NaCa}, \theta_{NaK}\}$ , representing variations in the ionic conductances relative to the default values in the ORd model,  $I_j = I_{j,ORd} \theta_j$ , where  $j \in \{Ks, Kr, to, CaL, K1, Na, NaCa, NaK\}$ . Note that the same factor  $\theta_j$  applies to the number of ion channels of each species:  $N_j = N_{j,ORd} \theta_j$ , as the unitary conductance of each ionic species was assumed to be constant based on reported experimental findings [165].

For  $\beta$ -AS conditions, model parameters to be estimated were the factors multiplying the phosphorylation levels of the PKA substrates whose phosphorylation had a remarkably higher impact on the AP, which were  $I_{Ks}$ ,  $I_{CaL}$  and  $I_{NaK}$  currents [37], in agreement with findings reported for other  $\beta$ -A signaling models [79]. Consequently, the vector of static model parameters was  $\boldsymbol{\theta} = \{\theta_{fKs}, \theta_{fCaL}, \theta_{fNaK}\}$ , representing variations in the phosphorylation levels  $f_{Ks}$ ,  $f_{CaL}$  and  $f_{NaK}$  relative to the default values in the modified Xie model,  $f_j = f_{j,Xie} \theta_j$ , where  $j \in \{Ks, CaL, NaK\}$ . For both baseline and  $\beta$ -AS conditions, the vector  $\boldsymbol{\theta}$  of model parameters was estimated for each given input AP trace.

The state-space representations used in this study were of the form:

$$\mathbf{x}(k) = f(\mathbf{x}(k-1), \mathbf{q}(k-1), \boldsymbol{\theta}) \quad (5.2)$$

$$y(k) = h(\mathbf{x}(k)) + r(k), \quad (5.3)$$

where the process equation (Eq. 5.2) was defined by a non-linear function  $f(\cdot)$  with three different input vectors:  $\mathbf{x}(k)$ , containing the state variables of the stochastic AP model;  $\mathbf{q}(k)$  representing non-additive process noises related to Wiener increments; and  $\boldsymbol{\theta}$  containing the model parameters to be estimated. On the other hand, the measurement equation (Eq. 5.3) was defined by the function  $h(\cdot)$  relating the measured variable (transmembrane voltage) with the vector of the model state variables. In this study,  $y(k) = v(k) + r(k)$ , where  $v(k)$  represents the noiseless AP and  $r(k)$  was assumed to be an additive white Gaussian noise.

### Augmented State-Space

To perform joint estimation of model parameters and state variables for a given input noisy AP, the state-space representation of Eq. (5.2)-(5.3) was reformulated as described in Chapter 4. In brief, *state augmentation* [158] was applied to convert the static parameter vector  $\boldsymbol{\theta}$  into a time-varying parameter vector  $\tilde{\boldsymbol{\theta}}(k)$  using a random walk model with drift:

$$\tilde{\boldsymbol{\theta}}(k) = \tilde{\boldsymbol{\theta}}(k-1) + \boldsymbol{\delta}(k), \quad (5.4)$$

where  $\boldsymbol{\delta}(k)$  represents an artificial noise whose components were defined by i.i.d. zero-mean Gaussian processes with very small variance. An augmented state vector  $\mathbf{z}(k)$  was built by joining the state variable vector  $\mathbf{x}(k)$  with the new parameter vector  $\tilde{\boldsymbol{\theta}}(k)$  and the process noise vector  $\mathbf{q}(k)$ :

$$\mathbf{z}(k) = [\mathbf{x}(k), \mathbf{q}(k), \tilde{\boldsymbol{\theta}}(k)]^T. \quad (5.5)$$

The previous process (Eq. 5.2) and measurement equations (Eq. 5.3) were replaced with:

$$\mathbf{z}(k) = f_a(\mathbf{z}(k-1)) + \boldsymbol{\epsilon}(k) \quad (5.6)$$

$$y(k) = h_a(\mathbf{z}(k)) + r(k), \quad (5.7)$$

where  $f_a$  and  $h_a$  are the augmented versions of  $f$  and  $h$ , respectively, and  $\boldsymbol{\epsilon}(k)$  contains noises related to the Wiener increments of the stochastic AP model represented by  $\mathbf{q}(k)$  and to the new parameter vector  $\tilde{\boldsymbol{\theta}}(k)$  represented by  $\boldsymbol{\delta}(k)$ .

## 5.2.4 Individual and Combined DGDR- and UKF-based Methods

### DGDR and Automatic Generation of Biomarkers

The DGDR method was used to estimate the parameters of the stochastic AP model, which represent part of the components of the augmented state vector  $\mathbf{z}(k)$ . DGDR is based on high-dimensional data analysis and aims at mitigating the curse of dimensionality [176] by projecting data into a low subspace through a sparse linear combination of the dictionary entries. In this work, the dictionary entries comprised a set of biomarkers related to AP amplitude and duration, such as  $V_{peak}$ , RMP and APD at different repolarization levels, biomarkers related to BVR, such as short and long-term variability, as well as wavelet decomposition of the input AP signal. In [177], data projection is performed such that a classification success rate is maximal, which can be achieved by maximizing a score function based on the distributions of the projected data of each class. To apply the DGDR method to regression problems, the cost function was replaced by an  $\ell^2$  norm that minimizes the error between the

actual values of the ionic conductances or phosphorylation levels and a sparse linear combination of the dictionary entries in a training set:

$$\omega_* = \arg \min_{\omega_i} \left\| \sum_{i=1}^{n_g} \omega_i g_i - \theta_c \right\|_{\ell^2} \quad (5.8)$$

where  $\omega_i$  are the weights to be determined,  $n_g$  is the number of dictionary entries,  $g_i$  is the  $i^{\text{th}}$  dictionary entry of the training set and  $\theta_c$  are the known values of the parameters in the training set.

As in [177], the early stopping criterion was applied on a validation set to avoid over-fitting risk, which leads to a sparse combination of the dictionary entries and the weight vector ( $\|\omega\|_{\ell^0} \ll n_g$ ). Thus, given a new AP trace in the validation set, the learned linear combination was applied to estimate the model parameters. For this study the number of extracted dictionary entries was 889, of which 100 were selected for the linear combination. For all ionic conductances and phosphorylation levels, the linear combination of 100 entries was a good choice to minimize the cost function in the training set while avoiding over-fitting in the validation set.

We performed a learning phase for each of the parameters, separately. The selected dictionary entries were not the same, which is a direct consequence of the goal-oriented concept of the DGDR method and ensures a certain explanation of the selected entries. The full process for the training step took around 3 hours on about 50 processors for the estimation of the eight ionic current conductances at baseline and proportionally less for the estimation of the three phosphorylation levels under  $\beta$ -AS. Once the learning phase was performed, the estimation of a new sample was immediate (scalar product between two vectors).

This training process was performed over a population of 2000 models while evaluation was carried out over 273 models, leading to adequate levels of accuracy. Fig. 5.1 (left panel) illustrates an example of  $\theta_{NaK}$  estimation by DGDR, showing the uniform dispersion of the point cloud that provides a measure of the uncertainty in the estimation. In addition, the DGDR method led to similar accuracy levels for training and evaluation populations as can be observed in Fig. 5.1 (right panel) where the distribution of the absolute error between the actual ( $\theta_{NaK}$ ) and estimated ( $\hat{\theta}_{NaK}$ ) parameter values is shown. Similar results were obtained in the estimation of the other model parameters.

## UKF

The UKF [167] was used to estimate the states of the nonlinear state-space formulation described by Eq. (5.6)-(5.7), which provides estimates for the parameters and state variables of a stochastic human ventricular cell model for any given AP trace. The values of three UKF setting parameters, commonly denoted by  $\alpha$ ,  $\beta$  and  $\kappa$ , were set to define the spreading of Sigma-Points around the mean state estimates (controlled by

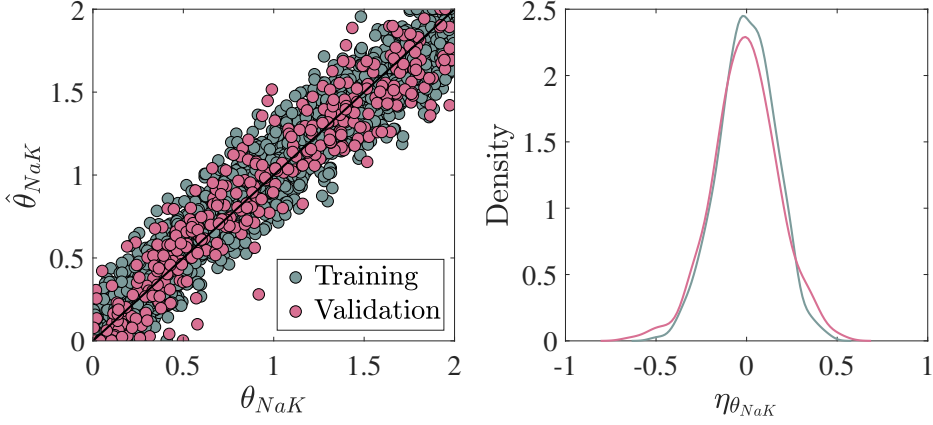


Figure 5.1: Left panel: Estimated ( $\hat{\theta}_{NaK}$ ) vs actual ( $\theta_{NaK}$ ) values of the factor multiplying maximal  $I_{NaK}$  in the training and validation populations. Right panel: Density of the absolute error in the estimation of  $\theta_{NaK}$  for the training and validation sets.

$\alpha$  and  $\kappa$ ) and to reflect prior knowledge of states' statistical distributions (controlled by  $\beta$ ). In this work,  $\alpha = 1$ ,  $\beta = 0$  and  $\kappa = 3 - L_s$  were set [181], being  $L_s$  the number of states ( $L_s = 71$  for baseline and  $L_s = 68$  for  $\beta$ -AS conditions). This led to a value for the spread of the state covariance matrix corresponding to  $\sqrt{\gamma} = 1.7321$ , in accordance with feasible values [182], and to sums of weights of means and covariances equal to one:  $\sum_{i=0}^{2L} W_i^{(c)} = 1$ ,  $\sum_{i=0}^{2L} W_i^{(m)} = 1$ .

Two additional hyper-parameters were set in the UKF implementation, which determine the process noise variance  $\sigma_\theta^2$  (the same for all components of the model parameter vector) and the measurement noise variance  $\sigma_r^2$ . A range of values for  $\sigma_\theta^2$  were tested and the one rendering best performance was selected. The value for  $\sigma_r^2$  was set to 1 mV, as in Chapter 4.

The initialization of the mean and covariance matrix of the state vector was obtained from the training population. The state variables related to stochastic AP model parameters (representing multiplying factors for ionic conductances at baseline and for phosphorylation levels under  $\beta$ -AS) were constrained to remain in the interval  $[0, 2]$ .

### Combined UKF-DGDR

DGDR and UKF methods were combined to enhance their individual characteristics in terms of estimation accuracy and computational cost. In particular, DGDR was used for **initialization** and **updating** of UKF estimation to take parameter estimates closer to their actual values and to avoid local minima in the estimation:

**Initialization (INI):** The model parameter estimates obtained by DGDR were used to initialize the corresponding elements of the state vector, which was subsequently estimated by UKF. DGDR provided estimates for both the mean of the parameter vector,  $\hat{\theta}^{DGDR}$ , and its covariance matrix,  $P^{DGDR}$ .

**Updating (UP):** The model parameter estimates obtained by DGDR were used to update the UKF-based parameter estimation in each cardiac cycle. At the end of each cycle, the corresponding elements of the state vector estimated by UKF (mean  $\hat{\mathbf{z}}_k$  and covariance matrix  $\mathbf{P}_k$ ) were updated according to the estimates for the mean  $\hat{\theta}^{DGDR}$  and covariance matrix  $\mathbf{P}^{DGDR}$  obtained by DGDR as follows:

$$\mathbf{d} = \hat{\mathbf{z}}^{DGDR} - \mathbf{H} \hat{\mathbf{z}}_k \quad (5.9)$$

$$\mathcal{S} = \mathbf{H} \mathbf{P}_k \mathbf{H}^T + \mathbf{P}^{DGDR} \quad (5.10)$$

$$\mathcal{K}_{up} = \mathbf{P}_k \mathbf{H}^T \mathcal{S}^{-1}, \quad (5.11)$$

with  $\hat{\mathbf{z}}^{DGDR} = [\mathbf{O}_{N_x} \hat{\theta}^{DGDR} \mathbf{O}_{N_q}]$ , where  $\mathbf{O}_{N_x}$  is a  $N_x \times 1$  zero vector and  $\mathbf{O}_{N_q}$  is a  $N_q \times 1$  zero vector, and  $\mathbf{H}$  is a  $(N_x + N_\theta + N_q) \times (N_x + N_\theta + N_q)$  matrix of 0 values everywhere except for the last  $N_\theta \times N_\theta$  submatrix occupied by an identity matrix. In the above,  $N_\theta$  is the number of model parameters,  $N_x$  is the number of model state variables and  $N_q$  is the number of Wiener processes.

The UKF-based updated estimates for the mean and the covariance matrix of the state vector were:

$$\hat{\mathbf{z}}_{k_{up}} = \hat{\mathbf{z}}_k^- + \mathcal{K}_{up} \mathbf{d} \quad (5.12)$$

$$\mathbf{P}_{k_{up}} = (\mathbf{I}_{N_\theta} - \mathcal{K}_{up} \mathbf{H}) \mathbf{P}_k. \quad (5.13)$$

### 5.2.5 Performance Evaluation

The performance of DGDR, UKF and their combination was evaluated for estimation of eight ionic current conductances at baseline conditions and for estimation of three phosphorylation levels under  $\beta$ -AS conditions. In the latter case, the values for the eight ionic conductances were set at those estimated at baseline. The estimation performance was evaluated as in previous Chapter 4:

#### AP Estimation

The root mean square error between the generated noiseless AP trace and the estimated AP trace was calculated over the last 5 cycles,

$$\xi_v = \sqrt{\frac{1}{K_N} \sum_{k=0}^{K_N-1} |v(k) - \hat{v}(k)|^2}, \quad (5.14)$$

where  $K_N$  is the number of samples contained within the last  $N = 5$  cycles.

### State and Parameter Estimation

The mean absolute error between the actual and estimated values of each state was calculated over the last 5 cycles,

$$\eta_{z_j} = \frac{1}{K_N} \sum_{k=0}^{K_N-1} \{|z_j(k) - \hat{z}_j(k)|\}, \quad (5.15)$$

where  $z_j$  is the actual value of the state variable  $j$  and  $\hat{z}_j$  is the estimated value, with  $j = 1, \dots, L_s$ , being  $L_s$  the length of the augmented state vector  $\mathbf{z}(k)$ .

A global accuracy measurement  $\bar{\eta}_\theta$  of model parameter estimation was defined as the average of the mean absolute errors  $\eta_{\theta_i}$ ,  $i = 1, \dots, N_\theta$ , corresponding to all estimated model parameters:

$$\bar{\eta}_\theta = \frac{1}{M} \sum_{\theta' \in \theta} \eta_{\theta'}, \quad (5.16)$$

where  $\eta_{\theta'}$  is the mean relative error for model parameter  $\theta' \in \theta$  and  $M = 8$  (for conductance factors) or  $M = 3$  (for phosphorylation factors).

### Reproducibility of AP Markers

AP-derived biomarkers were calculated from the noiseless AP trace and from the estimated AP trace calculated according to the estimated values for the model parameters. AP biomarkers comprised mean and standard deviation of  $\text{APD}_{90}$  (in the following denoted by APD) and STV of APD calculated as the average distance perpendicular to the identity line in the Poincaré plot (see Chapter 4), in both cases evaluated over the last 30 cycles:

$$m_{\text{APD}_{90}} = \frac{1}{N} \sum_{n=1}^N \text{APD}_{90}(n), \quad (5.17)$$

$$s_{\text{APD}_{90}} = \sqrt{\frac{1}{N-1} \sum_{n=1}^N (\text{APD}_{90}(n) - m_{\text{APD}_{90}})^2}, \quad (5.18)$$

$$\text{STV} = \sum_{n=1}^{N-1} \frac{|\text{APD}_{90}(n+1) - \text{APD}_{90}(n)|}{(N-1)\sqrt{2}}. \quad (5.19)$$



## 5.3 Results

### 5.3.1 Implementation of DGDR and UKF Methods

The performance of the UKF method as a function of the process noise standard deviation  $\sigma_\theta$  is illustrated in Fig. 5.2, which shows the mean parameter estimation error in the ORd model when varying  $\sigma_\theta$  by several orders of magnitude. The minimal average error  $E[\bar{\eta}_\theta]$  was achieved for  $\sigma_\theta = 10^{-8}$ , which was used for all subsequent analyses. In the case of the root mean square error in AP estimation,  $\xi_v$ , its values were minimally affected by the choice of  $\sigma_\theta$  for all tested  $\sigma_\theta$  values.

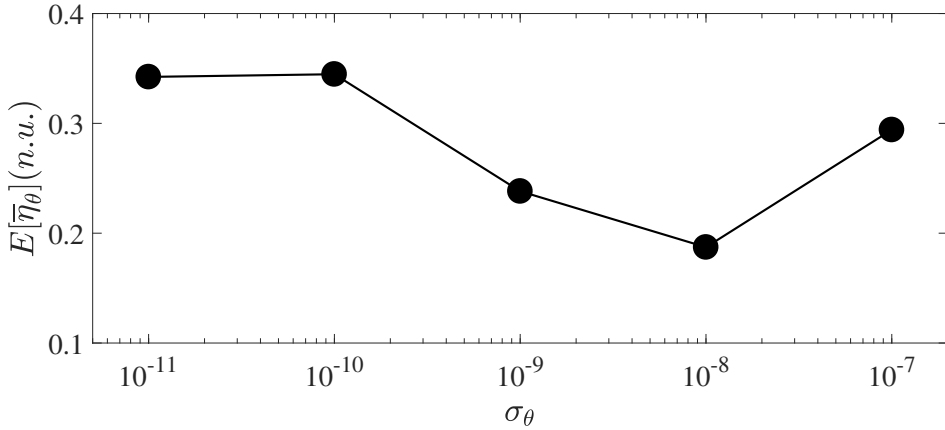


Figure 5.2: Average of mean absolute parameter estimation error  $E[|\bar{\eta}_\theta|]$  in the ORd model as a function of the standard deviation of the process noise  $\sigma_\theta$ .

In the following sections the estimation performances of the DGDR and UKF methods individually and in combination are presented.

### 5.3.2 Combined DGDR and UKF Methods: Initialization Effects

The use of the estimates obtained by DGDR for the mean,  $\hat{\theta}^{DGDR}$ , and the covariance matrix,  $P^{DGDR}$ , of the model parameter vector as initialization for the UKF method led to two important benefits. On the one hand, it reduced the time required for the estimates to reach convergence, in turn diminishing the computational cost. On the other hand, it led to more accurate estimates, as shown in Fig. 5.3 for the estimation of  $\theta_{Na}$  in one of the models of the population at baseline conditions. While for the individual UKF method more than 40 beats were required for the estimation error to be below 0.04, when the combined UKF+INI method was used the number of required beats was 5 for that particular example.

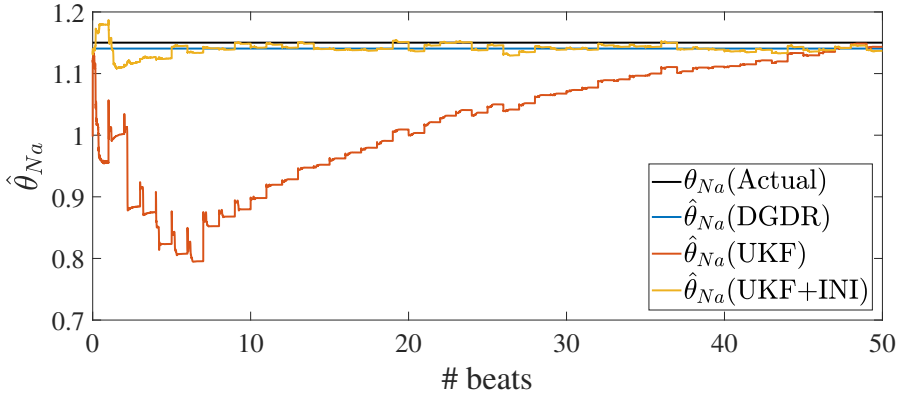


Figure 5.3: Actual  $\theta_{Na}$  value and time course of  $\hat{\theta}_{Na}$  as estimated by DGDR, UKF and UKF+INI methods.

### 5.3.3 Combined DGDR and UKF Methods: Updating Effects

The use of the estimates obtained by DGDR for the mean,  $\hat{\theta}^{DGDR}$ , and the covariance matrix,  $P^{DGDR}$ , of the model parameter vector to update the UKF estimation at the end of each beat helped to retain the parameter estimates close to the actual parameter values and to reduce the uncertainty in the estimation, as confirmed by a reduction in the estimation covariance matrix. Additionally, this UKF+UP approach diminished the convergence time and, thus, the associated computational cost. The benefit of using the DGDR-derived estimates for UKF updating is illustrated in Fig. 5.4 for the estimation of  $\theta_{Kr}$  in one of the models of the population at baseline conditions. When only UKF is employed, the parameter estimates may fall in a local minimum and may never reach a value close to the actual one. As can be observed from the figure, the UKF and UKF+UP estimates were the same for the first beat whereas the updating subsequently led to remarkably enhanced results.

### 5.3.4 Performance Comparison

The performances of the individual DGDR and UKF methods and their combinations, either by initialization and/or updating, were assessed in terms of the average mean  $E[\bar{\eta}_\theta]$  and standard deviation  $E[\bar{\sigma}_{\eta_\theta}]$  of the absolute error. Top panel of Fig. 5.5 illustrates  $E[\bar{\eta}_\theta]$  for the five evaluated methods at baseline conditions. As can be seen from the figure, the individual DGDR and UKF methods led to approximately the same level of error ( $E[\bar{\sigma}_{\eta_\theta}]$  values of 0.1806 and 0.1775, respectively), with a larger associated computational cost in the case of the UKF method. The combination of DGDR and UKF remarkably improved the estimation performance, either when combined through initialization or through update and, particularly, when combined through both ( $E[\bar{\sigma}_{\eta_\theta}]$  values of 0.1526 for UKF+INI, 0.1396 for UKF+UP and 0.1350

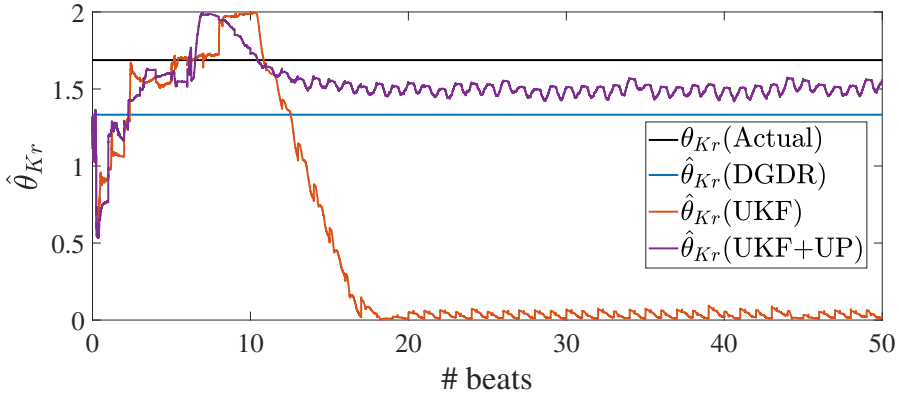


Figure 5.4: Actual  $\theta_{Kr}$  value and time course of  $\hat{\theta}_{Kr}$  as estimated by DGDR, UKF and UKF+UP methods.

for UKF+INI+UP). Bottom panel of Fig. 5.5 presents the estimation uncertainty for the five evaluated methods. As can be observed, initialization and updating by DGDR contributed to reduce the parameter estimation uncertainty of the UKF method.

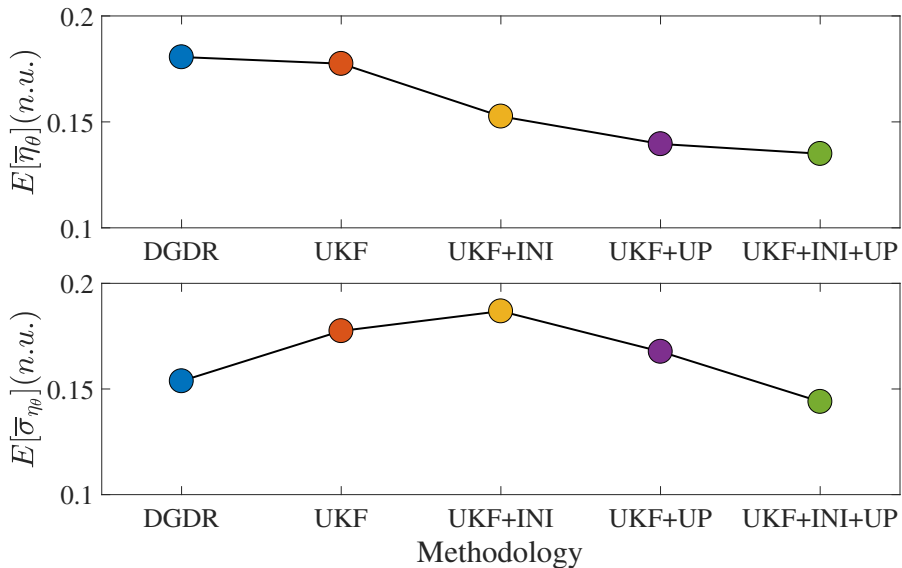


Figure 5.5: Average of mean (left panel) and standard deviation (right panel) of absolute parameter estimation error  $\bar{\eta}_\theta$  for the five evaluated methods.

Fig. 5.6 shows boxplots for the mean absolute error in the estimation of each ionic conductance factor by each of the five evaluated methods at baseline conditions. As can be observed from the figure, the combined UKF+INI+UP method presents better performance than the individual DGDR and UKF methods for practically all

estimated factors. The most accurate results were obtained for  $\theta_{Na}$ , with median estimation errors  $\hat{\theta}_{Na}$  being lower than 0.05. On the other hand, the least accurate results were obtained for  $\theta_{Ks}$ ,  $\theta_{NaCa}$  and  $\theta_{NaK}$ .

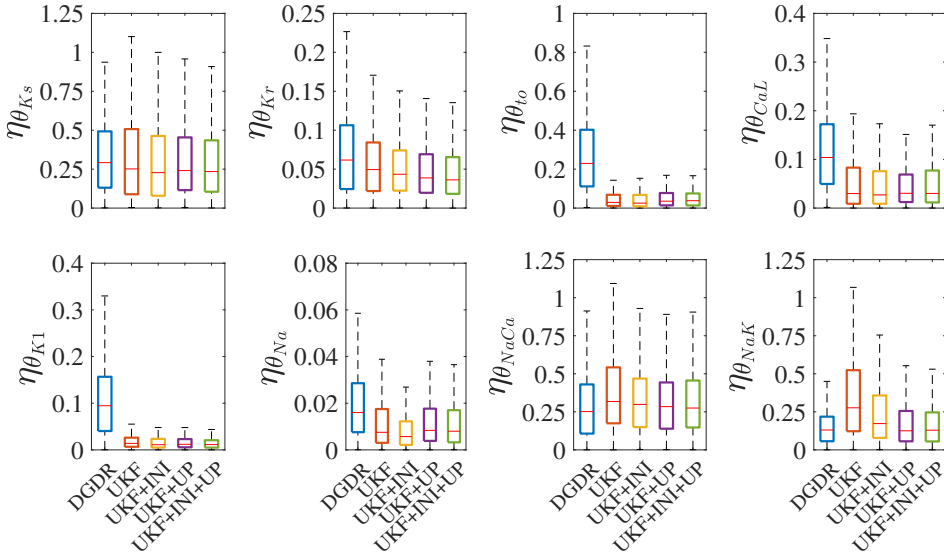


Figure 5.6: Boxplots of absolute estimation errors  $\eta_\theta$  for the factors multiplying ionic current conductances calculated for the five evaluated methods.

Fig. 5.7 presents results related to estimation uncertainty. Fig. 5.7 (left panel) illustrates the time course of the estimation uncertainty quantified by the square root of the covariance matrix  $\sqrt{P_{NaK}}$  in the estimation of  $\theta_{NaK}$  for one virtual cell in the population at baseline conditions. As can be observed from the figure, the combination of DGDR and UKF presented lower uncertainty than the individual DGDR and UKF methods, with the impact of updating being notably larger than that of initialization. Fig. 5.7 (right panel) provides an additional characterization of the estimation uncertainty quantified by the number of beats required by each UKF-based method to reach the same value of the averaged standard deviation of the absolute estimation errors as the individual UKF. The impact of updating on the reduction of the estimation uncertainty is clear from this figure too.

### 5.3.5 Replication of AP Traces and Biomarkers at Baseline

The performance of the five proposed methods to replicate AP traces at baseline conditions was assessed by generating APs from the ORd model with the different sets of estimated parameters and by comparing them with the input AP traces. Also, the comparison was established in terms of AP-derived biomarkers like APD and STV. Fig. 5.8 (left panel) shows the probability density function of the differences between

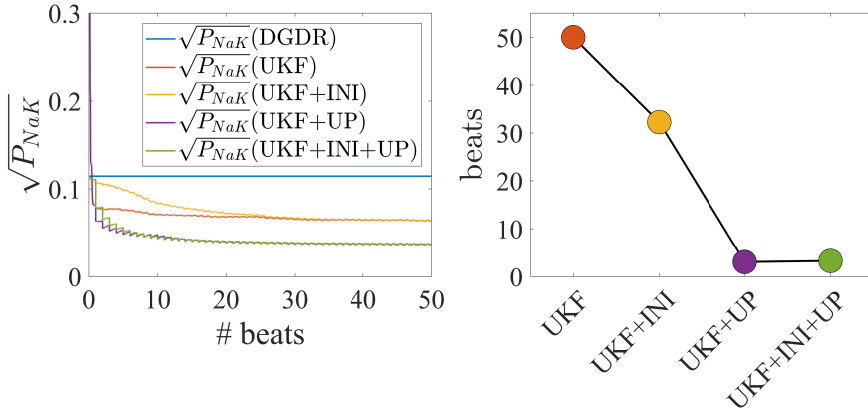


Figure 5.7: Left panel: Time course of estimation uncertainty in terms of square root of covariance matrix  $\sqrt{P_{NaK}}$  for each of the five evaluated methods. Right panel: Number of beats required by each evaluated method to reach the same level of accuracy as the UKF method, as quantified by the averaged covariance over all estimated model parameters.

the APD from the input AP trace and the APD calculated from the estimated AP trace for DGDR, UKF and UKF+INI+UP. Similarly, Fig. 5.8 (right panel) shows results for STV. As can be observed from the figure, the combined UKF+INI+UP method provides the best fitting to the actual data, as confirmed by the fact that the distributions of  $\Delta$ APD and  $\Delta$ STV are more concentrated around 0. On the other hand, the DGDR method presents reduced accuracy for APD estimation, although very similar to UKF and UKF+INI+UP for STV estimation.

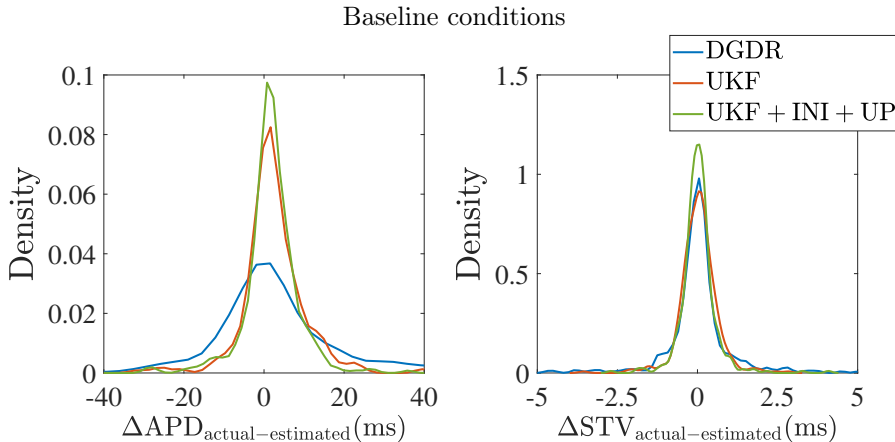


Figure 5.8: Probability density function of  $\Delta$ APD (left panel) and  $\Delta$ STV (right panel) for the validation population, with  $\Delta$ APD ( $\Delta$ STV, respectively) calculated as the difference between APD (STV, respectively) from the input AP trace and APD (STV, respectively) from the estimated AP trace for each evaluated method under baseline conditions.

### 5.3.6 Estimation of Phosphorylation Factors, AP Traces and Biomarkers under $\beta$ -AS

Considering the ionic conductance estimates obtained for baseline conditions, the next step was to test the performance of DGDR, UKF and UKF+INI+UP to estimate the phosphorylation levels for the validation population of models under  $\beta$ -AS effects. Fig. 5.9 shows boxplots of the mean absolute errors  $\bar{\eta}_\theta$  for the estimation of the three ISO-induced phosphorylation levels. As can be observed from the figure, the UKF+INI+UP method increased the accuracy in the estimation of  $\theta_{fKs}$  and  $\theta_{fNaK}$  with respect to the individual DGDR and UKF methods, whereas for  $\theta_{fCaL}$  UKF was slightly better in terms of median absolute error, but not in terms of averaged absolute error ( $\bar{\eta}_\theta = 0.34$  for both methodologies). Taking together the three estimated factors for the phosphorylation levels and results over the whole validation population, the combined UKF+INI+UP method led to a reduction in the averaged mean absolute error,  $E[\bar{\eta}_\theta]$ , of 15.29% and 20.01% with respect to the individual use of DGDR and UKF, respectively. The average mean absolute errors,  $E[\bar{\eta}_\theta]$ , for ISO-induced phosphorylation level factors were higher (0.38, 0.40 and 0.32 for DGDR, UKF and combination respectively) than those obtained for ionic conductance factors due to the fact that the error in the ionic conductance estimation was propagated into the phosphorylation level estimation.

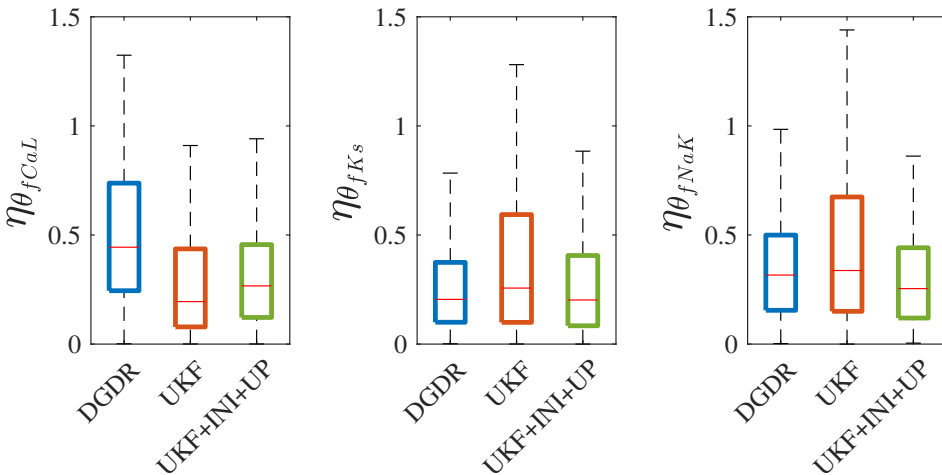


Figure 5.9: Boxplots of absolute estimation errors  $\eta_\theta$  for the factors multiplying ISO-induced phosphorylation levels calculated for three evaluated methods.

Fig. 5.10 (left panel) shows the probability density function of the differences between the APD from the input AP trace and the APD calculated from the estimated AP trace after estimation of the ionic conductances at baseline and phosphorylation factors under  $\beta$ -AS for DGDR, UKF and UKF-INI-UP. Fig. 5.8 (right panel) shows analogous results for STV. Again, the combined UKF-INI-UP provided the best fitting for both  $\Delta$ APD and  $\Delta$ STV, whereas the DGDR method presented the highest

differences between actual and estimated APD and comparable performance to UKF and UKF+INI+UP in the case of STV.

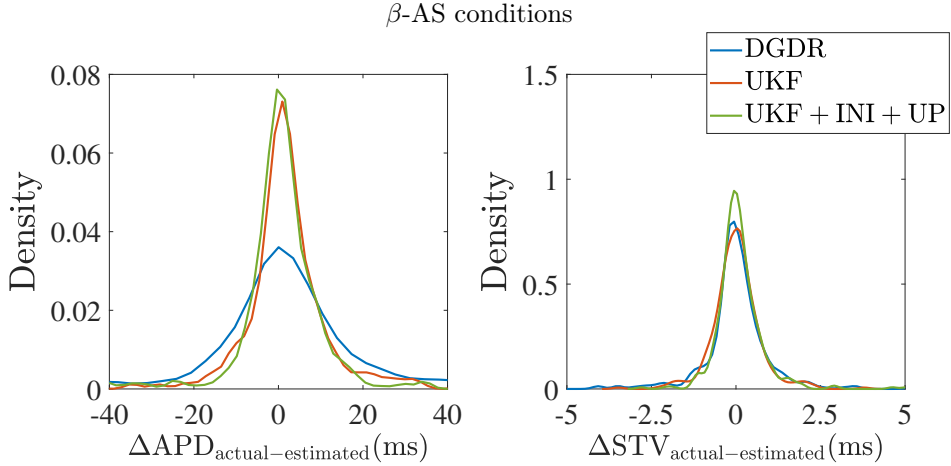


Figure 5.10: Probability density function of  $\Delta\text{APD}$  (left panel) and  $\Delta\text{STV}$  (right panel) for the validation population, with  $\Delta\text{APD}$  ( $\Delta\text{STV}$ , respectively) calculated as the difference between APD (STV, respectively) from the input AP trace and APD (STV, respectively) from the estimated AP trace for each evaluated method under  $\beta$ -AS conditions.

As an illustration of the above results, Fig. 5.11 shows the actual and estimated APs (mean over 100 beats) calculated from the set of estimated parameters by each of the evaluated methods for a cell in the validation population. Both at baseline and under  $\beta$ -AS, the AP estimated by DGDR+UKF remarkably better matched the actual AP as compared to those obtained by DGDR or UKF individually. Not only the mean AP, but also the variability over 100 beats was better reproduced by DGDR+UKF as compared to DGDR and UKF.

## 5.4 Discussion

A novel approach based on the combined use of the DGDR, with Automatic Generation of Biomarkers, and the UKF has been proposed as a method for joint estimation of parameters and state variables of computational human ventricular stochastic models from given input AP traces. By using this combined methodology, different sets of ionic parameters, namely ionic current conductances and phosphorylation levels of cellular substrates, are estimated for each given individual AP trace at baseline conditions and following  $\beta$ -AS. The proposed methodology outperforms individual DGDR and UKF methods and has an affordable computational cost. It allows realistic characterization of spatio-temporal variability at baseline and following  $\beta$ -AS, thus enabling improved investigation of variability mechanisms and arrhythmic risk prediction. This can prove

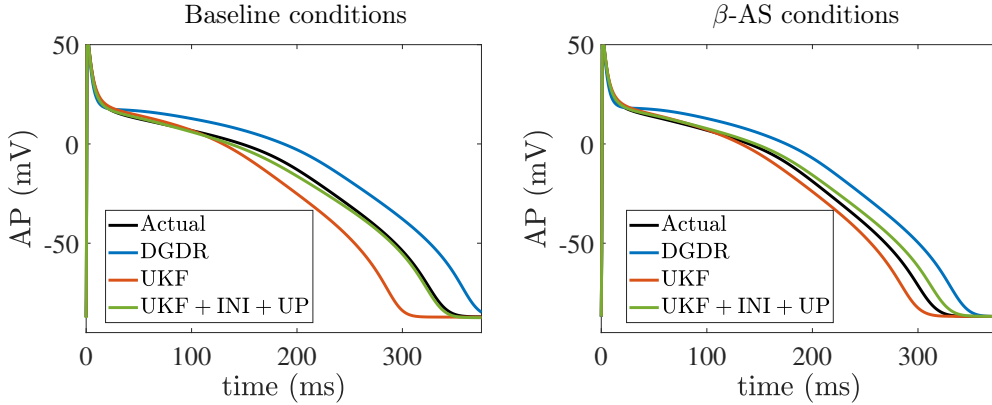


Figure 5.11: Actual and estimated APs (mean over 100 beats) calculated from the set of estimated parameters by each evaluated method at baseline (left panel) and under  $\beta$ -AS (right panel) for one of the virtual cells in the validation population.

fundamental to assess the role of  $\beta$ -AS in leading to exaggerated increases in BVR that facilitate the occurrence of arrhythmic events in certain cases but not in others [183]. In the following, relevant characteristics of the proposed methodology as well as major benefits and shortcomings associated with its use are discussed.

### 5.4.1 DGDR Method

The DGDR method was used to obtain estimates for the model parameters, which were subsequently fed to the UKF method to build the combined DGDR-UKF method. The intrinsic characteristics of the DGDR method, which include one-to-one matching between input AP traces and the set of estimated model parameters, ability to manage the stochastic behavior of the AP traces and low computational burden make this methodology suitable for the problem at hand.

A key factor in the performance of the DGDR method relies on a correct training phase. To obtain high levels of estimation accuracy, training should be performed over large populations, which in the case of this study corresponds to a large set of synthetic AP traces. Confirmation on the appropriateness of the training population dimension was provided by the fact that similar estimation errors were attained in both the training and validation populations. If training dimension had not been sufficient, estimation uncertainty in the validation population would have been much greater than that obtained in the training population. The time required to obtain the estimation dictionaries from the training population was just three hours, being subsequent calculation of parameter estimation immediate (scalar product of two vectors) when given a new AP trace of the validation population.



### 5.4.2 UKF Method

After formulating the problem to be solved as a nonlinear state-space representation where a noisy voltage trace is considered as the observed variable and SDEs defining a human ventricular cell model are used to describe the process equations, the UKF method was applied for joint estimation of model parameters and state variables, providing not only mean estimates but also measurements of estimation uncertainty. The UKF algorithm presents better performance than other methods used for parameter and state estimation of nonlinear state-space representations, such as the EKF algorithm, with the added advantage of not requiring calculation of Jacobians [167]. Also, as compared to other Monte-Carlo-based methods, such as Particle Filters [151], the UKF algorithm is associated with notably lower computational cost.

When using the UKF, appropriate calibration of its hyperparameters  $\sigma_\theta$  and  $\sigma_r$ , representing process and measurement variances, respectively, is a critical point to achieve high levels of accuracy. According to our results, an inadequate selection of these hyperparameters may lead to an increase in the estimation error above 50% of the value attained for optimally adjusted  $\sigma_\theta$  and  $\sigma_r$  values. Based on Chapter 4,  $\sigma_r$  was set to 1 mV, equal to the variance of the measurement noise added to the clean synthetic AP signal. In the case of  $\sigma_\theta$ , which is closely related to the convergence speed and potentially oscillatory behavior of the estimates, its value was set to  $\sigma_\theta = 10^{-8}$ , as this value led to a minimum average mean absolute error in parameter estimation, as shown in section 5.3.1. This value is in the range of feasible values shown in Chapter 4, with a slight difference in the optimal value justified by the fact that a higher number of model parameters were estimated in this study as well as to the fact that a subunit-based formulation of SDEs for ionic gates, rather than the channel-based formulation used in Chapter 4, was here employed.

### 5.4.3 Combined DGDR-UKF Method by Initialization and Updating

The use of DGDR estimates for both initialization and updating of the UKF estimates has been demonstrated to play a very significant role in improving the estimation performance. On the one hand, providing an initialization for the UKF method in terms of its mean and covariance matrix based on DGDR estimates allowed reducing the mean estimation error and the uncertainty around it. Also, the convergence time was remarkably diminished, as described in section 5.3.2. As a proof, the combined DGDR initialization + UKF approach required approximately 35% of the number of beats than the individual UKF method to reach the same level of estimation uncertainty.

On the other hand, updating the UKF estimates at the end of each cardiac beat by using the DGDR estimates allowed the solution of the combined method to remain within a relatively narrow range around the actual parameter values and avoided the estimation to fall into local minima. In addition, it contributed to accelerate the

estimation convergence, reducing by more than 95% the number of beats required by the UKF method to reach the same level of uncertainty. It is interesting to highlight that this updating process improved the estimation of not only the mean and the covariance of the model parameters, but also of all the other model state variables.

The enhanced performance and reduced convergence time attained by the combined DGDR-UKF method are particularly relevant for subsequent studies aimed at investigating repolarization variability from human ventricular experimental voltage traces, which are commonly of short duration.

#### 5.4.4 Estimation of Ionic Current Conductances at Baseline

Eight ionic current conductances were estimated at baseline conditions, as variations in those conductances have been postulated to be major factors for spatial (cell-to-cell) AP variability [56, 64, 147, 149, 184]. Other studies in the literature have addressed estimation of ionic current conductances, even if not in all cases for as many currents as in this work and not always considering temporal (beat-to-beat) AP changes but just focusing on a steady-state AP [115, 154, 185]. In the present study, stochastic human ventricular cell models accounting for temporal variability were developed to improve the estimation accuracy by considering dynamic information additional to the static information commonly considered in the literature. The eight estimated model parameters were multiplying factors for the conductances of six major ionic currents ( $I_{Ks}$ ,  $I_{Kr}$ ,  $I_{to}$ ,  $I_{CaL}$ ,  $I_{K1}$ ,  $I_{Na}$ ) and the maximal values of  $I_{NaCa}$  and  $I_{NaK}$  with respect to their nominal values in the ORd model.

The least accurate results with our DGDR-UKF method, as happened with all other tested methodologies (individual DGDR and UKF methods and UKF with only initialization or updating from DGDR), were obtained for  $\theta_{Ks}$ , in line with results reported in Chapter 4. This can be due to the intrinsic characteristics of the ORd model, in which the  $I_{Ks}$  current has little influence on the AP, and consequently on AP-derived biomarkers, at baseline conditions. Other experimental and computational studies support this outcome regarding the limited influence of  $I_{Ks}$  on the AP shape and duration at baseline [36, 171, 172]. Since a wide range of  $\theta_{Ks}$  values generate little differences in the corresponding AP traces, accurate identification becomes challenging. This issue is framed within the context of identifiability and observability and may be solved in future studies by complementing the estimation process with signals obtained while stimulating the cells at other pacing frequencies or under ionic current blocks. Similarly, the estimation errors associated with  $\theta_{NaCa}$  and  $\theta_{NaK}$  were among the highest for all tested methodologies, which can in this case be due to the longer time scale required for  $I_{NaCa}$  and  $I_{NaK}$  variations to impact the AP.

Of note, estimation of  $\theta_{to}$  rendered much higher errors when the DGDR method was used as compared with any of the other methods involving UKF. This can be attributed to the fact that none of the defined AP-derived biomarkers may be closely related to the AP notch, which is the AP phase where this current has the largest

influence. Similarly happened with  $\theta_{K1}$ , for which estimation errors were higher for DGDR than for any UKF-based method. In this case, despite considering biomarkers in the DGDR method like the resting membrane potential, which are expected to contribute to  $\theta_{K1}$  identification, the UKF-based methods can deliver more accurate results because they use all samples of the AP trace, both during the AP as well as during the resting phase, and thus have a larger amount of information to adjust  $\theta_{K1}$  estimation.

### 5.4.5 Estimation of Phosphorylation Levels of Cellular Substrates under $\beta$ -AS Conditions

The phosphorylation levels corresponding to the three cellular substrates most significantly contributing to AP changes under  $\beta$ -AS were estimated using our proposed DGDR-UKF method and compared with other tested methods. To the best of our knowledge, this is the first study where the phosphorylation levels of a  $\beta$ -A signaling model have been estimated, together with other state variables, based on the static and dynamic AP changes induced by  $\beta$ -AS. The results obtained with our proposed combined method were generally better than those of individual DGDR and UKF methods. Nevertheless, it should be noted that the average mean absolute errors obtained for phosphorylation levels under  $\beta$ -AS were higher than those obtained for ionic conductances at baseline. This can be partly explained because the errors in the estimated baseline conductances were propagated to the estimation of the phosphorylation levels, as the latter were calculated based on the corresponding APs estimated at baseline.

Although simultaneous estimation of ionic conductances and phosphorylation levels under  $\beta$ -AS could be thought of, this turns out to be unfeasible due to the multiplicative relation of ionic conductances and phosphorylation levels in the coupled electrophysiological-adrenergic signaling model. On the basis of such multiplicative relation, many combinations of conductance and phosphorylation level values could lead to the same estimation results even if the estimated parameter values were in fact far from their actual values.

### 5.4.6 Characterization of Spatio-Temporal AP Variability from Parameter Estimates

It is a main purpose of this study to propose a method suitable for investigation of temporal and spatial variability in human ventricular repolarization, with one-to-one identification of an underlying computational AP model for each experimentally available voltage trace. Provided data is available at baseline and under  $\beta$ -AS conditions, our proposed DGDR-UKF method can identify the specific electrophysiological and  $\beta$ -A signaling characteristics at those two conditions. This method was indeed able to precisely reproduce the AP shape, duration and variability of individual AP traces,

rendering statistical distributions of the errors in the estimation of APD and STV remarkably more concentrated around 0 than those obtained with other tested methods, particularly when comparing with the DGDR method.

On top of the DGDR-UKF method rendering better match between actual and estimated AP-derived biomarkers than other methods, it led to improved match between actual and estimated voltage traces, as illustrated in section 5.3.6. This can be justified on the basis that our methodology provides estimates of not only the parameter values but of the complete vector of model state variables, which allows for more accurate AP reconstruction than that based on estimated parameter values only.

### 5.4.7 Limitations and Future Works

In this work a total of 11 different human ventricular cell model parameters have been identified, corresponding to 8 ionic current conductances at baseline and 3 phosphorylation levels under  $\beta$ -AS. Future studies could include estimation of additional ionic currents conductances (e.g. for  $I_{Cab}$ ,  $I_{Nab}$ ,  $I_{Kb}$  or  $I_{pCa}$ ), phosphorylation levels (e.g. for ryanodine receptors, phospholamban or troponin I) or time constants of ionic gates (e.g.  $\tau_{xrs}$ ,  $\tau_{xs1}$  or  $\tau_{xk1}$ ).

To test the performance of our proposed methodology for estimation of model parameters and one-to-one replication of AP traces and AP-derived biomarkers, synthetic voltage traces were generated at 1 Hz stimulation frequency. Future studies could test the extent to which the estimation performance is improved by applying the proposed DGDR-UKF method onto voltage traces obtained at different stimulation frequencies. In addition, voltage traces could be generated under different ionic blocks to offer additional information to be used for parameter identification, which could prove particularly useful for identification of  $\theta_{Ks}$ ,  $\theta_{NaCa}$ ,  $\theta_{NaK}$ , whose estimation was the most challenging in the present work.

A set of AP-derived biomarkers were used in the DGDR method and, consequently, in the DGDR-UKF method. Those biomarkers reflect AP characteristics related to its upstroke, repolarization and resting potential as well as temporal APD variability. Novel AP-derived biomarkers reflecting additional information from the AP notch and plateau phases could help in the identification of model parameters, like  $\theta_{CaL}$  and  $\theta_{to}$ , thus globally improving the performance of the DGDR method and of the combined DGDR-UKF method.

This study has presented the combined DGDR-UKF method and has assessed its performance over a large set of synthetically generated AP traces. As a next step, the proposed method could be tested over experimental AP traces recorded from human ventricular cardiomyocytes or even extend the method to be applied onto voltage traces measured from human ventricular tissues. This would allow identification of underlying computational tissue models with representation of cell-to-cell electrical coupling.

## 5.5 Conclusion

A novel methodology based on the combined use of DGDR, with Automatic Generation of Biomarkers, and the UKF has been proposed to estimate parameters and state variables of an underlying human ventricular AP model for any given input voltage trace. The proposed methodology is tested over synthetic voltage traces generated from an experimentally-calibrated population of stochastic human ventricular cell models at baseline and under  $\beta$ -AS. The combined methodology remarkably improves the estimation performance of individual DGDR and UKF methods while reducing the computational cost. The estimated ionic current conductances at baseline conditions and phosphorylation levels of cellular substrates under  $\beta$ -AS allow for computational characterization of spatio-temporal ventricular repolarization, which can prove very useful to investigate variability changes induced by disease or drugs, uncover its underlying ionic mechanisms and establish a relationship with arrhythmic risk.



# 6 | Conclusions and Future Work

---

6.1	Conclusions . . . . .	131
6.1.1	General Conclusions . . . . .	131
6.1.2	Interactions between LF Oscillations and Temporal Variability in Human Ventricular Repolarization following Sympathetic Provocation: Mechanisms and Relation to Risk . . . . .	132
6.1.3	Theoretical Characterization of Spatio-Temporal Variability in Human Ventricular Repolarization at Baseline and following Sympathetic Provocation . . . . .	133
6.2	Future Work . . . . .	134

---

## 6.1 Conclusions

### 6.1.1 General Conclusions

This thesis investigates temporal and spatial variability in human ventricular repolarization by building computational stochastic AP models that couple theoretical descriptions of electrophysiology, calcium dynamics, mechanical stretch and  $\beta$ -A signaling. The constructed models are used to dissect the mechanisms underlying the experimentally observed interactions between a particular type of temporal variability associated with low-frequency oscillations of APD and the overall beat-to-beat APD variability quantified by the standard deviation or the STV of the APD series. Common ionic factors potentiating those two phenomena in response to increased sympathetic activity are elucidated and shown to be factors facilitating the generation of sympathetically-induced arrhythmic events. These findings are reached by using a population of models calibrated with experimental data regarding physiologically plausible ranges for a set of biomarkers describing AP shape, duration and amplitude characteristics. However, such calibration does not guarantee that the constructed population shares the same statistical distribution for each AP biomarker as the experimental data it was based on and not at all that each model in the population represents the measurements of an individual human ventricular cardiomyocyte. Based on such considerations, this thesis subsequently explores the use of methodologies for

parameter and state estimation that allow identifying an underlying computational AP model for each given voltage trace, both at baseline and following  $\beta$ -AS. Of all tested methodologies, the one based on combining DGDR with UKF is found to provide the most accurate results in terms of estimation of ionic current conductances at baseline and of phosphorylation levels under  $\beta$ -AS. Both temporal and spatial variability of AP repolarization are shown to be precisely reproduced by this combined DGDR-UKF methodology. Provided experimental human ventricular AP traces, or additional experimental measurements, are available, the population of models constructed by the DGDR-UKF methodology to fit such measurements would render a well suited computational ground to more robustly investigate the causes and consequences of spatio-temporal variability in its different forms. All in all, the research in this thesis offers a solid basis for future studies aiming at improving arrhythmic risk stratification and guiding the search for more efficient anti-arrhythmic therapies.

### **6.1.2 Interactions between LF Oscillations and Temporal Variability in Human Ventricular Repolarization following Sympathetic Provocation: Mechanisms and Relation to Risk**

Chapter 2 investigates the experimentally reported interactions between LF oscillations of APD and BVR following enhanced sympathetic activity. A population of stochastic human ventricular AP models with representation of cellular electrophysiology, calcium dynamics, mechanics and  $\beta$ -A signaling is proposed, which allows reproducing the concomitant increments in LF oscillatory behavior and BVR in response to SP. High spatial (i.e. inter-cellular) variability is quantified, in line with experimental observations, with some cells showing little increments whereas others present exaggerated increases in the two phenomena following enhanced sympathetic activity. The main ionic contributors to such inter-individual variability are dissected by ARD analysis and found to be related to the magnitude of the  $I_{Kr}$ ,  $I_{K1}$  and  $I_{CaL}$  currents. Under disease conditions involving reduced repolarization reserve and  $Ca^{2+}$  overload, electrical instabilities and arrhythmogenic events occur in some virtual cells, which by CCA are determined to be driven by the same ionic factors underlying elevated LF oscillations and BVR.

Chapter 3 deals with investigation of the time for the appearance of the LF oscillatory behavior whose magnitude was explored in Chapter 2 as a particular form of temporal repolarization variability. By using a population of models as in Chapter 2 and by developing an algorithm for robust quantification of the time lapse for LF oscillations to be manifested, such lapse is characterized to vary between a few seconds to more than three minutes. Prior stimulation of  $\beta$ -adrenoceptors remarkably reduces such time lapse. In terms of its underlying mechanisms, phasic mechanical stretch is found to induce oscillations in an almost immediate manner, whereas phasic  $\beta$ -AS is shown to induce a much more slow response, in agreement with experimentally analyzed data on ventricular cardiomyocytes subjected to ISO. Such slow response is



mediated by the phosphorylation and dephosphorylation kinetics of the  $I_{K_s}$  current. Consequently, depending on the magnitude of the  $I_{K_s}$  current of each individual cell, the time lapse may extensively vary. An inverse relationship between the time lapse (investigated in Chapter 3) and the magnitude (investigated in Chapter 2) of LF oscillations of APD is demonstrated, being such a relationship more accentuated in cells susceptible to develop arrhythmogenic events in response to SP under disease conditions.

### 6.1.3 Theoretical Characterization of Spatio-Temporal Variability in Human Ventricular Repolarization at Baseline and following Sympathetic Provocation

Chapter 4 proposes a novel methodology to construct computational populations of models that more faithfully recapitulate available experimental evidences. The virtual populations constructed in Chapter 2 and Chapter 3 are based on initially generating a large set of models, which are subsequently calibrated based on physiological ranges reported in the literature for a number of AP characteristics, including its duration, shape and amplitude at several relevant time points. Even if the results obtained with such models closely match experimental findings in terms of sympathetically-mediated LF oscillations and BVR, the method used to develop and calibrate the population of models does not guarantee that each individual cell of the population represents the characteristics of a human ventricular myocyte. It is for that reason that Chapter 4 deals with the development of individualized stochastic AP models directly fed with a voltage trace as could be measured experimentally. The methodology proposed in Chapter 4 is based on the formulation of nonlinear state-space representations and the use of the UKF algorithm to estimate the ionic current conductances of an underlying AP model provided a given voltage signal is input into the methodology. Tests are conducted over experimental and synthetic AP signals to demonstrate the ability of this UKF-based methodology to filter out the input voltage signals, estimate both parameters and state variables of an AP model and replicate the distributions of AP-based markers, including some describing BVR.

Chapter 5 deals with two relevant improvements to the methodology proposed in Chapter 4. On the one hand, identification of an underlying AP model for a given voltage signal is carried out not only for signals recorded at baseline but, importantly, also for signals recorded under  $\beta$ -AS. Considering the important role of  $\beta$ -AS in modulating spatio-temporal human ventricular repolarization variability and in facilitating the development of arrhythmias upon elevation of such variability, the possibility to theoretically characterize AP variability under  $\beta$ -AS is of high interest. On the other hand, the method developed in Chapter 4 has a high computational load due to its long convergence time. In Chapter 5 a methodology for model parameter and state estimation is proposed that combines the UKF method of Chapter 4 with the DGDR method including automatic generation of biomarkers to improve its performance and accelerate its convergence by either initializing or updating (along time) the UKF estimates with

those provided by DGDR. In contrast to Chapter 4, where only ionic current conductances at baseline were estimated, the approach presented in Chapter 5 additionally provides estimates for the phosphorylation levels of cellular substrates in response to  $\beta$ -AS. Also in this case, the new approach provides one-to-one matching between the input AP trace and the set of estimated ionic conductances and phosphorylation factors. The performance of the DGDR-UKF method is shown to be remarkably better than that of the individual DGDR and UKF methods while the computational load is significantly reduced. A highly accurate reproduction of AP traces and AP-derived biomarkers is proved. Consequently, the combined DGDR-UKF methodology is suggested for any future study aimed at theoretically investigating the mechanisms and the relation to arrhythmic risk associated with spatio-temporal variability in human ventricular repolarization. The only requirement for the use of such methodology is to have available experimental AP traces from a number of cells to construct the matched population of computational models.

## 6.2 Future Work

- The stochastic human AP computational models built in this thesis have been based on the ORd epicardial model [5], which was developed from extensive undiseased human data. Due to the intrinsic characteristics of the ORd model when simulating baseline conditions, the  $I_{K_s}$  current has much smaller influence on the AP shape and duration than other computational models such as the Ten TP06 model [31]. When the mechanisms underlying LF oscillations of APD and BVR were ascertained in this thesis, the  $I_{K_s}$  current was found to have little contribution, which might be related to the fact of using the ORd model for the investigations. Although based on previous work [57] qualitative conclusions are expected to remain the same, quantitative differences in the role of certain ionic currents, like  $I_{K_s}$ , might be found.

Similarly, when identifying an underlying human ventricular cell model for a given input AP trace and estimating ionic current conductances at baseline, the largest estimation error was obtained for the  $I_{K_s}$  current conductance by all tested estimation methods, which could again be explained by the fact of using the ORd model as the basis for building the models employed in this thesis.

Future studies could replicate the investigations here described while using other human computational cell models and could assess whether the conclusions reached in this thesis remain qualitatively or quantitatively the same.

- The research of this thesis has focused on the single cell level. Although the phenomena of interest for our research, namely LF oscillations of APD and BVR, occur in single cells, both the mechanisms and the consequences of the oscillations and the variability may be modulated by other factors involved in tissue and whole-heart levels. Future studies could extend the present work to run tissue simulations based on the cell simulations of this thesis. Nevertheless,

when investigating disease conditions, like heart failure or ischemic heart disease, cell-to-cell coupling has been shown to be remarkably reduced, which would render tissue results close to the cell results presented here.

- The populations of models developed in this thesis have been generated by varying the conductances of a number of ionic currents, including  $I_{Ks}$ ,  $I_{Kr}$ ,  $I_{to}$ ,  $I_{CaL}$ ,  $I_{K1}$ ,  $I_{Na}$ ,  $I_{NaCa}$  and  $I_{NaK}$ . The selection of these currents was based on their reported contributions to AP shape and duration, particularly in relation to repolarization, which is the main research target of this thesis. Other background and plateau currents, such as  $I_{Nab}$ ,  $I_{Kb}$ ,  $I_{Cab}$  or  $I_{pCa}$ , might still add relevant information and could be the focus of further research. Also, on top of varying ionic current conductances to build the populations of models, time constants of ionic gates could help to explain additional mechanisms for human ventricular spatio-temporal variability and could be added to the stochastic models developed in this thesis. This would allow for more degrees of freedom and might render more accurate results, both in terms of reproducing available experimental data by constructed AP models and in terms of the research conducted with those AP models.
- The stochastic human ventricular AP models developed in this thesis departed from deterministic versions built from the ORd model in which stochasticity was added into the four main ionic currents active during AP repolarization, i.e.  $I_{Ks}$ ,  $I_{Kr}$ ,  $I_{to}$  and  $I_{CaL}$ . Although the investigation of spatio-temporal variability in this thesis focuses on the repolarization phase and these four currents are the ones expected to contribute the most to the variability measures, additional work could be undertaken in which stochasticity were added to the ionic gates of other ionic currents. Of particular relevance is the  $I_{NaL}$  current. More work would be required to formulate the SDEs for the random gating of this current as well as to estimate the associated number of channels, as in the ORd model the fast and late sodium currents are not considered to be separate channels but rather to represent different gating modes being functionally separated in time.
- Some of the simulations of this thesis were run at more than one stimulation frequency. However, other simulations were carried out while stimulating the cells at 1 Hz pacing frequency only. The use of several stimulation frequencies for all conducted research could certainly improve the identification of computational AP models representative of human ventricular data and could be of major interest for the investigations of the mechanisms underlying spatio-temporal variability and its relation to arrhythmic risk. Future studies could extend the work of this thesis by including various stimulation frequencies.
- For the investigation of human ventricular spatio-temporal variability, several measures have been investigated. Still, novel markers quantifying variability in the overall AP morphology or in the morphology during the AP repolarization phase could be added for further characterizations.

- For theoretical characterization of spatio-temporal repolarization, variability methodologies based on DGDR and UKF were proposed in this thesis to estimate the parameters and state variables of underlying AP models. These methodologies allowed to accurately reproduce beat-to-beat and cell-to-cell variability at baseline and under  $\beta$ -AS. For investigation of additional conditions or to further improve the estimation accuracy, other methodologies based on Artificial Neural Networks, the combination of Linear Kalman Filters with Reduced Order Models or Bayesian Optimization could be explored in subsequent studies.

# Glossary

ANS	Autonomic Nervous System
AP	Action Potential
APD	Action Potential Duration
ARD	Automatic Relevance Determination
ARI	Activation Recovery Interval
AV	Atrio Ventricular
BVR	Beat-to-beat Variability of Repolarization
$\beta$ -A	$\beta$ -Adrenergic
$\beta$ -AS	$\beta$ -Adrenergic Stimulation
$\text{Ca}^{2+}$	Calcium
cAMP	3'-5'-Cyclic Adenosine MonoPhosphate
CaMKII	Calmoduline Kinase
CAVB	Chronic Atrioventricular Block
CCA	Canonical Correlation Analysis
CL	Cycle Length
CVD	Cardio Vascular Disease
DAD	Delayed After-Depolarization
DGDR	Double Greedy Dimension Reduction
EAD	Early After-Depolarization
ECG	Electrocardiogram
EGM	Electrogram
EKF	Extended Kalman Filter
GP	Gaussian Process
HH	Hodgkin & Huxley model
HR	Heart Rate
$I_{Ca}$	Calcium current
$I_{CaL}$	L-type calcium current
$I_K$	Potassium current
$I_{K1}$	Inward rectifier potassium current
$I_{Kr}$	Rapid delayed rectifier potassium current
$I_{Ks}$	Slow delayed rectifier potassium current
$I_{Na}$	Sodium current

$I_{NaCa}$	Sodium-calcium pump current
$I_{NaK}$	Sodium-potassium exchanger current
$I_{SAC}$	Stretch Activated Channels current
$I_{SAC,ns}$	Non-Specific cationic Stretch Activated Channels current
$I_{SAC,K}$	Potassium Specific Stretch Activated Channels current
$I_{to}$	Transient outward potassium current
INI	Intialization of UKF method by DGDR
ISO	Isoproterenol
$K^+$	Potassium
KF	Kalman Filter
LF	Low Frequency
LQT1	Long QT syndrome Type 1
LQT2	Long QT syndrome Type 2
$L_s$	Length of state vector
LTV	Long Term Variability
MCMC	Markov Chain Monte Carlo
MEF	Mechano-Electrical Feedback
ML-II	Maximun Likelihood type II
MM	Moment-Matching
NLTV	Normalized Long Term Variability
NKA	$Na^+ - K^+ - ATPase$
NSTV	Normalized Short Term Variability
NPLF	Normalized Power of Low Frequency
NPHF	Normalized Power of High Frequency
NSD	Normalized Standard Deviation
ODE	Ordinary Differential Equation
ORd	O'Hara-Virág-Varró-Rudy epicardial 2011 model
PDR	Periodic Repolarization Dynamics
PLF	Power of Low Frequency band
PHF	Power of High Frequency band
PKA	Protein Kinase A
PLM	Phospholemman
PSD	Power Spectral Density
RMP	Resting Membrane Potential
RRR	Reduced Repolarization Reserve
RyR	Ryanodine Receptors

---

SA	Sino Atrial
SAC	Stretch Activated Channel
SD	Standard Deviation
SDE	Stochastic Differential Equation
SERCA	Sarcoplasmic Reticulum Ca-ATPase
SL	Sarcomere Length
SNR	Signal-to-Noise Ratio
SP	Sympathetic Provocation
SR	Sarcoplasmic Reticulum
STV	Short-Term Variability
$\tau_{APD}$	Time lapse of APD oscillations
TdP	Torsade des Pointes
TP06	Ten Tusscher-Panfilov 2006 model
$V_{peak}$	Peak membrane potential in the upstroke phase
UKF	Unscented Kalman Filter
UP	Updating of UKF method by DGDR





# Publications Derived from the Thesis

## *Publications in Journal Articles*

- **D. A. Sampedro Puente**, J. Fernandez Bes, L. Virág, A. Varró, E. Pueyo. “Data-driven Identification of Stochastic Model Parameters and State Variables: Application to the Study of Cardiac Beat-to-beat Variability”. *IEEE Journal of Biomedical and Health Informatics*, 2019. DOI: 10.1109/JBHI.2019.2921881.
- **D. A. Sampedro Puente**, J. Fernandez-Bes, B. Porter, S. Duijvenboden, P. Taggart E. Pueyo. “Mechanisms Underlying Interactions Between Low-Frequency Oscillations and Beat-to-Beat Variability of Cellular Ventricular Repolarization in Response to Sympathetic Stimulation: Implications for Arrhythmogenesis.” *Frontiers in Physiology*, 2019. DOI: 10.3389/fphys.2019.00916.
- **D. A. Sampedro Puente**, J. Fernandez-Bes, N. Szentandrassy, P. P. Nánasi, P. Taggart and E. Pueyo. “Time Course of Low-Frequency Oscillatory Behavior in Human Ventricular Repolarization Following Enhanced Sympathetic Activity and Relation to Arrhythmogenesis.” *Frontiers in Physiology*, 2019. DOI: 10.3389/fphys.2019.01548.
- **D. A. Sampedro Puente**, F. Raphel, J. Fernandez-Bes, P. Laguna, D. Lombardi and E. Pueyo “Characterization of Spatio-Temporal Cardiac Action Potential Variability at Baseline and under  $\beta$ -Adrenergic Stimulation by Combined Unscented Kalman Filter and Double Greedy Dimension Reduction.” *IEEE Journal of Biomedical and Health Informatics*, 2019. Submitted, under review process.
- S. van Duijvenboden, B. Porter, E. Pueyo, **D. A. Sampedro Puente**, J. Fernandez-Bes, B. Sidhu, J. Gould, M. Orini, Martin Bishop, B. Hanson, P. Lambiase, R. Razavi, C. A. Rinaldi, J. S. Gill and P. Taggart. “Complex Interaction between Low-Frequency APD Oscillations and Beat-to-Beat APD Variability in Humans is Governed by the Sympathetic Nervous System.” *Frontiers in Physiology*, 2019. DOI: 10.3389/fphys.2019.01582.

## *Publications in Conference Proceedings*

- **D. A. Sampedro Puente**, J. Fernandez Bes, E. Pueyo Paules. “Unscented Kalman Filter for Unobservable Parameter Estimation in Heart Cell Signals.” *V Jornada de Jóvenes Investigadores del I3A*, Zaragoza (Spain), May 2016, pp. 27-28.
- **D. A. Sampedro Puente**, J. Fernandez-Bes, E. Pueyo. “Differential Responses to  $\beta$ -Adrenergic Stimulation in the Long-QT Syndrome Type 1: Characterization and Mechanisms.” *XLIV International Conference on Computing in Cardiology CINC*, Rennes (France), September 2017, pp. 1-4, DOI:10.22489/CinC.2017.250-453.
- J. Fernandez-Bes, **D. A. Sampedro Puente**, E. Pueyo. “Identification of Parameters describing Phenomenological Cardiac Action Potential Models using Sigma-Point Methods.” *XLIV International Conference on Computing in Cardiology CINC*, Rennes (France), September 2017, pp. 1-4. DOI:10.22489/CinC.2017.060-109.
- **D. A. Sampedro Puente**, J. Fernandez-Bes, E. Pueyo. “Caracterización de las respuestas a la estimulación beta-adrenérgica en escenarios de síndrome LQT1.” *XXXV Congreso de la Sociedad Española de Ingeniería Biomédica CASEIB*, Bilbao (Spain). November 2017. (pp. 337-340)
- J. Fernandez-Bes, **D. A. Sampedro Puente**, E. Pueyo. “Unscented Kalman Filter para el ajuste de parámetros de modelos fenomenológicos de potencial de acción.” *XXXV Congreso de la Sociedad Española de Ingeniería Biomédica CASEIB*, Bilbao (Spain). November 2017. (pp. 499-502)
- **D. A. Sampedro Puente**; J. Fernandez-Bes; B. Porter; S. Duijvenboden; P. Taggart; E. Pueyo Paules. “Mechanisms underlying interactions between low-frequency oscillations and beat-to-beat repolarization variability in human ventricles under sympathetic provocation.” *European Working Group on Cardiac Cellular Electrophysiology EWGCCE*. Essen (Germany). June 2018.
- **D. A. Sampedro Puente**, L. Garcia Mendivil, E. Ramos Marques, A. Oliván Viguera, J. Fernandez-Bes, E. Pueyo. “Cardiac dynamics and arrhythmic risk in aged and failing hearts: insights from experimental and computational research.” *V Virtual Physiological Human Conference VPH2018*, Zaragoza, (Spain). September 2018. (p.14)
- **D. A. Sampedro Puente**, J. Fernandez-Bes, B. Porter, S. Duijvenboden, P. Taggart, E. Pueyo. “Mechanisms underlying interactions between low-frequency oscillations and beat-to-beat repolarization variability under sympathetic provocation.” *V Virtual Physiological Human Conference VPH2018*, Zaragoza, (Spain). September 2018. (p.33)

- J. Fernandez-Bes, **D. A. Sampedro Puente**, E. Pueyo Paules. “A Bayesian Filtering methodology to identify key drivers of ventricular repolarization variability.” *V Virtual Physiological Human Conference VPH2018*, Zaragoza, (Spain). September 2018. (p.19)
- J. Fernandez Bes, **D. A. Sampedro Puente**, P. Taggart, E. Pueyo. “Time Course of Cardiac Electrical Oscillatory Behavior in Response to Enhanced Sympathetic Activity and Relation to Arrhythmogenesis.” *10th European Study Group on Cardiovascular Oscillations ESGCO*. Viena, (Austria). September 2018.
- **D. A. Sampedro Puente**, J. Fernandez-Bes, A. Olivan-Viguera, M. Perez-Zabalza, S. Orós, S. van Duijvenboden, B. Porter, P. Taggart, E. Pueyo. “The interplay of autonomic and mechanical modulation of ventricular repolarization in Human.” *8th International Workshop Cardiac Mechano-Electric Coupling and Arrhythmias*. Freiburg, (Germany). September 2019.



# Bibliography

- [1] “Cardiovascular diseases report,” *World Health Organisation*, 2017.
- [2] “Inebase,” *Instituto Nacional de Estadística de España*, 2017.
- [3] R. M. John, U. B. Tedrow, B. A. Koplan, C. M. Albert, L. M. Epstein, M. O. Sweeney, A. L. Miller, G. F. Michaud, and W. G. Stevenson, “Ventricular arrhythmias and sudden cardiac death,” *The Lancet*, vol. 380, no. 9852, pp. 1520–1529, 2012.
- [4] M. J. Shen and D. P. Zipes, “Role of the autonomic nervous system in modulating cardiac arrhythmias,” *Circ. Res.*, vol. 114, no. 6, pp. 1004–21, 2014.
- [5] T. O’Hara, L. Virág, A. Varró, and Y. Rudy, “Simulation of the undiseased human cardiac ventricular action potential: model formulation and experimental validation,” *PLoS Comput. Biol.*, vol. 7, no. 5, p. e1002061, 2011.
- [6] L. Sörnmo and P. Laguna, *Bioelectrical Signal Processing in Cardiac and Neurological Applications*. Elsevier, 2005.
- [7] A. C. Guyton and J. E. Hall, *Textbook of medical physiology*. Elsevier Inc., 2006.
- [8] E. N. Marieb and K. Hoehn, *Human Anatomy & Physiology*. Pearson, 2013.
- [9] F. H. Martini, J. L. Nath, and E. F. Bartholomew, *Fundamentals of anatomy & Physiology*. Pearson, 2015.
- [10] B. Sakmann and E. Neher, *Single-Channel Recording*. Springer, 1995.
- [11] K. Lollike, N. Borregaard, and M. Lindau, “Capacitance Flickers and Pseudoflickers of Small Granules, Measured in the Cell-Attached Configuration,” *Biophys. J.*, vol. 75, no. 1, pp. 53–59, 1998.
- [12] S. Veitinger, P. U. Marburg, I. of Cytobiology, and Cytopathology, “The patch-clamp technique: An introduction.”
- [13] M. Attin and W. T. Clusin, “Basic Concepts of Optical Mapping Techniques in Cardiac Electrophysiology,” *Biol. Res. Nurs.*, vol. 11, no. 2, pp. 195–207, 2009.
- [14] S. Niederer, P. Hunter, and N. Smith, “A Quantitative Analysis of Cardiac Myocyte Relaxation: A Simulation Study,” *Biophys. J.*, vol. 90, no. 5, pp. 1697–1722, 2006.
- [15] P. Kohl, C. Bollensdorff, and A. Garny, “Effects of mechanosensitive ion channels on ventricular electrophysiology: experimental and theoretical models,” *Exp. Physiol.*, vol. 91, no. 2, pp. 307–321, 2006.

- [16] L. D. Weise and A. V. Panfilov, "A discrete electromechanical model for human cardiac tissue: effects of stretch-activated currents and stretch conditions on restitution properties and spiral wave dynamics," *PLoS One*, vol. 8, no. 3, p. e59317, 2013.
- [17] P. Taggart and M. Lab, "Cardiac mechano-electric feedback and electrical restitution in humans," *Prog. Biophys. Mol. Biol.*, vol. 97, no. 2-3, pp. 452–460, 2008.
- [18] K. E. Barrett, S. M. Barman, S. Boltano, and H. L. Brooks, *Ganong's Review of Medical Physiology, 25th Ed.* McGraw-Hill, 2015.
- [19] A. Alcaine Otín, *Intracardiac Signal Processing for Mapping and Characterising Cardiac Arrhythmias*. University of Zaragoza, 2016.
- [20] B. Hanson, N. Child, S. Van Duijvenboden, M. Orini, Z. Chen, R. Coronel, C. A. Rinaldi, J. S. Gill, J. S. Gill, and P. Taggart, "Oscillatory behavior of ventricular action potential duration in heart failure patients at respiratory rate and low frequency," *Front. Physiol.*, vol. 5, p. 414, 2014.
- [21] Cables and Sensors, "12-lead ecg placement guide with illustrations,"
- [22] A. L. Hodgkin and A. F. Huxley, "A quantitative description of membrane current and its application to conduction and excitation in nerve," *J. Physiol. (Lond.)*, vol. 117, no. 4, pp. 500–544, 1952.
- [23] D. Noble, A. Garny, and P. J. Noble, "How the Hodgkin–Huxley equations inspired the cardiac physiome project," *J. Physiol.*, vol. 590, no. 11, pp. 2613–2628, 2012.
- [24] L. J. H. P. Lloyd, C.M. and P. Nielsen, "A quantitative description of membrane current and its application to conduction and excitation in nerve. hodgking & huxley model, 1952," *The CellML Model Repository (Bioinformatics)*, 2008.
- [25] S. Albreiki, A. AlAli, and R. M. Shubair, "Coding brain neurons via electrical network models for neuro-signal synthesis in computational neuroscience," in *2016 5th International Conference on Electronic Devices, Systems and Applications (ICEDSA)*, pp. 1–5, IEEE, 2016.
- [26] C. E. Dangerfield, D. Kay, and K. Burrage, "Modeling ion channel dynamics through reflected stochastic differential equations," *Phys. Rev. E.*, vol. 85, no. 5, p. 051907, 2012.
- [27] H. Krause, H. Antoni, and A. Fleckenstein, "An electronic model for the formation of local and transmitted stimuli on the myocardium fibers based upon variable current-voltage characteristics for potassium and sodium ions," *Pflugers Arch Gesamte Physiol Menschen Tiere.*, vol. 289, no. 1, pp. 12–36, 1966.
- [28] L. Priebe and D. J. Beuckelmann, "Simulation study of cellular electric properties in heart failure," *Circulation Research*, vol. 82, no. 11, pp. 1206–1223, 1998.

- [29] K. H. W. J. ten Tusscher, D. Noble, P. J. Noble, and A. V. Panfilov, "A model for human ventricular tissue," *Am. J. Physiol. Heart Circ. Physiol.*, vol. 286, no. 4, pp. H1573–H1589, 2004.
- [30] J. Carro, J. F. Rodríguez, P. Laguna, and E. Pueyo, "A human ventricular cell model for investigation of cardiac arrhythmias under hyperkalaemic conditions," *Philos. Trans. R. Soc., A*, vol. 369, no. 1954, pp. 4205–4232, 2011.
- [31] K. H. ten Tusscher and A. V. Panfilov, "Alternans and spiral breakup in a human ventricular tissue model," *Am. J. Physiol.: Heart Circ. Physiol.*, vol. 291, no. 3, pp. H1088–H1100, 2006.
- [32] N. A. Trayanova, J. Constantino, and V. Gurev, "Electromechanical models of the ventricles," *Am. J. Physiol. Heart Circ. Physiol.*, vol. 301, no. 2, pp. H279–H286, 2011.
- [33] E. Pueyo, M. Orini, J. F. Rodríguez, and P. Taggart, "Interactive effect of beta-adrenergic stimulation and mechanical stretch on low-frequency oscillations of ventricular action potential duration in humans," *J. Mol. Cell. Cardiol.*, vol. 97, pp. 93–105, 2016.
- [34] J. J. Saucerman and A. D. McCulloch, "Mechanistic systems models of cell signaling networks: a case study of myocyte adrenergic regulation," *Prog. Biophys. Mol. Biol.*, vol. 85, no. 2-3, pp. 261–278, 2004.
- [35] A. R. Soltis and J. J. Saucerman, "Synergy between CaMKII substrates and  $\beta$ -adrenergic signaling in regulation of cardiac myocyte Ca<sup>2+</sup> handling," *Biophys. J.*, vol. 99, no. 7, pp. 2038–2047, 2010.
- [36] Y. Xie, E. Grandi, J. L. Puglisi, D. Sato, and D. M. Bers, " $\beta$ -adrenergic stimulation activates early afterdepolarizations transiently via kinetic mismatch of PKA targets," *J. Mol. Cell. Cardiol.*, vol. 58, pp. 153–161, 2013.
- [37] J. A. Negroni, S. Morotti, E. C. Lascano, A. V. Gomes, E. Grandi, J. L. Puglisi, and D. M. Bers, " $\beta$ -adrenergic effects on cardiac myofilaments and contraction in an integrated rabbit ventricular myocyte model," *J. Mol. Cell. Cardiol.*, vol. 81, pp. 162–175, 2015.
- [38] M. Baumert, A. Porta, M. A. Vos, M. Malik, J.-P. Couderc, P. Laguna, G. Piccirillo, G. L. Smith, L. G. Tereshchenko, and P. G. Volders, "QT interval variability in body surface ECG: measurement, physiological basis, and clinical value: position statement and consensus guidance endorsed by the European Heart Rhythm Association jointly with the ESC Working Group on Cardiac Cellular Electrophysiology," *Europace*, vol. 18, no. 6, pp. 925–944, 2016.
- [39] M. B. Thomsen, P. G. Volders, J. D. Beekman, J. Matz, and M. A. Vos, "Beat-to-beat variability of repolarization determines proarrhythmic outcome in dogs susceptible to drug-induced Torsades de Pointes," *J. Am. Coll. Cardiol.*, vol. 48, no. 6, pp. 1268–1276, 2006.

- [40] L. Tereshchenko, B. Fetits, P. Domitrovich, B. Lindsay, and R. Berger, "Prediction of ventricular tachyarrhythmias by intracardiac repolarization variability analysis," *Circ.: Arrhythmia Electrophysiol.*, vol. 2, no. 3, p. 276, 2009.
- [41] M. Hinterseer, M. B. Thomsen, B.-M. Beckmann, A. Pfeufer, R. Schimpf, H.-E. Wichmann, G. Steinbeck, M. A. Vos, and S. Kaab, "Beat-to-beat variability of QT intervals is increased in patients with drug-induced long-QT syndrome: a case control pilot study," *Eur. Heart J.*, vol. 29, no. 2, pp. 185–190, 2008.
- [42] M. Hinterseer, B.-M. Beckmann, M. B. Thomsen, A. Pfeufer, M. Ulbrich, M. F. Sinner, S. Perz, H.-E. Wichmann, C. Lengyel, R. Schimpf, S. K. G. Maier, A. Varró, M. A. Vos, G. Steinbeck, and S. Kääh, "Usefulness of short-term variability of QT intervals as a predictor for electrical remodeling and proarrhythmia in patients with nonischemic heart failure," *Am. J. Cardiol.*, vol. 106, no. 2, pp. 216–20, 2010.
- [43] J. Paavola, H. Väänänen, K. Larsson, K. Penttinen, L. Toivonen, K. Kontula, M. Laine, K. Aalto-Setälä, H. Swan, and M. Viitasalo, "Slowed depolarization and irregular repolarization in catecholaminergic polymorphic ventricular tachycardia: a study from cellular  $\text{Ca}^{2+}$  transients and action potentials to clinical monophasic action potentials and electrocardiography," *Eurospace*, vol. 18, no. 10, pp. 1599–1607, 2015.
- [44] S. C. Wijers, D. J. Sprenkeler, A. Bossu, A. Dunnink, J. D. Beekman, R. Varkevisser, A. A. Hernández, M. Meine, and M. A. Vos, "Beat-to-beat variations in activation-recovery interval derived from the right ventricular electrogram can monitor arrhythmic risk under anesthetic and awake conditions in the canine chronic atrioventricular block model," *Heart Rhythm*, vol. 15, no. 3, pp. 442–448, 2018.
- [45] D. J. Gallacher, A. Van de Water, H. van der Linde, A. N. Hermans, H. R. Lu, R. Towart, and P. G. Volders, "In vivo mechanisms precipitating Torsades de Pointes in a canine model of drug-induced long-QT1 syndrome," *Cardiovas. Res.*, vol. 76, no. 2, pp. 247–256, 2007.
- [46] R. L. Verrier, T. Klingenheben, M. Malik, N. El-Sherif, D. V. Exner, S. H. Hohnloser, T. Ikeda, J. P. Martínez, S. M. Narayan, T. Nieminen, *et al.*, "Microvolt T-wave alternans: physiological basis, methods of measurement, and clinical utility-consensus guideline by International Society for Holter and Noninvasive Electrocardiology," *J. Am. Coll. Cardiol.*, vol. 58, no. 13, pp. 1309–1324, 2011.
- [47] J. Ramírez, M. Orini, J. D. Tucker, E. Pueyo, and P. Laguna, "Variability of ventricular repolarization dispersion quantified by time-warping the morphology of the T-waves," *IEEE Trans. Biomed. Eng.*, vol. 64, no. 7, pp. 1619–1630, 2017.
- [48] K. D. Rizas, T. Nieminen, P. Barthel, C. S. Zürn, M. Kähönen, J. Viik, T. Lehtimäki, K. Nikus, C. Eick, T. O. Greiner, *et al.*, "Sympathetic activity-associated periodic repolarization dynamics predict mortality following myocardial infarction," *J. Clin. Invest.*, vol. 124, no. 4, pp. 1770–1780, 2014.



- [49] K. D. Rizas, W. Hamm, S. Kääb, G. Schmidt, and A. Bauer, “Periodic repolarisation dynamics: a natural probe of the ventricular response to sympathetic activation,” *Arrhythm Electrophysiol Rev*, vol. 5, no. 1, p. 31, 2016.
- [50] K. D. Rizas, S. McNitt, W. Hamm, S. Massberg, S. Kääb, W. Zareba, J.-P. Couderc, and A. Bauer, “Prediction of sudden and non-sudden cardiac death in post-infarction patients with reduced left ventricular ejection fraction by periodic repolarization dynamics: MADIT-II substudy,” *Eur. Heart J.*, vol. 38, no. 27, pp. 2110–2118, 2017.
- [51] B. Porter, S. Van Duijvenboden, M. J. Bishop, M. Orini, S. Claridge, J. Gould, B. J. Sieniewicz, B. Sidhu, R. Razavi, C. A. Rinaldi, *et al.*, “Beat-to-Beat Variability of Ventricular Action Potential Duration Oscillates at Low Frequency During Sympathetic Provocation in Humans,” *Front. Physiol.*, vol. 9, p. 147, 2018.
- [52] B. Porter, M. J. Bishop, S. Claridge, J. Behar, B. J. Sieniewicz, J. Webb, J. Gould, M. O’Neill, C. A. Rinaldi, R. Razavi, *et al.*, “Autonomic modulation in patients with heart failure increases beat-to-beat variability of ventricular action potential duration,” *Front. Physiol.*, vol. 8, p. 328, 2017.
- [53] G. Antoons, D. M. Johnson, E. Dries, D. J. Santiago, S. Ozdemir, I. Lenaerts, J. D. Beekman, M. J. Houtman, K. R. Sipido, and M. A. Vos, “Calcium release near L-type calcium channels promotes beat-to-beat variability in ventricular myocytes from the chronic AV block dog,” *J. Mol. Cell. Cardiol.*, vol. 89, pp. 326–334, 2015.
- [54] K. Kistamás, N. Szentandrassy, B. Hegyi, K. Vaczi, F. Ruzsnavszky, B. Horvath, T. Banyasz, P. P. Nanasi, and J. Magyar, “Changes in intracellular calcium concentration influence beat-to-beat variability of action potential duration in canine ventricular myocytes,” *J. Physiol. Pharmacol.*, vol. 66, no. 1, pp. 73–81, 2015.
- [55] M. Lemay, E. de Lange, and J. P. Kucera, “Effects of stochastic channel gating and distribution on the cardiac action potential,” *J. Theor. Biol.*, vol. 281, no. 1, pp. 84–96, 2011.
- [56] E. Pueyo, A. Corrias, L. Virág, N. Jost, T. Szél, A. Varró, N. Szentandrassy, P. P. Nánási, K. Burrage, and B. Rodríguez, “A multiscale investigation of repolarization variability and its role in cardiac arrhythmogenesis,” *Biophys. J.*, vol. 101, no. 12, pp. 2892–2902, 2011.
- [57] E. Pueyo, C. Dangerfield, O. Britton, L. Virág, K. Kistamás, N. Szentandrassy, N. Jost, A. Varró, P. Nánási, K. Burrage, *et al.*, “Experimentally-based computational investigation into beat-to-beat variability in ventricular repolarization and its response to ionic current inhibition,” *PLoS One*, vol. 11, no. 3, p. e0151461, 2016.

- [58] P. P. Nánási, J. Magyar, A. Varró, and B. Ördög, “Beat-to-beat variability of cardiac action potential duration: underlying mechanism and clinical implications,” *Can. J. Physiol. Pharmacol.*, vol. 95, no. 10, pp. 1230–1235, 2017.
- [59] M. Zaniboni, A. E. Pollard, L. Yang, and K. W. Spitzer, “Beat-to-beat repolarization variability in ventricular myocytes and its suppression by electrical coupling,” *Am. J. Physiol.: Heart Circ. Physiol.*, vol. 278, no. 3, pp. H677–H687, 2000.
- [60] J. Magyar, T. Bányász, N. Szentandrásy, K. Kistamás, P. P. Nanasi, and J. Satin, “Role of gap junction channel in the development of beat-to-beat action potential repolarization variability and arrhythmias,” *Curr. Pharm. Des.*, vol. 21, no. 8, pp. 1042–1052, 2015.
- [61] M. Yamabe, S. N. Sanyal, S. Miyamoto, T. Hadama, S. Isomoto, and K. Ono, “Three Different Bradycardic Agents, Zatebradine, Diltiazem and Propranolol, Distinctly Modify Heart Rate Variability and QT-Interval Variability,” *Pharmacology*, vol. 80, no. 4, pp. 293–303, 2007.
- [62] B. Hegyi, J. Bossuyt, K. S. Ginsburg, L. M. Mendoza, L. Talken, W. T. Ferrier, S. M. Pogwizd, L. T. Izu, Y. Chen-Izu, and D. M. Bers, “Altered Repolarization Reserve in Failing Rabbit Ventricular Myocytes: Calcium and  $\beta$ -Adrenergic Effects on Delayed- and Inward-Rectifier Potassium Currents,” *Circ.: Arrhythmia Electrophysiol.*, vol. 11, no. 2, 2018.
- [63] D. M. Johnson, J. Heijman, C. E. Pollard, J.-P. Valentin, H. J. Crijns, N. Abi-Gerges, and P. G. Volders, “I<sub>Ks</sub> restricts excessive beat-to-beat variability of repolarization during beta-adrenergic receptor stimulation,” *J. Mol. Cel. Cardiol.*, vol. 48, no. 1, pp. 122–130, 2010.
- [64] N. Szentandrásy, K. Kistamás, B. Hegyi, B. Horváth, F. Ruzsnavszky, K. Vácz, J. Magyar, T. Bányász, A. Varró, and P. P. Nánási, “Contribution of ion currents to beat-to-beat variability of action potential duration in canine ventricular myocytes,” *Pflug. Arch. Eur. J. Phy.*, vol. 467, no. 7, pp. 1431–1443, 2015.
- [65] J. Heijman, A. Zaza, D. M. Johnson, Y. Rudy, R. L. Peeters, P. G. Volders, and R. L. Westra, “Determinants of beat-to-beat variability of repolarization duration in the canine ventricular myocyte: a computational analysis,” *PLoS Comput. Biol.*, vol. 9, no. 8, 2013.
- [66] D. M. Johnson, J. Heijman, E. F. Bode, D. J. Greensmith, H. van der Linde, N. Abi-gerges, D. A. Eisner, A. W. Trafford, and P. G. Volders, “Diastolic spontaneous calcium release from the sarcoplasmic reticulum increases beat-to-beat variability of repolarization in canine ventricular myocytes after  $\beta$ -adrenergic stimulation,” *Circ. Res.*, vol. 112, no. 2, pp. 246–256, 2013.
- [67] D. J. MacKay, “Bayesian methods for Backpropagation networks,” in *Models of Neural Networks III*, pp. 211–254, Springer, 1996.

- [68] H. Hotelling, "Relations between two sets of variates," *Biometrika*, vol. 28, no. 3/4, pp. 321–377, 1936.
- [69] M. D. McKay, R. J. Beckman, and W. J. Conover, "A comparison of three methods for selecting values of input variables in the analysis of output from a computer code," *Technometrics*, vol. 21, no. 2, p. 239, 1979.
- [70] D. Guo, Q. Liu, T. Liu, G. Elliott, M. Gingras, P. R. Kowey, and G.-X. Yan, "Electrophysiological Properties of HBI-3000: A New Antiarrhythmic Agent With Multiple-channel Blocking Properties in Human Ventricular Myocytes," *J. Cardiovasc. Pharmacol.*, vol. 57, no. 1, pp. 79–85, 2011.
- [71] O. J. Britton, A. Bueno-Orovio, L. Virág, A. Varró, and B. Rodriguez, "The electrogenic Na<sup>+</sup>/K<sup>+</sup> pump is a key determinant of repolarization abnormality susceptibility in human ventricular cardiomyocytes: A population-based simulation study," *Front. Physiol.*, vol. 8, p. 278, 2017.
- [72] N. Jost, A. Varro, V. Szuts, P. P. Kovacs, G. Seprényi, P. Biliczki, C. Lengyel, J. Prorok, M. Bitay, B. Ördög, J. Szabad, Z. Varga-Orvos, L. Puskas, D. Cotella, J. G. Papp, L. Virag, and S. Nattel, "Molecular basis of repolarization reserve differences between dogs and man," *Circulation*, vol. 118, no. 18, p. S342, 2008.
- [73] E. Grandi, F. S. Pasqualini, and D. M. Bers, "A novel computational model of the human ventricular action potential and Ca transient," *J. Mol. Cell. Cardiol.*, vol. 48, no. 1, pp. 112–121, 2010.
- [74] M. W. Veldkamp, A. C. van Ginneken, T. Opthof, and L. N. Bouman, "Delayed rectifier channels in human ventricular myocytes," *Circulation*, vol. 92, no. 12, pp. 3497–3504, 1995.
- [75] D. Fedida and W. R. Giles, "Regional variations in action potentials and transient outward current in myocytes isolated from rabbit left ventricle," *J. Physiol.*, vol. 442, pp. 191–209, 1991.
- [76] T. Shibasaki, "Conductance and kinetics of delayed rectifier potassium channels in nodal cells of the rabbit heart.," *J. Physiol.*, vol. 387, pp. 227–50, 1987.
- [77] T. Nakayama and H. Irisawa, "Transient outward current carried by potassium and sodium in quiescent atrioventricular node cells of rabbits," *Circ. res.*, vol. 57, no. 1, pp. 65–73, 1985.
- [78] A. Guia, M. D. Stern, E. G. Lakatta, and I. R. Josephson, "Ion concentration-dependence of rat cardiac unitary l-type calcium channel conductance," *Biophys. J.*, vol. 80, no. 6, pp. 2742–2750, 2001.
- [79] J. Heijman, P. G. Volders, R. L. Westra, and Y. Rudy, "Local control of  $\beta$ -adrenergic stimulation: effects on ventricular myocyte electrophysiology and Ca<sup>2+</sup>-transient," *J. Mol. Cell. Cardiol.*, vol. 50, no. 5, pp. 863–871, 2011.

- [80] D. Benoist, R. Stones, A. P. Benson, E. D. Fowler, M. J. Drinkhill, M. E. Hardy, D. A. Saint, O. Cazorla, O. Bernus, and E. White, "Systems approach to the study of stretch and arrhythmias in right ventricular failure induced in rats by monocrotaline," *Prog. Biophys. Mol. Biol.*, vol. 115, no. 2-3, pp. 162–172, 2014.
- [81] S. N. Healy and A. D. McCulloch, "An ionic model of stretch-activated and stretch-modulated currents in rabbit ventricular myocytes," *Europace*, vol. 7, pp. S128–S134, 2005.
- [82] A. Kamkin, I. Kiseleva, and G. Isenberg, "Stretch-activated currents in ventricular myocytes: amplitude and arrhythmogenic effects increase with hypertrophy," *Cardiovasc. Res.*, vol. 48, no. 3, pp. 409–20, 2000.
- [83] G. Isenberg, V. Kazanski, D. Kondratev, M. F. Gallitelli, I. Kiseleva, and A. Kamkin, "Differential effects of stretch and compression on membrane currents and  $[Na^+]_c$  in ventricular myocytes," *Prog. Biophys. Mol. Biol.*, vol. 82, no. 1-3, pp. 43–56, 2003.
- [84] P. Kohl, K. Day, and D. Noble, "Cellular mechanisms of cardiac mechano-electric feedback in a mathematical model," *Can. J. Cardiol.*, vol. 14, no. 1, pp. 111–9, 1998.
- [85] P. Kohl, P. Hunter, and D. Noble, "Stretch-induced changes in heart rate and rhythm: clinical observations, experiments and mathematical models," *Prog. Biophys. Mol. Biol.*, vol. 71, no. 1, pp. 91–138, 1999.
- [86] J. H. C. Tan, W. Liu, and D. A. Saint, "Differential expression of the mechanosensitive potassium channel TREK-1 in epicardial and endocardial myocytes in rat ventricle," *Exp. Physiol.*, vol. 89, no. 3, pp. 237–242, 2004.
- [87] M. Pagani, N. Montano, A. Porta, A. Malliani, F. M. Abboud, C. Birkett, and V. K. Somers, "Relationship between spectral components of cardiovascular variabilities and direct measures of muscle sympathetic nerve activity in humans," *Circulation*, vol. 95, no. 6, pp. 1441–1448, 1997.
- [88] C. E. Rasmussen and C. K. Williams, *Gaussian processes for machine learning*. MIT Press, 2006.
- [89] S. R. Gunn and J. S. Kandola, "Structural modelling with sparse kernels," *Machine learning*, vol. 48, no. 1-3, pp. 137–163, 2002.
- [90] S. Boyd and L. Vandenberghe, *Convex optimization*. Cambridge university press, 2004.
- [91] D. R. Hardoon, S. Szedmak, and J. Shawe-Taylor, "Canonical Correlation Analysis: An overview with application to learning methods," *Neural Comput.*, vol. 16, no. 12, pp. 2639–2664, 2004.

- [92] X. Zhu, H.-I. Suk, and D. Shen, "Multi-modality canonical feature selection for alzheimer's disease diagnosis," in *International Conference on Medical Image Computing and Computer-Assisted Intervention*, pp. 162–169, Springer, 2014.
- [93] H. Kaya, F. Eyben, A. A. Salah, and B. Schuller, "Cca based feature selection with application to continuous depression recognition from acoustic speech features," in *IEEE International Conference on Acoustics, Speech and Signal Processing (ICASSP)*, pp. 3729–3733, IEEE, 2014.
- [94] D. A. Torres, D. Turnbull, B. K. Sriperumbudur, L. Barrington, and G. R. Lanckriet, "Finding musically meaningful words by sparse cca," in *Neural information processing systems (nips) workshop on music, the brain and cognition*, 2007.
- [95] R. Negoescu, S. Dinca-Panaitescu, V. Filcescu, D. Ionescu, and S. Wolf, "Mental stress enhances the sympathetic fraction of QT variability in an RR-independent way.," *Integr. Physiol. Behav. Sci.*, vol. 32, no. 3, pp. 220–7, 1997.
- [96] K. Satomi, W. Shimizu, H. Takaki, K. Suyama, T. Kurita, N. Aihara, and S. Kamakura, "Response of beat-by-beat QT variability to sympathetic stimulation in the LQT1 form of congenital long QT syndrome," *Heart Rhythm*, vol. 2, no. 2, pp. 149–154, 2005.
- [97] V. P. Long, I. M. Bonilla, P. Vargas-Pinto, Y. Nishijima, A. Sridhar, C. Li, K. Mowrey, P. Wright, M. Velayutham, S. Kumar, N. Y. Lee, J. L. Zweier, P. J. Mohler, S. Györke, and C. A. Carnes, "Heart failure duration progressively modulates the arrhythmia substrate through structural and electrical remodeling," *Life Sci.*, vol. 123, pp. 61–71, 2015.
- [98] M. B. Thomsen, S. C. Verduyn, M. Stengl, J. D. Beekman, G. de Pater, J. van Opstal, P. G. Volders, and M. A. Vos, "Increased short-term variability of repolarization predicts d-sotalol-induced torsades de pointes in dogs," *Circulation*, vol. 110, no. 16, pp. 2453–2459, 2004.
- [99] A. Nummenmaa, T. Auranen, M. S. Hämäläinen, I. P. Jääskeläinen, M. Sams, A. Vehtari, and J. Lampinen, "Automatic relevance determination based hierarchical Bayesian MEG inversion in practice," *Neuroimage*, vol. 37, no. 3, pp. 876–889, 2007.
- [100] J. P. Jacobs, "Bayesian support vector regression with automatic relevance determination kernel for modeling of antenna input characteristics," *IEEE Trans. Antennas Propag.*, vol. 60, no. 4, pp. 2114–2118, 2012.
- [101] P. A. Gorski, D. K. Ceholski, and R. J. Hajjar, "Altered myocardial calcium cycling and energetics in heart failure - a rational approach for disease treatment," *Cell Metab.*, vol. 21, no. 2, pp. 183–194, 2015.

- [102] J. D. Nissen, M. B. Thomsen, B. H. Bentzen, J. G. Diness, T. G. Diness, T. Jespersen, and M. Grunnet, "Attenuated ventricular  $\beta$ -adrenergic response and reduced repolarization reserve in a rabbit model of chronic heart failure," *J. Cardiovasc. Pharmacol.*, vol. 59, no. 2, pp. 142–150, 2012.
- [103] A. Varró and I. Baczkó, "Cardiac ventricular repolarization reserve: a principle for understanding drug-related proarrhythmic risk," *Br. J. Pharmacol.*, vol. 164, no. 1, pp. 14–36, 2011.
- [104] N. S. Dhalla and R. M. Temsah, "Sarcoplasmic reticulum and cardiac oxidative stress: an emerging target for heart disease," *Emerging Ther. Targets*, vol. 5, no. 2, pp. 205–217, 2001.
- [105] X. Guo, X. Gao, Y. Wang, L. Peng, Y. Zhu, and S. Wang, "Iks protects from ventricular arrhythmia during cardiac ischemia and reperfusion in rabbits by preserving the repolarization reserve," *PLoS ONE*, vol. 7, no. 2, 2012.
- [106] A. Sridhar, Y. Nishijima, D. Terentyev, R. Terentyeva, R. Uelmen, M. Kukielka, I. M. Bonilla, G. A. Robertson, S. Györke, G. E. Billman, *et al.*, "Repolarization abnormalities and afterdepolarizations in a canine model of sudden cardiac death," *Am. J. Physiol.: Regul., Integr. Comp. Physiol.*, vol. 295, no. 5, pp. R1463–R1472, 2008.
- [107] M. Meo, O. Meste, S. Signore, A. Sorrentino, A. Cannata, Y. Zhou, A. Matsuda, M. Luciani, R. Kannappan, P. Goichberg, *et al.*, "Reduction in Kv current enhances the temporal dispersion of the action potential in diabetic myocytes: insights from a novel repolarization algorithm," *J. Am. Heart Assoc.*, vol. 5, no. 2, p. e003078, 2016.
- [108] V. A. Maltsev, N. Silverman, H. N. Sabbah, and A. I. Undrovinas, "Chronic heart failure slows late sodium current in human and canine ventricular myocytes: implications for repolarization variability," *Eur. J. heart failure*, vol. 9, no. 3, pp. 219–227, 2007.
- [109] L. Wu, D. Guo, H. Li, J. Hackett, G.-X. Yan, Z. Jiao, C. Antzelevitch, J. C. Shryock, and L. Belardinelli, "Role of late sodium current in modulating the proarrhythmic and antiarrhythmic effects of quinidine," *Heart Rhythm*, vol. 5, no. 12, pp. 1726–1734, 2008.
- [110] T. R. Stams, P. Oosterhoff, A. Heijdel, A. Dunnink, J. D. Beekman, R. van der Nagel, H. V. van Rijen, M. A. van der Heyden, and M. A. Vos, "Beat-to-beat variability in preload unmasks latent risk of Torsade de Pointes in anesthetized chronic atrioventricular block dogs," *Circulation*, vol. 80, no. 6, pp. 1336–1345, 2016.
- [111] M. Veldkamp, A. Verkerk, A. Van Ginneken, A. Baartscheer, C. Schumacher, N. De Jonge, J. de Bakker, and T. Opthof, "Norepinephrine induces action potential prolongation and early afterdepolarizations in ventricular myocytes isolated

- from human end-stage failing hearts,” *Eur. Heart J.*, vol. 22, no. 11, pp. 955–963, 2001.
- [112] C. Lang, M. Menza, S. Jochem, G. Franke, S. P. Feliz, M. Brunner, G. Koren, M. Zehender, H. Bugger, B. Jung, *et al.*, “Electro-mechanical dysfunction in long QT syndrome: role for arrhythmogenic risk prediction and modulation by sex and sex hormones,” *Prog. Biophys. Mol. Biol.*, vol. 120, no. 1-3, pp. 255–269, 2016.
- [113] S. M. Pogwizd, K. Schlotthauer, L. Li, W. Yuan, and D. M. Bers, “Arrhythmogenesis and contractile dysfunction in heart failure: roles of sodium-calcium exchange, inward rectifier potassium current, and residual  $\beta$ -adrenergic responsiveness,” *Circ. Res.*, vol. 88, no. 11, pp. 1159–1167, 2001.
- [114] A. I. Undrovinas, L. Belardinelli, N. A. Undrovinas, and H. N. Sabbah, “Ranolazine improves abnormal repolarization and contraction in left ventricular myocytes of dogs with heart failure by inhibiting late sodium current,” *J. Cardiovas. Electrophysiol.*, vol. 17, pp. S169–S177, 2006.
- [115] E. Tixier, D. Lombardi, B. Rodriguez, and J.-F. Gerbeau, “Modelling variability in cardiac electrophysiology: a moment-matching approach,” *J. R. Soc., Interface*, vol. 14, no. 133, p. 20170238, 2017.
- [116] D. M. Johnson and G. Antoons, “Arrhythmogenic Mechanisms in Heart Failure: Linking  $\beta$ -Adrenergic Stimulation, Stretch, and Calcium,” *Front. Physiol.*, vol. 9, p. 1453, 2018.
- [117] R. V. Madhvani, M. Angelini, Y. Xie, A. Pantazis, S. Suriany, N. P. Borgstrom, A. Garfinkel, Z. Qu, J. N. Weiss, and R. Olcese, “Targeting the late component of the cardiac L-type  $\text{Ca}^{2+}$  current to suppress early afterdepolarizations,” *J. Gen. Physiol.*, vol. 145, no. 5, pp. 395–404, 2015.
- [118] A. Bauer, M. Klemm, K. D. Rizas, W. Hamm, L. von Stülpnagel, M. Dommasch, A. Steger, A. Lubinski, P. Flevari, M. Harden, T. Friede, S. Kääb, B. Merkely, C. Sticherling, R. Willems, H. Huikuri, M. Malik, G. Schmidt, M. Zabel, B. Merkely, P. Perge, Z. Sallo, G. Szeplaki, M. Zabel, L. Lüthje, S. Schlögl, H. Haarmann, L. Bergau, J. Seegers, G. Hasenfuß, P. Munoz-Exposito, T. Tichelbäcker, A. Kirova, T. Friede, M. Harden, M. Malik, K. Hnatkova, M. Vos, S. N. Willich, T. Reinhold, R. Willems, B. Vandenberk, M. Klinika, K. Toplice, P. Flevari, A. Katsimardos, D. Katsaras, R. Hatala, M. Svetlosak, A. Lubinski, T. Kuczejko, J. Hansen, C. Sticherling, D. Conen, S. Milosrdnice, N. Pavlović, Š. Manola, O. Vinter, I. Benko, A. Tuinenburg, A. Bauer, C. Meyer-Zürn, C. Eick, J. Hastrup, J. Brugada, E. Arbelo, G. Kaliska, J. Martinek, M. Dommasch, A. Steger, S. Kääb, M. F. Sinner, K. D. Rizas, W. Hamm, N. Vdovin, M. Klemm, L. von Stülpnagel, I. Cygankiewicz, P. Ptaszynski, K. Kaczmarek, I. Poddebska, S. Iovev, T. Novotný, M. Kozak, H. Huikuri, T. Kenttä, A. Pelli, J. D. Kasprzak, D. Qavoq, S. Brusich, E. Avdovic, M. Klasan, J. Galuszka,

- M. Taborsky, V. Velchev, R. Dissmann, P. Guzik, D. Bimmel, C. Lieberz, S. Stefanow, N. Rüb, C. Wolpert, L. S. Maier, S. Behrens, Z. Jurisic, F. Braunschweig, F. Blaschke, B. Pieske, Z. Bakotic, A. Anic, R. H. Schwinger, and P. Platonov, "Prediction of mortality benefit based on periodic repolarisation dynamics in patients undergoing prophylactic implantation of a defibrillator: a prospective, controlled, multicentre cohort study," *Lancet*, vol. 0, no. 0, 2019.
- [119] D. J. Sprenkeler, J. D. M. Beekman, A. Bossu, A. Dunnink, and M. A. Vos, "Pro-Arrhythmic Ventricular Remodeling Is Associated With Increased Respiratory and Low-Frequency Oscillations of Monophasic Action Potential Duration in the Chronic Atrioventricular Block Dog Model," *Frontiers in Physiology*, vol. 10, p. 1095, 2019.
- [120] F. Ruzsnaszky, B. Hegyi, K. Kistamás, K. Váczi, B. Horváth, N. Szentandrassy, T. Bányász, P. P. Nánási, and J. Magyar, "Asynchronous activation of calcium and potassium currents by isoproterenol in canine ventricular myocytes," *Naunyn-Schmiedeberg's archives of pharmacology*, vol. 387, no. 5, pp. 457–467, 2014.
- [121] G.-X. Liu, B.-R. Choi, O. Ziv, W. Li, E. de Lange, Z. Qu, and G. Koren, "Differential conditions for early after-depolarizations and triggered activity in cardiomyocytes derived from transgenic LQT1 and LQT2 rabbits," *J. Physiol.*, vol. 590, no. 5, pp. 1171–1180, 2012.
- [122] R. Furlan, A. Porta, F. Costa, J. Tank, L. Baker, R. Schiavi, D. Robertson, A. Malliani, and R. Mosqueda-Garcia, "Oscillatory patterns in sympathetic neural discharge and cardiovascular variables during orthostatic stimulus," *Circulation*, vol. 101, no. 8, pp. 886–92, 2000.
- [123] G. Iribe, T. Kaneko, Y. Yamaguchi, and K. Naruse, "Load dependency in force-length relations in isolated single cardiomyocytes," *Prog. Biophys. Mol. Biol.*, vol. 115, no. 2-3, pp. 103–114, 2014.
- [124] S. A. Niederer and N. P. Smith, "A mathematical model of the slow force response to stretch in rat ventricular myocytes," *Biophys. J.*, vol. 92, no. 11, pp. 4030–4044, 2007.
- [125] R. Guinamard, M. Demion, C. Magaud, D. Potreau, and P. Bois, "Functional Expression of the TRPM4 Cationic Current in Ventricular Cardiomyocytes From Spontaneously Hypertensive Rats," *Hypertension*, vol. 48, no. 4, pp. 587–594, 2006.
- [126] E. Pueyo, P. Smetana, P. Caminal, A. DeLuna, M. Malik, and P. Laguna, "Characterization of QT Interval Adaptation to RR Interval Changes and Its Use as a Risk-Stratifier of Arrhythmic Mortality in Amiodarone-Treated Survivors of Acute Myocardial Infarction," *IEEE Trans. Biomed. Eng.*, vol. 51, no. 9, pp. 1511–1520, 2004.



- [127] E. Pueyo, M. Malik, and P. Laguna, "A dynamic model to characterize beat-to-beat adaptation of repolarization to heart rate changes," *Biomed. Signal Process. Control*, vol. 3, no. 1, pp. 29–43, 2008.
- [128] E. Nosakhare, G. C. Verghese, R. C. Tasker, and T. Heldt, "Qt interval adaptation to changes in autonomic balance," in *Comput. in Cardiology*, vol. 41, pp. 605–608, 2014.
- [129] L. Wang, S. Morotti, S. Tapa, S. D. Francis Stuart, Y. Jiang, Z. Wang, R. C. Myles, K. E. Brack, G. A. Ng, D. M. Bers, E. Grandi, and C. M. Ripplinger, "Different paths, same destination: divergent action potential responses produce conserved cardiac fight-or-flight response in mouse and rabbit hearts," *J. Physiol.*, vol. 597, no. 15, pp. 3867–3883, 2019.
- [130] P. G. Volders, M. Stengl, J. M. van Opstal, U. Gerlach, R. L. Spätjens, J. D. Beekman, K. R. Sipido, and M. A. Vos, "Probing the Contribution of  $I_{Ks}$  to Canine Ventricular Repolarization," *Circulation*, vol. 107, no. 21, pp. 2753–2760, 2003.
- [131] M. Varshneya, R. A. Devenyi, and E. A. Sobie, "Slow Delayed Rectifier Current Protects Ventricular Myocytes From Arrhythmic Dynamics Across Multiple Species," *Circ. Arrhythm. Electrophysiol.*, vol. 11, no. 10, p. e006558, 2018.
- [132] D. S. Rosenbaum, "T wave alternans: A mechanism of arrhythmogenesis comes of age after 100 years," *J. Cardiovasc. Electrophysiol.*, vol. 12, no. 2, pp. 207–209, 2001.
- [133] B. Porter, M. J. Bishop, S. Claridge, N. Child, S. Van Duijvenboden, J. Bostock, B. J. Sieniewicz, J. Gould, B. Sidhu, B. Hanson, Z. Chen, C. A. Rinaldi, P. Taggart, and J. S. Gill, "Left ventricular activation-recovery interval variability predicts spontaneous ventricular tachyarrhythmia in patients with heart failure," *Heart Rhythm*, vol. 16, no. 5, pp. 702–709, 2019.
- [134] Y. Xie, L. T. Izu, D. M. Bers, and D. Sato, "Arrhythmogenic Transient Dynamics in Cardiac Myocytes," *Biophys. J.*, vol. 106, no. 6, pp. 1391–1397, 2014.
- [135] Y. Xie, E. Grandi, D. M. Bers, and D. Sato, "How does  $\beta$ -adrenergic signalling affect the transitions from ventricular tachycardia to ventricular fibrillation?," *Europace*, vol. 16, no. 3, pp. 452–457, 2014.
- [136] J. Winter, M. J. Tipton, and M. J. Shattock, "Autonomic conflict exacerbates long QT associated ventricular arrhythmias," *J. Mol. Cell. Cardiol.*, vol. 116, pp. 145–154, 2018.
- [137] G. Szabó, N. Szentandrassy, T. Bíró, B. I. Tóth, G. Czifra, J. Magyar, T. Bányász, A. Varró, L. Kovács, and P. P. Nánási, "Asymmetrical distribution of ion channels in canine and human left-ventricular wall: epicardium versus midmyocardium," *Pfluegers Arch.-Eur. J. Physiol.*, vol. 450, no. 5, pp. 307–316, 2005.

- [138] N. Szentandrásy, T. Bányász, T. Biro, G. Szabó, B. Toth, J. Magyar, J. Lazar, A. Várro, L. Kovacs, and P. P. Nánási, “Apico-basal inhomogeneity in distribution of ion channels in canine and human ventricular myocardium,” *Cardiovasc. Res.*, vol. 65, no. 4, pp. 851–860, 2005.
- [139] J. Magyar, K. Kistamás, K. Váczi, B. Hegyi, B. Horváth, T. Bányász, P. P. Nánási, and N. Szentandrásy, “Concept of relative variability of cardiac action potential duration and its test under various experimental conditions,” *Gen. Physiol. Biophys.*, vol. 35, no. 1, pp. 55–62, 2016.
- [140] M. Zaniboni, F. Cacciani, and N. Salvarani, “Temporal variability of repolarization in rat ventricular myocytes paced with time-varying frequencies,” *Exp. Physiol.*, vol. 92, no. 5, pp. 859–869, 2007.
- [141] C. Antzelevitch, S. Sicouri, S. H. Litovsky, A. Lukas, S. C. Krishnan, J. M. Di Diego, G. A. Gintant, and D. W. Liu, “Heterogeneity within the ventricular wall. Electrophysiology and pharmacology of epicardial, endocardial, and M cells,” *Circ. Res.*, vol. 69, no. 6, pp. 1427–1449, 1991.
- [142] R. Varkevisser, S. C. Wijers, M. A. van der Heyden, J. D. Beekman, M. Meine, and M. A. Vos, “Beat-to-beat variability of repolarization as a new biomarker for proarrhythmia in vivo,” *Heart Rhythm*, vol. 9, no. 10, pp. 1718–1726, 2012.
- [143] J. W. Waks, E. Z. Soliman, C. A. Henrikson, N. Sotoodehnia, L. Han, S. K. Agarwal, D. E. Arking, D. S. Siscovick, S. D. Solomon, W. S. Post, M. E. Josephson, J. Coresh, and L. G. Tereshchenko, “Beat-to-Beat Spatiotemporal Variability in the T Vector Is Associated With Sudden Cardiac Death in Participants Without Left Ventricular Hypertrophy: The Atherosclerosis Risk in Communities (ARIC) Study,” *Journal of the American Heart Association*, vol. 4, no. 1, pp. e001357–e001357, 2015.
- [144] Y. Sobue, E. Watanabe, M. Yamamoto, K. Sano, H. Harigaya, K. Okuda, and Y. Ozaki, “Beat-to-beat variability of T-wave amplitude for the risk assessment of ventricular tachyarrhythmia in patients without structural heart disease,” *Europace*, vol. 13, no. 11, pp. 1612–1618, 2011.
- [145] C. Lerma, T. Krogh-Madsen, M. Guevara, and L. Glass, “Stochastic aspects of cardiac arrhythmias,” *J. Stat. Phys.*, vol. 128, no. 1-2, pp. 347–374, 2007.
- [146] A. J. Tanskanen, J. L. Greenstein, B. O’Rourke, and R. L. Winslow, “The role of stochastic and modal gating of cardiac L-type Ca<sup>2+</sup> channels on early afterdepolarizations,” *Biophys. J.*, vol. 88, no. 1, pp. 85–95, 2005.
- [147] G.-R. Li, J. Feng, L. Yue, and M. Carrier, “Transmural heterogeneity of action potentials and Ito1 in myocytes isolated from the human right ventricle,” *Am. J. Physiol.: Heart Circ. Physiol.*, vol. 275, no. 2, pp. H369–H377, 1998.

- [148] A. Muszkiewicz, O. J. Britton, P. Gemmell, E. Passini, C. Sánchez, X. Zhou, A. Carusi, T. A. Quinn, K. Burrage, A. Bueno-Orovio, and B. Rodriguez, “Variability in cardiac electrophysiology: using experimentally-calibrated populations of models to move beyond the single virtual physiological human paradigm,” *Prog. Biophys. Mol. Biol.*, vol. 120, no. 1-3, pp. 115–127, 2016.
- [149] B. A. J. Lawson, C. C. Drovandi, N. Cusimano, P. Burrage, B. Rodriguez, and K. Burrage, “Unlocking data sets by calibrating populations of models to data density: A study in atrial electrophysiology,” *Sci. Adv.*, vol. 4, no. 1, p. e1701676, 2018.
- [150] A. X. Sarkar and E. A. Sobie, “Quantification of repolarization reserve to understand interpatient variability in the response to proarrhythmic drugs: A computational analysis,” *Heart Rhythm*, vol. 8, no. 11, pp. 1749–1755, 2011.
- [151] A. X. Sarkar, D. J. Christini, and E. A. Sobie, “Exploiting mathematical models to illuminate electrophysiological variability between individuals,” *J. Physiol.*, vol. 590, no. 11, pp. 2555–2567, 2012.
- [152] O. J. Britton, A. Bueno-Orovio, K. Van Ammel, H. R. Lu, R. Towart, D. J. Gallacher, and B. Rodriguez, “Experimentally calibrated population of models predicts and explains intersubject variability in cardiac cellular electrophysiology,” *Proc. Natl. Acad. Sci.*, vol. 110, no. 23, pp. E2098–E2105, 2013.
- [153] J. Walmsley, G. R. Mirams, J. Pitt-Francis, B. Rodriguez, and K. Burrage, “Application of stochastic phenomenological modelling to cell-to-cell and beat-to-beat electrophysiological variability in cardiac tissue,” *J. Theor. Biol.*, vol. 365, pp. 325–336, 2015.
- [154] R. H. Johnstone, E. T. Y. Chang, R. Bardenet, T. P. de Boer, D. J. Gavaghan, P. Pathmanathan, R. H. Clayton, and G. R. Mirams, “Uncertainty and variability in models of the cardiac action potential: Can we build trustworthy models?,” *J. Mol. Cell. Cardiol.*, vol. 96, pp. 49–62, 2016.
- [155] E. T. Chang, M. Strong, and R. H. Clayton, “Bayesian sensitivity analysis of a cardiac cell model using a Gaussian Process emulator,” *PLoS One*, vol. 10, no. 6, 2015.
- [156] R. H. Johnstone, R. Bardenet, D. J. Gavaghan, L. Polonchuk, M. R. Davies, and G. R. Mirams, “Hierarchical Bayesian modeling of variability and uncertainty in synthetic action potential traces,” in *Comput. in Cardiology*, vol. 43, pp. 1089–1092, 2017.
- [157] Z. Syed, E. Vigmond, S. Nattel, and L. J. Leon, “Atrial cell action potential parameter fitting using genetic algorithms,” *Med. Biol. Eng. Comput.*, vol. 43, no. 5, pp. 561–571, 2005.
- [158] S. Särkkä, *Bayesian filtering and smoothing*, vol. 3. Cambridge University Press, 2013.

- [159] S. J. Julier and J. K. Uhlmann, "A new extension of the Kalman filter to Non-linear systems," in *AeroSense '97*, pp. 182–193, Proc. of AeroSense: The 11th Int. Symp. on Aerospace/Defence Sensing, Simulation and Controls., 1997.
- [160] R. Van Der Merwe, E. A. Wan, and S. Julier, "Sigma-point Kalman filters for nonlinear estimation and sensor-fusion: Applications to integrated navigation," in *Proc. AIAA Guidance, Navigation & Control Conference*, pp. 16–19, 2004.
- [161] J. Fernandez-Bes, D. A. Sampedro-Puente, and E. Pueyo, "Identification of parameters describing phenomenological cardiac action potential models using sigma-point methods," in *Comput. in Cardiology*, vol. 44, 2017.
- [162] G. D. Smith, "Modeling the stochastic gating of ion channels," in *Computational cell biology*, pp. 285–319, Springer, 2002.
- [163] Y. Chen and X. Ye, "Projection onto a simplex," *arXiv preprint arXiv:1101.6081*, 2011.
- [164] J. Carro, J. F. Rodríguez-Matas, V. Monasterio, and E. Pueyo, "Limitations in electrophysiological model development and validation caused by differences between simulations and experimental protocols," *Prog. Biophys. Mol. Biol.*, 2016.
- [165] T. Furukawa, S. Kimura, N. Furukawa, A. L. Bassett, and R. J. Myerburg, "Potassium rectifier currents differ in myocytes of endocardial and epicardial origin.," *Circ. Res.*, vol. 70, pp. 91–103, 1992.
- [166] S. Haykin, *Adaptive filter theory*. Pearson Higher Ed, 2013.
- [167] S. Julier and J. Uhlmann, "Unscented filtering and nonlinear estimation," *Proc. IEEE*, vol. 92, no. 3, pp. 401–422, 2004.
- [168] O. A. Chkrebtii, D. A. Campbell, B. Calderhead, M. A. Girolami, *et al.*, "Bayesian solution uncertainty quantification for differential equations," *Bayesian Anal.*, vol. 11, no. 4, pp. 1239–1267, 2016.
- [169] S. Diop and M. Fliess, "Nonlinear observability, identifiability, and persistent trajectories," in *1991 Proc. IEEE Conf. Decision and Control*, pp. 714–718, IEEE, 1991.
- [170] J. Schumann-Bischoff and U. Parlitz, "State and parameter estimation using unconstrained optimization," *Phys. Rev. E*, vol. 84, no. 5, p. 056214, 2011.
- [171] N. Jost, L. Virág, M. Bitay, J. Takács, C. Lengyel, P. Biliczki, Z. Nagy, G. Bogáts, D. A. Lathrop, J. G. Papp, *et al.*, "Restricting excessive cardiac action potential and QT prolongation: a vital role for IKs in human ventricular muscle," *Circulation*, vol. 112, no. 10, pp. 1392–1399, 2005.

- [172] T. O'Hara and Y. Rudy, "Quantitative comparison of cardiac ventricular myocyte electrophysiology and response to drugs in human and nonhuman species.," *Am. J. Physiol.: Heart Circ. Physiol.*, vol. 302, no. 5, pp. H1023–30, 2012.
- [173] S. Dokos and N. H. Lovell, "Parameter estimation in cardiac ionic models," *Prog. Biophys. Mol. Biol.*, vol. 85, no. 2-3, pp. 407–431, 2004.
- [174] A. C. Daly, D. J. Gavaghan, C. Holmes, and J. Cooper, "Hodgkin–Huxley revisited: reparametrization and identifiability analysis of the classic action potential model with approximate Bayesian methods," *R. Soc. Open Sci.*, vol. 2, no. 12, p. 150499, 2015.
- [175] J. Ramírez, M. Orini, A. Mincholé, V. Monasterio, I. Cygankiewicz, A. B. de Luna, J. P. Martínez, E. Pueyo, and P. Laguna, "T-wave morphology restitution predicts sudden cardiac death in patients with chronic heart failure," *J. Am. Heart Assoc.*, vol. 6, no. 5, 2017.
- [176] R. E. Bellman, *Adaptive control processes: a guided tour*, vol. 2045. Princeton university press, 2015.
- [177] D. Lombardi and F. Raphel, "A greedy dimension reduction method for classification problems," *HAL*, pp. hal-02280502, 2019.
- [178] D. M. Hawkins, "The problem of overfitting," *J. Chem. Inf. Comput. Sci.*, vol. 44, no. 1, pp. 1–12, 2004.
- [179] B. Pieske, L. S. Maier, V. Piacentino, J. Weisser, G. Hasenfuss, and S. Houser, "Rate Dependence of  $[Na_i^+]$  and Contractility in Nonfailing and Failing Human Myocardium," *Circulation*, vol. 106, no. 4, pp. 447–453, 2002.
- [180] U. Schmidt, R. J. Hajjar, P. A. Helm, C. S. Kim, A. A. Doye, and J. K. Gwathmey, "Contribution of Abnormal Sarcoplasmic Reticulum ATPase Activity to Systolic and Diastolic Dysfunction in Human Heart Failure," *Journal of Molecular and Cellular Cardiology*, vol. 30, pp. 1929–1937, oct 1998.
- [181] E. A. Wan and R. van der Merwe, "The Unscented Kalman Filter," in *Kalman Filtering and Neural Networks*, pp. 221–280, John Wiley & Sons, Inc., 2001.
- [182] C. Bertoglio, P. Moireau, and J.-F. Gerbeau, "Sequential parameter estimation for fluid-structure problems: Application to hemodynamics," *Int. J. Numer. Meth. Biomed. Engng.*, vol. 28, no. 4, pp. 434–455, 2012.
- [183] D. A. Sampedro-Puente, J. Fernandez-Bes, B. Porter, S. van Duijvenboden, P. Taggart, and E. Pueyo, "Mechanisms Underlying Interactions Between Low-Frequency Oscillations and Beat-to-Beat Variability of Cellular Ventricular Repolarization in Response to Sympathetic Stimulation: Implications for Arrhythmogenesis," *Front. Physiol.*, vol. 10, p. 916, 2019.

- [184] C. Sánchez, A. Bueno-Orovio, E. Wettwer, S. Loose, J. Simon, U. Ravens, E. Pueyo, and B. Rodriguez, “Inter-subject variability in human atrial action potential in sinus rhythm versus chronic atrial fibrillation,” *PLoS ONE*, vol. 9, no. 8, 2014.
- [185] D. A. Sampredo-Puente, J. Fernandez-Bes, and E. Pueyo, “Data-driven Identification of Stochastic Model Parameters and State Variables: Application to the Study of Cardiac Beat-to-beat Variability,” *J. Biomed. Health Inform.*, no. 5, pp. 1697–1722, 2019.

